AWARD NO. DE-FG22-92PC92527-O

FINAL REPORT

Research Period: September 18, 1992 - December 17, 1995

HINDERED DIFFUSION OF COAL LIQUIDS

Theodore T. Tsotsis, Co-Principal Investigator

Muhammad Sahimi, Co-Principal Investigator

University of Southern California

Department of Chemical Engineering

Los Angeles, California 90089-1211

Ian A. Webster, Co-Principal Investigator

UNOCAL Corporation

1201 West 5th Street

Los Angeles, California 90051

DISCLAIMER

PREFACE

A significant portion of the experimental work on this grant (DE-FG22-92PC92527) was performed with coal-derived materials. However, much of the data from this work was part of an unfinished doctoral thesis that has been lost due to circumstances beyond the control of the authors and the Department of Energy. Readers are cautioned to view the Final Report and Addendum accordingly. A publication resulting from this work (Yang, L., Zhu, Y. and Tsotsis, T. T., 1996,"The Use of Inorganic Membranes in Reactive Liquid Phase Applications" *Proceedings of the Fourth International Conference on Inorganic Membranes*, D. G. Fain, ed., 128-142) contains the following reference which is not available: Yang, L., "The Use of Membranes in the Study of Coal Liquids," 1996, Ph.D. Thesis, University of Southern California.

TABLE OF CONTENTS

HINDERED DIFFUSION OF COAL LIQUIDS

INTRODUCTION

The design of industrial catalysts requires that the diffusivity of the reacting species within the catalyst be accurately known. Nowhere is this more important than in the area of coal liquefaction and upgrading of coal liquids. In this area one is faced with the task of processing a number of heavy oils, containing metals and other contaminants, in a variety of process dependent solvents. It is important, therefore, on the basis of predicting catalyst activity, selectivity, and optimizing reactor performance, that the diffusivities of these oil species be accurately known.

Several studies exist [1], emphasizing the importance of diffusion in processes involving coal and petroleum liquids. Spry and Sawyer [2] measured the demetallization rates of a crude oil using various catalysts and found these rates to depend on average pore size, in agreement with their simple model, based on the theory of Anderson and Quinn [3]. Inoguchi [4] observed that optimum activity for desulfurization of heavy crudes occurs with catalysts with pore sizes of 100Å and for vanadium removal with pore sizes between 120 and 140Å. Eigenson *et al.* [5] found increased catalytic activity for MoO_3 on Al_2O_3, when the pore size increased from 70 to 150Å. Significant intraparticle diffusion effects have been observed during asphaltene cracking and the desulfurization of asphaltenic and nonasphaltenic fractions of a residuum by Philippopoulos and Papayannakos [6]. Ternan and coworkers [7] have reported significant pore size effects during the catalytic processing of Athabasca bitumen. Studies have also been published on the importance of intraparticle diffusion during coal liquefaction and coal liquid upgrading, including those of Polinski and coworkers [8], Scooter and Crynes [9], and Yen *et al.* [10]. Workers at Amoco have found [11] that micropore volume in a critical pore size range, i.e. narrowly distributed about 120Å diameter pores, was very important in coal liquefaction catalyst activity. McCormick *et al.* [12] have shown during their hydrotreating studies that activities for both hydrogenation and dehydrogenation reactions are highly correlated ($>$ 99% confidence) with the pore volume in the preferred range (60-200Å) in diameter. The importance of catalyst average pore diameter and pore length during the hydrocracking of solvent refined coals and lignites has been discussed by Berg and Kim [13]. Theoretical studies have also been published, which incorporate hindered diffusion in order to predict optimal pore sizes during petroleum liquid upgrading [14] and catalytic coal liquefaction [15].

The molecules comprising coal liquids can range from less than 10 to several hundred Å in diameter. Their size is, therefore, comparable to the average pore size of most hydroprocessing catalysts. Thus, during processing, transport of these molecules into the catalyst occurs mainly by "configurational" or "hindered diffusion," which is the result of two phenomena occurring in

the pores; the distribution of solute molecules in the pores is affected by the pores and the solute molecules experience an increased hydrodynamic drag. The field of hindered diffusion has been reviewed by Deen [16]. The earliest studies in the field were by Renkin *et al.* [17]. Based on the work of Ferry [18], they developed an expression to describe hindered diffusion

$$\frac{D_e}{D_b} = (1-\lambda)^2(1 - 2.1044\lambda + 2.089\lambda^3 - 0.948\lambda^5) \quad , \tag{1}$$

where D_e is the effective "hindered" diffusivity, D_b the bulk diffusivity and λ the ratio of solute to pore radius. The first factor in this expression accounts for the partitioning effect, and the second for increased hydrodynamic drag in the pore. Anderson and Quinn [3] and Brenner and Gaydos [19] have theoretically verified these results in the region of small λs (their work is a generalization of Taylor-Aris dispersion theory [20] for spherical molecules with sizes comparable to the diameter of the cylindrical tube). A number of other theoretical studies have also been devoted to this problem [21]. Since the work of Renkin *et al.* [17], there have been a number of additional experimental studies of diffusion in restricted porous environments. Satterfield *et al.* [22] investigated hindered diffusion of binary systems of paraffins and aromatic hydrocarbons in silica alumina catalysts. They concluded that reduced diffusivity, in these systems, was only due to the hydrodynamic effects and their results indicate a linear dependence of $\ln(D_e/D_b)$ on λ.

Prasher *et al.* [23] also carried out studies using hydrocarbon solutes in aromatic and hydroparaffinic solvents. Contrary to Satterfield's results, they observed a solute partitioning effect dependent on the nature of the diffusing chemical species, rather than its molecular size, as one expects based on Renkin's theory. Colton *et al.* [24] studied diffusion of proteins and polystyrene in porous glass and found that protein diffusion follows Renkin's theory, while polystyrene behaves as a free draining molecule. Cannel and Rondelez [25] measured diffusion of polystyrene through a Nuclepore membrane and found that polystyrene diffusion follows Renkin's theory, if λ is corrected by a factor of 1.45. The above studies have been useful in showing that reduced diffusivities are observed in restricted environments. The pore systems utilized, however, were not well-defined and probably too complex to allow for fundamental questions to be answered. In the sixties, well-defined planar porous systems were developed. Price and Walker [26] demonstrated that uniform parallel pores of molecular dimensions can be formed, by a track etching process, in a number of alumino-silicate materials. Mica membranes prepared by this method were subsequently utilized in diffusivity measurements of nonhydrocarbon systems [27].

Studies of diffusion of petroleum and coal liquids are recent and few in number. In one of the earliest studies, Thrash and Pildes [28] studied the transport of asphaltenes derived from a Middle East high sulfur vacuum resid through mica membranes. The mica membranes had a pore diameter of $\sim$ 1200Å. Thrash and Pildes claim that what they measure are bulk diffusivities from

which they calculate Stokes-Einstein diameters of 16Å. For the asphaltene concentration range of their experiments (50-500 ppm), they report no evidence of asphaltene molecular association. Shimura *et al.* [29] studied asphaltene diffusion in toluene through porous catalysts by uptake-type experiments. The bulk diffusivity of molecular weight (MW) fractionated petroleum pitches in dilute chloroform solutions was measured in a Northrup-McBain diaphragm cell by Sakai and coworkers [30]. Their studies led them to conclude that the pitch molecules examined are three-dimensional structures with an oblate ellipsoidal shape, their equatorial diameter being 10-20Å and their axial ratio between 1 and 3. Jost *et al.* [31] also measured the bulk diffusivities of various oil residues in a THF/methanol solution by Taylor dispersion techniques. Recently, Mieville *et al.* [32] measured the diffusion of various asphaltenes, by uptake experiments, through catalysts with both unimodal and bimodal pore size distributions. In their experiments, Hondo asphaltene was found to have the highest diffusivity, which was attributed to its smaller average aromatic cluster.

Configurational diffusivity measurements of petroleum liquids, utilizing mica membranes, were first made by Baltus and Anderson [33] using a Wicke-Kallenbach-type diffusion cell to measure the diffusivity, through mica membranes, of asphaltenes derived from Kuwaiti atmospheric bottoms. They divided the overall MW range into five regions and assigned each to a "hypothetical" asphaltene fraction. Using GPC, they measured the diffusivity of each fraction for pore diameters ranging from 160 to 4400Å. An experimental expression was found to relate the diffusivity D_e of each fraction to its bulk diffusivity D_∞, i.e. $D_e/D_\infty = \exp(-3.89\lambda)$. Following the work of Baltus and Anderson, two other research groups have, in the last five years or so, focused their attention on the study of hindered transport of petroleum liquid macromolecules through restricted porous environments. Baltus and coworkers [34] have measured the diffusivity through polycarbonate and polyester membranes of asphaltenes isolated from Athabasca tar sand bitumen vacuum bottoms and a vacuum resid from a blend of Canadian crudes. They have also coupled the diffusivity measurements with intrinsic viscosity measurements of asphaltene solutions. Using models previously developed by Garcia de la Torre and Bloomfield [35], which represent the asphaltene in terms of assemblages of solid spheres, and by varying the size and number of such spheres, they were able to obtain a reasonable fit between their experimental results and theory.

Our group has also studied the diffusivity of petroleum derived asphaltenes [36]. We have investigated asphaltenes derived from a variety of California heavy crudes. Although our studies, in some aspects, paralleled those of Baltus and coworkers, our main objective was distinctly different from their objective. Voluminous literature exists on the detailed chemical structure of asphaltenes and other petroleum and coal liquid fractions like resins and oils. For asphaltenes, in particular, interest in their structure and reactive and transport properties has been steadily increasing among

those working in the field of petroleum and coal liquid upgrading.

The term asphaltenes has been historically used to collectively describe the chemical components of a crude (or a coal liquid), which are generally more polar and larger in size. Since the earlier stages of the field of heavy oil upgrading, asphaltenes were defined as a solubility class of various components. Through the years, this definition attracted discussion and criticism (see, for example, Bunger and Cogswell [37]). Since some asphaltene properties are dependent on their isolation techniques, the relevant question here is whether or not the asphaltenes produced by such isolation techniques bear any resemblance and similarity to compounds found in the original crude, and whether or not the asphaltenes themselves exist in the original crude rather than simply being an artifact of their separation process. The debate over whether or not asphaltenes even exist, and if they do, how does one properly isolate and characterize them, has continued for years and will not be dealt with here. Comprehensive descriptions can be found in a number of papers [38]. The generally held view today is that asphaltenes do exist and are found in the original resid. One, however, cannot uniquely characterize an asphaltene (and, for that matter, any other resid fraction) based on a single property alone, such as solubility. For petroleum resids, two properties are needed to differentiate one resid fraction from the other. Which two properties one should use, however, still remains a matter of debate. In his pioneering paper, Long [39] first suggested that the composition of petroleum liquids can be represented in terms of a plot of MW versus polarity. Long and Speight [39], furthermore, opted to use the solubility parameter as a measure of polarity and the 5% and 95% points of the MW distribution (as measured by GPC) as a measure of the MW. Wiehe [38], on the other hand, uses the number average MW (as measured by VPO) as a measure of MW and the average hydrogen content as a measure of the molecular attraction. For coal liquids, a measure of molecular attraction involving oxygen functionality would be required in addition to the average hydrogen content (in lieu of aromacity) and MW. This was the conclusion of Snape and Bartle [40] who found that three independent variables, i.e. number average MW, the proportion of internal aromatic carbon to total carbon and the percent acidic OH were needed to distinguish between benzene insolubles, asphaltenes and *n*-pentane solubles for coal-derived liquids.

Generally, the heavier the liquid one deals with, the larger the percentage of asphaltenes one finds in it. One of the obstacles in coal liquid (and resid) upgrading is the presence of heteroatoms, such as sulfur, nitrogen, oxygen and metals, which poison the catalysts used for hydroprocessing. In terms of composition, asphaltenes contain a greater percentage of heteroatoms than all other fractions and, therefore, present the greatest challenge during resid upgrading. Furthermore, most of the molecular components of an asphaltene are very large structures with sizes approaching that of a typical catalyst pore. Hydroprocessing of asphaltenes involves a number of parallel and/or

consecutive reactions like hydrodesulfurization, hydrodenitrogenization, hydrodemetallation and cracking. Due to the large size of most asphaltene entities, all these reactions, as they occur within the catalyst pellets, are diffusion limited.

For many years, asphaltene and resid upgrading rector design has utilized the concept of asphaltenes being a single molecular entity, to which one can assign a unique effective diffusivity and other effective transport properties. This was one of the first issues we addressed in our studies of asphaltene diffusivity. Our experiments showed that the effective diffusivity of an asphaltene, as measured in a standard Wicke-Kallenbach cell using model porous membranes, varies as a function of experimental time by as much as an order of magnitude for the duration of an experimental run [36]. The diffusivity, furthermore, is a strong function of temperature and pressure, and whether the membrane is impregnated with a catalyst or not. One cannot, therefore, assign a unique experimental diffusivity value to an asphaltene molecule. Our experimental findings, though new, were surprising neither to us nor to those intimately involved in research on asphaltene chemical structure and properties. Asphaltenes are not uniquely defined simple molecular entities and generic structures, but rather a complex mixture of colloidal entities (micelles) of various sizes and shapes, consisting of assemblages of smaller particles, which in turn result from the clustering of lower MW components, all in a state of dynamic exchange strongly affected by the presence and polarity of solvents, temperature, pressure and fluid mechanical conditions [36, 41].

Our studies subsequently focused on the issue of whether the picture of an asphaltene "molecule" as described above, which emerges from the available chemical information, i.e., a dynamic system in a constant state of interchange is consistent with the experimental findings of diffusivity and transport of asphaltenes through model porous membranes. An experimental plan was devised, as outlined in Fig. 1 to test these concepts. The asphaltenes used were n-pentane insolubles extracted from Hondo Crude, a California outer continental shelf oil, furnished by UNOCAL. The diffusion cell was a stainless steel Wicke-Kallenbach-type apparatus consisting of two well-mixed compartments (half cells). During experiments of asphaltene diffusion, the half-cells were separated by a polycarbonate membrane containing straight, parallel, non-intersecting, cylindrical pores (supplied by Nuclepore Corp., Pleasanton, California). The membrane pore size varied between 100Å and 4000Å. (Further details about our experimental system and techniques can be found elsewhere [36]. The first experiment was conducted with a 100Å membrane. We started with a 5 weight percent solution of asphaltene in xylenes, which was loaded in one of the half-cells, hereinafter referred to as the high concentration side (HCS). Pure xylenes were loaded in the other half-cell, the low concentration side (LCS). The asphaltenes were allowed to diffuse through the membrane for a predetermined period of time. During the experiment, samples were withdrawn

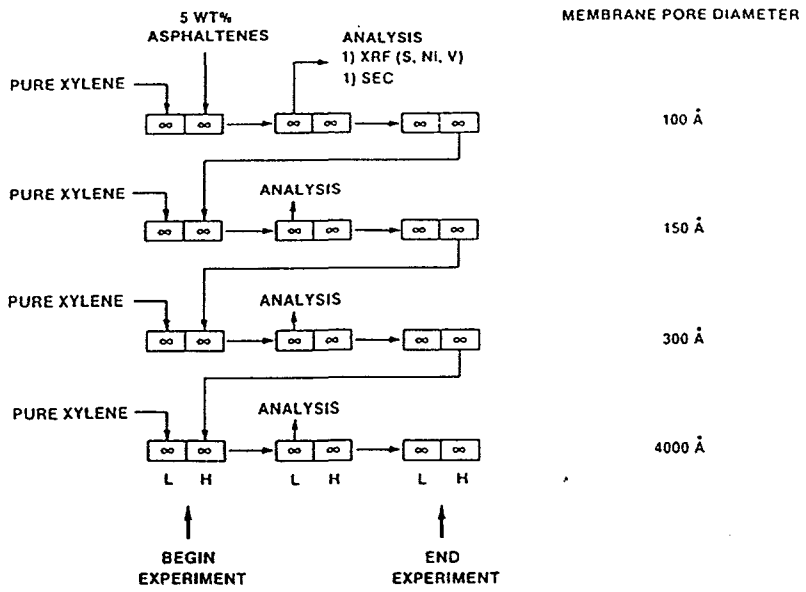

Fig.1. Experimental plan

from the LCS and analyzed for sulfur, nickel and vanadium concentrations by X-ray Fluoresence (XRF), and for MW distributions by Size Exclusion Chromatography (SEC), MW distribution of the various metal containing components by SEC/ICP and for overall asphaltene content. After the first experiment ended the second experiment was initiated with a 150Å membrane. Again, pure xylenes were loaded in the LCS. In this experiment, however, the HCS was filled with the asphaltene solution remaining in the HCS at the end of the first experiment with the 100Å membrane. Further experiments were done with the rest of the membranes starting again with pure xylenes in the LCSs and the HCSs containing the HCS solution carried over from the preceding experiment.

Some of the data collected from the diffusion experiments, depicting nickel and vanadium concentrations in the LCS as a function of run time are plotted in Figs. 2 and 3. Figs. 4 and 5 show typical SEC analyses of the LCS samples at various experimental times for two different pore sizes. One can draw the following conclusions from these figures (and the rest of the experimental data). First note Figs. 4 and 5, which show SEC analyses of LCS samples withdrawn at different run times. The polydisperse nature of asphaltenes is clear from these figures. Asphaltenes are not simple and uniquely defined molecules but rather consist of a whole range of molecular components of various sizes. The components with smaller sizes diffuse faster than the components with larger sizes and as a result the MW distribution of the asphaltene in the LCS at smaller times is skewed towards the lower MWs. At larger times, the MW distribution of the asphaltene in the LCS approaches that of the asphaltenes initially loaded in the HCS.

This, obviously, is an oversimplified picture of how asphaltenes diffuse through porous mem-

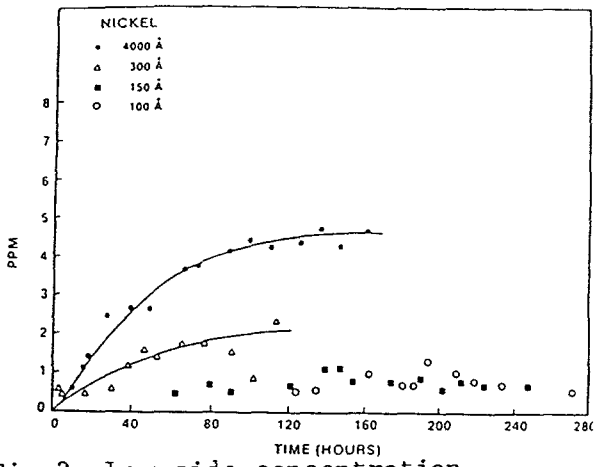

Fig.2. Low side concentration

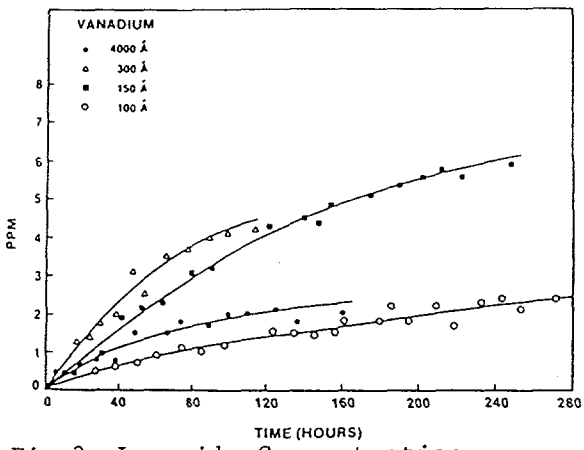

Fig.3. Low side Concentration.

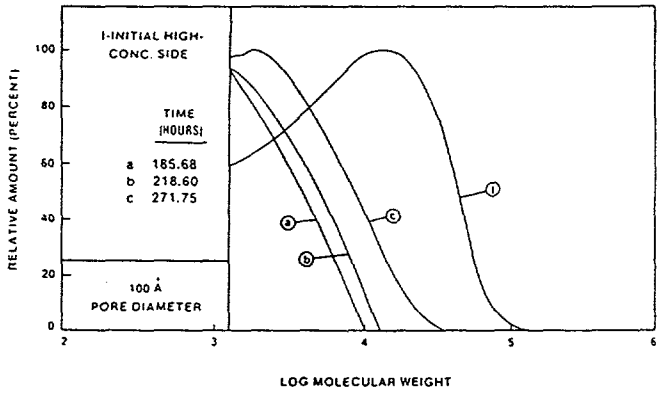

Fig.4. Log Molecular weight

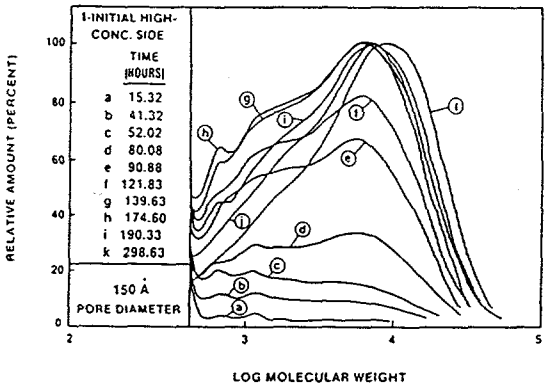

Fig.5. Log Molecular weight

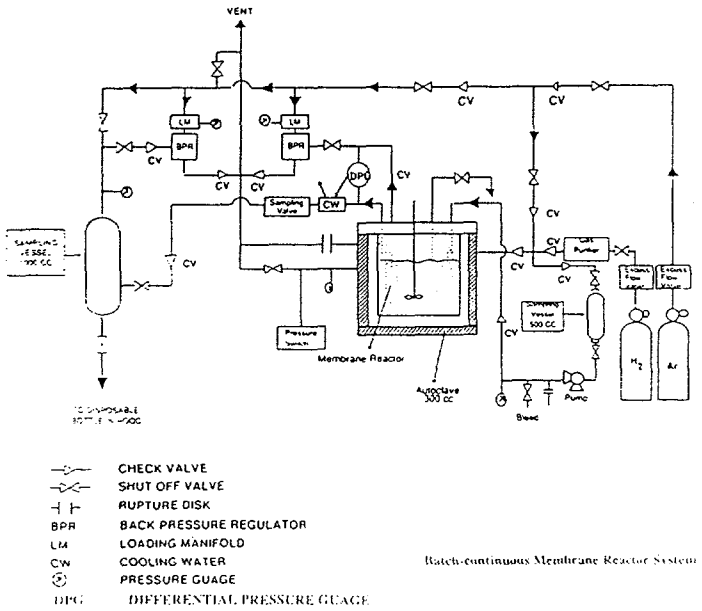

Fig.6. High temperature and pressure diffusion system.

Table 1: Activation energies in kcal/mole calculated from effective diffusivities.

Nominal Pore Size	Asphaltene	Sulfur	Nickel	Vanadium
100Å	-	12.7	10.2	9.9
150Å	8.7	8.6	10.0	9.6
300Å	8.2	8.1	6.7	8.6
500Å	6.4	7.2	6.3	7.6
4000Å	4.6	5.7	5.5	6.5

branes. This mechanism of asphaltene transport is only consistent with the polydisperse nature of asphaltenes. On the other hand, any polydisperse polymer would diffuse in a similar fashion, as indicated in Figs. 4 and 5. To realize that asphaltenes diffuse in a uniquely different fashion, one has to examine Figs. 4 and 5 in conjunction with Figs. 2 and 3. Note, for example, Fig. 2. Clearly there are components in the initial asphaltene that are larger than 150Å. In fact, out of the total nickel diffused throughout the whole series of experiments, only approximately 20% permeates, in the time allotted, through the 100 and 150Å membranes. How could it then be possible that the asphaltene at large times in Fig. 5 closely resembles the asphaltene initially loaded in the HCS? The only asphaltene structure capable of describing the data in Fig. 5 is the one we have previously described, namely that "*the asphaltenes are not simple, single generic species but rather complex mixtures of micelles of various sizes and shapes, of unformed micelles, of small particles and of low MW components and attached alkyl chains, all in a state of dynamic exchange strongly affected by the presence of solvents, temperature and pressure and fluid mechanical conditions.*" Only a dynamic association-disassociation process can explain the fact that the large components of the asphaltenes, with nominal sizes larger than the diameter of the pore find their way from the HCS to the LCS.

The dynamic nature of the asphaltene molecule manifests itself in the effect of temperature and concentration on its transport. Table 1, for example, lists the activation energies calculated from the diffusivity data from heptane-insoluble asphaltenes at various temperatures. Activation energies for diffusion are generally of the order of 1 Kcal/mole. The values in Table 1 are more typical of the association energies for individual asphaltene sheets reported by Dickie and Yen [41], typically 14 to 20 Kcal/mole, rather than diffusion activation energies. The trends in terms of the pore size can be understood on the basis that asphaltene dissociation is expected to affect

more strongly the transport through more constricted pores. The simplest model of an asphaltene molecule, which accounts for both its polydisperse character and its dynamic nature will faithfully reproduce the behavior in Table 1.

There is obviously a lot more information included in Figs. 2-5 and similar such figures. For example, the mechanism of heteroatom transport emerging for these data is consistent with the detailed chemical information as to where these heteroatoms lie in the original asphaltene micelles and particles. More detailed such discussions can be found in the original publications [36]. Of more importance, however, are the implications of the transport mechanism for petroleum and coal asphaltenes that is emerging on resid and coal liquid upgrading reactor design. In our opinion, the implications are many and significant. Traditionally, upgrading reactor design has utilized the concept of overall effective transport properties for asphaltenes and other oil fractions. In view of the existing chemical information on the structure of asphaltenes, the practice has been characterized as simplistic but of some engineering utility. Our thesis in this proposal is that the practice is outright wrong and can lead to erroneous design calculations. For one thing, such effective properties cannot be measured (one order of magnitude variation in effective diffusivity was observed in some of our experiments). More elaborate techniques, furthermore, must be devised to relate diffusivities measured in a Wicke-Kallenbach cell or by uptake experiments to transport properties of relevance under reactive conditions.

Is the previously stated concept of the structure of an asphaltene, i.e., of an asphaltene being "*a complex mixture in a state of dynamic exchange*" significant for upgrading catalyst design? In our opinion, it is, because it offers plausible explanations for what is happening during upgrading. Look at Figs. 2 and 3. Most of the nickel, for example, found in a petroleum asphaltene should not even be penetrating the structure of a typical upgrading catalyst, if it was not for the concept of "*dynamic exchange*" between the various asphaltene components. The other plausible reason why typical upgrading catalysts can process the heteroatoms found in resids or coal liquids is that the structure of an asphaltene represented by the above model, although valid at low temperatures, will not survive the higher upgrading temperature and pressure conditions, i.e., the micelles and even the particles will break apart. Superficially, this explanation is in contrast with experimental data (like those, for example, by Wiehe [38] and our group [36]), which show that thermal treatment at upgrading conditions of asphaltenes does not completely destroy the asphaltenes, but instead results in their incomplete conversion to both lower MW fractions, like volatiles, saturates, aromatics and resins but also to higher MW components like coke. In our opinion, these data are significant but not necessarily conclusive about the structure of asphaltenes at higher temperatures and pressures in view of the asphaltenes being considered as "*complex mixtures in a state of dynamic*

exchange." Assuming, on the other hand, that the asphaltene structure does not survive thermal treatment at upgrading conditions, what then is the purpose of studying such structures? In our opinion, the issue here is one of rates. Even if one is to assume that at elevated temperatures and pressures "micelles" and even "particles" break apart, the question to be raised is at which rate does this breakdown process occur? Contrary to laboratory reactors, where most of the studies of asphaltene's chemical structure have taken place, most industrial reactors are continuous systems. The state of the asphaltene "molecule" therefore does not only depend on the temperature, pressure and polarity of the solvent but also on the reactor's residence time. It is, therefore, very important to have a correct concept of the asphaltene's structure and through careful experimentation, one can then decide whether such a concept has any practical implications at realistic upgrading conditions.

PROJECT DESCRIPTION

It was the purpose of the project described here to carry out careful and detailed investigations of petroleum and coal asphaltene transport through model porous systems under a broad range of temperature conditions. The experimental studies were to be coupled with detailed, in-depth statistical and molecular dynamics models intended to provide a fundamental understanding of the overall transport mechanisms and a more accurate concept of the asphaltene structure. The following discussion describes some of our accomplishments..

1. **Measurement of Asphaltene Diffusivity**

   Throughout the experimental runs described below we have utilized a high pressure, high temperature diffusion cell system, a schematic of which is shown in Fig. 6. This apparatus was available before the start of the project. After the start of the project the high pressure diffusion apparatus of Fig. 6 was refurbished to make sure that all gases produced during the high temperature runs, under reactive conditions, would be better accounted for both in the upstream and downstream of the membrane. And it was also modified to hold a total of four membranes. The pressure gradient range was extended to 250 psi. Problems with seals and gaskets delayed somewhat our experiments in the early stages of the project but they were later resolved.

   The heart of the experimental system is a high pressure autoclave, which in its interior can accommodate one or several ceramic membranes. One side of these membranes is exposed to the contents of the autoclave, while the other side, through an independent flow system, is exposed to flowing pure solvent. The pressure in the interior and exterior of the membranes

can be independently adjusted and controlled. This is also true with the flow rate of the solvent in the interior of the membrane. The diffusion experiments are initiated by placing the liquid solution (model liquids or asphaltenes) in the autoclave space exterior of the membrane, pressurizing the exterior and interior membrane volumes and initiating the flow of the solvent. One has the option of running the experiment in a batch (exterior)-continuous (interior) or batch-batch mode. The option also exists for loading catalyst in the exterior volume either in a pellet or slurry form or using metal impregnated membranes for simultaneously studying transport and reaction.

The experimental technique followed is straightforward. The asphaltene solution is loaded in the autoclave in the space exterior to the membrane and pressurized under H_2 or mixtures of H_2 in Ar (see below). The interior and exterior membrane volumes were sampled periodically and analyzed by techniques such as XRF for heteroatom analysis, SEC for MW distribution, SEC/ICP for heteroatom specific MW distribution, overall asphaltene content, NMR and FTIR for overall functional group identification and by Gas Chromatography. Parameters investigated included (but are not limited to): (1) the effect of asphaltene concentration on the overall transport mechanism; (2) the effect of temperature and overall pressure and pressure gradient across the membrane (the pressure of the interior and exterior membrane volumes can be independently adjusted and controlled); (3) the effect of solvent and type of asphaltene (i.e., pentane or heptane insoluble, type of coal liquid it came from); and (4) the effect of pore size and membrane surface morphological properties.

Diffusivity measurements were carried out with a number of model coal liquid compounds, and asphaltenes isolated from real coal liquids provided to us by PETC and coal liquids produced by us by the thermal dissolution of two model coals. Sol-Gel and CVD modified Sol-Gel membranes were used during our diffusivity measurements. Transport investigations were also carried out under high tempearture (360°C) and pressure (1500 psi) reactive (H_2) and nonreactive (Ar) conditions. The rejection characteristics of various membranes during thermal coal dissolution were also investigated. Results of our experimental investigations were presented at various technical meetings as outlined during the various quarterly reports.

2. The Study of Asphaltene Agglomeration and Delamination Phenomena

The asphaltenes due to the action of solvents and their interaction with other asphaltene molecules and the solid porous walls, are constantly fragmenting and agglomerating. In the absence of a porous barrier one would expect an asphaltene solution to reach a state of pseudo-dynamic equilibrium. When a porous barrier is present, however, as in the case with

our experiments, this dynamic equilibrium is shifted towards lower MW fragments, since these fragments preferentially leak out of the membrane, i.e., one attains a form of facilitated fragmentation. In a real catalyst particle the situation, of course, is very similar. One does not have a LCS, where the low MW fragments will diffuse to but the low MW fragments are removed by the chemical reaction, i.e., again a chromatographic separation of the asphaltene occurs as it moves from the bulk solution into the particle's center. Gaining a better fundamental understanding of asphaltene agglomeration and delamination phenomena has been the goal of this Task. We have begun to analyze the effect of aggregation/delamination phenomena on the transport characteristics of asphaltene. Our efforts are of both experimental and theoretical character. Our experiments so far have focused on fundamental investigations of asphaltene precipitation in resids and in solution. We have shown that the data for asphaltenes from various sources and for various solvents all obey the same scaling relationship similar to those encountered in aggregation and gelation phenomena. Movitated by this finding we have proposed a novel model based on aggregation and gelation phenomena that appears to explain both our own data and the SANS, SAXS data of other investigators. We have applied fractal concepts to the description of the aggregation/delamination phenomena. We have shown by computer simulation and precise experiments that formation of such macromolecules involves diffusion-limited particle and cluster aggregation. The data suggest the presence of both small and large aggregates which have fractal structure with well-defined fractal dimensions. If the system is in equilibrium and its temperature is low enough, then large asphaltene particles have the structure of diffusion-limited particle cluster-cluster (DLCC) aggregates with a fractal dimension $D_f \simeq 1.8$ in three dimensions, while small asphaltene particles are similar to diffusion-limited particle aggregates with a fractal dimension $d_f \simeq 1.45$, which is similar to *two-dimensional* DLCC aggregates, and eventually to aggregates that are essentially linear with a fractal dimension $D_f \simeq 1$. Non-equilibrium effects, as well as the effects of the concentration of the asphaltene molecules in the solution, and the type of the solvent and the oil, on the structure of the aggregates have all been investigated. The implications of these results for the structure, mechanical stability, and molecular weight distribution of asphalts and asphaltenes were studied. Our research shows that the fractal structure of the aggregates places an upper bound on their size and average molecular weight. Moreover, we have proposed a new molecular weight distribution for the asphaltene aggregates, which is based on the cluster-size distribution of the aggregates. The new MW distribution provides very good predictions for the experiment data. Thus, from the knowledge that the asphaltene aggregates are fractal structures, and given the mechanisms of their

formation, we have obtained considerable new insights. This new knowledge can now be used to study other properties of the asphaltene aggregates, such as the time-evolution of their structure, and their effect on the permeability and wettability of a porous medium. Research in this area is continuing.

3. Models of Asphaltene Transport in a Single Pore

A simulation code has been developed to model the structure and transport characteristics of asphaltenes in a single straight pore. Asphaltene molecules are generated by using the distributions of structural elements for asphaltenes available in the literature or measured experimentally. Assuming that the cumulative distributions of the number of unit sheets in a molecules, the number of aromatic and saturated rings, and the length of the alkyl chains are available, the numerical code stochastically arranges the aromatic and saturated rings. It calculates the number of peripheral carbons and the number of peripheral carbons that can be substituted with aliphatic chains. The peripheral carbons are then randomly substituted with alkyl chains, whose lengths are determined from the cumulative distributions. The numerical code geneates up to 1,000,000 molecules in each calculation. Asphaltenic molecules typically contain 2-5 aromatic sheets. The code calculates the geometric size of each molecule and, to a first approximation, it considers it to be a cylinder with an oval cross-section. It calculates the MW of each molecule for the number of carbons and hydrogens in each molecule and then it generates a MW distribution, which it averages over many calculations to smooth out the noise.

As already mentioned, the code, as it is now written, approximates each asphaltene molecule as a spheroid (see discussion below). The code then proceeds to calculate the partition coefficient of the spheroid-shaped molecules in a cylindrical pore. These are calculated using the exact formulations for spheroidal molecules and cylindrical pores reported by Giddings and coworkers (J. C. Giddings *et al. J. Phys. Chem* **72** 4397, 1968; see also K. W. Limbach *et al. AIChE J.* **35**, 42, 1989). To calculate the transport within the pore both MC and continuum hydrodynamic theory approaches are being utilized. Currently in both approaches the solvent is assumed to be a continuum. In the MC part of the code the molecule is allowed to move randomly along orthogonal axes. At any given time, the molecule can take a step randomly along six principal directions ($\pm x$, $\pm y$, $\pm z$), and it can also rotate itself and change its alignment with the pore axis. To simulate diffusion from a high concentration region to a low concentration region, and to exit the pore, the motion of the molecules along the axis of the cylinder from its entrance to its exit is biased. If the molecule hits the wall it goes back

to its original position and induces a drag on the molecule in the forward direction. For each molecule the diffusivity is calculated from the following relationship:

$$D_{eff} \approx \frac{< [r(t) - r(O)]^2 >}{t} \tag{2}$$

In the physicochemical hydrodynamics part of the code, each asphaltene molecule is approximated by a spheroid. The number of sheets fixes its thickness. We equate the size of one of the axes of the spheroid to this thickness. Subsequently based on the molecular structure of the molecule, one calculates using molecular volume additivity rules, the molecular volume of the molecule. The length of the second axis of the spheroid is chosen so that the volume of the spheroid equals the molecular volume of the asphaltene molecule. The process of assigning the length of each axis is somewhat arbitrary. The experimental data however, do not justify a more elaborate process. In the initial efforts the hindered diffusivity within the pores was calculated using the theory of Scalak and Chen (T. C. Chen and R. Skalak, *Appl. Sci. Res.* **22** 403, 1970) utilizing the centerline approximation. The effect of the parameters of the MW distribution, and the distributions of the number of asphaltene sheets per molecule, the number of aromatic and saturated rings per sheet and the number and length of side alkyl chains on asphaltene diffusivity and partition coefficients have all been calculated. (See relevant papers in Appendix.) More recently we are utilizing BEM codes for calculating the effective diffusivity both off and on the centerline.

The MC numerical code discussed above has been used to simulate the diffusion experiments. First, 100,000 molecules are generated to simulate the high concentration side (HCS) of the membrane. Randomly selected molecules are then continuously introduced into the pores and then all the molecules inside the pore are allowed to make random changes in their positions and orientations as long as they do not hit each other or the wall. The concentrations and the molecullar weight distributions of asphaltenes in the HCS and LCS of the membrane are monitored at different times and the diffusivities of asphaltenes are calculated.

The numerical results have been encouraging and the calculated diffusivity values are in qualitative agreement with the experimental data generated by our group and by Baltus and coworkers for model membranes with straight nonintersecting pores.

4. Asphaltene Transport in Networks of Interconnected Pores

To extend the above model to Sol-Gel type membranes represents a major challenge. An appropriate model must be developed of the pore structure. In this project an effort was made to develop a statistical model to represent the structure of the Sol-Gel alumina membranes.

The effort was carried out in collaboration with the Process and Media Technology group in Pittsburgh, PA. The statistical modelling was combined with an investigation of the structural properties of these membranes using BET and mercury and flow porocimetry techniques, high resolution SEM and TEM investigations and the measurement of the transport of various model coal compounds through such membranes.

5. **Monte Carlo and Molecular Dynamic Simulations**

No effort was made to model the transport processes in such a complex 3-D porous medium. Instead our effort forcused on model porous media. For example, we studied the diffusivity of Lennard-Jones particles in porous systems with dimensionality between two and three. Examples of model porous systems of such dimensionality are pillared clays. In our simulations the pillared clays were represented by parallel sheets separated by a given distance, and connected by pillars of a given size. Two different spatial distributions of the pillars, namely, random and uniform, were studied to determine their effect on the properties of the system. Our calculations did not indicate a strong dependence of the diffusivity on the spatial distribution of the pillars, except at low porosities. The solvation force was found to be monotonically increasing with decreasing distance between the clay layers and increasing density of the molecules. The percolation threshold of the system, i.e., the critical porosity, φ_C and the diffusivity D_l relate according to the power law, $D_l \infty (\varphi - \varphi_C)^n$, where φ is the porosity of the system, and n an universal constant.

The Appendix contains all papers that either were published or accepted for publication during the period of performance of this project. A number of other papers are either under review or in preparation. We will be happy to provide copies of these papers as they become available.

LITERATURE REFERENCES

1. F. M. Dautzenberg, J. Van Klinken, K. M. A. Pronk, S. T. Sie and J. B. Wiffels, *ACS Symp. Ser.*, **55**, pp. 254-267, Washington, D.C. (1978); R. B. Galbreath and R. P. Van Driesen, *Proc. 8th World Petrol. Congr.*, 4, 129 (1971); D. C. Green and D. H. Broderick, *Chem. Eng. Prog.*, **77**, 33 (1981); Y. T. Shah and J. A. Paraskos, *Ind. Eng. Chem. Proc. Des. Dev.*, **14**, 368 (1975).

2. J. C. Spry and W. H.Sawyer, paper presented at the AIChE Annual Meeting, Los Angeles (1975).

3. J. L. Anderson and J. A. Quinn, *Biophys. J.*, **14**, 130 (1979).

4. M. Inoguchi, *Sokubai*, **18**, 78 (1976).

5. A. S. Eigenson, Y. A. Zaitova, G. A. Berg, L. I. Volkova, N. A. Kochetova, T. P. Anmdryshenko, L. Y. Shudina and A. A. Ioakimis, *Int. Chem. Eng.*, **9**, 332 (1977).

6. C. Philippopoulos and N. Papayannakos, *Ind. Eng. Chem. Res.*, **27**, 415 (1988).

7. M. Ternan, *Can. J. Chem. Eng.*, **61**, 689 (1983); A. H. Hardin, R. H. Packwood and M. Ternan, *Prep. Div. Petrol. Chem. Am. Chem. Soc.*, **23**(4), 1450 (1978; A. H. Hardin and M. Ternan, *Prep. 2nd World Congr. on Chem. Eng.*, **3**, 134 (1981).

8. L. M. Polinski, G. J. Steigel and L. Saroff, *Ind. Eng. Chem. Proc. Res. Dev.*, **21**(3), 477 (1982); G. J. Steigel, L. M. Polinski and R. E. Tischer, *Ind. Eng. Chem. Proc. Res. Dev.*, **21**(3), 477 (1982).

9. M. C. Scooter and B. L. Crynes, *Ind. Eng. Chem. Proc. Res. Dev.*, **14**, 199 (1975).

10. Y. K. Yen, D. E. Furlani and S. W. Weller, *Ind. Engng. Chem. Prod. Res. Dev.*, **15**, 24 (1976).

11. J. A. Brooks, R. J. Bertolacini, L. C. Gutbertlet and D. K. Kim, EPRI Publication, AF-160 (1976); R. J. Bertolacini, L. C. Gutherlet, D. K. Kim and K. K. Robinson, EPRI Final Report AF 1084, June, 1979; D. K. Kim, R. J. Bertolacini, J. M. Forgac, R. J. Pellet, K. K. Robinson and C. V. McDaniel, EPRI Final Report AF 1233, November 1979.

12. R. L. McCormick, J. A. King, T. R. King and H. W. Haynes, *Ind. Eng. Chem. Res.*, **28**, 940 (1989).

13. L. Berg and N. K. Kim, *Chem. Eng. Commun.*, **32**, 391 (1985).

14. M. C. Tsai and E. Ruckenstein, *AIChE J.*, **27**, 697 (1981).

15. P. E. Savage and M. Javanmardian, *Ind. Eng. Chem. Res.*, **28**, 381 (1989); K. S. Tsakalis, T. T. Tsotsis and G. J. Steigel, *J. Catal.*, **88**, 188 (1984).

16. W. M. Deen, *AIChE J.*, **33**(9), 1409 (1987).

17. J. R. Peppenheimer, E. M. Renkin and L. M. Borrero, *Am. J. Physiol.*, **13**, 167 (1951); E. M. Renkin, *J. Gen. Physiol.*, **38**, 225 (1954).

18. J. D. Ferry, *J. Gen. Physiol.*, **20**, 95 (1936).

19. H. Brenner and L. J. Gaydos, *J. Coll. Int. Sci.*, **43**, 312 (1977); H. Brenner, *Physicochem. Hydro.*, **1**, 91 (1980); L. C. Nitsche and H. Brenner, to be published.

20. R. Aris, *Proc. Roy. Soc. Lond.*, **A235**, 67 (1941); G. I. Taylor, *Proc. Roy. Soc. Lond.*, **A219**, 186 (1953).

21. E. A. Dimarzio and C. M. Guttman, *Polym. Lett.*, **7**, 131 (1970); *J. Chromatogr.*, **55**, 83 (1971); D. G. Leuitt, *Biophys. J.*, **15**, 533 (1975); E. N. Lightfoot, J. D Bassingthwaite and E.F. Babrowski, *Biophys. J.*, **9**, 167 (1977).

22. C. N. Satterfield, C. K. Colton and W. H. Pitcher, *AIChE J.*, **19**, 478 (1973).

23. B. D. Prasher and Y. H. Ma, *AIChE J.*, **23**, 303 (1977); B. D. Prasher, G. A. Gabriel and Y. H. Ma, *AIChE J.*, **24**, 1118 (1978).

24. C. K. Colton, C. N. Satterfield and C. J. Lai, *AIChE J.*, **21**, 289 (1975).

25. D. S. Cannel and F. Rondelez, *Macromolecules*, **13**, 1449 (1950).

26. P. B. Price and R. M. Walker, *J. Appl. Phys.*, **33**, 3400 (1947); **33**, 3407 (1947).

27. C. P. Bean, M. V. Doyle and G. J. Entine, *J. Appl. Phys.*, **41**, 1454 (1970); J. A. Quinn, J. L. Anderson, W. H. Ho and W. J. Petzny, *Biophys. J.*, **12**, 990 (1972); R. E. Beck and J. S. Schultz, *Biochim. Biophys. Acta*, **255**, 273 (1972); D. M. Malone and J. L. Anderson, *AIChE J.*, **23**, 97 (1977).

28. R. J. Thrash and R. H. Pildes, *ACS Preprints, Div. Pet. Chem.*, **26(2)**, 515 (1981).

29. M. Shimura, Y. Shiroto and C. Takeuchi, paper presented at the ACS Meeting, Div. Coll. Surf. Chem., Las Vegas, NV (1982).

30. M. Sakai, K. Sasaki and M. Inagaki, *Carbon*, **21**, 593 (1983).

31. K. Jost, W. Steuer and I. Halasz, *Chromatographia*, **20**, 700 (1985).

32. R. L. Mieville, D. M. Trauth and K. K. Robinson, *ACS Preprints, Div. Pet. Chem.*, **34(3)**, 635 (1989).

33. R. E. Baltus and J. L. Anderson, *Chem. Eng. Sci.*, **38**, 1959 (1983); R. E. Baltus, *Catalysis on the Energy Scene*, S. Kaliagne and A. Mahay, eds., Elsevier, Amsterdam, p. 533 (1984); R. E. Baltus and J. L. Anderson, *Fuel*, **63**, 530 (1984);

34. R. E. Baltus, K. C. Kyriacou, V. V. Sivaramakrishna and P. Rahimi, *AIChE Symp. Ser.*, No. 266, **84**, 50 (1988); K. C. Kyriacou, V. V. Sivaramakrishna, R. E. Baltus and P. Rahimi, *Fuel*, **67**, 15 (1988); K. C. Kyriacou, R. E. Baltus and P. Rahimi, *Fuel*, **67**, 109 (1988); R. L. Nortz, R. E. Baltus and P. Rahimi, *Ind. Eng. Chem. Res.*, **29(9)**, 1968 (1990).

35. J. Garcia de la Torre and V. A. Bloomfield, *Biopolymers*, **17**, 1605 (1978).

36. R. C. Sane, I. A. Webster and T. T. Tsotsis, *Stud. Surf. Sci. Catal.*, **38**, 705 (1988); *ACS Symp. Ser.*, Amer. Chem. Soc., **33**(3), 237 (1988); *AIChE Symp. Ser.*, **84**, 57 (1988); R. C. Sane, I. A. Webster, T. T. Tsotsis and V. S. Ravi Kumar, in press, *Asphalt and Asphaltenes*, T. F. Yen, ed.; R. C. Sane, I. A. Webster, T. T. Tsotsis and V. S. Ravi Kumar, submitted for publication, *Chem. Eng. Sci.*; R. C. Sane, Ph.D. Thesis, University of Southern California, December, 1990.

37. J. W. Bunger and D. E. Cogswell, *Adv. Chem. Ser.*, "The Chemistry of Asphaltenes," **195**, 219 (1981).

38. J. F. McKay, P. J. Amend, T. E. Cogswell, P. M. Harnsberger, R. B. Erikson and D. R. Latham, *Adv. Chem. Ser.*, "Petroleum Asphaltenes: Chemistry and Composition," **170**, 128-142 (1978); J. A. Koots and J. G. Speight, *Fuel*, **54**, 179 (1975); I. A. Wiehe, paper presented at the AIChE Spring National Meeting, Orlando, Florida, March 18-22 (1990).

39. R. B. Long, *Adv. Chem. Ser.*, "The Chemistry of Asphaltenes," **195**, 17 (1981); R. B. Long and J. G. Speight, *Revue de L'Institut Français du Petrolé*, **44**, 205 (1989).

40. C. E. Snape and K. D. Bartle, *Fuel*, **63**, 883 (1984); **64**, 427 (1985).

41. J. P. Dickie and T. F. Yen, *Anal. Chem.*, **39(14)**, 1897 (1967).

42. N. Nourbakhsh, I. A. Webster and T. T. Tsotsis, *Appl. Catal.*, **50**, 65 (1989); N. Nourbakhsh, A. Champagnie, I. A. Webster and T. T. Tsotsis, *AIChE Symp. Ser.*, **85**, 75 (1989); N. Nourbakhsh, B. J. Smith, I. A. Webster, J. Wei and T. T. Tsotsis, *J. Catal.*, **27**, 178 (1991).

43. D. L. Cocke, E. D. Johnson and R. F. Merrill, *Cat. Rev. Sci. Eng.*, **26**, 148 (1984); L. Young, *Anodic Oxide Films*, Academic Press, New York (1961); K. Itaya, S. Sugawara, K. Arai and S. Saito, *J. Chem. Eng. Japan*, **17**(s), 514 (1984).

44. A. M. Champagnie, T. T. Tsotsis, R. G. Minet and I. A. Webster, *Chem. Eng. Sci.*, **45(6)**, 1443 (1990).

45. W. T. Mo and J. Wei, *Chem. Eng. Sci.*, **41**, 4, 703 (1986); N. Otani and J. M. Smith, *J. Catal.*, **5**, 332 (1966).

46. D. Ryan, R. G. Carbonell and S. Whitaker, *Chem. Eng. Sci.*, **35**, 10 (1980).

47. T. T. Tsotsis, R. Sane, I. A. Webster and J. D. Goddard, *J. Catal.*, **101**, 416 (1986); J. D. Goddard, T. T. Tsotsis and M. N. Kassem, paper presented at the AIChE Annual Meeting, Miami, Florida, November (1986).

48. J. S. Schultz, J. D. Goddard and S. R. Suchdeo, *AIChE J.*, **20**, 625 (1974); J. D. Goddard, *Chem. Eng. Sci.*, **32**, 795 (1977).

49. J. D. Goddard, in *Transport With Chemical Reaction*, P. Stroeve and W. J. Wards, eds., *AIChE Symp. Ser.*, **202**, 114 (1982).

50. M. Sahimi, G. R. Gavalas and T. T. Tsotsis, *Chem. Eng. Sci.*, **45**, 1443 (1990).

51. P. L. Paine and P. Scherr, *Biophys. J.*, **15**, 1087 (1975).

52. M. Sahimi and A. O. Imdakm, *J. Phys. A*, **21**, 3833 (1988); *Phys. Rev. Lett.*, **66**, 1169 (1991); *Chem. Eng. Sci.*, **46**, 1977 (1991); M. Sahimi and V. L. Jue, *Phys. Rev. Lett.*, **62**, 629 (1989).

53. M. Sahimi, *J. Chem. Phys.*, **92**, 5107 (1990).

54. D. Fincham, N. Quirke and D. J. Tildeshy, *J. Chem. Phys.*, **84**, 4553 (1986).

55. M. P. Allen and D. J. Tildeshy, *Computer Simulations of Liquids*, (Clarendon, Oxford, 1987); D. J. Adams , E. M. Adams, and G. J. Hills, *Mol. Phys.*, **38**, 387 (1979); S. Murad, A.

Papaioannou and J. G. Powler, *Mol. Phys.*, **56**, 431 (1985); P. J. Rossky, *Ann. Rev. Phys. Chem.*, **36**, 321 (1985).

56. G. Jacucci and I. R. McDonald, *Physica*, **80A**, 607 (1975).

57. K. L. Jolly and R. J. Bearman, *Mol. Phys.*, **41**, 137 (1980).

58. M. Schoen and C. Hohiesel, *Mol. Phys.*, **52**, 33 (1984); **52**, 1024 (1984).

59. J. M. Stoker and R. L. Rowley, *J. Chem. Phys.*, **91**, (1989).

60. J. J. Magda, M. V. Tirrell and H. T. Davis, *J. Chem. Phys.*, **83**, 1888 (1985); **85**, 6674 (1986); I. Bitsanis, J. J. Magda, M. V. Tirrell and H. T. Davis, *J. Chem. Phys.*, **87**, 1733 (1987).

Appendix A
Papers

Pergamon

Chemical Engineering Science, Vol. 49, No. 24B, pp. 5789–5801, 1994
Elsevier Science Ltd
Printed in Great Britain
0009-2509/94 $7.00+0.00

0009–2509(94)00330–0

STUDIES OF TRANSPORT OF ASPHALTENES THROUGH POROUS MEMBRANES: STATISTICAL STRUCTURAL MODELS AND CONTINUUM HYDRODYNAMIC THEORIES

V. S. RAVI-KUMAR†, THEODORE T. TSOTSIS*†, MUHAMMAD SAHIMI† and IAN A. WEBSTER‡

†Department of Chemical Engineering, University of Southern California, Los Angeles, California 90089-1211, U.S.A. and ‡Unocal Corporation, 1201 West 5th Street, Los Angeles, California 90051, U.S.A.

(*Received* 10 *May* 1994; *accepted for publication* 27 *September* 1994)

Abstract—The results of our ongoing studies of the transport of asphaltene molecules through model membranes are presented. The experimental results are briefly reviewed, and a model is presented which aims to capture the effect on the transport of the polydisperse nature of the asphaltene molecules. The asphaltene molecular structure is first generated stochastically using a Monte Carlo technique. The individual asphaltene molecules are then approximated as spheroids for the purpose of calculating their hindered diffusivities. Continuum hydrodynamic theories of hindered diffusion are then used to calculate the individual transport coefficients.

INTRODUCTION

Among the various crude-oil and coal-liquid fractions, asphaltenes, which consist primarily of macromolecular species, create difficulties during hydrocracking and upgrading. This is due to their high heteroatom content and their macromolecular colloidal nature, which result in reduced yields during hydrotreating. To increase the efficiency of the asphaltene hydrotreating processes it would be helpful to have a better understanding of the asphaltene structure and the mechanism of asphaltene diffusion through restricted porous systems like the typical hydrotreating catalysts.

The name asphaltene has been used to describe the components of a resid, which are generally polar and large in size. Since the early stages of the field of heavy oil upgrading, asphaltenes have been defined as a solubility class. This definition has attracted considerable debate (Bunger and Cogswell, 1981). Some of the asphaltene properties are known to depend on their isolation technique. Questions, therefore, exist as to whether the asphaltenes bear similarity to compounds found in the original liquids, and whether the asphaltenes themselves even exist rather than being artifacts of their isolation process. This debate has continued for years, and comprehensive descriptions can be found in a number of papers (Koots and Speight, 1975; McKay *et al.*, 1978; Wiehe, 1992; Sane *et al.*, 1994). The view commonly held today is that asphaltenes do exist and are found in the original heavy liquid. However, one cannot uniquely characterize asphaltenes based on a single property alone such as, for example, solubility. For petroleum resids, two properties are needed to differentiate one resid fraction from the other (at least three for heavy coal liquids). However, which two properties to use is still under debate. Molecular weight (as measured by gel permeation chromatography) and polarity (as measured by the solubility parameter) have been suggested (Long and Speight, 1989). The average molecular weight (as measured by vapor pressure osmometry) and the average hydrogen content have been used by Wiehe (1992).

Interest in asphaltenes goes back to the 1940s and has been steadily increasing in recent years, due to the relative abundance of heavy crudes and the ongoing research activities in coal liquefaction. Asphaltene chemistry has attracted the major share of attention. Several reviews on this topic have already appeared (Yen, 1990; Speight, 1991). Some of the earliest studies in the field are by Yen *et al.* (1961) who proposed a model of the asphaltene's structure. In their model, the building blocks of the asphaltene structure consist of condensed heterocyclic aromatic sheets with attached alkyl chains restricted to the plane of the sheet, typically 8.5–15 Å in diameter. These molecules then associate with each other in the third dimension in the presence of non-polar or slightly polar solvents to form stacked clusters (commonly referred to as particles) about 16–20 Å in height. The forces causing the stacking, though not completely understood, are believed to be both chemical, and weak physical like van der Waals and hydrogen bonding. The important observation of Yen and coworkers that clustering occurs and that concentration, temperature and aging all affect the degree of association, has been verified by a number of other studies.

*To whom correspondence should be addressed.

For example, it was observed (Mieville *et al.*, 1989) that different gel permeation chromatography (GPC) cuts of asphaltenes contain different numbers of sheets per asphaltene particle. But the size of the unit sheet is essentially the same and relatively small (five aromatic and two naphthenic rings). It was also reported (Moschopedis *et al.*, 1976; Speight *et al.*, 1985) that asphaltenes do associate in non-polar solvents and dissociate in polar solvents.

The association and clustering do not stop at the cluster (or particle) level. Several molecular weight distribution studies have shown the presence of components (called "micelles" in the asphaltene literature) of very large molecular weight and diameters of the order of 100–300 Å. The clustering and association of the particles may be aided by the presence of various metals in the asphaltene. The nature of the forces responsible is not clear, though they are believed to be primarily weak in nature (Pfeiffer and Saal, 1940; Rao and Serrano, 1986; Sheu *et al.*, 1990). Where metals and other heteroatoms are located in the structure of asphaltenes has also attracted attention. Whether the metals are primarily porphyrinic or non-porphyrinic in nature, and how they participate in the clustering process still remain matters of debate.

The literature on the chemistry of asphaltenes is voluminous with a wealth of information on the subject. The technical details are many and often obscure, but overall a consistent (but not necessarily universally accepted) picture is starting to emerge. It is apparent that asphaltenes are not simple molecules but rather complex mixtures of components (micelles) of various sizes and shapes, consisting of assemblies of smaller particles, which in turn result from the clustering of lower molecular weight components, all in a state of dynamic exchange strongly affected by the presence of solvents, temperature, concentration and fluid mechanical conditions. The type and exact nature of forces resulting in the clustering of the lower molecular weight components are still being studied. Furthermore, the exact chemical composition of these compounds is still not clear and is the subject of ongoing investigations (Strausz *et al.*, 1994; Yen, 1994). One would expect such structures, consisting of aggregates of the primary particles, to be highly sensitive to their environment, i.e. whether the environment is polar or non-polar, the temperature and pressure, the presence of surfactants, etc.

An important contribution in this area is by Klein and coworkers (Savage and Klein, 1989; Trauth *et al.*, 1994). They have taken the vast knowledge of the chemical structure of asphaltenes and have succeeded in instilling in it a degree of mathematical formalism. They have developed a technique that combines routine analytical tests and an iterative stochastic modeling approach to develop a representative molecular structure of a petroleum resid. This represents an important development in the field of heavy-crude/coal-liquid upgrading reactor design.

Prior studies of asphaltene diffusion

Most of the molecular components of an asphaltene are large structures, with sizes approaching those of typical catalyst pores. Hydroprocessing of asphaltenes involves a number of parallel and/or consecutive reactions like hydrodesulfurization, hydrodenitrogenation, hydrodemetallation, and cracking. Owing to the large size of most asphaltene entities, all these reactions occuring within the catalyst pellet are diffusion-limited. This being the case, it is unclear, from the standpoint of resid upgrading reactor design, why considerably fewer studies have dealt with the subject of asphaltene transport and diffusion through restricted porous catalysts and systems, especially in view of the voluminous literature on asphaltene chemistry.

Studies of asphaltene hindered diffusion are few in number. In one of the earliest studies, Thrash and Pildes (1981) measured the diffusion coefficient of asphaltenes through mica membranes. Shimura *et al.* (1986) studied asphaltene diffusion in porous catalysts by uptake-type experiments. A more detailed study of asphaltene transport was done by Baltus (1984) and Baltus and Anderson (1983, 1984), who used a Wicke–Kallenbach-type diffusion cell to measure the diffusivity, through mica membranes, of asphaltenes derived from Kuwaiti atmospheric bottoms. They divided the overall molecular weight (MW) range into five regions and assigned each to a hypothetical asphaltene fraction. Using GPC, they measured the diffusivity of each fraction for pore diameters varying from 160 Å to 4,400 Å. The diffusivity D_e of each fraction was found to relate to its bulk diffusivity D_∞ as $D_e/D_\infty = \exp(-3.89\lambda)$, where λ is the ratio of the Stokes–Einstein radius and the pore radius. These studies have been continued (Kyriakou *et al.*, 1988 ; Nortz *et al.*, 1990) with various fractionated samples of heavy oils using polycarbonate membranes and Taylor-dispersion-type experiments. Using hydrodynamic models for macromolecular complexes (Garcia de la Torre and Bloomfield, 1978), Baltus and coworkers have also attempted to model the asphaltene structure as assemblages of interconnected spheres (Nortz *et al.*, 1990). Mieville *et al.* (1989) measured the diffusion of asphaltenes, by uptake-type experiments, through catalysts with both unimodal and bimodal pore size distributions. Hondo asphaltene was found to have the highest diffusivity, which was attributed to its smaller average aromatic cluster. The present authors have also studied experimentally the transport of asphaltene for a number of years (Sane *et al.*, 1988; Sane, 1992; Sane *et al.*, 1994). In these studies model membranes (polymeric, anodic aluminas and sol–gel) were utilized and experiments carried out under steady-state conditions utilizing Wicke–Kallenbach-type diffusion cells. Membranes offer a number of advantages when it comes to fundamental investigations of transport and reaction. Polymeric and anodic membranes have straight, non-intersecting and fairly uniform pores, thus eliminating the need for describ-

ing the tortuosity and the topology of the pore space. Sol–gel membranes with their fairly unimodal pore size distributions represent an intermediate step in the knowledge tree, leading to a better understanding of the transport phenomena occuring in real catalyst systems.

Before describing the model of asphaltene diffusion, some of our experimental results are briefly reviewed. Further details are outlined in prior publications (Sane, 1992; Sane *et al.*, 1988, 1992, 1994).

EXPERIMENTAL PROCEDURES

Most of the experiments were carried out in a stainless steel Wicke–Kallenbach-type diffusion cell (Sane, 1992) consisting of two half-cells separated by the microporous membrane, each equipped with an externally driven rotor shaft for good mixing to eliminate external mass transfer limitations. The temperature of each half-cell was individually controlled. During the experiments, samples were withdrawn from the high and low concentration cell sides (HCS and LCS, respectively). The samples were analyzed by X-ray fluorescence (XRF) for elemental concentrations, size-exclusion chromatography (SEC) for MW distribution, and for total asphaltene content. The asphaltenes were isolated from resids using *n*-heptane (or *n*-pentane) (Dolbear and Phan, 1988). Before each experiment the thickness, pore size and pore density of the membranes were measured.

EXPERIMENTAL RESULTS

As already mentioned, from the earlier years (Pfeiffer and Saal, 1940; Yen *et al.*, 1961; Dickie and Yen, 1967) asphaltenes were thought to be complex mixtures containing many compounds with a broad MW distribution. The polydisperse nature of asphaltenes has significant implications for their transport. It implies for example that one cannot define a unique, time-independent effective diffusivity even for steady-state-type diffusion experiments. This fact had been overlooked until it was reported by the present authors six years ago (Sane *et al.*, 1988) in transport experiments with *n*-pentane insoluble Hondo asphaltenes.

SEC is a technique well-suited for studying the polydisperse nature of asphaltenes, though quantitative interpretation of the SEC data is difficult, because the elution time of a given solute depends not only on its size, but also on its shape and surface properties. In our experiments we have analyzed the solutions in the HCS and LCS of the diffusion cell by SEC. What we have observed is that the asphaltene in the LCS has initially different elution characteristics than the asphaltene in the HCS, but eventually approaches the behavior in the HCS.

The data are, of course, consistent with the polydisperse nature of the asphaltene molecules. Polydisperse compounds including asphaltenes and polymers should behave in such a manner. Asphaltene diffusion is a more complex phenomenon, however. The authors of this study have found, for example, that asphaltene components with nominal sizes exceeding those of the membrane pores somehow find their way from the HCS to the LCS. For small pore size membranes (< 150 Å), even after long experimental times, only a relatively small percentage of total asphaltenes has penetrated in the LCS. That the LCS asphaltene has almost similar characteristics to the HCS asphaltene is consistent with the "dynamic nature" of the asphaltene molecule that has been already described, which imparts to it the ability to generate itself from its fragments. To reiterate, asphaltenes are not simple generic species but rather complex mixtures consisting of micelles of various sizes and shapes, of small particles and of high- and low-molecular-weight heterocyclic aromatic sheets with attached alkyl chains, all in a state of dynamic exchange, strongly affected by the presence of solvents, temperature, concentration, and fluid mechanical conditions.

This dynamic nature of asphaltenes manifests itself in the effect of temperature and concentration on their transport properties. The measured activation energies for diffusion, for example, are more typical of the association energies for individual asphaltene sheets reported by Dickie and Yen (1967), rather than typical diffusion activation energies. They increase, furthermore, as the pore size decreases, an effect which can be understood on the basis that asphaltene dissociation would affect more strongly the transport through more constricted pores. The present authors have found that asphaltene diffusivity is also dependent on their initial concentration in the HCS, as expected, since the increased concentrations increase the association of the various asphaltene components in solution and increase their average MW. The manner in which the concentrations of the metals and other heteroatoms behave with time in the LCS and HCS during diffusion is an indicator of the relative abundance of these species in the asphaltene components during transport, and provides insight into the aspects of the asphaltene structure that are of importance during asphaltene upgrading. The data, detailed accounts of which can be found elsewhere (Sane, 1992), are again consistent with the overall asphaltene picture emerging from the structural investigations of asphaltenes and upgrading reactor data.

A MODEL OF ASPHALTENE TRANSPORT

There is no shortage of broad conceptual models of the asphaltenes structure, and recently even some continuum (Sane *et al.*, 1988; Nortz *et al.*, 1990) and geometric models of transport have emerged. A model of asphaltene transport, however, which is consistent not only with the literature on the detailed chemistry of asphaltenes, but also with their transport measurements, is currently missing. This paper presents such a model. The mathematical formalism of Klein and coworkers is its foundation, since it is

capable in our opinion of encompassing the vast knowledge about the chemical nature and structure of asphaltenes. In this model, the molecular models are coupled with the detailed description of the transport of asphaltene clusters through cylindrical pores. The model in its present form does not explicitly account for the agglomeration/delamination phenomena (Sheu *et al.*, 1990, 1992) which characterize the dynamic nature of asphaltene molecules. The omission is deliberate and does not represent a weakness of the model. The authors have recently (Rassamdana *et al.*, 1994), begun to look at agglomeration/delamination behavior. Little, if anything, concrete is known in this area. Using, for example, asphaltene precipitation by a solvent as a measure of agglomeration/delamination behavior, the group has shown, that a single gelation-type scaling equation describes data from a variety of solvents under diverse conditions. Asphaltene precipitation may also obey a universal scaling relationship at the precipitation point.

In what follows the model of asphaltene transport is described. The effect of various model parameters on the resulting asphaltene structure is first examined. Subsequently, the model predictions in terms of asphaltene hindered resistance and partition coefficients are described.

The generation of the asphaltene molecules

Klein and coworkers (Savage and Klein, 1989; Trauth *et al.*, 1994) have developed a mathematical framework for utilizing available chemical and structural data (Speight, 1972; Speight and Moschopedis, 1981; Yen *et al.*, 1984a,b; Speight, 1991) to describe the structure of asphaltenes and other resid fractions. The technique requires the knowledge of the probability distribution functions for the number of the sheets in the asphaltene particles, the number of aromatic and saturated rings and the number and length of paraffinic chains. Direct analytical techniques for identifying all these structural elements are available, but this approach involves a lot of experimental resources and is time-consuming. Klein and coworkers have proposed instead an iterative stochastic modeling approach, whereby one tries to determine the probability distribution functions of the structural elements by matching measured macroscopic properties like average MW, density, viscosity, etc.

In these studies, the structural element probability distributions of the number of unit sheets, and of aromatic and saturated rings, and the length of alkyl chains were assumed to be 2-parameter log-normal distribution functions, widely used to describe polymer molecular weight distributions. The probability distribution P_d is given as

$$P_d = \frac{\exp[-(\ln x - \ln \bar{x})^2/2\sigma^2]}{\sqrt{2\pi}\sigma x} \qquad (1)$$

where x is the number/size of the structural element, $\bar{x}$ is the mean, and σ is the standard deviation (SD).

After one defines the various probability distribution functions, the number of unit sheets in every asphaltene particle and the number of aromatic rings and saturated rings in every sheet are determined. The aromatic and saturated rings are stochastically arranged with a condensation index of 0.8. The condensation index, as defined by Savage and Klein (1989), depends on the number of peripheral carbons. The aromatic and saturated rings in the sheet are packed as closely as possible. The packing is done by starting with one ring at the center and then adding rings adjacent to it in a clockwise manner. The molecule is now peri-condensed. Then the peripheral rings are arranged randomly so that the condensation index, calculated from the number of peripheral rings, is close to 0.8. The number of peripheral carbons and the number of peripheral carbons that can be substituted with aliphatic chains are then calculated. Typically 45% of aromatic carbons and 25% of saturated carbons can be substituted with alkyl chains. The peripheral carbons are randomly substituted with alkyl chains, whose lengths are determined from the cumulative distributions. The alkyl chains extend away from the condensed rings. The MW of each particle is calculated from the number of carbons and hydrogens in each molecule. The effect of the two parameters (mean and SD) of the various structural element distribution functions on the MW distributions and transport and partition coefficients was then studied.

In the generation of the molecular weight distributions of various hypothetical asphaltene molecules (Figs 1–3) five different cases were studied. The distribution function parameters for the so called "base-case" are shown in Table 1 and they correspond to the generic asphaltene of Savage and Klein (1989). In the other cases (b, c, d, e) either the mean is varied as indicated in each figure, while keeping the SD equal to the "base-case" value, or the SD is varied while keeping the mean the same.

By adjusting the parameters of the probability distribution functions and using an iterative stochastic structure determination procedure, one can generate asphaltene molecules whose MW distribution and structure match those experimentally measured and reported in the literature.

Calculation of transport coefficients using hydrodynamic theory

There are at least three approaches for modeling the hindered resistance of asphaltene particles through membrane pores and their partitioning between the bulk and the membrane structure, each with its intrinsic advantages and disadvantages. Molecular dynamic calculations of the motion of the particles would, of course, be the preferred technique but its implementation for asphaltene particles is presently numerically intractable. Monte Carlo simulations of transport and partitioning is the second technique and such calculations have been carried out (Ravi-Kumar *et al.*, 1994). They are the preferred

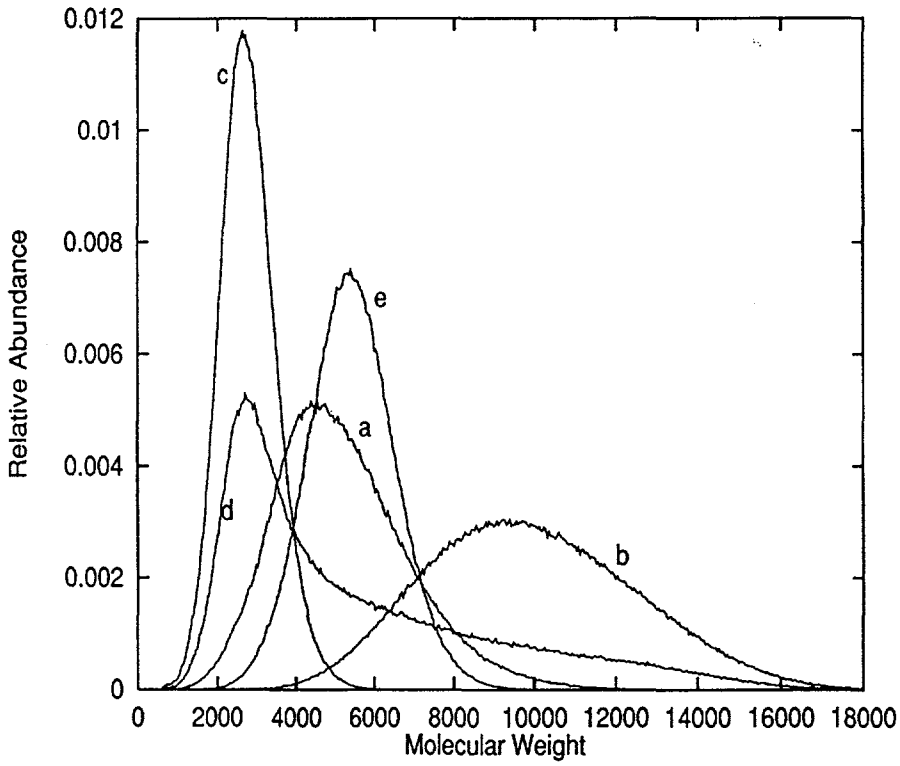

Fig. 1. Changes in molecular weight distribution of asphaltenes with varying sheet distribution. (a) Base case; (b) mean*2; (c) mean/4; (d) SD*4; (e) SD/4.

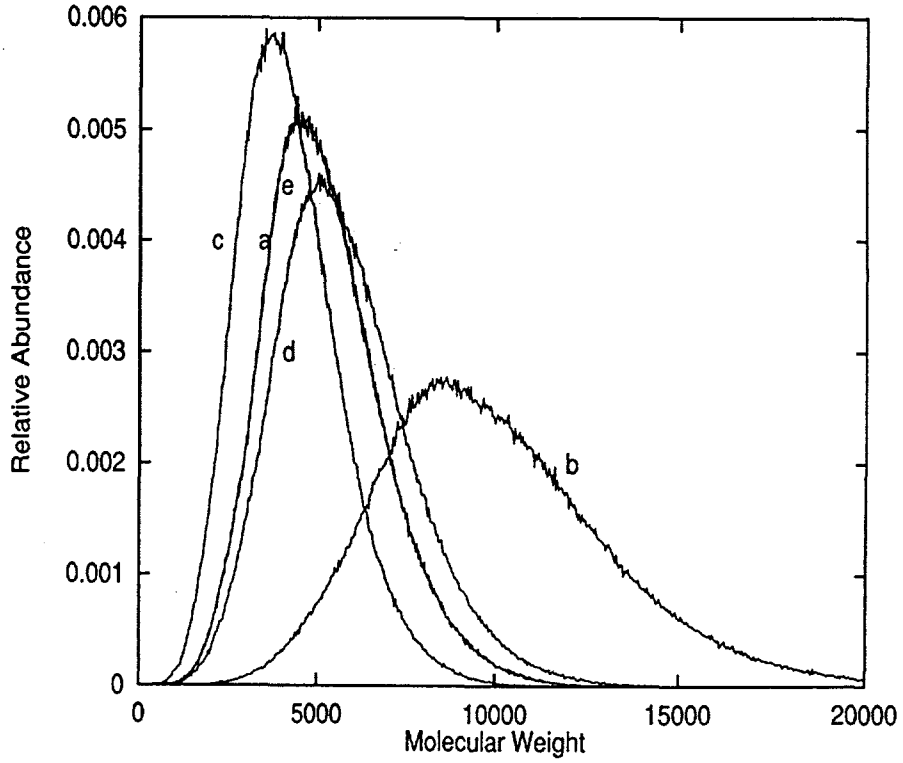

Fig. 2. Changes in molecular weight distribution of asphaltenes with varying chain distribution. (a) Base case; (b) mean*4; (c) mean/4; (d) SD*4; (e) SD/4.

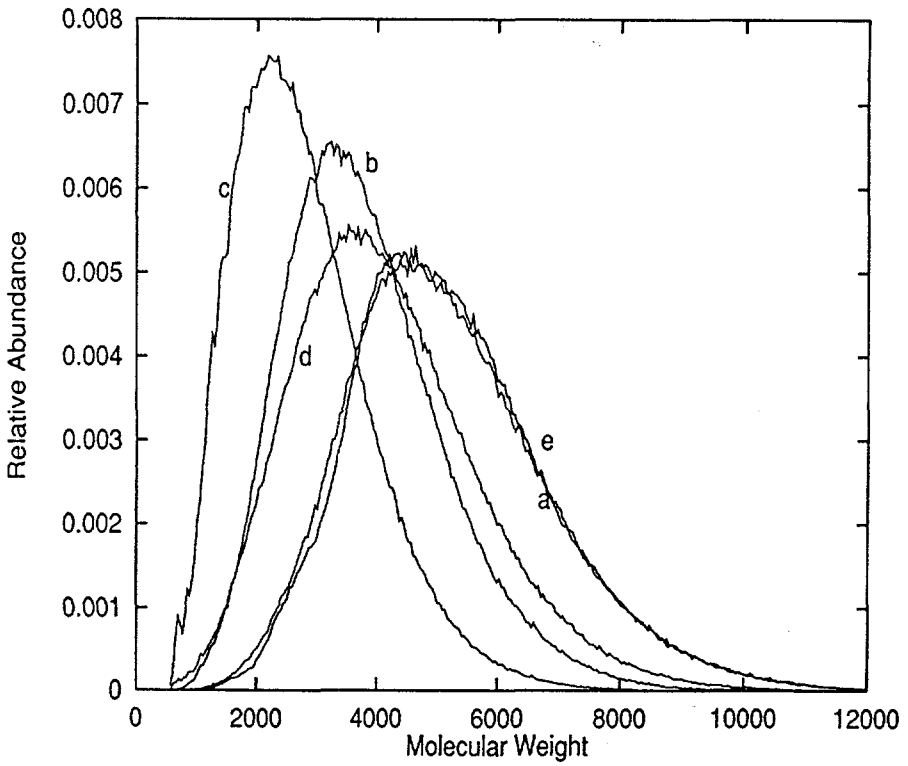

Fig. 3. Changes in molecular weight distribution of asphaltenes with varying aromatic ring distribution. (a) Base case; (b) mean/2; (c) mean/4; (d) SD*4; (e) SD/4.

option for calculating partition coefficients, but are not without shortcomings in the calculation of transport coefficients, since one is forced to introduced ambiguous parameters for the motion of the molecules and hindered drag resistance. Moreover, the relation between the Monte Carlo time and the real (molecular) time is not yet clear.

In this paper continuum hydrodynamic theory is used to simulate the hindered resistance to the transport of asphaltenes. The advantages and limitations of this technique are discussed in detail by Deen (1987) and will not be repeated here. The transport coefficients of the asphaltene molecules were calculated by approximating the molecules to be rigid, neutrally buoyant and uncharged particles. The porous membrane is assumed to consist of non-intersecting, straight, chemically inert cylindrical pores. The solvent is assumed to be a continuum. The solute transport in such a system is hindered by the pore walls. The effective diffusivity of the molecule through the pore is reduced as a result of the partitioning of the particles between the bulk phase and the porous medium, and the steric hindrance and the hydrodynamic viscous drag resistance due to the pore walls. The quantity describing the partitioning is called the partition coefficient Φ, and the steric hindrance and hydrodynamic resistance are quantified by the hydrodynamic viscous drag coefficient K_d (Deen, 1987). The diffusivity through the pore D_p is given as

$$D_p = D_\infty \Phi K_d \tag{2}$$

where D_∞ is the corresponding bulk diffusivity. For the calculation of Φ and K_d the asphaltene particles were approximated as spheroids following the original idea of Baltus and Anderson (1983). As already discussed, the asphaltene particle is thought to consist of a stack of condensed-polyaromatic sheets, referred to as the "condensed-portion" and "paraffinic-chains" extending away from the "condensed-portion". The condensed-portion is characterized by two dimensions. The first dimension is the "height" of the stack which can be directly calculated from the average inter-sheet distance, reported in the literature (Yen *et al.*, 1961). The second dimension is the critical diameter which is the largest linear dimension of any of the sheets found in the stack. The volume of the condensed portion is taken to be the volume of the spheroid with these two dimensions. To this volume we added the volume of the paraffinic chains, which is calculated from the van der Waals radii and the inter-atom distances between carbon–carbon atoms and carbon–hydrogen atoms.

Table 1. The parameters of the log-normal distribution functions for various structural elements

Structural element	Mean	SD
Number of sheets	3.58	0.26
Length of chains	6.77	0.23
Number of aromatic rings	10.50	0.30

Since the paraffinic chains are thought to lie in the plane of the polyaromatic sheet they are attached to (Yen *et al.*, 1961), the present model assumes that the height of the entire asphaltene particle is the height of the condensed-portion. The diameter of the entire asphaltene particle is calculated based on the total volume, which is the sum of the condensed-portion volume and the molar volume of the paraffinic-chains. The diameter of the asphaltene particle is the spheroidal diameter, and it is the major axis for an oblate spheroid and the minor axis for a prolate spheroid. The height of the asphaltene particle is the height of the spheroid, and it is the minor axis for an oblate spheroid and the major axis for a prolate spheroid.

The molar volumes of the entire asphaltene particle were not used in the calculation of the hindered diffusivities and partition coefficients, since the authors found [as did Tsai *et al.* (1991)] that the hindered diffusivity values so calculated are usually overestimated. For the hindered diffusivity and partition coefficient calculations, in the authors' opinion, critical dimensions of the condensed asphaltene portion are more suitable.

Calculation of partition coefficient

The partition coefficient between the bulk phase and the pores, defined as the equilibrium ratio of the solute concentration in the pores and that in the bulk solution, was calculated using the corrected (Limbach *et al.*, 1989) statistical mechanical formulas of Giddings *et al.* (1968). For an axisymmetrically-shaped particle Φ can be calculated as the fraction of the orientationally averaged pore volume accessible to the center of the molecule. The partition coefficient is given by:

$$\Phi = \frac{4}{\pi}\int_0^1 d\zeta \int_0^{\pi/2} d\theta \sin\theta (1-\zeta^2)^{1/2} \times \left(1 - \frac{(\alpha_a^2 - \alpha_b^2)cos^2\theta + \alpha_b^2}{\{\alpha_a^2\zeta^2 + [(\alpha_a^2 - \alpha_b^2)cos^2\theta + \alpha_b^2](1-\zeta^2)\}^{1/2}}\right) \times \left(1 - \frac{\alpha_a^2[(\alpha_a^2 - \alpha_b^2)cos^2\theta + \alpha_b^2]}{\{\alpha_a^2\zeta^2 + [(\alpha_a^2 - \alpha_b^2)cos^2\theta + \alpha_b^2](1-\zeta^2)\}^{3/2}}\right) \quad (3)$$

where ζ is the ratio of the radial coordinate and the ellipsoidal radius, θ is the angle between the pore and the molecule axes, α_a and α_b are the ratios of the ellipsoidal radius and half axial length, and the pore radius, respectively.

Calculation of hydrodynamic viscous drag coefficient

The averaged hydrodynamic viscous drag coefficient (K_d) is dependent on the steric and the hydrodynamic viscous drag effects due to the presence of the pore wall. For non-spherical rigid molecules (with scaled vector dimensions Λ) in cylindrical pores, Anderson and Quinn (1974) gave an expression for K_d which involves the integral of the normalized hydrodynamic viscous drag coefficient $K_U(\Lambda,\beta,\Theta)$ over all radial positions β and all orientations Θ

$$K_d(\Lambda) = \frac{\int_\Theta \int_0^{\bar{\beta}(\Lambda,\Theta)} \beta K_U^{-1}(\Lambda,\beta,\Theta) d\beta d\Theta}{\int_\Theta \int_0^{\bar{\beta}(\Lambda,\Theta)} \beta d\beta d\Theta} \quad (4)$$

where $\bar{\beta}(\Lambda,\Theta)$ is the radial position where the molecule first touches the pore wall for any given orientation.

The normalized hydrodynamic drag coefficient $K_U(\Lambda,\beta,\Theta)$ of any molecule for a given Θ and β can be calculated by solving the Navier–Stokes equations. For creeping Newtonian flow of incompressible viscous fluids, the Stokes equation of motion and the equation of continuity are

$$-\nabla p + \mu\nabla^2 \mathbf{V} = 0 \quad (5)$$

$$\nabla \cdot \mathbf{V} = 0 \quad (6)$$

where $\mathbf{V}$ is the fluid velocity, p is the pressure, and μ is the viscosity of the fluid. Almost all hydrodynamic theories assume that the random fluctuations in the motion of the molecule can be averaged over long times, and hence the particle is thought to move axially with a steady arbitrary velocity U. Once the Stokes equation has been solved, the drag of the entire molecule is known and hence K_U can be calculated. Tullock *et al.* (1992) and Kim and Karrila (1991) have described numerical techniques (mostly boundary-element methods) which can in principle be used for solving the Stokes equations for non-spherical particles. Their techniques are, however, computationally very intensive.

The rigorous analytical calculation of $K_U(\Lambda,\beta,\Theta)$ for all β and Θ is quite formidable for non-spherical particles. For spherical particles in cylindrical and slit pores, the hindrance factors that were calculated based on the centerline approximation agree reasonably well with the values calculated by integrating over the entire pore area (Anderson and Quinn, 1974; Deen, 1987). It is assumed here that the asphaltene particles are spheroids (axisymmetrical), and that they translate axisymmetrically along the center line. There is no reason to believe (but no proof either) that this approximation does not perform well for spheroids. For an axisymmetric Stokes problem, eqs (5) and (6) can be simplified by formulating them in terms of the Stokes stream function Ψ. For a steady, axisymmetric, creeping flow $\mathbf{V}$ can be expressed as

derivatives of Ψ so that the equation of continuity is automatically satisfied and then the equation of motion leads to a fourth order partial differential equation:

$$\nabla^4\Psi = 0 \quad (7)$$

The boundary conditions are $\Psi = 0$ and $V_z = 0$ at the cylinder walls, and $V_z = U$ and $V_r = 0$ on the spheroidal surface, where (r,θ,z) are the cylindrical coordinates.

The singularity technique of Chen and Skalak (1970) was used to solve the Stokes flow problem in a cylindrical tube, containing a line of spheroidal particles located axisymmetrically along the centerline. Chen and Skalak solved eq. (7) for the Stokes stream function and then calculated the viscous drag on the particle. Their solution was periodic and even in the axial coordinate z, and was given in terms of an infinite set of linear algebraic equations for the Stokes stream function coefficients. The unknown Stokes stream function coefficients were determined numerically by a boundary-element method by satisfying the boundary conditions on the spheroidal surface. The collocation points were equally spaced along the surface of the spheroid.

Chen and Skalak (1970) gave an expression [which, corrected for a few typographical errors, can be found in Ravi-Kumar (1995)] for the hydrodynamic viscous drag $\mathfrak{D}$ for a spheroidal particle of spheroidal-radius to pore-radius b_0, and spheroidal dimensions Λ, translating axisymmetrically with velocity U in a cylindrical pore filled with a fluid of viscosity μ and moving with a velocity V as

$$\mathfrak{D} = 6\pi\mu b_0[K_U(\Lambda,0,\overline{\Theta})U - K_V(\Lambda,0,\overline{\Theta})V] \quad (8)$$

$K_U(\Lambda,\beta,\overline{\Theta})$ and $K_V(\Lambda,\beta,\overline{\Theta})$ are the normalized drag coefficients for diffusion and convection, respectively, and $\overline{\Theta}$ is the axisymmetrical orientation. Chen and Skalak (1970) showed that the coefficients $K_U(\Lambda,0,\overline{\Theta})$ are directly related to one coefficient of the Stokes stream function equation set. By using the first few terms of the Stokes stream function equation set, they solved for the coefficient, and hence $K_U(\Lambda,0,\overline{\Theta})$. They found it practical to calculate the drag for the range $0 < b_0 \leq 0.8$. However, they tabulated the values of $K_U(\Lambda,0,\overline{\Theta})$ and $K_V(\Lambda,0,\overline{\Theta})$ for only eight pairs of (Λ,b_0) (within the range of interest).

To calculate the diffusivities for the broad size range of asphaltene particles the hydrodynamic coefficients were calculated over a much wider range of Λ and b_0. For the calculation reported here a dilute asphaltene solution was assumed by using spheroidal spacing six times larger than the pore radius. The present authors followed the method of Chen and Skalak (1970), and calculated the values for $K_U(\Lambda,0,\Theta)$ and $K_V(\Lambda,0,\overline{\Theta})$ in the range $0.0 \leq b_0 \leq 0.5$ and $0.4 \leq \gamma \leq 2.5$, where γ is the ratio of spheroidal-diameter to spheroidal-thickness. The collocation points were spaced evenly along the surface of the spheroid. A system of 24 stream function terms and 32 equations and a modified boundary-element method (Chen and Skalak, 1970) were used to solve for the Stokes stream function coefficients. If the matrix was singular or numerically close to being singular, singular value decomposition was used to solve for the Stokes stream function. Once the Stokes stream function is known, the hydrodynamic drag coefficient K_d can be directly calculated.

RESULTS AND DISCUSSION

Model results are presented in terms of the partition and transport coefficient distributions as a function of the molecular weight. The effect of the parameters of the probability distribution functions of the structural elements on molecular weight and transport coefficient distributions were also studied.

To generate the structures of a given asphaltene, model results were averaged over five simulation runs, each involving 200,000 particles. The molecular weight distribution of the asphaltene molecules was calculated by counting the number of particles that are within a particular range of molecular weights. The molecular weight distribution of the asphaltene molecules generated by using the original probability distributions is shown in Figs 1–3. Asphaltene molecules seem to follow a Schultz-type distribution, as was observed experimentally (Sheu *et al.*, 1990).

The effect of varying sheet probability distributions on the molecular weight distributions is shown in Fig. 1. It is clearly seen that the mean and SD affect the molecular weight distribution significantly. The effect of varying the mean of the chain lengths and the number of aromatic rings on the molecular weight distribution is also significant, but changing the SD has a weaker effect on the molecular weight distributions (see Figs 2–3).

The diffusion and partition coefficients were plotted versus molecular weight by averaging over all the molecules within a range of molecular weights. The scatter in the data at small and large molecular weights is due to the small fraction of asphaltene molecules in that range. Figure 4 shows how the partition coefficient changes with the molecular weight and the pore size. The distribution of the hindered diffusivity of asphaltene at 90°C is shown in Fig. 5. The partition and diffusion coefficients decrease with increasing molecular weight and decrease for more constricted pores. Calculated asphaltene diffusivities are of the same order of magnitude as the experimental results in the literature (Baltus and Anderson, 1983; Sane *et al.*, 1992).

The effects of the change in parameters of the probability distribution functions of the various structural elements on the partition coefficient distributions are presented in Figs 6 and 7, and on the diffusion coefficient distributions are presented in Figs 8 and 9. The parameters of the sheet distributions do not affect the partition coefficient distributions significantly, as can be seen in Fig. 6, and the same is true for the diffusion coefficients. The effect

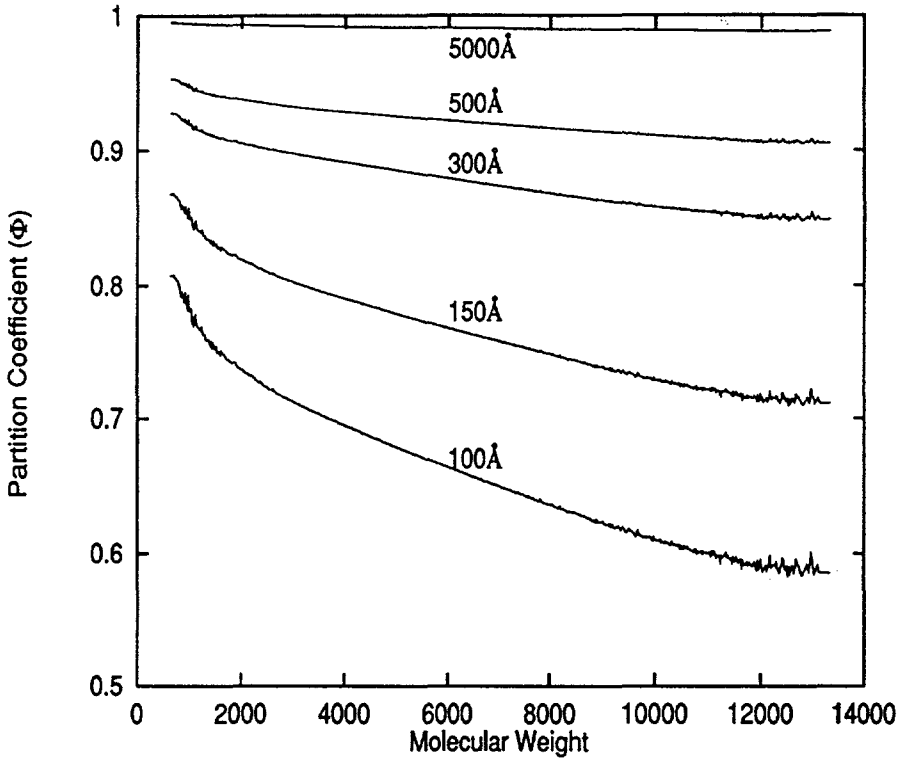

Fig. 4. Distribution of the partition coefficients of a simulated asphaltene through membranes.

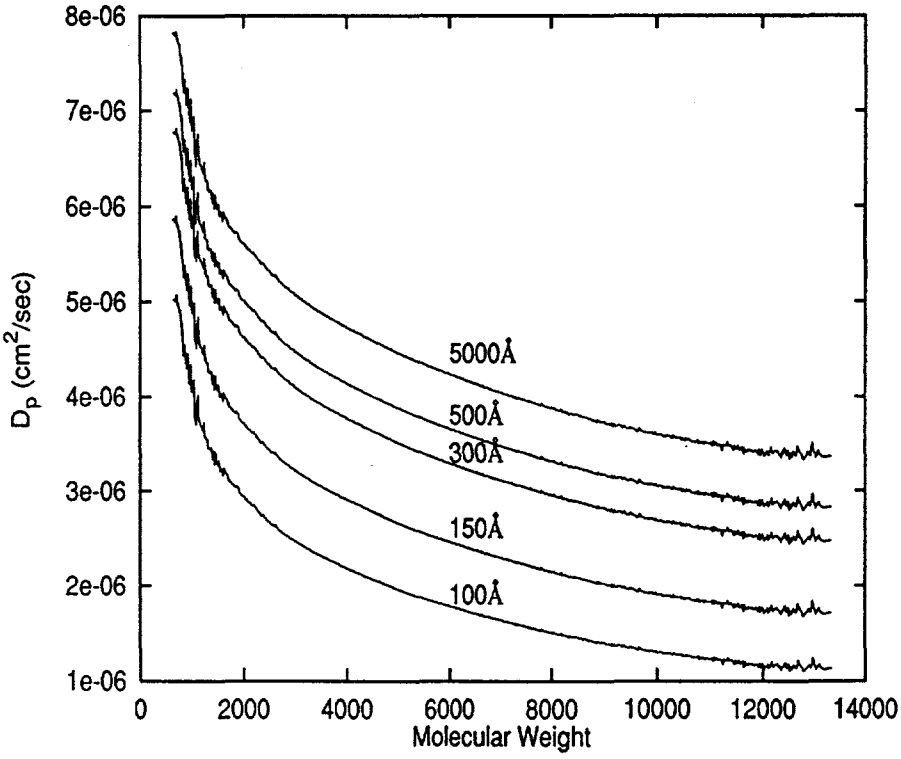

Fig. 5. Distribution of the hindered diffusion coefficients D_p of a simulated asphaltene through membranes at 90°C.

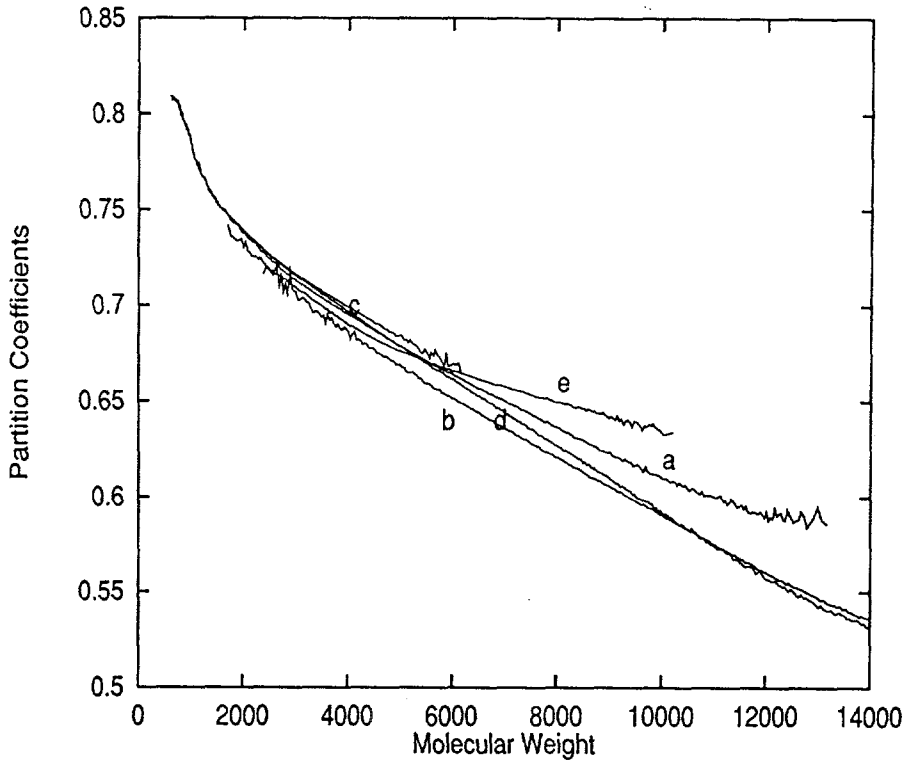

Fig. 6. Changes in the partition coefficients of asphaltenes with varying sheet distribution through a 100 Å membrane. (a) Base case; (b) mean*2; (c) mean/4; (d) SD*4; (e) SD/4.

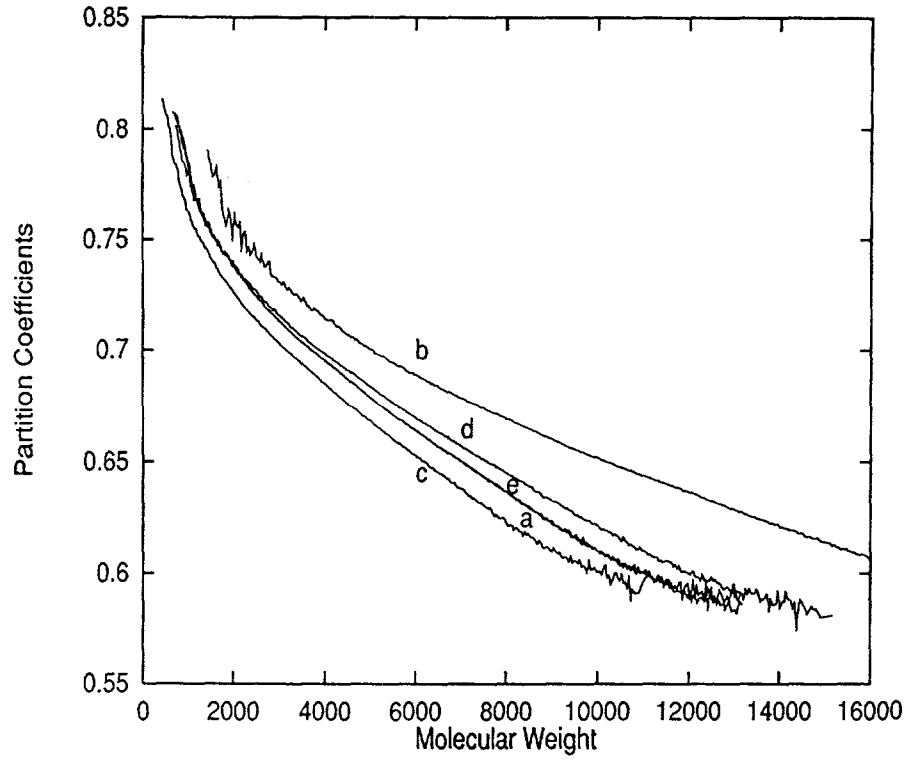

Fig. 7. Changes in the partition coefficients of asphaltenes with varying chain distribution through a 100 Å membrane. (a) Base case; (b) mean*4; (c) mean/4; (d) SD*4; (e) SD/4.

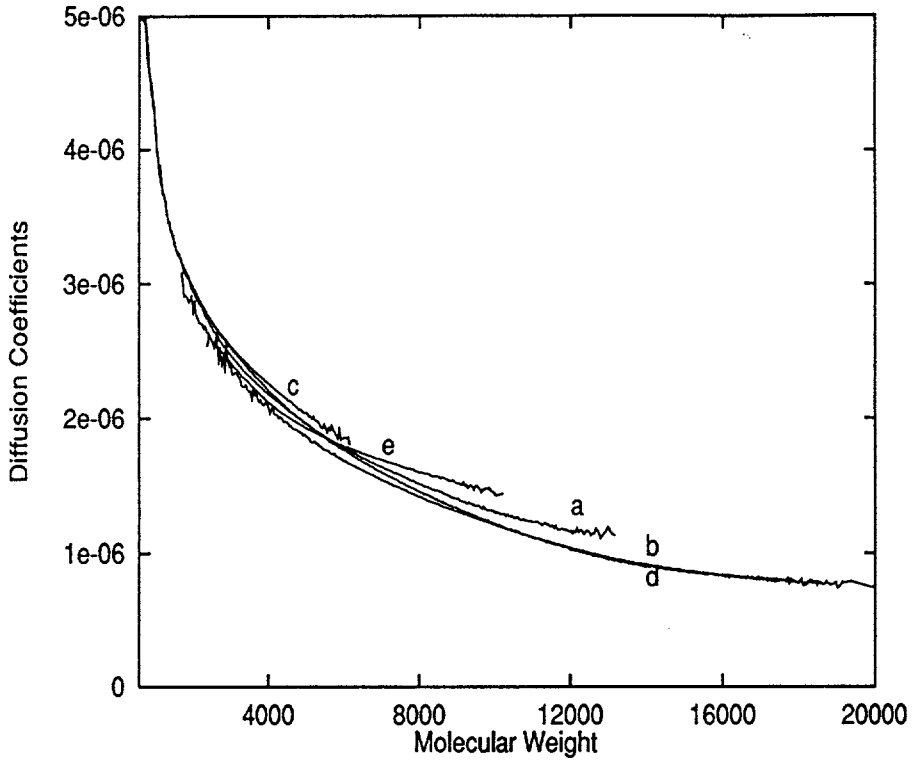

Fig. 8. Changes in the diffusion coefficients of asphaltenes with varying sheet distribution through a 100 Å membrane at 90°C. (a) Base case; (b) mean*2; (c) mean/4; (d) SD*4; (e) SD/4.

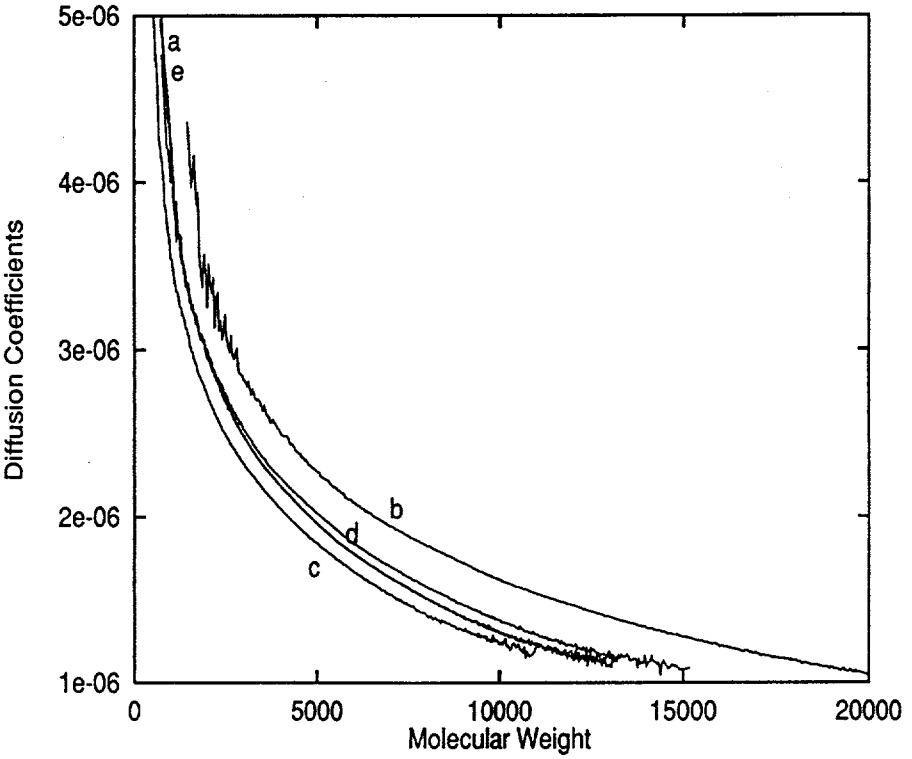

Fig. 9. Changes in the diffusion coefficients of asphaltenes with varying chain distribution through a 100 Å membrane at 90°C. (a) Base case; (b) mean*4; (c) mean/4; (d) SD*4; (e) SD/4.

of the sheet distribution on the partition and diffusion coefficients is basically manifested through the changes in the MW distribution. The mean of the chain probability distributions affects the partition and diffusion coefficients significantly, while the SD has no significant effect. The changes in the distribution of aromatic rings also has no significant effect on the partition and diffusion coefficients. Thus, molecular weight and the mean chain length appear to be the major factors affecting the partition coefficient and diffusivity of asphaltenes. These effects, however, can be the result of the particular technique used to calculate the spheroidal dimensions. Well-designed experiments in this area would be of great value.

The authors of this study have so far identified the parameters which significantly affect the MW distribution and the transport coefficients. By adjusting the parameters of the probability distribution functions and using an iterative stochastic structure determination model, one can generate asphaltene molecules whose MW distributions and molecular structures match those measured/reported in the literature. There is no reliable technique available today, however, that can be used for measuring such MW distributions. Size-exclusion chromatography appears to be more commonly used, and modeling SEC data using the physics of SEC and our transport model is the subject of our ongoing investigation.

CONCLUSIONS

The authors have presented a model which they believe faithfully captures some of the unique features of asphaltene transport through cylindrical pores. The statistical molecular structure models developed by Klein and coworkers have been used to generate the asphaltene molecules. Hydrodynamic continuum theories have been used for calculating the partition coefficients and hindered resistance for asphaltene molecules by approximating them as spheroids. The model described here is still at an early stage of development. To truly begin describing asphaltene transport, one must incorporate into the model the physics of the agglomeration/delamination process. It goes without saying that the idea of approximating an asphaltene particle as a rigid spheroid, though useful for making the calculations numerically tractable, is an oversimplification.

The validity of any model (and its further development) must eventually be judged by its agreement with experimental data. To critically evaluate the asphaltene transport model presented here one must have structural information and diffusion data over a wide range of conditions. The authors are aware of no such comprehensive data that would allow at this time meaningful comparisons. Work in this area is continuing in the authors' group.

Acknowledgment—The authors wish to thank the National Science Foundation, the U.S. Department of Energy and the Unocal Corporation for their support.

REFERENCES

Anderson, J. L. and Quinn, J. A., 1974, Restricted transport in small pores: A model for steric exclusion and hindered particle motion. *Biophys. J.* **14**, 130–150.

Baltus, R. E., 1984, Hindered diffusion of petroleum asphaltenes, in *Catalysis on the Energy Scene, Studies in Surface Science and Catalysis* (Edited by S. Kaliaguine and A. Mahay), pp. 553–560. Elsevier, New York.

Baltus, R. E. and Anderson, J. L., 1983, Hindered diffusion of asphaltenes through microporous membranes. *Chem. Engng Sci.* **38**, 1959–1969.

Baltus, R. E. and Anderson, J. L., 1984, Comparison of GPC elution characteristics and diffusion coefficients of asphaltenes, *Fuel*, **63**, 530.

Bunger, J. W. and Cogswell, D. E., 1981, Characteristics of tar and bitumen asphaltenes as studied by conversion of bitumen by hydropyrolysis, in *Chemistry of Asphaltenes* (Edited by J. W. Bunger and C. N. Li), pp. 219–236. *Adv. Chem. Ser.* Vol. 195, American Chemical Society, Washington, DC.

Chen, T. C. and Skalak, R., 1970, Stokes Flow in a cylindrical tube containing a line of spheroidal particles. *Appl. Sci. Res.* **22**, 403–441.

Deen, W. M., 1987, Hindered transport of large molecules in liquid-filled pores. *A.I.Ch.E. J.* **33**, 1409–1425.

Dickie, J. P. and Yen, T. F., 1967, Macrostructures of the asphaltic fractions by various instrumental methods. *Anal. Chem.* **39**, 1847–1852.

Dolbear, G. E. and Phan, H. Y., 1988, Isolation of asphaltenes using a continuous precipitation method. *Fuel Sci. Technol. Int.* **6**, 471–481.

Garcia de la Torre, J. G. and Bloomfield, V. A., 1978, Hydrodynamic properties of macromolecular complexes. IV. Intrinsic viscosity theory with applications to once broken rods and multisubunit proteins. *Biopolymer* **17**, 1605–1627.

Giddings, J. C., Kucera, E., Russell, C. P. and Myers, M. N., 1968, Statistical theory for the equilibrium distribution of rigid molecules. Exclusion chromatography. *J. Phys. Chem.* **72**, 4397–4408.

Kim, S. and Karrila, S., 1991, *Microhydrodynamics. Principles and Selected Applications*. Butterworth-Heinemann, Stoneham, Massachusetts.

Koots, J. A. and Speight, J. G., 1975, Relation of petroleum resins to asphaltenes. *Fuel* **54**, 179–184.

Kyriakou, K. C., Sivaramakrishna, V. V., Baltus, R. E. and Rahimi, P., 1988, Measurement of diffusion coefficients of oil residual fractions using porous membranes. *Fuel* **67**, 15–18.

Limbach, K. W., Nitsche, J. M. and Wei, J., 1989, Partitioning of non-spherical molecules between bulk solution and porous solids. *A.I.Ch.E. J.* **35**, 42–52.

Long, R. B. and Speight, J. G., 1989, Studies in petroleum composition. Development of a compositionqal "map" for various feedstocks. *Revue de l'Institut Français du Pétrole* **44**, 205–217.

McKay, J. F., Amend, P. J., Cogswell, T. E., Harnsberger, P. M., Erikson, R. B. and Latham, D. R., 1978, Petroleum asphaltenes. Chemistry and composition. In *Analytical Chemistry of Liquid Fuel Sources: Tar Sands, Oil Shale, Coal, and Petroleum* (Edited by P. C. Uden and H. B. Jensen), pp. 128–142. Siggia, Sidney.

Mieville, R. L., Trauth, D. M. and Robinson, K. K., 1989, Asphaltene characterization and diffusion measurements. *Prepr. Am. Chem. Soc. Div. Pet. Chem.* **34**, 635–643.

Moschopedis, S. E., Fryer, J. F. and Speight, J. G., 1976, Investigation of asphaltene molecular weights. *Fuel* **55**, 227–232.

Nortz, R. L., Baltus, R. E. and Rahimi, P., 1990, Determination of the macroscopic structure of heavy oils by measuring hydrodynamic properties. *Ind. Engng Chem. Res.* **29**, 1968–1976.

Pfeiffer, J. P. and Saal, R. N. H., 1940, Asphaltene bitumen as a colloid system. *J. Phys. Chem.* **44**, 139–149.

Rao, B. M. L. and Serrano, J. E., 1986, Viscometric study of aggregation interactions in heavy oil. *Fuel Sci. Technol. Int.* **4**, 483–500.

Rassamdana, H., Dabir, B., Nematy, M., Farhani, M. and Sahimi, M., 1994, Asphalt flocculation and deposition I. The onset of precipitation. *A.I.Ch.E. J.* (in press).

Ravi-Kumar, V. S., 1995, Experimental and theoretical studies of transport and reaction of asphaltenes through membranes. Ph.D. thesis (to be submitted), University of Southern California.

Ravi-Kumar, V. S., Tsotsis, T. T., Sahimi, M. and Webster, I. A., 1994, *Inorganic membranes for the Study of Transport and Reaction of Petroleum and Coal Liquids.* Paper presented at the *3rd International Conference on Inorganic Membranes*, Worcestershire, Massachusetts.

Sane, R. C., 1992, Diffusion of petroleum asphaltenes in porous membranes. Ph.D. thesis, University of Southern California.

Sane, R. C., Webster, I. A. and Tsotsis, T. T., 1988, A study of asphaltene diffusion through unimodal porous membranes. *Stud. Surf. Sci. Catal.* **38**, 705–716.

Sane, R. C., Tsotsis, T. T., Webster, I. A. and Ravi-Kumar, V. S., 1992, Studies of asphaltene diffusion and structure and their implications for resid upgrading. *Chem. Engng Sci.* **47**, 2638–2688.

Sane, R. C., Tsotsis, T. T., Webster, I. A. and Ravi-Kumar, V. S., 1994, Studies of asphaltene diffusion. Implications for asphaltene structure and optimal upgrading reactor design, in *Asphaltenes and Asphalts, 1. Developments in Petroleum Science, vol. 40.* (Edited by T. F. Yen and G. V. Chilingar). Elsevier Science, Amsterdam.

Savage, P. E. and Klein, M. T., 1989, Asphaltene reaction pathways – V. Chemical and mathematical modeling. *Chem. Engng Sci.* **44**, 393–404.

Sheu, E. Y., Liang, K. S., Sinha, S. K. and Overfield, R. E., 1990, Polydispersity of asphaltenes in toluene. *Prepr. Am. Chem. Soc. Div. Pet. Chem.* **35**, 813–818.

Sheu, E. Y., De Tar, M. M., Storm, D. A. and DeCanio, S. J., 1992, Aggregation and kinetics of asphaltenes in organic-solvents. *Fuel* **71**, 299–302.

Shimura, M., Shiroto, Y. and Takeuchi, C., 1986, Effect of catalyst pore structure on hydrotreating of heavy oil. *Ind. Engng Chem. Fundam.* **25**, 330–337.

Speight, J. G., 1972, The application of spectroscopic techniques to the structural analysis of coal and petroleum. *Appl. Spectrosc. Rev.* **5**, 211–263.

Speight, J. G., 1991, *The Chemistry and Technology of Petroleum.* Marcel Dekker, New York.

Speight, J. G. and Moschopedis, S. E., 1981, On the molecular nature of petroleum asphaltenes, in *Chemistry of Asphaltenes* (Edited by J. W. Bunger and C. N. Li), pp. 1–15. *Adv. Chem. Ser.*, Vol. 195, American Chemical Society, Washington, DC.

Speight, J. G., Wernick, D. L., Gould, K. A., Overfield, R. E., Rao, B. M. L. and Savage, D. W., 1985, Molecular weight and association of asphaltenes: A critical review. *Revue de l'Institut Français du Pétrole* **40**, 51–61.

Strausz, O. P., Lown, E. M. and Mojelsky, T. W., 1994, The molecular structure of asphaltene. *Prepr. Am. Chem. Soc. Div. Fuel. Chem.* **39**, 199.

Thrash, R. J. and Pildes, R. H., 1981, The diffusion of petroleum asphaltenes through well-characterized porous membranes. *Prepr. Am . Chem. Soc. Div. Pet. Chem.* **26**, 515–525.

Trauth, D. M., Stark, S. M., Petti, T. F., Neurock, M. and Klein, M. T., 1994, Representation of the molecular structure of petroleum resid through characterization and Monte Carlo modeling. *Energy and Fuels* **8**, 576–580.

Tsai, C. H., Massoth, F. E., Lee, S. Y. and Seader, J. D., 1991, Effects of solvent and solute configuration on restrictive diffusion in hydrotreating catalysts. *Ind. Engng Chem. Res.* **30**, 22–28.

Tullock, D. L., Phan-Thien, N. and Graham, A. L., 1992, Boundary element simulations of spheres settling in circular, square and triangular conduits. *Rheol. Acta* **31**, 139–150.

Wiehe, I. A., 1992, A solvent–resid phase diagram for tracking resid conversion. *Ind. Engng Chem. Res.* **31**, 530–536.

Yen. T. F., 1990, Asphaltic materials, in *Encyclopedia of Polymer Science and Engineering* (Edited by H. F. Mark, N. M. Bikales, C. G. Overberger and G. Menges), pp. 1–10. Index Volume, Second Edition. John Wiley & Sons Inc., New York.

Yen, T. F., 1994, The overall properties of asphaltenes as deduced from structure. *Prepr. Am. Chem. Soc. Div. Pet. Chem.* **39**, 198.

Yen, T. F., Erdman, J. L. and Pollack, S. P., 1961, Investigation of the structure of petroleum asphaltenes by X-ray diffraction. *Anal. Chem.* **33**, 1587–1594.

Yen, T. F., Wu, W. H. and Chilingar, G. V., 1984a, A study of the structure of petroleum asphaltenes and related substances by infrared spectroscopy. *Energy Sources* **7**, 203–235.

Yen, T. F., Wu, W. H. and Chilingar, G. V., 1984b, A study of the structure of petroleum asphaltenes and related substances by proton nuclear magnetic resonance. *Energy Sources* **7**, 275–304.

FRACTALS IN POROUS MEDIA: FROM PORE TO FIELD SCALE

MUHAMMAD SAHIMI, HOSSEIN RASSAMDANA, AND ALIREZA MEHRABI
Department of Chemical Engineering, University of Southern California, Los Angeles, CA 90089-1211

ABSTRACT

Two applications of fractal concepts to problems involving porous media are discussed. One of them occurs at the pore level and involves the formation of large molecular aggregates as the result of injecting a fluid into an oil reservoir, or because of compositional changes in the oil. Formation of such aggregates and their precipitation on the pore surfaces cause severe problems for enhanced recovery of oil, and also many processes which use porous catalysts. We argue that these molecular structures are similar to diffusion-limited cluster-cluster aggregates, and small-angle neutron scattering data support our argument. The second application involves field-scale distributions of the porosity and permeability of oil reservoirs. We show that, contrary to the recent assertions that such distributions are described by fractional Brownian motion or fractional Gaussian noise with positive correlations (persistence), they are described by Lévy distributions with *negative* correlations (*anti-persistence*).

INTRODUCTION

In recent years the complex behavior of wide variety of phenomena of interest to chemists, physicists, and engineers has been characterized quantitatively by using the ideas of fractal distributions that correspond in a unique way to the geometrical shape and dynamical properties of the system under study. The key to this remarkable progress has been the fact that many disordered systems possess scale symmetry and invariance. Isotropic systems with such scale symmetry and invariance are self-similar, and can be characterized by a fractal dimension D_f, a property that corresponds in a unique fashion to the geometrical shape of the system. Anisotropic systems with scale symmetry are *self-affine* which means that such systems preserve their scale invariance only if lengths in different directions are rescaled by direction-dependent scale factors. Such self-affine fractals no longer can be described by a single fractal dimension. Examples of self-affine fractals include the fractional Brownian motion (fBm) and fractional Gaussian noise (fGn) which are discussed in this paper. Several books and articles discuss various aspects of fractal phenomena and their applications to many branches of science and technology [1-6].

An area in which the application of fractal concepts has proven fruitful is characterization of, and flow and transport through, porous media [7,8]. In addition, fractal concepts have provided us with a much deeper understanding of reaction and precipitation in porous media [4,9-11] which result in the dynamical evolution and restructuring of porous media, and nucleation and propagation of fractures in natural rock [12,13], which are crucial to flow of oil in underground reservoirs, the development of groundwater resources, and the generation of heat and vapor from geothermal reservoirs for use in power plants. Such fractures provide high permeability paths for fluid flow in reservoirs that are otherwise of very low permeabilities and porosities, and would not be able to produce at economical rates. We

Mat. Res. Soc. Symp. Proc. Vol. 367 © 1995 Materials Research Society

do not intend to discuss all the applications of fractal concepts to porous media, as they are well-documented [7-14]. Instead, we focus on just two of such applications. One of them, which occurs at the pore level, is new and has not been discussed before. This is a phenomenon in which large molecular aggregates are formed and precipitate on the surface of the pores of an oil reservoir, when a fluid is injected into the pore space to displace the oil and enhance its recovery. A similar phenomenon occurs in many processes involving porous catalysts. For example, during catalytic coal liquefaction and coal liquid upgrading, and also many refining processes that use porous catalysts, large molecular aggregates are formed whose precipitation on the surfaces of the catalyst's pores cause severe problems for efficient operation of such processes. In the chemical and petroleum industries such molecular aggregates are referred to as *asphalts*. These aggregates have many unusual properties, and have also been used [15] for manufacturing strong composites that have many industrial applications. The second application we discuss is characterization of field-scale distributions of the porosities and permeabilities of reservoir rock. Such an application was pioneered by Hewett [16,17], who showed that the porosities and permeabilities of many oil reservoirs obey fractal statistics. However, our recent work indicates that, although the original ideas of Hewett about the applicability of fractals to field-scale reservoirs are valid, many of his conclusions regarding the type of fractal distributions that the porosities and permeabilities follow need to be re-evaluated.

This paper is organized as follows. In the next section we discuss the application of fractals to the formation and precipitation of molecular aggregates in porous media. Next, we discuss fractal characterization of field-scale porous media. In the last section the paper is summarized, and possible future research directions are pointed out.

FORMATION OF MOLECULAR AGGREGATES IN POROUS MEDIA

The asphalt aggregates usually are highly polar, and there is strong evidence [18] that they are colloidal particles, which means that they cannot be processed with the current refining technology. When they are formed in an oil reservoir, they precipitate on the surface of the pores and plug them and thus reduce the effective permeability of the reservoir. In order to disperse the asphalt aggregates in refining operations, or prevent their formation and precipitation in an oil reservoir or in a porous catalyst, it is of fundamental importance to understand their molecular structure and the mechanisms that give rise to their formation. However, despite many years of research, and particularly extensive experimental work [19], up until very recently a model of the asphalt aggregates whose properties are all consistent with the experimental data had not emerged.

There are several methods for measuring various properties of the asphalt aggregates that provide insight into their structure. One popular method has been measuring their effective diffusivity in a well-defined system such as a porous membrane with non-intersecting pores. Since the pores are non-intersecting, possible complications due to the tortuosity of the membrane do not arise. Because the size of the aggregates is comparable with that of the pores, diffusion of the asphalts is *hindered* or restricted, which means that their effective diffusivity in the pores is smaller than its corresponding value in an unbounded solution. The experimental data are then correlated using the hydrodynamic theories of hindered diffusion [20-23]. These theories provide reasonably accurate approximate description of the data, but as far as providing insight into the structure of the aggregates is concerned, they can be used only if we assume that the aggregates can be respresented as spherical molecules with an effective hydrodynamic radius, or as ellipsoidal molecules with given major and

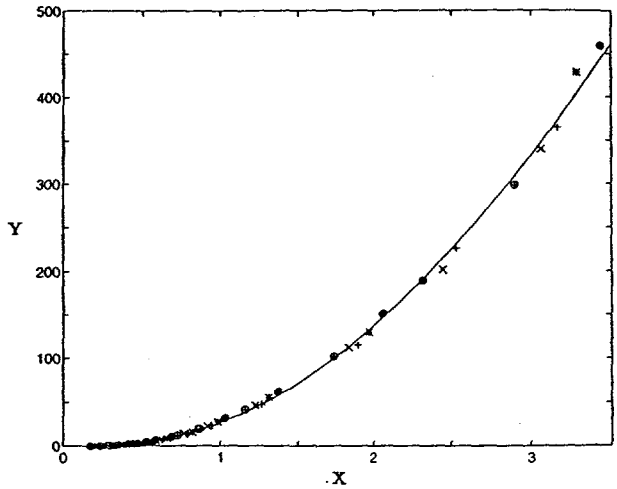

Figure 1: The rescaled experimental data (symbols) for precipitation of the asphalts with $X = r/M^{1/4}$ and $Y = Wr^2$. The curve is the universal scaling function and represents the best fit of the data.

minor axial lengths. Despite this severe shortcoming, such correlations have been derived by several authors [24,25], mainly because an understanding of transport properties of asphalts is essential to the successful design of refining and coal liquefaction operations. Another approach was proposed by Klein and coworkers [26,27] by which an iterative stochastic model of the aggregates is constructed, beginning with some hypothesized structure and matching its properties with measured macroscopic properties such as the average molecular weight of the aggregates, their viscosity, density, etc. However, this approach is very tedious and requires a considerable amount of accurate experimental data, some of which are not even available yet.

As far as oil recovery and refining processes involving porous catalysts are concerned, it is of great importance to know the amount of precipitated aggregates on the surface of the pores [28]. However, despite their significance, accurate precipitation data are relatively rare, because their measurement is difficult. The structure of the aggregates and their precipitation on the pore surface are sensitive to the temperature and pressure of the system, the chemical composition of the fluid that is injected into the pore space, and a variety of other factors. We have recently carried out [29] a careful experimental study of asphalt formation in a pore using crude oils and a variety of alkanes, ranging from C_3 to C_{10}, as the injection or solvent fluid. We have measured the amount of the precipitated asphalt that is formed when an alkane is injected into the pore that contains a crude oil. At a given temperature and pressure, the parameters of the measurements were the molecular weight M of the solvent, the solvent to crude ratio r (in cm^3/gr), and the weight percent W of the precipitated asphalt. We have shown [29] that an scaling equation can be developed by combining the three variables into two variables $X = r/M^z$ and $Y = Wr^{z'}$, thereby collapsing all the experimental data for various values of M, W, and r onto a single curve. We have shown that z and z' are *universal*, i.e., they are independent of the temperature

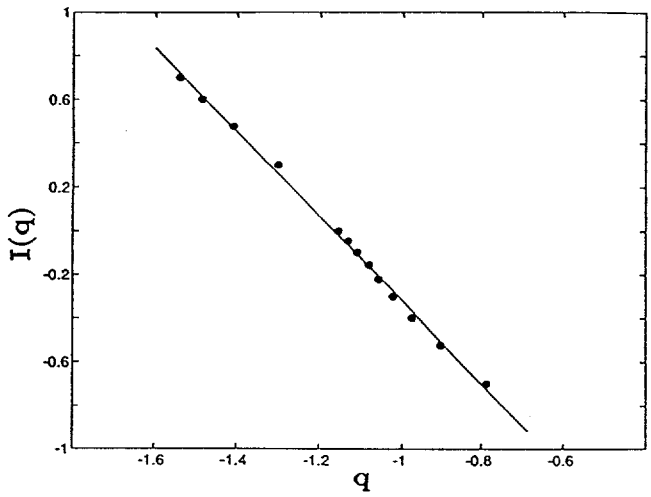

Figure 2: Logarithmic plot of the SANS intensity $I(q)$ versus the magnitude of the scattering vector q, for a toluene solution that contains 5% asphalt, at $T = 25°$.

and pressure of the system, or the composition of the crude oil, and that $z = 1/4$ and $z' = 2$. Therefore, the scaling function provides a universal equation of state that may be used for predicting the amount of the precipitated asphalts under wide variety of conditions. Figure 1 shows the universal scaling equation together with the experimental data at $T = 26°$C. We have shown [30] that our universal scaling equation can successfully predict the experimental data for a variety of crude oils.

The existence of such universal scaling variables and functions strongly suggests that the asphalt aggregates are fractal and self-similar. Thus, motivated by this observation, we have analyzed [31] small-angle neutron scattering (SANS) data on asphalt solutions in toluene at various temperatures [32,33]. Suppose that $I(q)$ is the scattering intensity, where q is the magnitude of the scattering vector. If the aggregates have a fractal structure, then [34]

$$I(q) \sim q^{-D_f} , \tag{1}$$

where D_f is the fractal dimension of the aggregates. Figure 2 shows the log-log plot of $I(q)$ versus q for a solution that contains 5% asphalt in toluene at $T = 25°$C, very close to the temperature at which the data shown in Fig. 1 were measured. As can be seen, over about one order of magnitude variations in q, we have a straight line with an slope

$$D_f = 1.8 \pm 0.05 . \tag{2}$$

What is the interpretation of this value of the fractal dimension? From our experimental observations the following picture of formation of the aggregates emerges. As the solvent is injected into the oil, very small solid particles are formed in the solution. These particles diffuse in the solution, and upon collision with each other they stick together. After some time, one has a number of small clusters of solid particles in the solution, whose sizes are not yet large enough to prevent their diffusion in the solution. Thus, the solid clusters also

diffuse in the solution until they collide and are attached to each other. After some time the aggregate becomes too large and heavy, and thus it precipitates onto the pore surface. This picture of formation of the aggregates is based on the experimental observations, but it is also the way diffusion-limited cluster-cluster (DLCC) aggregates are formed [35]. Such aggregates have a fractal dimension $D_f \simeq 1.75 - 1.8$, in very good agreement with our result. This confirms our assertion that the asphalt aggregates have a fractal structure, and the SANS data as well as and precipitation data indicate that these aggregates are in fact DLCC aggregates that have been studied extensively in the past several years.

The discovery that asphalts are colloidal aggregates with a fractal structure has important practical implications. The kinetics of the aggregation of asphalts can be described in terms of the mean-field Smoluchowsky equation

$$\frac{dn_k}{dt} = \frac{1}{2}\sum_{i+j=k} K(i,j)n_i n_j - \sum_{j=1}^{\infty} K(k,j)n_k \ , \tag{3}$$

where n_i is the number of clusters of size i, and $K(i,j)$ is a kernel. The first term of the right hand side represents the formation of clusters of size k from the two smaller clusters of sizes i and $j = k - i$, while the second term represents the loss of clusters of size k by reaction with other clusters to form larger clusters. For DLCC aggregates the appropriate kernel is given by [36]

$$K(i,j) = \left(i^{\delta} + j^{\delta}\right)\left(i^{1/D_f} + j^{1/D_f}\right) \tag{4}$$

where δ is the exponent the relates the diffusion coefficient $\mathcal{D}$ of the individual clusters to their mass M, $\mathcal{D} \sim M^{\delta}$. This mean-field description is valid in three or higher dimensions, and thus should be highly accurate for the asphalt aggregation. Using this mean-field theory, one can calculate various quantities of interest, such as the molecular weight distribution of the asphalts. Identifying the asphalts as DLCC aggregates also enables us to impose an upper bound on the typical molecular weight M of the asphalt aggregates, an unsolved problem to date. Moreover, this upper bound tells us that M cannot exceed a few thousands, contrary to some assertions in the literature that M can be as large as 10^5, since if M becomes too large thermal fluctuations in the solution disturb the mechanical stability of the aggregates and force them to rearrange themselves. Thus, the mean-field approach, together with our universal scaling equation for the amount of the precipitated asphalts, give us a relatively complete theory of aggregation and deposition of molecular aggregates in porous media.

CHARACTERIZATION OF FIELD-SCALE POROUS MEDIA

Although characterization of laboratory-scale, or *macroscopic* porous media can be done in great detail, and reasonable understanding of such systems has been obtained, the same is not true about field-scale, or *megascopic* porous media. Experimental data for the morphology of such porous media is incomplete, their effective properties such as the porosity and the permeability vary greatly at different length scales, often by several orders of magnitude, and the relations between such properties and the volume or the linear size of the porous media which one wishes to study or exploit are often unknown. For this reason, modelling field-scale porous media usually involves *stochastic* techniques. Thus, although field-scale reservoirs are, in principle, intrinsically deterministic, because of the great uncertainties one often has to speak of the stochastic nature of such porous media, and describe their properties in terms of statistical quantities. As flow in field-scale porous media is greatly important

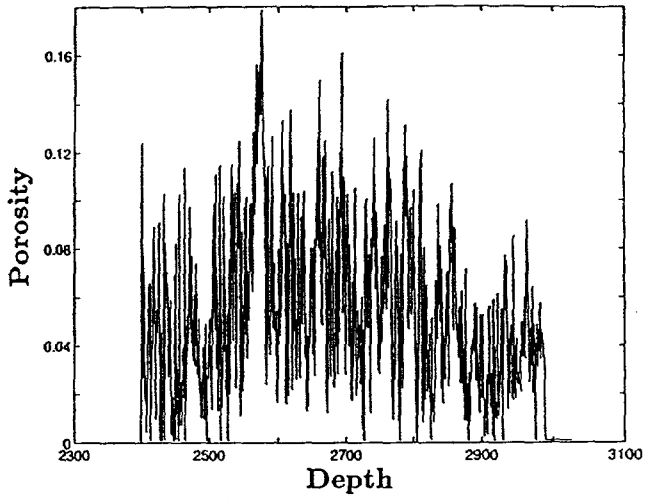

Figure 3: The porosity log of a 600m-deep well in the Middle East.

to oil and gas recovery from underground reservoirs, and to the development of groundwater resources in aquifers, it has captured the attention of scientist and *politicians*, since pollution of groundwater resources has become a "hot" political issue in the USA.

To give the reader some idea about the complexities that are involved in the characterization of a field-scale porous medium, we show in Fig. 3 a vertical porosity log that was obtained from an oil well in the Middle East. The well's depth was about 600m and the porosity ϕ was measured every 20cm, so that over 3,000 data points were collected. As can be seen, the pattern of the variations of ϕ is very complex. How do we analyze such complex variations of ϕ and uncover any mathematical structure that they may have? The analysis of such data is usually done by using the rescaled-range technique by which a quantity $R(L)/S(L)$ is calculated, where $R(L)$ is the range of the accumulated departure from the mean of the variable at length scale L, and $S(L)$ is the standard deviation (see Feder [3] for more details). This method was first used by Hurst [37] for analyzing annual flows in rivers. In mathematical terms, if a variable v takes the value $v(\ell)$ at position ℓ, $R(L)$ is given by

$$R(L) = X_{max}(\ell, L) - X_{min}(\ell, L) \,, \quad 1 \leq \ell \leq L \,, \tag{5}$$

$$X(\ell, L) = \sum_{u=1}^{\ell} [v(u) - \langle v \rangle_L] \,, \tag{6}$$

$$\langle v \rangle_L = \frac{1}{L} \sum_{\ell=1}^{L} v(\ell) \,, \tag{7}$$

and $S(L)$ is given by

$$S(L) = \left\{ \frac{1}{L} \sum_{\ell=1}^{L} [v(\ell) - \langle v \rangle_L]^2 \right\}^{1/2} \,. \tag{8}$$

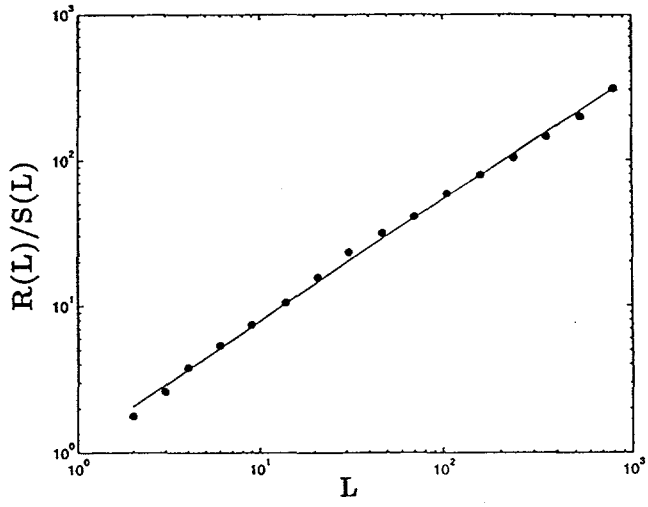

Figure 4: Rescaled-range analysis of the porosity log shown in Fig. 3. The slope of the straight line is $H \simeq 0.83$.

It can be shown that if the data follow an fBm, then [38]

$$\frac{R(L)}{S(L)} \sim L^H \ , \tag{9}$$

where H is called the Hurst exponent, and $0 \leq H \leq 1$. $H > 0.5$ signifies positive correlations or persistence, i.e., a trend (a low or high value) at x is followed by a similar trend at $x + \Delta x$, whereas $H < 0.5$ is indicative of negative correlations or anti-persistence. An fBm is a fractal distribution whose spectral density $\mathcal{S}(\omega)$, the Fourier transform of its variance, in one dimension is given by

$$\mathcal{S}(\omega) \sim \frac{1}{\omega^{2H+1}} \tag{10}$$

where ω is the Fourier component. An fGn has a similar spectral density with the exponent $2H + 1$ replaced by $2H - 1$. We carried out a rescaled-range analysis of the data shown in Fig. 3, the results of which are shown in Fig. 4. For nearly 3 orders of magnitude variations in L we obtain $H \simeq 0.83$. A similar value of H was obtained by Hewett [16] who carried out the first rescaled-range analysis of a porosity log. However, $H \simeq 0.83$ is indicative of strong persistence and positive correlations in the data, whereas the porosity log shown in Fig. 3 indicates clearly the existence of anti-persistence or negative correlations, as a high value of ϕ is followed by a low value, and vice versa. From a geological point of view, the existence of anti-persistence seems more plausible, since reservoir rock usually is stratified and layered, and the properties of the neighboring layers differ greatly.

To obtain a better understanding of the data, we first construct the experimental histogram of the increments $\phi(x + \ell) - \phi(x)$, where we fix the separation length ℓ [39]. The results are shown in Fig. 5 for $\ell = 20$cm. Also shown is the fit of the data to a Lévy

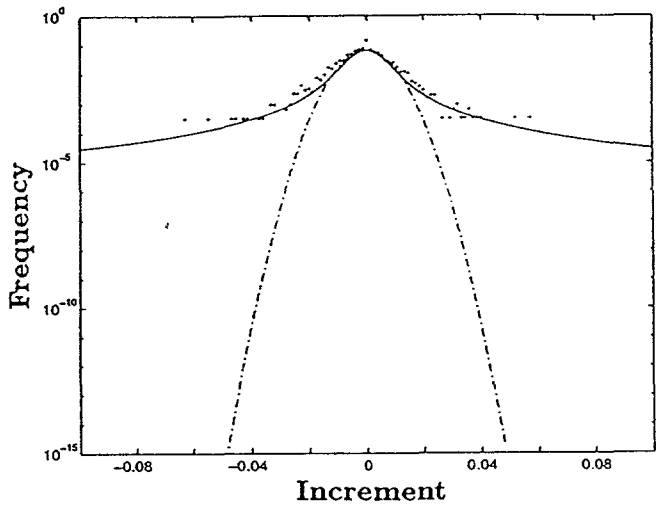

Figure 5: Frequency distribution of the increments in the data shown in Fig. 3 (symbols) and its fit by a Lévy distribution (solid curve). Also shown is the Gaussian distribution (dashed curve).

distribution, a fractal distribution given by [40]

$$P(y) = \frac{1}{\pi}\int_0^\infty \exp\left\{-[C(\ell)\omega]^{D_w}\right\}\cos(\omega y)d\omega\ , \tag{11}$$

where D_w is the fractal dimension of the set of points that are visited by a random walker whose step sizes obey the Lévy distribution, and $C(\ell)$ is a scale parameter. Of course, $D_w = 2$ corresponds to a Gaussian distribution of the data, which has been used extensively in the petroleum engineering literature, but Fig. 5 shows clear deviations of the data from a Gaussian distribution. From Fig. 5 we obtain $D_w \simeq 1.49$ and $C \simeq 0.0043$. Moreover, as is well-known, because of the long tails of the distribution the second and higher moments of a Lévy distribution are all divergent. Such tails decay very slowly, which make the moments of the distribution divergent. A similar analysis was carried out by Painter and Paterson [39] for acoustic transit time of some oil wells in northwest Australia. Note that up until now an fBm or fGn with $H > 0.5$ has been used by many researchers to characterize the porosity or permeability distribution of rock.

The fact that the increments in the porosities obey a Lévy distribution also suggests another method for estimating the parameter H. If we vary the separation length ℓ, the same value of D_w is obtained. This is indicative of self-similarity of the data, and suggests that if we plot $C(\ell)$ as a function of the separation distance ℓ, we should obtain

$$C(\ell) \sim \ell^H\ . \tag{12}$$

If the increments are not correlated, then $H = D_w^{-1}$. For positive (negative) correlations and persistence (anti-persistence) we should have $H > D_w^{-1}$ ($H < D_w^{-1}$). For short separation distances we obtain $H \simeq 0.68 \simeq D_w^{-1} \simeq 0.67$, indicating that at such length scales the

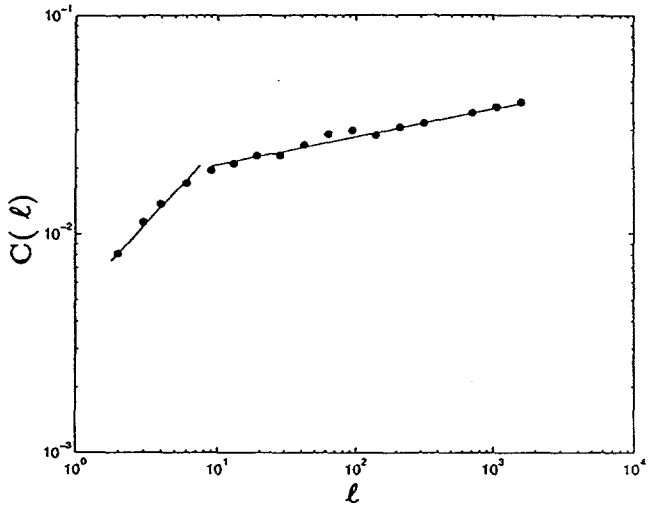

Figure 6: Logarithmic plot of the scale parameter $C(\ell)$ versus the separation distance ℓ for the data shown in Fig. 3. The slope of the straight line is $H \simeq 0.13$.

porosities are distributed essentially at random. This is presumably because at such short length scales one samples the rock properties within a stratum where the morphology is more or less random. However, at large separation distances that are of interest to us, which span many strata, the rock is highly heterogeneous, since the strata's properties greatly differ, and thus we expect negative correlations and anti-persistence, and indeed from Fig. 6 we obtain $H \simeq 0.13 << D_w^{-1} \simeq 0.67$, i.e., the data indicate negative correlations and anti-persistence, completely consistent with the porosity log shown in Fig. 3.

Another method for uncovering the fractal nature of the data is based on calculating the variance of the increments $\gamma(\ell)$, since for a fractal distribution one has

$$\gamma(\ell) \sim \ell^{2H} . \tag{13}$$

Figure 7 shows the results using this method. Note the similarity between this figure and Fig. 6. From Fig. 7 and for large separation distances we obtain $H \simeq 0.17$, consistent with the result obtained from Fig. 6, and confirming our assertion that, at least for the porosity log that we have analyzed, there are long-range negative correlations in the data.

To further check these results, we used an fBm to generate several one-dimensional sequences of numbers with various values $0 < H < 1$, and then analyzed the resulting synthetic data with the rescaled-range method. We found that, *regardless of the value of H* used in the generation of the synthetic data by an fBm, the rescaled-range analysis *always* predicts that $H \simeq 0.9$. This indicates that there is a fundamental bias in such an analysis, and therefore it may not be a reliable tool for analyzing geological as well as other types of data. We intend to carry out an extensive study of the previous data that have been analyzed by this method, in order to assess its reliability.

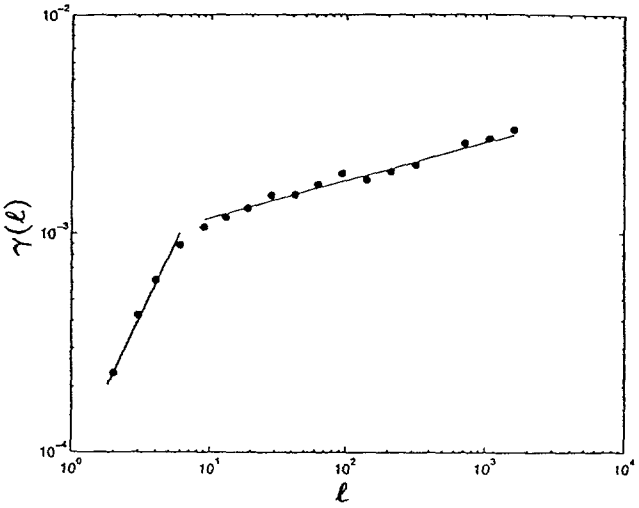

Figure 7: Logarithmic plot of the variogram of the data of Fig. 3.

SUMMARY

We discussed application of fractal concepts to two problems involving porous media. One of them, the formation of large molecular aggregates and their precipitation on the surfaces of the pores, gives rise to diffusion-limited cluster-cluster aggregates that have been studied extensively over the past decade. In the second application, we considered characterization of the distribution of the porosity of a field-scale reservoir. We argued that previous studies that used a rescaled-range analysis of the data could not reveal the true nature of the statistical correlations in the data.

Work is currently in progress to analyze extensive porosity and permeability data of several oil fields, as well as other types of data. The results will be published elsewhere [41].

ACKNOWLEDGMENTS

This work was supported in part by the Department of Energy. We would like to thank Scott Painter and Lincoln Paterson for many useful discussions, and for providing us with the copies of their papers prior to publication.

REFERENCES

1. F. Family and T. Vicsek (eds.), *Dynamics of Fractal Surfaces* (World Scientific, Singapore, 1991).

2. B. B. Mandelbrot, *The Fractal Geometry of Nature* (Freeman, San Francisco, 1982).

3. J. Feder, *Fractals* (Plenum, New York, 1988).

4. D. Avnir (ed.), *The Fractal Approach to Heterogeneous Chemistry* (Wiley, New York, 1990).

5. A. Bunde and S. Havlin (eds.), *Fractals and Disordered Systems* (Springer, Berlin, 1991).

6. T. Vicsek, *Fractal Growth Phenomena*, 2nd ed. (World Scientific, Singapore, 1992).

7. M. Sahimi, *Flow and Transport in Porous Media and Fractured Rock* (VCH, Weinheim, Germany, 1995).

8. M. Sahimi, *Rev. Mod. Phys.* **65**, 1393 (1993).

9. M. Sahimi, G. R. Gavalas, and T. T. Tsotsis, *Chem. Eng. Sci.* **45**, 1343 (1990).

10. M. Sahimi, *Chemtech* **22**, 687 (1992).

11. M. Sahimi, T. T. Tsotsis, and G. R. Gavalas, *Statistical and Continuum Models of Fluid-Solid Reactions in Porous Media* (Oxford University Press, New York, in press).

12. M. Sahimi, *Physica A* **186**, 160 (1992).

13. M. Sahimi, M. C. Robertson, and C. G. Sammis, *Phys. Rev. Lett.* **70**, 2186 (1993).

14. M. Sahimi, *Applications of Percolation Theory* (Taylor and Francis, London, 1994).

15. K. Drake, J. Bauer, T. Serafini, and P. Cheng (eds.), *Moving Forward with 50 Years of Leadership in Advanced Materials*, Proceedings of the 39th International SAMPE Symposium and Exhibition (Society for the Advancement of Material and Process Engineering, Anaheim, California, 1994).

16. T. A. Hewett, Society of Petroleum Engineers paper 15386, New Orleans, LA (1986).

17. T. A. Hewett and R. A. Behrens, *SPE Form. Eval.* **5**, 217 (1990).

18. See, e.g., S. E. Moschopedis, J. F. Fryer, and J. G. Speight, *Fuel* **55**, 227 (1976).

19. J. G. Speight, *The Chemistry and Technology of Petroleum* (Marcel Dekker, New York, 1991).

20. J. L. Anderson and J. A. Quinn, *Biophys. J.* **14**, 130 (1974).

21. H. Brenner and L. J. Gaydos, *J. Colloid Interface Sci.* **58**, 312 (1977).

22. W. M. Deen, *AIChE J.* **33**, 1409 (1987).

23. M. Sahimi, *J. Chem. Phys.* **96**, 4718 (1992).

24. R. E. Baltus and J. L. Anderson, *Chem. Eng. Sci.* **38**, 1959 (1983).

25. V. S. Ravi-Kumar, T. T. Tsotsis, M. Sahimi, and I. A. Webster, *Chem. Eng. Sci.* 49 (December 1994).

26. P. E. Savage and M. T. Klein, *Chem. Eng. Sci.* **44**, 393 (1989).

27. D. M. Trauth, S. M. Stark, T. F. Petti, M. Neurock, and M. T. Klein, *Energy and Fuels* **8**, 576 (1994).

28. A. Hirschberg, L. N. J. de Jong, B. A. Schipper, and J. G. Meijer, *SPE J.* **24**, 283 (1984).

29. H. Rassamdana, B. Dabir, M. Nemati, M. Farhani, and M. Sahimi, *AIChE J.* (in press).

30. H. Rassamdana and M. Sahimi, *Fuel* (to be published).

31. M. Sahimi and H. Rassamdana, *Phys. Rev. Lett.* (submitted).

32. B. Overfield, E. Y. Shue, K. S. Liang, and S. K. Sinha, *Fuel Sci. & Tech. Int.* **7**, 611 (1989).

33. E. Y. Shue, K. S. Liang, S. K. Sinha, and R. E. Overfield, *J. Colloid Interface Sci.* **153**, 399 (1992).

34. D. W. Schaefer, J. E. Martin, P. Wiltzuis, and D. S. Cannel, *Phys. Rev. Lett.* **52**, 2371 (1984).

35. P. Meakin, in *Phase Transitions and Critical Phenomena,* vol. 12, edited by C. Domb and J. L. Lebowitz (Academic, London, 1988), p. 335.

36. R. M. Ziff, E. D. McGrady, and P. Meakin, *J. Chem. Phys.* **82**, 5269 (1985).

37. H. E. Hurst, *Trans. Amer. Soc. Civil Eng.* **116**, 770 (1951).

38. B. B. Mandelbrot and J. W. Van Ness, *SIAM Rev.* **10**, 422 (1968).

39. S. Painter and L. Paterson, *Geophys. Res. Lett.* (in press).

40. M. F. Shlesinger, *Annu. Rev. Phys. Chem.* **39**, 269 (1987).

41. A. Mehrabi, H. Rassamdana, and M. Sahimi (to be published).

Pergamon

Chemical Engineering Science, Vol. 51, No. 00, pp. 0000-0000, 1996

0009-2509/96 $9.50 + 0.00

0009-2509(95)00415-7

phase not th attached

MOLECULAR SIMULATION OF ADSORPTION AND DIFFUSION IN PILLARED CLAYS

XIAOHUA YI, and KATHERINE S. SHING
Department of Chemical Engineering, University of Southern California, Los Angeles, CA 90089-1211, U.S.A.

and

MUHAMMAD SAHIMI*
HLRZ Super Computer Center, KFA Jülich, 52425 Jülich, Germany

(*First received* 13 *September* 1995; *revised manuscript received and accepted* 1 *December* 1995)

Abstract—Using grand-canonical-ensemble Monte Carlo and molecular dynamics simulations, adsorption equilibria and diffusion of finite-size molecules in model pillared clays are studied. Our simulations show that, at moderate and high porosities, clustering of the pillars and their spatial distribution do not have a significant effect on the adsorption isotherms. However, the dependence of the adsorption isotherms on the porosity is different at low and high pressures. At low pressures, the equilibrium loading increases as the porosity decreases, whereas at high pressures it increases with increasing porosity. The difference is due to the competition between the adsorption surface and the accessible volume of the system, which are the two most important factors that control the adsorption behavior of the system. At low enough temperatures and at any porosity, a first-order phase transition (condensation) occurs. The self-diffusivity D is found to be a monotonically increasing function of the temperature. Unlike adsorption isotherms, however, clustering of the pillars does have a strong effect on the diffusivity of the molecules. Moreover, over the entire loading range studied, D increases monotonically as the porosity increases.

INTRODUCTION

Diffusion, adsorption, and reaction in porous catalysts have been the subject of considerable research activity in the last few decades [for a review see, for example, Sahimi *et al.* (1990)]. In industrial applications, such phenomena usually involve the transport, adsorption, and reaction of large molecules in small pores, and therefore porous catalysts represent ideal model systems well-suited for theoretical and experimental studies of hindered diffusion, adsorption and reaction processes, which are caused by the molecules being excluded from a fraction of the pore volume, and by the hydrodynamic resistance hindering the transport of the molecules through the porous medium.

Among all catalytic systems zeolites have received the greatest attention. But considerably less attention and research effort have been focused on studying diffusion, adsorption and reaction phenomena in another class of catalytic materials, namely, pillared clays. In recent years, a number of studies have been carried out, almost all of which are experimental in nature [see, for example, Occelli and Tindwa, (1980), Pinnavaia (1983), Pinnavaia *et al.* (1985), Occelli *et al.* (1985), Plee *et al.* (1985), Tennakoon *et al.* (1987), Giannelis *et al.* (1988), Lee *et al.* (1989), Baksh and Yang (1991, 1992), Baksh *et al.* (1992), Yang and Baksh (1991) and Ohtsuka *et al.* (1993); for a review see, Kloprogge (1992)]. The original idea for producing pillared clays, due to Barrer and MacLeod (1955), was to insert molecules into clay minerals to prop apart the aluminosilicate sheets, thereby producing larger pores than in native clays, or even in zeolites. However, such materials did not have the thermal stability that zeolites usually possess. But pillars of hydroxyaluminum and other cations, which are capable of being dehydrated to oxide pillars and to support temperatures of up to 500°C without structural collapse under catalytic cracking conditions, are new and were first reported by Brindley and co-workers (Brindley and Sempels, 1977; Yamanaka and Brindley, 1978) and independently by Lahav *et al.* (1978) and Vaughan and Lussier (1980).

In general, pillared montmorillomites are 2:1 dioctahedral clay minerals consisting of layers of silica in tetrahedral coordination, holding in between them a layer of alumina in octahedral coordination. Substituting Si^{4+} with Al^{3+}, or Al^{3+} with Mg^{2+} gives the silicate layer a negative net charge, which is normally compensated by Na^+, Ca^{2+} and Mg^{2+} ions (Grim, 1986). By exchanging the charge compensating cations with large cationic oxyaluminum polymers, one can synthesize molecular sieve-type materials (Lahav *et al.*, 1978; Vaughan and Lussier, 1980). These inorganic polymers, when heated, form pillars which prop open the clay layer structure and form permanent

*Corresponding author.

CES 1105/Ans/BMP/Bala

pillared clays. The location and size of the pillars can, in general, vary, depending on such parameters as the type of the pillaring agent and preparation conditions. The structure of pillared clays is such that they behave as systems with an effective dimensionality between two and three, since molecules are forced to move in a very restricted pore space between the clay layers. The molecules might also be able to move from one layer to another, although this may be difficult, especially if the molecular sizes are large. Similar to zeolite-based catalysts, pillared clays have shown high catalytic activities for gas oil cracking. They have also shown large initial activities towards methanol conversion to olefins and toluene ethylation, but they are substantially deactivated by coke deposition (Figueras, 1988). Two important reasons for the interest in pillared clays are that their pore sizes can be made larger than those of faujastic zeolites, and that access to the interior pore volume of pillared clays is controlled by the distance between silicate layers and the distance between the pillars, and thus one or both distances can be adjusted to suit a particular application. Due to their versatility, they have also been suggested as a new class of materials for separation processes (Baksh and Yang, 1991; Yang and Baksh, 1991).

Despite their many potential applications and the existence of the wealth of valuable information obtained through extensive experimental efforts, very few fundamental theoretical studies have been undertaken so far to investigate transport and adsorption processes in pillared clays. In contrast, zeolites, which are chemically similar but structurally and morphologically very different from pillared clays, have been the subject of extensive theoretical and experimental studies. However, even for zeolites, detailed molecular simulation studies are relatively scarce [see, for example, June *et al.* (1992), Snurr *et al.* (1993) and references therein] and under restricted (usually low coverage) conditions. For pillard clays, a few computer simulation studies, using random walk and percolation concepts, have been carried out (Politowicz and Kozak, 1988; Politowicz *et al.*, 1989; Cai *et al.*, 1990; Sahimi, 1990; Chen *et al.*, 1994). Fundamental molecular simulations of diffusion in model pillared clays have been initiated by our group [Yi *et al.* (1995), hereafter referred to as Part I]. Using molecular dynamics (MD) simulations we studied in Part I diffusion in model pillared clays. However, many more issues remain to be studied, and our results obtained so far represent only the beginning phase of this research. In this paper, we use MD and grand-canonical-ensemble Monte Carlo (GCEMC) simulations to study both diffusion and adsorption in such catalytic materials, with a particular emphasis on the effects of porosity and pillar distribution.

The plan of this paper is as follows. In the next section we describe the morphology of our model of pillared clays and their energetics. We then discuss the MD and GCEMC methods that we employ in this paper. Next, our results are presented and discussed. The paper is summarized in the last section, where we also discuss some important issues that remain to be studied.

THE MODEL

The model used in this study is the same as the one used in our previous MD study of diffusion in pillared clays reported in Part I. The tetrahedral sheets of the clays, which we call the solid walls, are represented by the (100) face of a face-centered cubic solid with specified surface number density. The pillars are represented by rigid chains consisting of a given number of Lennard–Jones-type spheres separated by their size parameter σ_p. They are intercalated vertically in the space between the solid walls. The z-coordinate of the centers of the end spheres of the pillar chains is $0.5 \times (\sigma_w + \sigma_p)$, where σ_w is the size parameter of the atoms (or groups of atoms) representing the solid walls. The pillars are distributed either uniformly or randomly between the solid walls, or allowed to cluster together. In the uniform distribution, the centers of the pillars are placed at the nodes of an imaginary square lattice attached to the walls. In the random distribution of the pillars, the locations of their centers are distributed randomly, but with the constraint that the distance between any pair of pillars must be no less than the diameter of the spheres that comprise the pillars. A schematic representation of our model with a uniform distribution of the pillars and a height of $3\sigma_p$ is given in Fig. 1. In the clustering configurations, the pillars are allowed to aggregate into groups or clusters according to certain coordinations. The idea is to mimic the formation of metal oxide clusters in pillared clays (Ocelli *et al.*, 1985; Ohtsuka *et al.*, 1993). In this paper, we only consider clusters of two and three pillars, which we call the *diploid* and *triad* clusters, respectively. The distribution of the centers of the clusters between the solid walls is assumed to be uniform for both types of clusters. A schematic representation of the top view of the spatial distributions of the various pillar clusters used in this paper is shown in Fig. 2. Obviously, for a given type of pillar configuration, i.e. for a given size of the pillar clusters and their spatial distribution, two parameters are sufficient to define the morphology of the model. One is the interlayer spacing h_w, which is the separation between the centers of the atoms on the upper and lower layers. The other one is the surface density of the pillars ρ_p, which is the number of pillars per unit area of the solid walls. The porosity of the system, defined as the volume fraction of the system not occupied by the pillars, is estimated from the following equation:

$$\varphi = 1 - \tfrac{1}{6}\pi\rho_p\sigma_p^2 . \qquad (1)$$

The conventional *pairwise additivity* and *rigid solid* assumptions in dealing with solid–fluid systems are adopted in this study in describing the adsorbate–solid and adsorbate–adsorbate interactions. By rigid solid we mean that the solid walls or the pillars do not swell upon adsorption of guest molecules, and

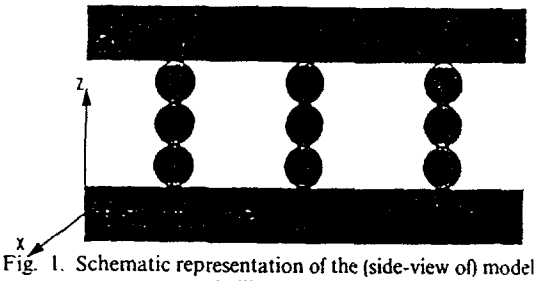

Fig. 1. Schematic representation of the (side-view of) model of pillared clays.

the vibrational motions of the atoms in the solid are ignored. With the pairwise additivity assumption, the total potential energy can be partitioned into three attributes belonging to adsorbate–adsorbate, adsorbate–pillar, and adsorbate–solid wall interaction energies. The lattice energy which holds the solid together will not enter our calculation explicitly since it is a constant based on the rigid solid assumption. We use the cut and shifted Lennard–Jones potential

$$\phi(r) = \begin{cases} \phi_{LJ}(r) - \phi_{LJ}(r_c) & \text{if } r \leqslant r_c \\ 0 & \text{if } r > r_c \end{cases} \quad (2)$$

to describe the interactions between the guest molecules (adsorbates) as well as between them and the spheres that comprise the pillars. In this equation r is the separation between interacting pairs, r_c is the truncation distance of the potential, and ϕ_{LJ} is the standard Lennard–Jones potential:

$$\phi_{LJ}(r) = 4\varepsilon\left[\left(\frac{\sigma}{r}\right)^{12} - \left(\frac{\sigma}{r}\right)^{6}\right] \quad (3)$$

where ε and σ are the usual energy and size parameters, respectively. The value of r_c that we used in our simulation was 3.5σ. The interaction between the guest molecules and the solid walls, which is the sum of the interactions between a single molecule and all the atoms that comprise the solid walls, is approximated by the well-known 10–4–3 potential (Steele, 1973)

$$\phi_w = 2\pi\varepsilon_w\left[\frac{2}{5}\left(\frac{\sigma_w}{z}\right)^{10} - \left(\frac{\sigma_w}{z}\right)^{4} - \frac{0.4714}{(z/\sigma_w + 0.4314)^3}\right] \quad (4)$$

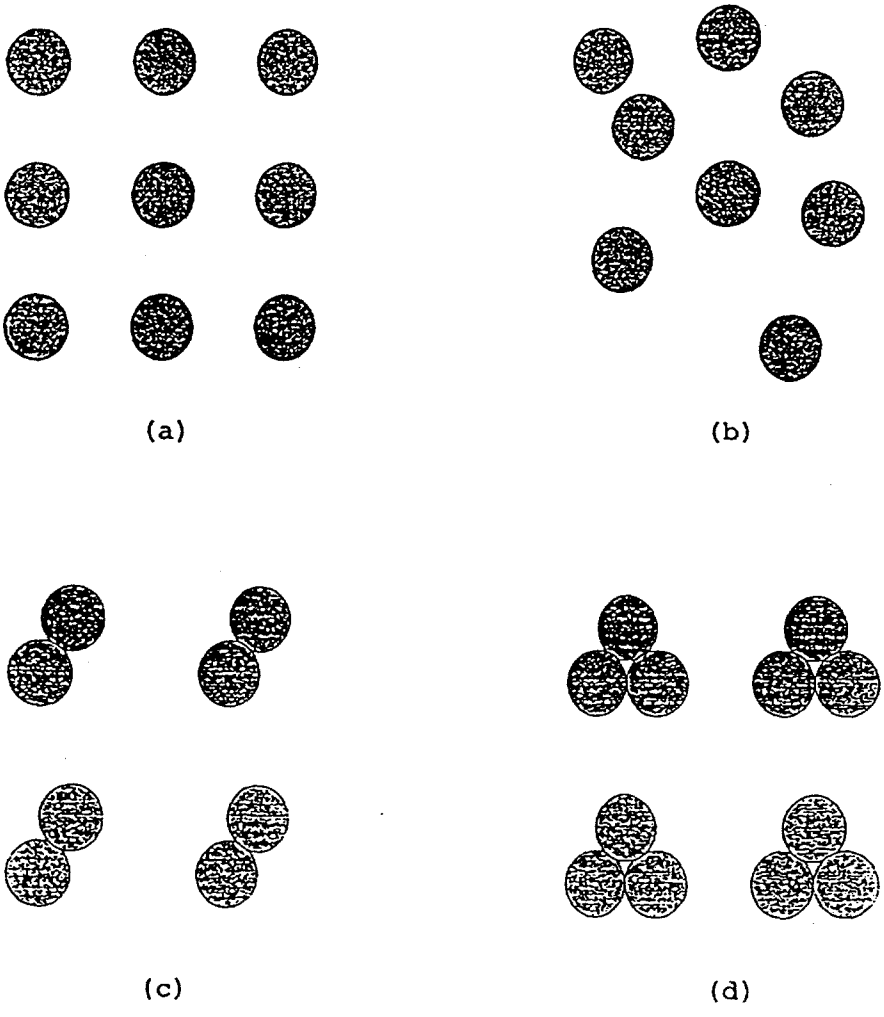

Fig. 2. Schematic representation of (a) uniform, (b) random, (c) diploid, and (d) triad pillar clusters.

where ε_w and σ_w are the energy and size parameters characterizing the interactions between the guest molecules and the atoms that comprise the solid walls, and z is the vertical distance form the walls. This equation is obtained from a mean-field treatment of the interaction between a guest molecule and the Lennard–Jones-type f.c.c solid with surface density 1.0.

The total potential energy can then be written as

$$\Phi = \frac{1}{2}\sum_{i}^{N}\sum_{j}^{N}\phi_{LJ}(r_{ij};\sigma_0,\varepsilon_0) + \sum_{i}^{N}[\phi_w^{(L)}(z_i;\sigma_w,\varepsilon_w) + \phi_w^{(U)}(z_i;\sigma_w,\varepsilon_w)] + \sum_{i}^{N}\sum_{k}^{N_p}\phi_{LJ}(r_{ik};\sigma_k,\varepsilon_k), \quad (5)$$

where N_p is the number of the pillars, N is the number of the guest molecules, and superscripts L and U are used to distinguish between the potential energies associated with the lower and the upper walls.

MOLECULAR SIMULATION METHODS

We now describe the molecular simulation methods that we used in this study. To study adsorption phenomena, we used a GCEMC method, whereas a MD method was used to investigate diffusion of the molecules in the model pillared clays.

Grand-canonical-ensemble Monte Carlo simulation

In a grand-canonical ensemble, both the energy and density are allowed to fluctuate. The GCEMC simulation is therefore appropriate for studying the thermodynamic equilibria of multiphase systems. Consequently, it has been widely used for studying adsorption equilibria of guest molecules in various materials and systems, including simple systems such as slit pores (Snook and Megen, 1980), cylindrical pores (Peterson and Gubbins, 1987), and complex materials such as silicalite (June *et al.*, 1992) and aluminophosphates (Cracknell and Gubbins, 1993). Although some discrepancies have been observed between the simulation results and the experimental data, it is believed that they are due to the inaccuracy of interaction potentials or the geometrical models of the systems, rather than any possible numerical errors associated with the algorithm, unless a system is close to its critical point, or is in high density region, or the adsorbate molecules are too complex, such as heavy hydrocarbons. Even for these situations, modifications of the original algorithm of Adams (1975) have been proposed and tested. For example, "biased insertion" methods have been tested by several groups and proven very effective in improving the probability of successful adsorption of the molecules under high density conditions, or when dealing with complex molecules (Siepmann and Frankel, 1992; Snurr *et al.*, 1993). The algorithm we used in this study is basically the same as the one originally developed by Adams (1975), which we summarize in this section. A more detailed discussion of this method is given in the standard reference of Allen and Tildesley (1984).

Each step in a GCEMC simulation typically consists of three types of operations or movements, with the corresponding probability of occurence consistent with that in the subspace of the particle number N and the configuration $\mathbf{r}^N$ of the phase space of the grand-canonical ensemble in question, where $\mathbf{r}^N$ represents the set of the position vectors of the N molecules $(\mathbf{r}_1, \mathbf{r}_2, ..., \mathbf{r}_N)$. The first type of operation in any GCEMC method is the insertion of a guest molecule into the system with the following probability:

$$p^+ = \min\left[\frac{\exp(\beta\mu_c - \beta\delta U^+)}{N+1}, 1\right] \quad (6)$$

where U is the potential energy, $\beta = (k_B T)^{-1}$ is the reciprocal temperature, k_B is the Boltzmann's constant, μ_c is the configurational chemical potential of the guest molecules, which is the same for the molecules both inside the system and in the ambient phase when adsorption equilibrium is achieved, and δU^+ is the change in the potential energy as a result of adding the molecule. The second type of operation is the removal of a guest molecule from the system, with the following probability of realization:

$$p^- = \min[N\exp(-\beta\mu_c - \beta\delta U^-), 1] \quad (7)$$

where δU^- is the change in the potential energy as a result of removing the molecule. Finally, the third type of operation is the displacement of a guest molecule inside the system from its present position to a new position, the probability of which is given by

$$p^d = \min[\exp(-\beta\delta U^d), 1] \quad (8)$$

where δU^d is the change in the configurational energy accompanying the displacement of the molecule. Both the molecule being displaced and its displacement, which is restricted to be between 0 and a maximum allowed value, are randomly selected. The maximum allowed value of the displacement is adjusted periodically during each simulation to achieve a specified acceptance ratio of the trial movements, which was chosen to be 0.50 in our simulations.

The macroscopic condition of the ambient phase surrounding the system is uniquely specified by its temperature and chemical potential, since we are dealing with a single-component system and the range of chemical potentials is chosen such that its maximum value is close to, but does not exceed, the value at which a vapor–liquid phase transition occurs. The pressure of the ambient phase can be easily calculated from the specified temperature and chemical potential using the equation of state of the Lennard–Jones system defined by eqs (1) and (2).

A typical GCEMC simulation begins with 1 million steps of equilibration followed by the generation of the configurations of the adsorbed states. The simulation is not terminated until about 3–5 millions steps are successfully generated. However, depending on the equilibrium loading range in which the simulation is carried out, the number of steps may vary from 6 to

8 millions. In addition to the loading, other equilibrium properties including the interlayer density profile, the configurational energy and the solvation force are also calculated from the generated configurations. The interlayer density profile, which is essentially the probability density of finding a guest molecule at a distance z from the wall, regardless of its (x, y) coordinates, is evaluated from the following equation:

$$\rho_z(z) = \frac{1}{A}\left\langle \frac{\partial N(z)}{\partial z} \right\rangle \tag{9}$$

where $\langle\cdot\rangle$ is the ensemble average, approximated by averaging over all the configurations collected, $N(z)$ is the number of guest molecules centered between 0 and z, and A is the area of the wall. The solvation force is defined as the force experienced by a unit surface of upper solid wall, which can be calculated from

$$f_s = \frac{1}{A}\left\langle \sum_{i=1}^{N} \left[\frac{\partial \phi_w^{(U)}(z_i)}{\partial z_i} \right]_{z_i = h\sigma_{ff}} \right\rangle. \tag{10}$$

Obviously, the arbitrary choice of the upper wall does not affect the results, since the force experienced by each wall is the same based on symmetry considerations. The results obtained with the GCEMC method are compared with the corresponding results obtained from our MD simulations, which we now discuss.

Molecular dynamics simulation

Similar to any Monte Carlo method, the major disadvantage of the GCEMC simulation is that time is not explicitly a parameter of the simulation, and therefore one cannot obtain any truely dynamic property and its dependence on time, such as the autocorrelation functions and the transport properties, except for some simple and noninteracting systems (Fichthorn and Weinberg, 1991) in which the real time can be related to the Monte Carlo time. Thus, to study the diffusive motion of the guest molecules in our model, we employ the MD method.

Our MD simulation is performed in the micro-canonical ensemble with periodic boundary conditions applied along the x and y directions (see Fig. 1). Theoretically, the results given by a micro-canonical ensemble simulation should be equal to those obtained from a grand-canonical-ensemble simulation in the thermodynamic limit, namely, the limit in which the volume of system and the adsorbed guest molecules both go to infinity, keeping their ratio finite. The trajectories of the molecules are calculated by solving Newton's equation of motion using a standard fifth-order predictor-corrector method (Gear, 1971; Haile, 1990) with the forces calculated from the interaction potentials (see above and Part I). In our system, the force experienced by a guest molecule is due to the potential field generated by both the rest of the guest molecules, the pillars, and the walls. The macroscopic properties, such as the solvation force, the configurational energy, and the interlayer density profile can be calculated from the trajectories of the molecules, which are collected in a typical duration of 50000 time steps, after spending about 10000 time steps for system equilibration. According to linear-response theory, the transport properties can also be obtained from such equilibrium simulations (Zwanzig, 1968). The self-diffusivity D_x of the molecules in the x-direction can be calculated from either the Einstein equation

$$D_x = \frac{1}{6N}\lim_{t\to\infty}\left\langle \sum_i^N \frac{|\mathbf{r}_i(t+t_0) - \mathbf{r}_i(t_0)|^2}{t} \right\rangle \tag{11}$$

or the Green–Kubo equation (Green, 1952; Kubo, 1957)

$$D_x = \frac{1}{3}\int_0^\infty \left\langle \sum_{i=1}^{N} [\mathbf{v}_{ix}(t+t_0)\cdot\mathbf{v}_{ix}(t_0)] \right\rangle dt, \tag{12}$$

where $\mathbf{v}_{ix}$ is the velocity of the ith molecule in the x-direction, and $\langle\cdot\rangle$ indicates an average over all the trajectories with a series of independently selected time origins t_0. Note that, some of the particles can collide with the walls and the pillars, and thus their velocities will be reversed. However, the fraction of such particles for *diffusion simulations* is not large.

Energy conservation in the system was monitored in each simulation, and the time step was adjusted depending on the loading of the guest molecules and the porosity of the system to guarantee that energy "leaking" was controlled in a reasonable range (typically about 0.1% in 10^4 time steps). The linear correlation coefficients between the mean square displacement and the time elapsed were also calculated and used as an indication of how the system follows Fickian diffusion.

The computer programs were written in reduced units, namely, the energy parameter ε_0 and the size parameter σ_0 of the guest molecules were used as the units of energy and length in both the GCEMC and the MD simulations, and the quantity $\sqrt{m\sigma_0^2/\varepsilon_0}$ was used as the unit of time in the MD simulations. The conversion factors that convert the results in the reduced units to the values in the SI units for the temperature, pressure, energy, density, and the self-diffusivity, along with the numerical values calculated using the m, ε, and σ of oxygen atoms are listed in Table 1. The numerical uncertainties in the quantities calculated were estimated using the so called block-averaging method (Bishop and Frinks, 1987). Their typical values were 2%–10% of the calculated quantities of interest.

RESULTS AND DISCUSSIONS

Although only the most important features of pillared clays are incorporated into our model, and some details have been ignored due to the complexity of the system and the incompleteness and uncertainties in the experimental information, the parameter space that defines the morphology of the system and the molecular interactions is still quite large. Among the

Table 1. The conversion factors for converting the dimensionless parameters of the simulations into dimensional quantities

Variable	Program Units	SI value	Equivalent
Length	σ	3.405×10^{-10} m	3.405 Å
Energy	ε	0.996 kJ/mol	$\varepsilon/k_B = 119.8$ K
Mass	M	6.63×10^{-26} kg	39.95 a.u.
Time (τ)	$\sigma\sqrt{M/\varepsilon}$	2.156×10^{-12} s	2.156 ps
Temperature	ε/k_B	119.8 K	119.8 K
Density	$1/\sigma^3$	4.206×10^4 mol/m^3	42.06 mol/lit.
Surface density	$1/\sigma^2$	6.98×10^{-4} mol/m^2	0.104 /Å^2
Pressure	$M/(\tau^2\sigma)$	4.19×10^7 N/m^2	413.4 atm
Diffusivity	σ^2/τ	5.38×10^{-8} m^2/s	5.38×10^{-4} cm^2/s

important features that affect the adsorption isotherms and diffusivities of the molecules are those that control the pillar configuration, the relative magnitude of the interlayer and interpillar spacing, the relative strength of the adsorbate–adsorbate, adsorbate–pillar, adsorbate–solid wall interactions, as well as the macroscopic conditions of the surrounding bulk fluid. The computational effort involved is also very demanding, with each GCEMC and MD simulations taking typically about 10 to 15 h on a SUN SPARC10 station. In this study, we focus our attention on investigating the dependence of the adsorption isotherms and the diffusive motion of guest molecules on, (1) macroscopic condition of the surrounding fluid, namely, its temperature and chemical potential (or, equivalently, pressure); (2) the pillar configuration and clustering, and (3) the porosity of the system. Without loss of generality, we use the same size and energy parameter for all types of interactions involved (i.e. $\sigma_p = \sigma_w = \sigma$). The uncertainties for the equilibrium properties (with the exception of the equilibrium loadings) were calculated as the difference between the GCEMC and the corresponding MD simulations, and the uncertainties for the diffusivity are calculated as the difference between the values as evaluated from each half-trajectory in each MD simulation.

ADSORPTION ISOTHERMS

Fig. 3 presents the adsorption isotherms at various temperatures for a uniform pillar configuration, with an interlayer spacing $h_w = 4.0$, and an interpillar spacing (the distance between the centers of neighboring pillars) $h_p = 4.5$, corresponding to a porosity $\varphi = 0.97$. The amount of the adsorbed molecules is normalized with the total solid wall surface (including the parts shadowed by the pillars). As this figure shows, the amount adsorbed at a given pressure decreases as the temperature increases, which is expected. At reduced temperature $T = 0.80$, a finite jump in the adsorption isotherm is found at a reduced pressure around 4.5×10^{-3}. However, such a discontinuity is not observed in the adsorption isotherms at the higher temperatures. This phenomenon is of course a first-order phase transition, in which the chemical potential (pressure) changes continuously but the molecular density does not, and is commonly called capillary condensation for macropore systems (Gregg and Sing, 1982). To better understand these results, the density profiles in the vicinity of $P = 4.5 \times 10^{-3}$ are given in Fig. 4, which show clearly that, as the pressure passes the transition point, multilayer adsorption occurs with the formation of an adsorbed layer centered at $z = 2$ (i.e. half-way between the two solid walls), in addition to the two next to the walls. At $T = 1.0$, the amount adsorbed increases sharply at pressures around $P = 4 \times 10^{-3}$, but the rate of increase (the slope of the curve) slows down quickly as the pressure is increased further. Such a change is a manifestation of the *packing effect*, i.e. the limit in the amount that can be adsorbed due to the confinement of the porous medium. A similar pattern is observed in the adsorption isotherm at $T = 1.20$, except that the curve is not as sharp in the intermediate pressure region. Loosely speaking, this is a natural result of the competition between thermal and potential energies. On the one hand, thermal agitations at higher temperatures can effectively block fast condensation, which is induced mainly by the adsorbate–solid and the adsorbate–adsorbate attractions at low pressures. On the other hand, thermal agitations can make the packing effect at higher loadings to be more moderate, since the guest molecules (here modelled as the Lennard–Jones hard spheres) become "softer", in the sense that their equivalent hard-core diameter decreases as the temperature is increased (Weeks *et al.*, 1971). We expect a similar change in the equivalent hard-core dimension of the solid. Such a "softening" can be viewed as an effective increase in the porosity, which results in a shift of the plateau of the high-T isotherms to higher pressures.

We also studied the effect of the porosity on the adsorption isotherms, by carrying out a series of simulations at $\varphi = 0.89$, the results of which are shown in Fig. 5. As can be seen, the adsorption isotherms are very similar to those shown in Fig. 3, except that the location of the first-order phase transition has been shifted to a lower temperature (and pressure). We thus expect that, as the porosity of the system approaches the percolation threshold, i.e., the porosity below which no macroscopic phenomenon can occur, the critical temperature for the first-order phase transition would approach zero.

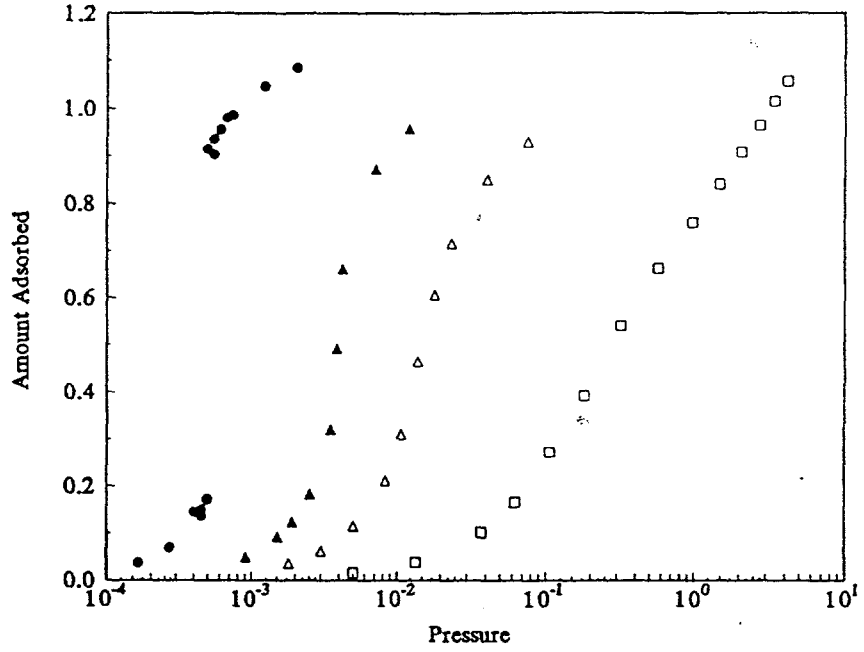

Fig. 3. Adsorption isotherms at temperatures $T = 0.8$ (circles), 1.0 (solid triangles), 1.2 (triangles), and 2.0 (squares), for a uniform distribution of the pillars with porosity 0.97.

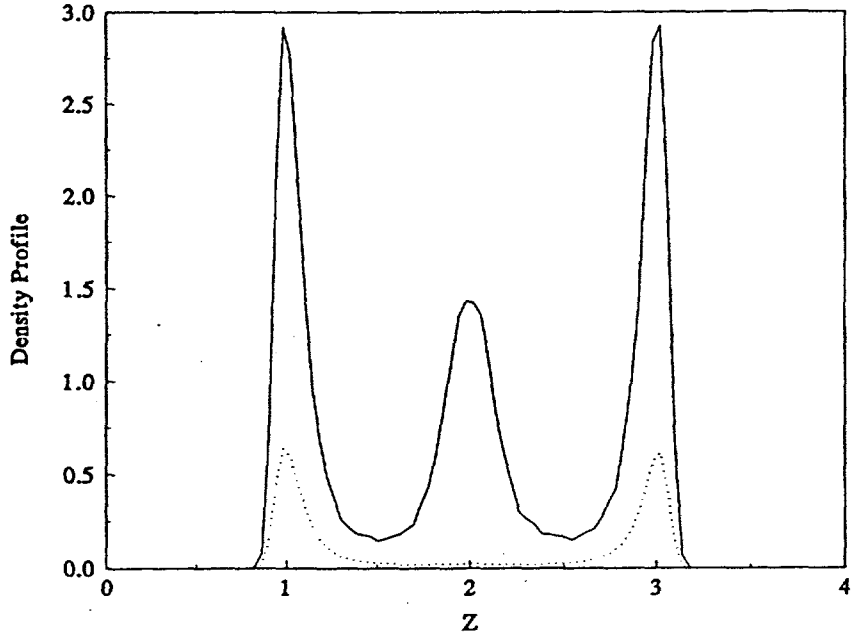

Fig. 4. Interlayer density profiles at temperature $T = 0.8$, and pressures $P = 5 \times 10^{-3}$ (solid curve) and 4×10^{-3} (dashed curve), for a uniform distribution of the pillars with porosity 0.97.

To study the effect of the pillar configuration on the adsorption equilibria, we carried out a series of simulations for different distributions and cluster sizes of the pillars. The results are shown in Fig. 6. In these calculations, the temperature T and the interlayer spacing h_w are fixed at 1.20 and 4.0, respectively, while the porosity is 0.97. The interpillar spacing h_p for the uniform pillar configuration is fixed at $h_p = 4.50$. To maintain constant φ, the number of pillars per unit wall surface for the other three pillar configurations is chosen to be the same as that of the uniform configuration. For the random distribution of the pillars, several pillar configurations were generated and used in the computations, in order to minimize the effect of the system size and the periodic boundary conditions along the x and y directions. The results reported are

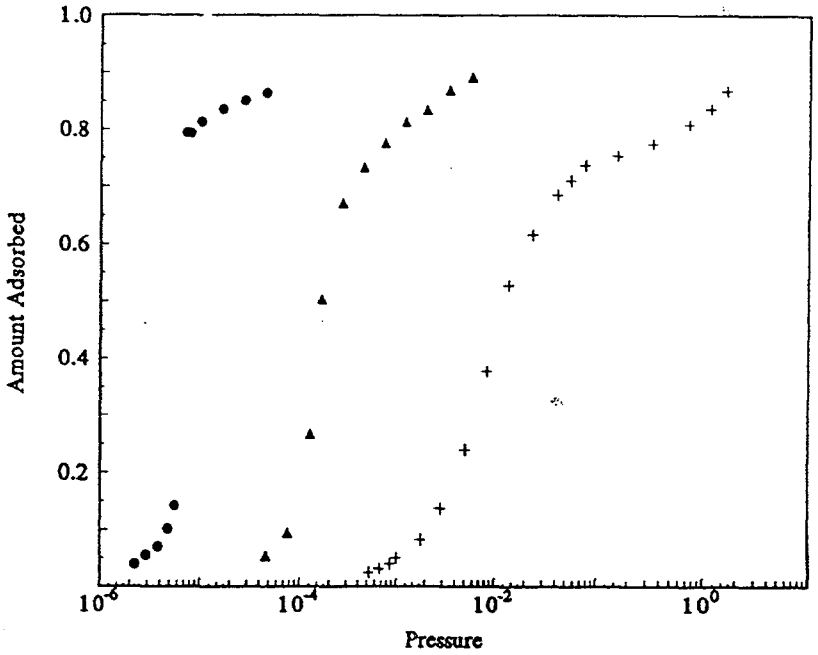

Fig. 5. Adsorption isotherms at temperatures $T = 0.6$ (circles), 0.8 (triangles), and 1.2 (+), for a uniform distribution of the pillars at porosity 0.89.

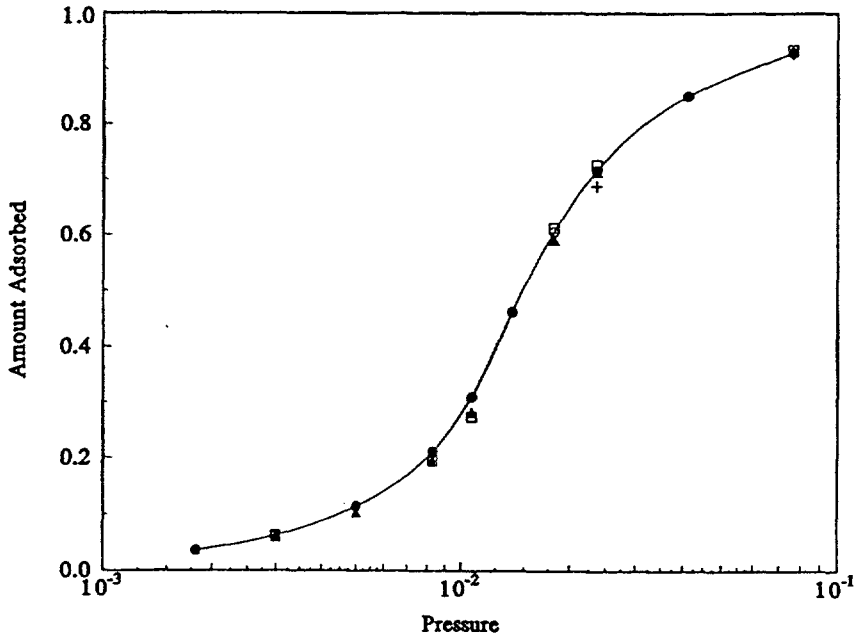

Fig. 6. The effect of the pillar distribution on the equilibrium loading at temperature 1.20 and porosity 0.97. The results are for uniform (circles), random (+), diploid (squares), and triad (triangles) configurations.

thus averaged quantities, where the averaging was taken over all realizations of the system.

Figure 6 indicates that there exists an inflection point at a reduced pressure around 1.5×10^{-2}. The solvation force exhibits a steep minimum at about the same pressure, as Fig. 7 shows. The density profiles which are presented in Fig. 8 can help us understand such features in both figures. At low equilibrium loadings, and as the pressure increases, the guest molecules are gradually adsorbed in the two layers next to the walls. As the pressure is increased further, the interaction between the guest molecules begins to manifest itself, and one more layer is formed. As a result, it becomes difficult to have more guest molecules accommodated in the layers, as indicated by the change in the slope of the adsorption isotherms, and the force

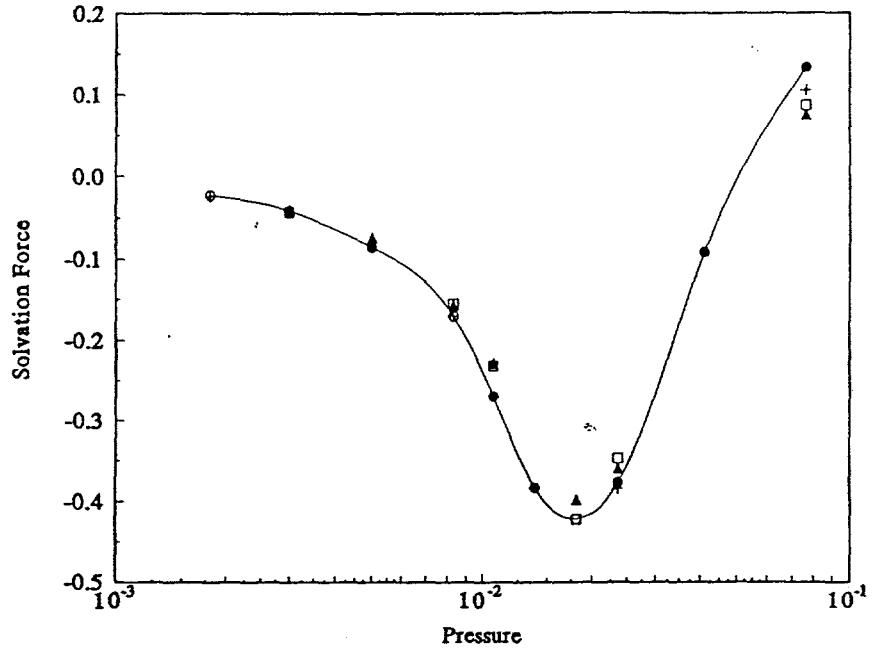

Fig. 7. The effect of the pillar distribution on the solvation force at temperature 1.20 and porosity 0.97. Symbols are the same as in Fig. 6.

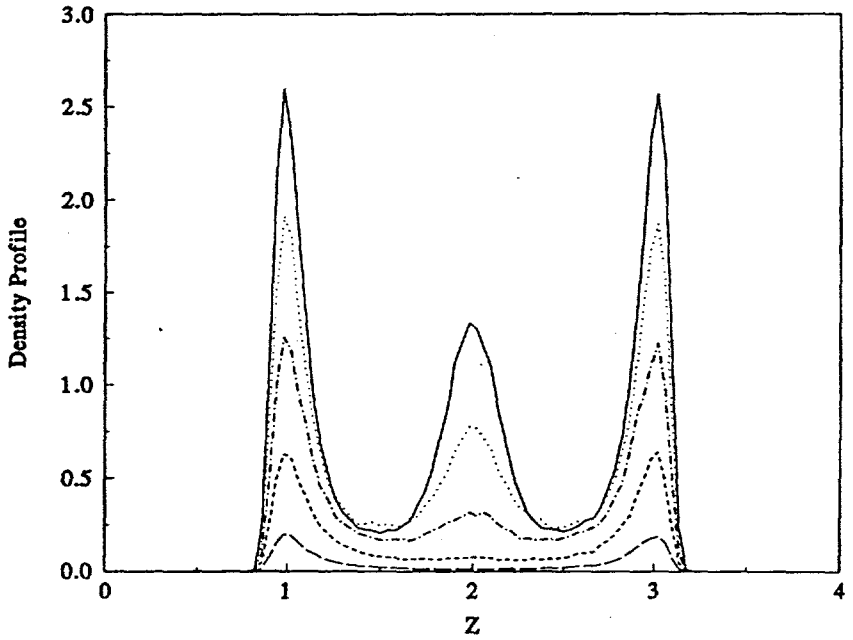

Fig. 8. Interlayer density profile at various pressures for a uniform distribution of the pillars with porosity 0.97 at temperature $T = 1.2$. The results are, from top to bottom, for pressures $P = 7.6 \times 10^{-2}$, 4.1×10^{-2}, 1.4×10^{-2}, 8.0×10^{-3}, and 3.0×10^{-3}, respectively.

experienced by the walls becomes negative or less negative. Fig. 6 also shows convincingly that for our model the amount of adsorbed molecules is not sensitive to the spatial distribution and the size of the pillar clusters over the entire range of pressures studied. The apparent insensitivity of the adsorption isotherms to the pillar configurations persists at lower values of φ. Fig. 9 shows the adsorption isotherms at temperature $T = 1.2$ and porosity $\varphi = 0.89$, for two different pillar configurations, namely, a uniform and a random distribution. As can be seen, there is little difference between the two isotherms.

The insensitivity of the equilibrium loading to the pillar configuration suggests that classical continuum approaches to adsorption in porous media, which correlate the adsorption isotherms with the pore size

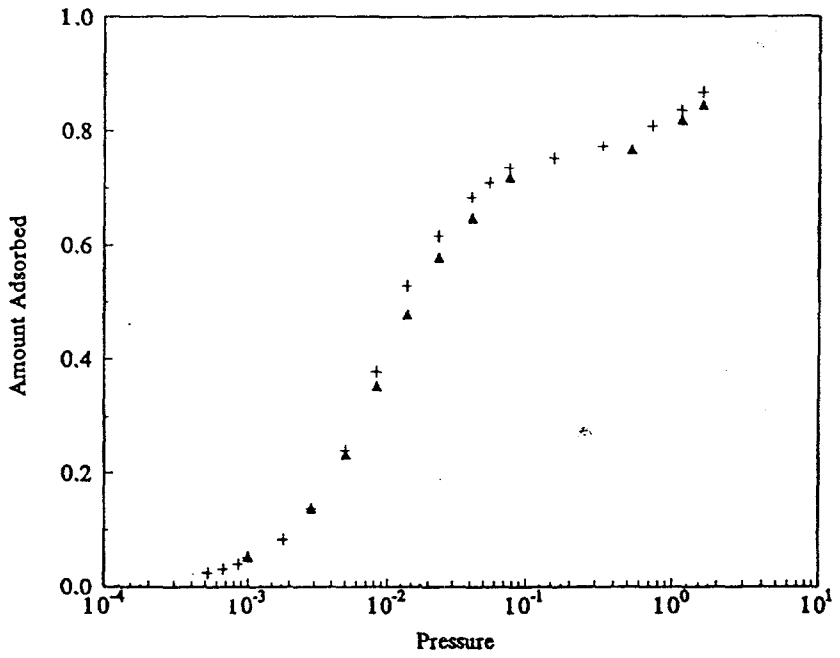

Fig. 9. Dependence of the adsorption isotherms on the spatial distribution of the pillars at porosity 0.89. The results are for uniform (+) and random (triangles) distribution of the pillars.

distribution of the system, may not be able to provide meaningful information about the pore structure of pillared clays, since our results demonstrate clearly that the difference between the adsorption isotherms of the guest molecules in intercalated systems with the same porosity but quite different pore structures is very small. In other words, it is doubtful that, in the absence of any specific interactions (such as acid-base), the adsorption isotherms alone can determine the pore size distribution of a microporous material, such as pillared clays. Although in these simulations h_w was fixed, we expect the insensitivity of the adsorption isotherms to the pillar distribution and configuration to persist for other values of h_w, unless it is very small and no more than two molecular diameters, in which case, instead of h_p, h_w is the controlling length scale.

In general, the porosity of a porous material is an important parameter that controls both the adsorption and transport behavior of a porous medium. To investigate the effect of the porosity on the equilibrium loading of the guest molecules, we performed four sets of simulations at a fixed temperature $T = 1.2$ and a uniform distribution of the pillars. The results are presented in Fig. 10, where the equilibrium loadings at four porosities are given as a function of the pressure. The variation in the porosity was achieved by changing the interpillar spacing h_p. The smallest interpillar spacing was $h_p = 2.25$, corresponding to the porosity $\varphi = 0.89$, and the highest porosity $\varphi = 1.0$ is simply a slit-like pore. The isotherms at high and low pressures show different patterns. At high pressures, the equilibrium loading is a monotonically increasing function of the porosity, while it is a decreasing function at low pressures. These patterns can be attributed to the competition between two factors that affect the equilibrium loadings, namely, the *accessible* volume and the *total* adsorption surface of the system (walls surface plus pillar surface). Clearly, an increase in both of them results in an increase in the equilibrium loading. But their dependence on the porosity is totally different, since the accessible volume increases as the porosity does, whereas the adsorption surface due to the pillars decreases with increasing porosity. The results thus suggest that the accessible volume is the most important controlling factor at high pressures, where packing effect becomes important, whereas the total adsorption surface is the factor most responsible at lower pressures. This dependence of the adsorption isotherms and the diffusivity (discussed below) on the accessible volume and surface area of a material is a percolation effect (Sahimi, 1994,1995).

To study the sensitivity of the adsorption isotherms on the potential parameters that define the adsorbate–pillar interactions, we performed two sets of GCEMC simulations. In one set, the energy parameter ε_p was changed from 1.0 to 2.0 to 0.5, representing moderately, strongly, and weakly attractive pillars, respectively. The amounts adsorbed, normalized with the value corresponding to $\varepsilon_p = 1.0$, are shown as a function of pressure in Fig. 11. As the results indicate, the larger ε_p, the larger the amount adsorbed. This behavior can be explained by noting that a large ε_p implies a deeper potential well, i.e. a stronger attraction between the adsorbate and the pillars, which

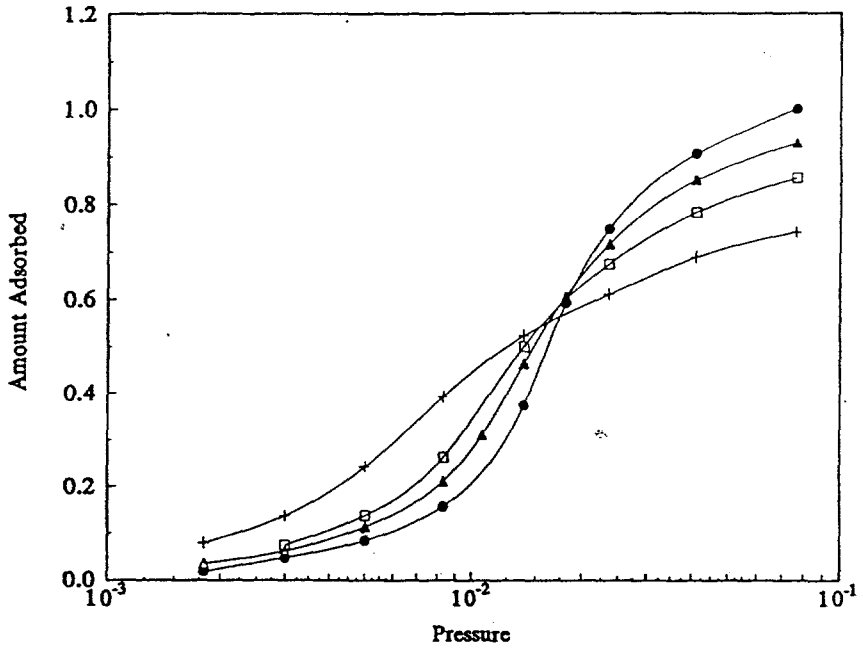

Fig. 10. The effect of the porosity φ on the equilibrium loading for a uniform distribution of the pillars at temperature $T = 1.2$. The results are for $\varphi = 1.0$ (circles), 0.97 (triangles), 0.94 (squares), and 0.9 (+), respectively.

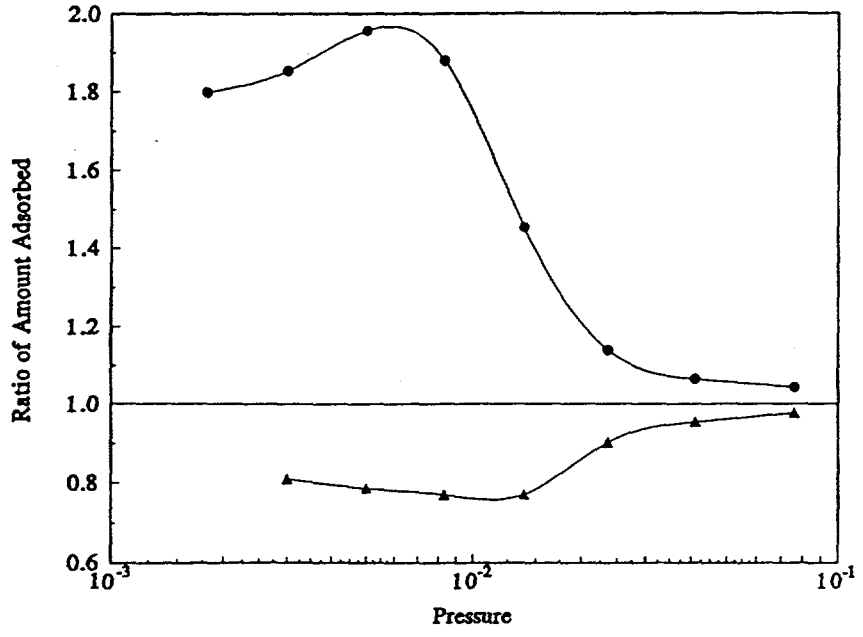

Fig. 11. The effect of pillar-adsorbate energy parameter ε_p on the adsorption isotherms at $T = 1.2$, for a uniform distribution of the pillars with porosity $\varphi = 0.97$. The results are for $\varepsilon_p = 2.0$ (circles) and 0.5 (triangles), respectively.

means that more molecules can be adsorbed at the same pressure. An interesting feature demonstrated by these results is that, adsorption equilibria are less sensitive to ε_p at high pressures (or, equivalently, high loadings) than at low pressures, with the normalized amount adsorbed approaching unity as the pressure approaches 0.8. This is understandable if we note that the adsorbate–adsorbate interactions become stronger as pressure increases, and make comparable or larger contributions to the total potential energy than the adsorbate–pillar interactions do when P approaches 0.8, and therefore the dependence of the adsorption isotherms on ε_p becomes weaker. Furthermore, at high pressures/loadings, the fluid behavior is

dominated by repulsive rather than attractive forces. Hence we expect a sensitivity to σ_p not ε_p. This insight will be valuable in both developing an approximate analytical model for our simulation results in the high loading limit, and in using our model for predicting or correlating experimental adsorption data of an intercalated system. For example, it tells us that more attention should be paid to the adsorption data at low pressures than those at high pressures, if we want to estimate the adsorbate–pillar interaction parameters from the experimental data.

DIFFUSION COEFFICIENTS

In Part I we studied the dependence of the self-diffusivity D, measured in the direction parallel to the solid walls, on the molecular density, the porosity of the system, the distribution of the pillars, and the interlayer spacing between the solid walls. However, the effect of the temperature and pillar clustering on D was not studied. It is therefore natural to carry out a parallel study for the self-diffusivity of the guest molecules in the present model, and investigate the effect of the parameters and factors that were studied in the GCEMC simulations, on D. To do this, we computed the self-diffusivities by carrying out MD simulations, using the molecular densities (i.e. equilibrium loadings) obtained from the GCEMC simulations for the corresponding model parameters and macroscopic fluid conditions. In addition to giving insight into the effect of the temperature and pillar configuration on the diffusive motion of the molecules, a comparison of the equilibrium properties obtained from GCEMC and MD simulations also serves an a further check of our results.

In Fig. 12, the self-diffusivities, measured parallel to the walls, at three temperatures and with a uniform distribution of the pillars are shown as a function of equilibrium loading. The rest of the parameters of the system are the same as those of Fig. 3. The corresponding bulk fluid phase pressure can be estimated easily from the GCEMC results shown in Fig. 3. As Fig. 12 shows, all three curves exhibit a similar pattern, and as may be expected, the self-diffusivity increases as the temperature does. Over a wide range of the guest molecules loading (about 0.3–1.1), the self-diffusivity increases slowly as the loading decreases. For adsorbate loadings less than 0.3, the diffusivity increases rather rapidly. At the lowest temperature, $T = 0.8$, there is a discontinuity in D, which corresponds to the first-order phase transition shown in Fig. 3. In Fig. 13 we present the dependence of the diffusivity on the equilibrium loading at porosity 0.89 and three different temperatures. For this series of simulations the pillars were distributed uniformly between the walls. The qualitative features of these results are similar to those shown in Fig. 12, except that the discontinuity in D has shifted to a lower temperature, in agreement with Fig. 5. Fig. 14 shows the dependence of the self-diffusivity on the pressure. All the parameters are the same as those of Fig. 13 and, as expected, the trends in the results are also similar to those shown in Fig. 13.

Shown in Fig. 15 are the self-diffusivities for four different pillar configurations and distributions at $T = 1.20$, as a function of the equilibrium loading. For all the four pillar configurations, the diffusivity is a monotonically decreasing function of the loading. At high loadings ($\geqslant 0.7$) D is not strongly correlated

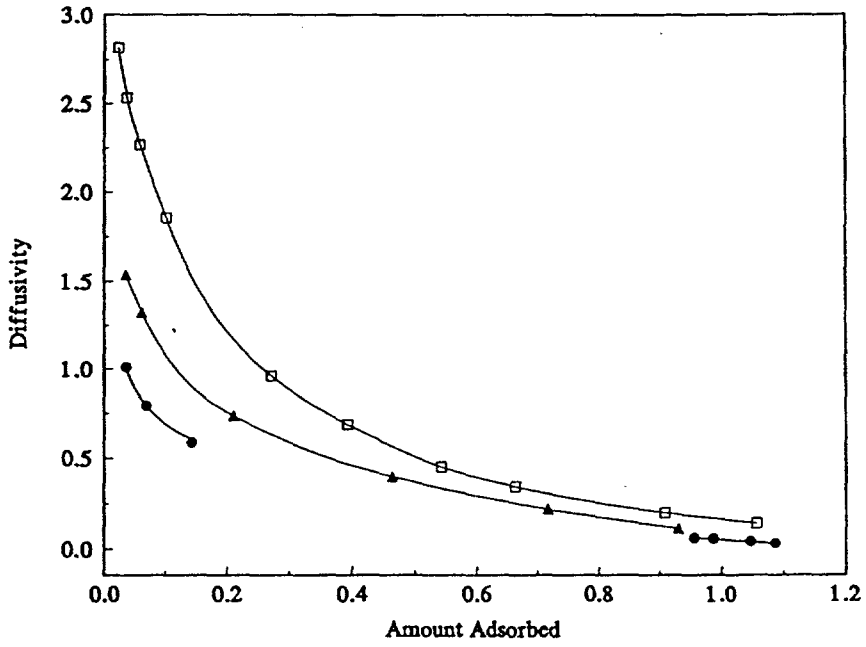

Fig. 12. The self-diffusivity D as a function of the equilibrium loading for a uniform distribution of the pillars with porosity $\varphi = 0.97$ at temperatures $T = 0.80$ (circles), 1.2 (triangles), and 2.0 (squares), respectively.

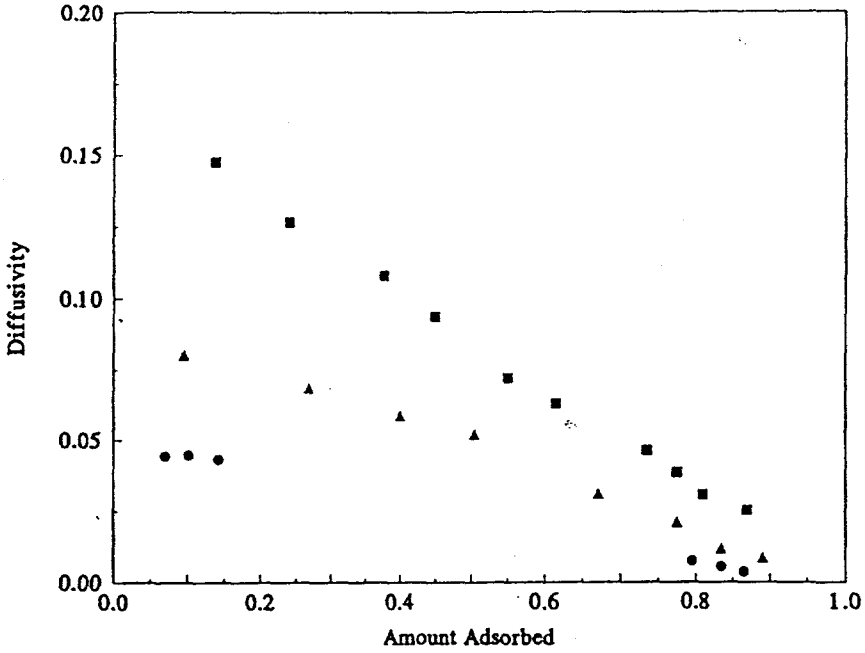

Fig. 13. Dependence of the self-diffusivity on the equilibrium loading at the porosity 0.89, in which the pillars are distributed uniformly. The results are for $T = 1.2$ (squares), 0.8 (triangles), and 0.6 (circles).

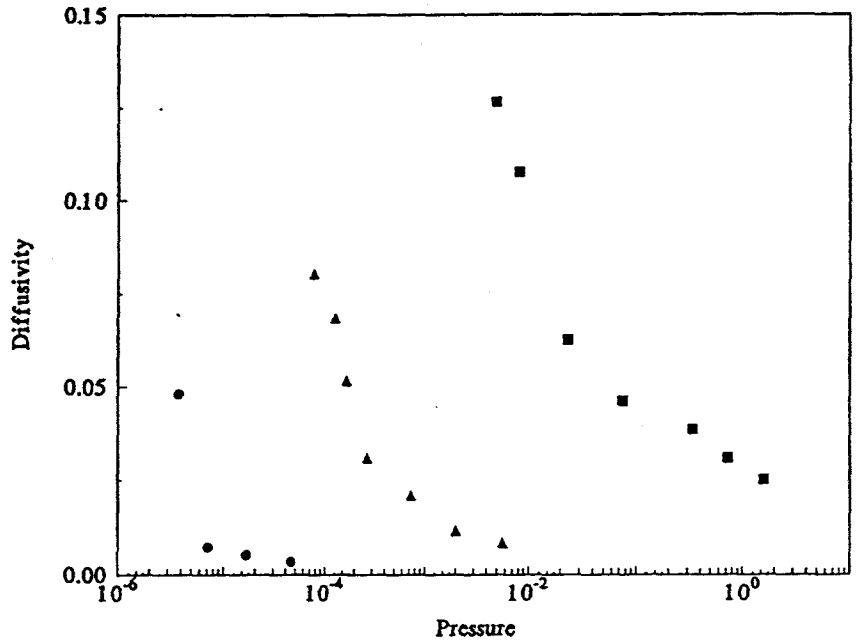

Fig. 14. Dependence of the self-diffusivity on the pressure in a system with a porosity $\varphi = 0.89$ and a uniform distribution of the pillars. Symbols are the same as in Fig. 13.

with the pillar distribution, which is similar to what we observed for the equilibrium loading in the GCEMC simulation. At lower loadings, however, D has a much stronger dependence on the pillar configuration than that of the equilibrium loading (see Figs 3 and 6 for comparison). Fig. 15 shows that, the values corresponding to the triad cluster configurations represent the upper bound to the self-diffusivity, while those corresponding to the uniform pillar configuration give the lower bound. These results can be understood by noting that the pillar-guest molecule collisions are the main source of resistance to the diffusive motion of the molecules in the low loading region, while both molecule–pillar and molecule–molecule collisions become important at higher loadings. Among the four pillar configurations, the triad

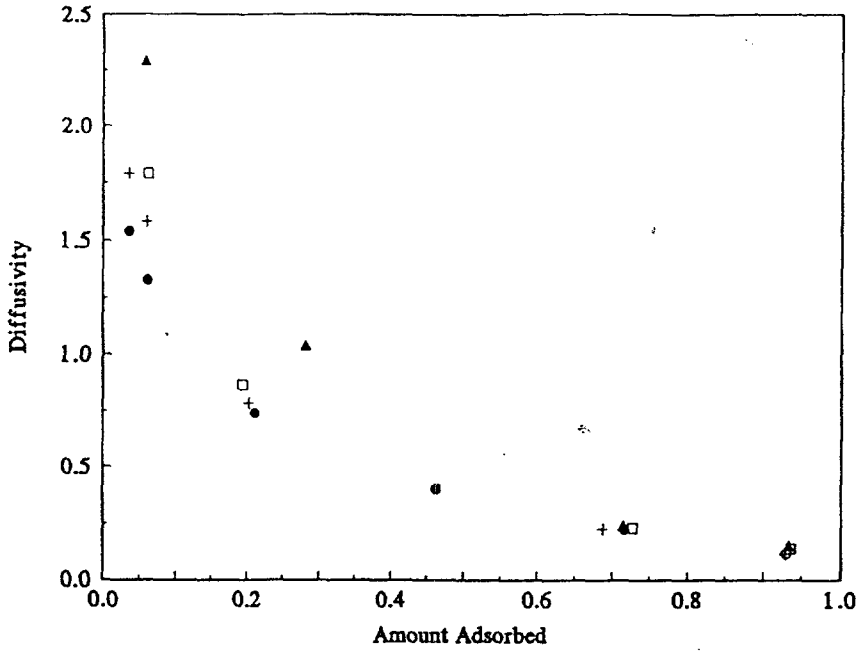

Fig. 15. The effect of the spatial distribution and clustering of the pillars on the self-diffusivity in a system with a porosity $\varphi = 0.97$ at temperature $T = 1.2$. The symbols are the same as in Fig. 6.

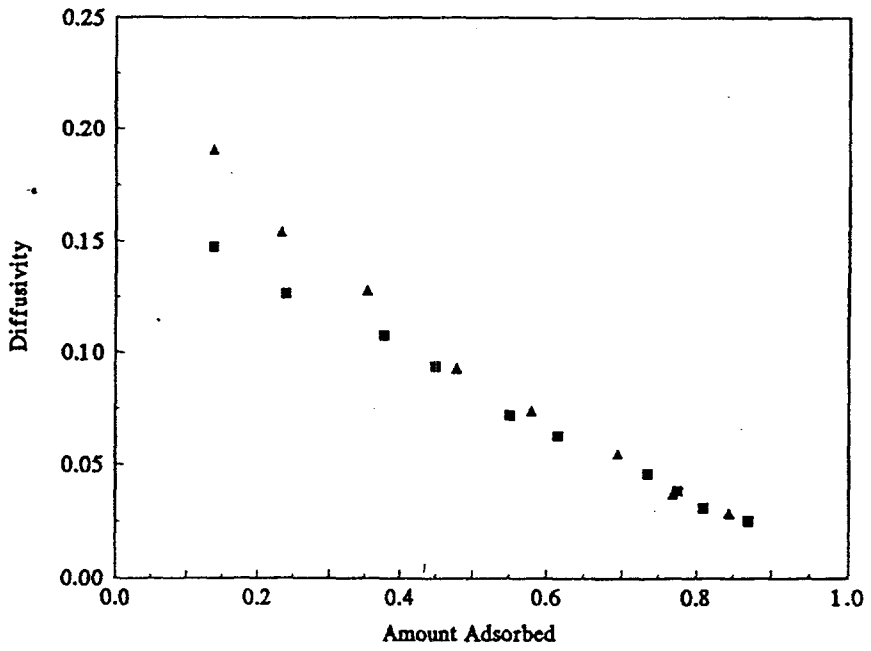

Figure 16. Dependence of the self-diffusivity on the equilibrium loading at $T = 1.2$ and $\varphi = 0.89$. The results are for a uniform (squares) and random (triangles) distribution of the pillars.

clusters have the largest pore opening due to the grouping of pillars. Consequently, compared with the other pillar configurations, the molecules collide less frequently with the pillars, and therefore have the highest self-diffusivities. Following the same argument, it is not difficult to understand why a uniform pillar configuration gives rise to the lowest diffusivities. The diffusivities for the diploid cluster configurations lie between the higher and lower bounds, in clear conformity with our reasoning. The results for the random pillar configurations, for which the average pore opening is about the same as that of the uniform pillar configuration, are slightly larger than that of the latter. To understand this, we only need to note that for the random pillar configurations, some wider channel or "easy" paths may be formed, due to the

randomness of the pillar configurations, and thus result in the enhancement of the self-diffusivity. This result is also in agreement with our previous study of the effect of the spatial distribution of single-sized pillars on the diffusivity reported in Part I. Figures 16 and 17 present the results at porosity $\varphi = 0.89$, and compare the diffusivities for two different pillar configurations. The qualitative features of Figures 16 are similar to those shown in Fig. 15, and confirm our arguments regarding their interpretation. The trends in Fig. 17 are also similar to those of Fig. 16, which is expected.

Fig. 18 presents self-diffusivities at four porosities with uniform pillar distribution. The temperature and the interlayer spacing are again fixed at $T = 1.20$ and $h_w = 4.5$, respectively. As this figure indicates, with the

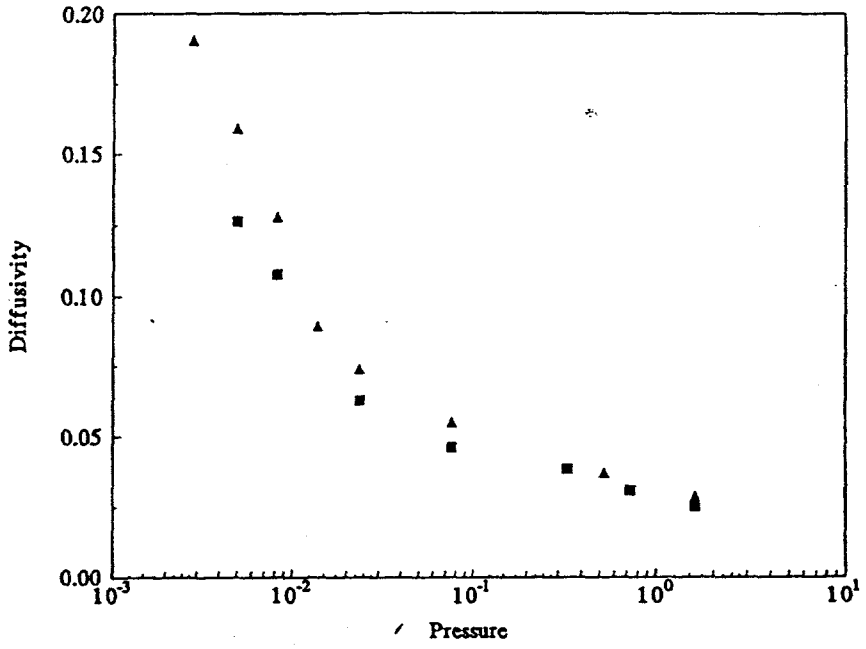

Fig. 17. Pressure-dependence of the self-diffusivity at temperature $T = 1.2$ and porosity $\varphi = 0.89$. The results are for a uniform (squares) and random (triangles) distribution of the pillars.

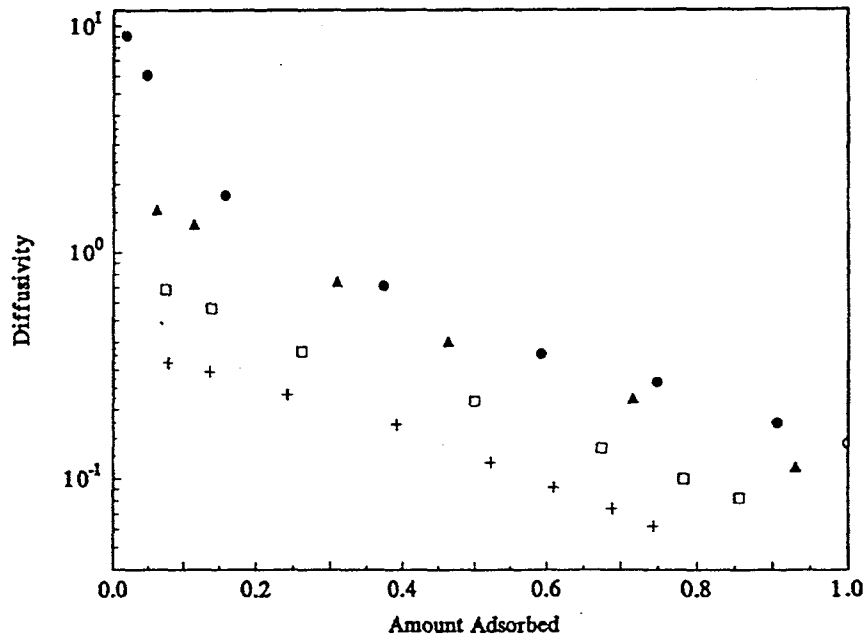

Fig. 18. The effect of the porosity on the self-diffusivity for a uniform distribution of the pillars at temperature $T = 1.2$. The symbols are the same as in Fig. 10.

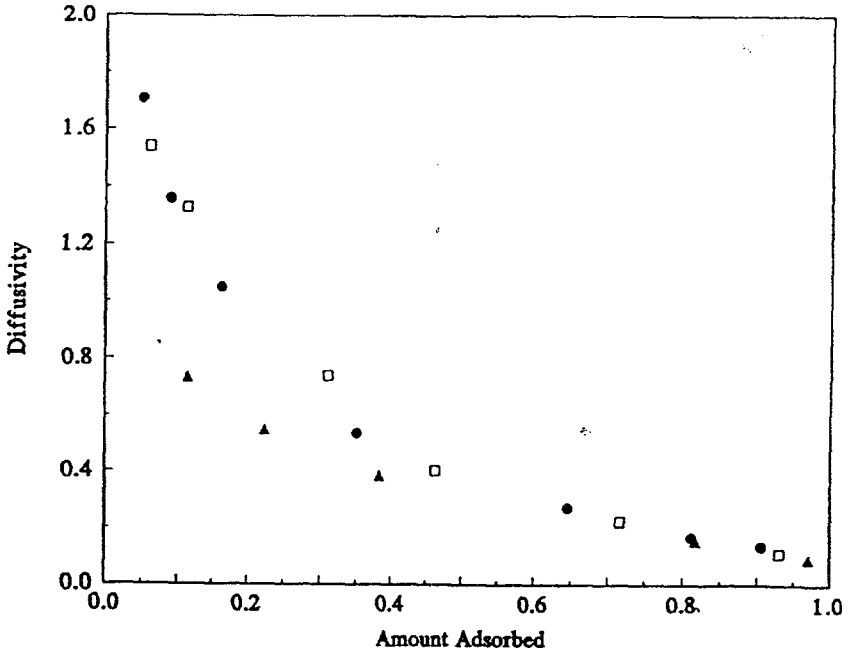

Fig. 19. The effect of pillar-adsorbate energy parameter ε_p on the self-diffusivity at $T = 1.2$, for a uniform distribution of the pillars with porosity $\varphi = 0.97$. The results are for $\varepsilon_p = 0.5$ (circles), 1.0 (squares), and 2.0 (triangles), respectively.

same guest molecules loading, the ratio of the highest and lowest self-diffusivities is as high as 10 at very low guest molecules loadings. In agreement with our study reported in Part I, the diffusivity is a monotonically increasing function of the porosity. As our discussion given above indicates, this is an expected result, since with a uniform pillar distribution, the pore opening increases with increasing porosity.

Similar to Fig. 11, where we showed the dependence of the amount of the adsorbed molecules on the pillar-adsorbate energy parameter ε_p, Fig. 19 presents the same for the diffusivity. The trends in the results are somewhat similar to those in Fig. 11, and as both figures indicate, in the limit of high adsorption there is little difference between the diffusivities for all three cases. However, at low adsorption, the difference between the diffusivities is large, a result that can be explained using arguments similar to those given for Fig. 11.

SUMMARY

Molecular simulations were carried out to study the adsorption equilibria and diffusive motion of guest molecules in model pillared clays. The dependence of the adsorption isotherms and the self-diffusivities of the molecules on temperature, pillar configuration, porosity, and pressure (chemical potential) were studied systematically. The adsorption isotherms predicted by the GCEMC simulation were found to be monotonically increasing functions of the pressure and monotonically decreasing functions of the temperature. A first-order phase transition (condensation) was observed at low enough temperatures. At moderate and high porosities, the adsorption isotherms show no strong dependence on the spatial distribution of the pillars. Depending on the pressure, the dependence of equilibrium loading on the porosity exhibits two different patterns. In the high pressure range, the equilibrium loading increases as the porosity increases, whereas in the low pressure range this dependence is reversed. This complex dependence of the equilibrium loading on the porosity is due to the competition between the accessible pore volume of the system and its total adsorption surface, the two factors that control adsorption equilibria in any porous medium, and represent percolation effects.

An important finding of this work is the relative insensitivity of adsorption isotherms to the pore structure of the system (as represented by pillar clustering) at the same porosity, at least at moderate and high porosities. This implies that experimental adsorption isotherm data alone may not be able to uniquely determine parameters such as the pore size distribution. However, we caution that this conclusion is limited to the model we used in this study, and may need modification for low porosity cases, and where very specific interactions are involved in adsorption.

When the comparison is possible, the MD simulation results are in good agreement with our results reported in Part I, and the equilibrium properties obtained from corresponding GCEMC and MD simulations are in close agreement. With the exception of states involving condensation transition, the self-diffusivity of the guest molecules, as obtained from the MD simulations, was found to be a

monotonically decreasing function of the equilibrium loading (and therefore the pressure of the surrounding fluid), and a monotonically increasing function of the temperature. Our results show that the diffusivity is more strongly dependent upon the spatial distribution of the pillars than is the equilibrium loading, especially at low and moderate loadings. The diffusivity also has a much stronger dependence on the porosity than that of the equilibrium loading.

Based on the available experimental information, and the insight we have obtained from the molecular simulations of our model of intercalated porous materials, we are currently developing a more refined model of pillared clays, in which detailed information about their structure and the energetics are incorporated. The model will then be used for molecular simulations of diffusion and adsorption in typical pillared clays, such as *Al*-intercalated montmorillomites. The results will be reported in a future paper.

Acknowledgement—This work was partially supported by the National Science Foundation under Grant CTS-9122529. The work of MS was also supported by the Department of Energy. We are grateful to Dietrich Wolf for allowing us to have continued access to the computer facilities at the HLRZ-KFA Supercomputer Center in Jülich, Germany, where most of our computations were carried out.

REFERENCES

Adams, D. J., 1975, Grand canonical ensemble Monte Carlo for a Lennard–Jones fluid. *Mol. Phys.* **29**, 307.

Allen, M. P., and Tildesley, D. J., 1987, *Computer Simulation of Liquids*. Oxford University Press, Oxford.

Baksh, M. S., Kikkinides, E. S. and Yang, R. T., (1992), Characterization by physiosorption of a new class of microporous adsorbent: pillared clays. *Ind. Engng. Chem. Res.* **31**, 2181.

Baksh, M. S. and Yang, R. T., 1991, Chromatographic separation by pillared clays. *Separet. Sci. Tech.* **10**, 1377.

Baksh, M. S. and Yang, R. T., 1992, Unique adsorption properties and potential energy profiles of microporous pillared clays. *A.I.Ch.E. J.* **38**, 1357.

Barrer, R. M. and MacLeod, D. M., 1977, Activation of montmorillonite by ion exchange and sorption complexes of tetra-alkyle ammonium montmorillonites. *Trans. Faraday Soc.* **51**, 1290.

Bishop, M. and Frinks, S., 1987, Error analysis in computer simulations. *J. Chem. Phys.* **87**, 3675.

Brindley, G. W. and Sempels, R. E., 1977, Preparation and properties of some hydroxy-aluminum beidellites. *Clay Minerals* **12**, 229.

Cai, Z.-X., Mahanti, S. D., Solin, S. A. and Pinnavaia, T. J., 1990, Dual percolation threshold in two-dimensional microporous media. *Phys. Rev. B* **42**, 6636.

Chen, B. Y., Kim, H., Mahanti, S. D., Pinnavaia, T. J. and Cai, Z. X., 1994, Percolation and Diffusion in two-dimensional microporous media: pillared clays. *J. Chem. Phys.* **100**, 3872.

Cracknell, R. F. and Gubbins, K. E., 1993, Molecular simulation and diffusion in VPI-5 and other aluminophosphates. *Langmuir* **9**, 824.

Fichthorn, K. A. and Weinberg, W. H., 1991, Theoretical foundations of dynamical Monte-Carlo simulations. *J. Chem. Phys.* **95**, 1090.

Figueras, F., 1988, Pillared clays as catalysts. *Catal. Rev.- Sci. Engng* **30**, 457.

Gear, C. W., 1971, *Numerical Initial Value Problems in Ordinary Differential Equations*. Prentice-Hall, Englewood Cliffs, NJ.

Giannelis, E. P., Rightor, E. G. and Pinnavaia, T. J., 1988, Reaction of metal-cluster Carbonyls in pillared clay galleries: surface coordination chemistry and Fischer–Tropsch catalysis. *J. Am. Chem. Soc.* **110**, 3880.

Green, M. S., 1952, Markoff random processes and the statistical mechanics of time-dependent phenomena. *J. Chem. Phys.* **20**, 1281.

Gregg, S. J., and Sing, K. S. W., 1982, *Adsorption, Surface Area and Porosity*. Academic Press, New York.

Grim, R. E., 1986, *Clay Mineralogy*. McGraw-Hill, New York.

Haile, J. M., 1990, *Molecular Dynamics Simulation*. Wiley, New York.

June, R. L., Bell, A. T. and Theodorou, D. N., 1992, Molecular dynamics studies of butane and hexane in silicalite. *J. Phys. Chem.* **96**, 1051.

Kloprogge, J. T., 1992, *Pillaed Clays. Preparation and Characterization of Clay Minerals and Aluminum-Based Pillaring Agents*. Faculteit Aardwestenschappen der Rijksuniversiteit, Utrecht.

Kubo, R., 1957, Statistical-mechanical theory of irreversible processes. I. General theory and a simple application to magnetic and conduction problems. *J. Phys. Soc. Japan* **12**, 570.

Lahav, H., Shani, V. and Shabtai, J., 1978, Cross-linked smectites. I. Synthesis and properties of hydroxy-aluminum-montmorillonite. *Clays Clay Miner.* **26**, 107.

Lee, W. Y., Raythatha, R. H. and Tatarchuk, B. J., 1989, Pillared-clay catalysts containing mixed-metal complexes. 1. Preparation & characterization. *J. Catal.* **115**, 159.

Occelli, M. L., Haru, F. S. S., and Hightower, J. W., 1985, Sorption and catalysis on sodium-montmorillonite interlayed with aluminum oxide clusters. *Appl. Catal.* **14**, 69.

Occelli, M. L. and Tindwa, R. W., 1980, Physicochemical properties of montomorillonite interlayered with cationic oxyaluminum pillars. *Clays Clay Miner.* **31**, 22.

Ohtsuka, K., Hayashi, Y. and Suda, M., 1993, Microporous ZrO_2-pillared clays derived from three kinds of Zr polynuclear ionic species. *Chem. Mater.* **5**, 1823.

Peterson, B. K. and Gubbins, K. E., 1987, Phase transitions in a cylindrical pore, grand-canonical Monte Carlo, mean-field theory and the Kelvin equation. *Mol. Phys.* **62**, 215.

Pinnavaia, T. J., 1983, Intercalated clay catalysts. *Science* **220**, 365.

Pinnavaia, T. J., Landau, S. D., Tzou, M. S. and Johnson, I. D., 1985, Layer cross-linking in pillared clay. *J. Am. Chem. Soc.* **107**, 7222.

Plee, D., F. Borg, Gatineau, L. and Fripiat, J. J., 1985, High-resolution solid-state ^{27}Al and ^{29}Si nuclear magnetic resonance study of pillared clays. *J. Am. Chem. Soc.* **107**, 2362.

Politowicz, P. A. and Kozak, J. J., 1988. Influence of swelling on reaction efficiency in intercalated clay minerals. *J. Phys. Chem.* **92**, 6078.

Politowicz, P. A., Leung, L. B. S. and Kozak, J. J., 1989, Influence of swelling on reaction efficiency in intercalated clay minerals. 2. Pillared clays. *J. Phys. Chem.* **93**, 923.

Sahimi, M., 1990, Diffusion, adsorption, and reaction in pillared clays. I. Rod-like molecules in a regular pore space. *J. Chem. Phys.* **92**, 5107.

Sahimi, M., 1994, *Applications of Percolation Theory*. Taylor and Francis, London.

Sahimi, M., 1995, *Flow and Transport in Porous Media and Fractured Rock*. VCH, Weinheim, Germany.

Sahimi, M., Gavalas, G. R. and Tsotsis, T. T., 1990, Statistical and continuum models of fluid-solid reactions in porous media. *Chem. Engng Sci.* **45**, 1443.

Siepmann, J. I. and Frenkel, D. 1992, Configurational biased Monte Carlo: a new sampling scheme for flexible chains. *Mol. Phys.* **75**, 59.

Snook, I. K. and van Megen, W., 1980, Solvation forces in simple dense fluids. I. *J. Chem. Phys.* **72**, 2907.

Snurr, R. Q., Bell, A. T. and Theodorou, D. N., 1993, Prediction of adsorption of aromatic hydrocarbons in silicalite

from grand canonical Monte Carlo simulation with biased insertions. *J. Phys. Chem.* **97**, 13742.

Steele, W. A., 1973, The physical interaction of gases with crystal solids. I. Gas–solid energies and properties of isolated adsorbed atoms. *Surface Sci.* **36**, 317.

Tennakoon, D. T. B., Jones, W., Thomas, J. M., Ballantine, J. H. and Purnell, J. H., 1987, Characterization of clay and pillared clay catalysts. *Solid State Ion.* **24**, 205.

Vaughan, D. E. W. and Lussier, R. J., 1980, *Proceedings of the International Conference on Zeolites*. Naples.

Weeks, J. D., Chandler, D. and Andersen, H. C., 1971, Role of repulsive forces in determining the equilibrium structure of simple fluids. *J. Chem. Phys.* **54**, 5237.

Yamanaka, S. and Brindley, G. W., 1978, Hydroxy-nickel-interlayering in montmorillonite by titration method. *Clays Clay Miner.* **26**, 21.

Yi, X., Shing, K. S. and Sahimi, M., 1995, Molecular dynamics simulation of diffusion in pillared clays. *A.I.Ch.E. J.* **41**, 456.

Yang, R. T. and Baksh, M. S., 1991, Pillared clays as a new class of sorbents for gas separation. *A.I.Ch.E. J.* **37**, 679.

Zwanzig, R., 1965, Time-correlation functions and transport coefficients in statistical mechanics. *Ann. Rev. Phys. Chem.* **16**, 67.

SPE 35707

Asphalt Formation and Precipitation: Experimental Studies and Theoretical Modelling

Muhammad Sahimi, SPE, Hossein Rassamdana, SPE, University of Southern California, and Bahram Dabir, Amir Kabir University, Tehran, Iran

This paper was prepared for presentation at the Western Regional Meeting held in Anchorage, Alaska, 22-24 May, 1996.

Abstract

We present extensive new experimental data for the amount of precipitated asphalt and asphaltene aggregates formed with crude oil and various solvents, and their molecular weight (MW) distributions. A new scaling equation is proposed for predicting the onset and amount of the precipitates, somewhat similar to those encountered in aggregation and gelation phenomena. The scaling function takes on a very simple form, and its predictions are in very good agreement with the available data. We also present an analysis of small-angle X-ray and neutron scattering data to delineate the structure of the asphalt and asphaltene aggregates. Our analysis suggests that the asphalt and asphaltene aggregates are fractal structures with well-defined fractal properties. We identify the mechanisms that give rise to such fractal aggregates, based on which we propose a new analytical form for the MW distribution of the asphalt and asphaltene aggregates which provides accurate predictions for our data.

INTRODUCTION

An important phenomenon in the petroleum industry is deposition of heavy organic compounds on the pore surfaces of oil reservoirs during enhanced oil recovery processes[1,2]. Miscible displacement of oil by carbon dioxide or natural gas is considered one of the most efficient methods of increasing oil production. However, this process often causes some changes in the fluid flow behavior and the equilibrium properties of the fluids. Under certain conditions such changes lead to the formation of asphaltenes and asphalts, which are large molecular aggregates with complex structure and properties. Although many authors do not distinguish between asphalt and asphaltene, we define the former as the latter plus resin, and use this terminology throughout this paper. Formation of asphalts and asphaltenes is a function of the composition of the crude oil and the displacing agents, and the pressure and temperature of the reservoir. Their deposition on the surface of the pores reduces the permeability of the pore space, leading to the eventual isolation of oil from the flowing fluid in the reservoir[3], and reduction of the efficiency of oil recovery processes. As enhanced oil recovery processes by miscible displacements have become popular, formation of heavy organic aggregates in the form of asphalt and asphaltene and their deposition on the pore surfaces have gained increasing importance. Deposition of such aggregates on the pore surfaces can also alter the wettability of the reservoir, which is a crucial factor in the distribution of *immiscible* fluids in a porous medium and displacement of oil by an immiscible fluid such as water[4]. Although over the past several decades the nature of asphalts and asphaltenes and the mechanism of their precipitation on the pore surfaces of a porous medium have been studied intensively[1,2,5-15], no general consensus has emerged. One important reason for this lack of consensus is that these studies were not systematic in that each study considered only one aspect of the problem, and did not investigate several important and related aspects of the problem, all in one study and with similar compounds, and under similar conditions. The complexity of the structure of asphalt and asphaltenes aggregates has also hindered progress. Problems arising from asphalt and asphaltene precipitation have been encountered in many field-scale operations around the world, including those in Algeria[16], in the Ventura field in California[6,17], in the production tubing in the Little Creek, Mississippi, during CO_2 injection for enhanced oil recovery[17], and in some Iranian oil fields.

The purpose of this paper is to present the results of a systematic study of formation of the asphalt and asphaltene aggregates, their structure, and the onset and amount of their precipitation. Their transport properties, such as their effective diffusivity in a pore, have been reported elsewhere[18]. We first present our new experimental data

for the onset and amount of asphalt and asphaltene precipitation, which is then followed by their theoretical modelling. We then present an analysis of small-angle X-ray and neutron scattering (SAXS and SANS, respectively) data, showing that they provide key insights into the structure of the asphalt and asphaltene aggregates, based on which we propose the mechanisms that give rise to these aggregates. This leads us to a new analytical equation for the MW distribution of the asphalt and asphaltene aggregates, which provides accurate predictions for the new data presented here.

PRECIPITATION RESULTS

To measure the amount of the precipitated asphalt or asphaltene aggregates we used a crude oil, from an Iranian oil field, which we filtered to remove its solid contents, such as sand. We then diluted the oil by a solvent, which was a normal alkane with a carbon number ranging from 5 to 10. Several different dilution ratios R, measured in terms of the cm^3 of the solvent/gr of the oil, were used. The diluted oil was then agitated in a tube, which caused the formation and precipitation of the aggregates. After one day the solid content of the oil, i.e., the precipitated aggregates, was measured. The asphaltene content was separated and measured by the standard IP-143 method. During the entire experiment the temperature was kept at about 25°C. Complete details of such experiments are given elsewhere[19].

Figure 1 shows our experimental results for the weight percent of the precipitated asphalt W, in weight of the asphalt/gr of the crude oil, for five different solvents (n-alkanes) and various solvent to crude ratios R. Our data are consistent with the previous experimental data. For example, Hirschberg *et al.*[13] have presented very limited data for n-C_5, n-C_7, and n-C_{10} at three different values of R. The trend of their data are consistent with ours, although a numerical comparison between their data and ours is not possible, because they do not specify the temperature of their experiments. Kokal *et al.*[20] presented two sets of precipitation data obtained with two different Canadian crude oils. One was for Suffield heavy oil, and the solvents were n-C_5, n-C_6, n-C_7, n-C_8, and n-C_{10}. The other one was for Lindberg heavy oil, with n-C_5, n-C_6, n-C_8 and n-C_{10} as the solvents. Our data are consistent with theirs, although, as they pointed out, the fluctuations and uncertainties in their data are large.

To study the effect of pressure on the precipitation, we also measured the amount of precipitated asphalt in a tank oil at 25°C with two solvents, namely, n-C_6 and n-C_7, at various pressures. The results are shown in Figure 2, indicating that as the pressure increases the amount of the precipitated asphalt decreases. However, beyond a certain pressure no significant changes are observed in the precipitation. This behavior, which is also supported by the small-angle scattering data that are discussed below, is explained as follows. At a fixed temperature, lower pressures are associated with lower fluid density and solubilizing ability, and a large mean distance between the asphalt particles and the surrounding fluid particles. As a result, the amount of the asphalt aggregates, and hence the precipitation amount, is larger at low pressures. As the pressure increases, the solubilizing ability of the solution increases, resulting in smaller amount of the asphalt (and asphaltene) aggregates and precipitation.

We also measured the amount of precipitated asphaltene with n-C_6 and n-C_7 for various values of R and at 8°C and 19°C. The results are presented in Figures 3 and 4. The qualitative trends of these data are similar to those shown in Figure 1, implying that their modelling and predictions must also be similar to them. We show below that this is indeed the case.

THEORETICAL MODELLING OF PRECIPITATION DATA

Predicting the onset and amount of asphalt and asphaltene precipitation is a difficult problem which has not yet found a satisfactory solution. In the past various thermodynamic models have been used[2,13,19–22] for predicting the precipitation, based on the assumption that the process is a reversible phenomenon. Aside from the fact that the reversibility of this process is in question, to be predictive, this approach requires many adjustable parameters and assumptions, many of which are not justified, and therefore it is not satisfactory. We present an alternative approach that uses the analogy between asphalt and asphaltene formation and aggregation phenomena, and builds on the universal properties that they possess.

The data presented in Figures 1, 3, and 4 are strongly suggestive of the possibility that they may all be collapsed onto universal scaling curves, since all the curves start at about the same point (close to their onset of precipitation), and at large values of R they become more or less parallel. As a result, it may be possible to collapse the data onto a single scaling curve. This is in fact typical of aggregation processes by which asphalt and asphaltene aggregates are also formed. The variables in Figures 1, 2, and 4 are R, W, and M, the MW of the solvent. Similar to aggregation phenomena in which independent variables are combined and reduced to fewer variables, we find that, if let $X = R/M^z$ and $Y = WR^{z'}$, then the experimental data shown in Figures 1, 3, and 4 can be collapsed onto scaling curves with

$$z = \frac{1}{4}, \quad z' = 2. \tag{1}$$

The results are shown in Figures 5 and 6. Note that, we could not find any other values for z and z' that could collapse the data onto scaling curves with the same accuracy, nor could we find any other combinations of the three variables that could do the same. Thus these combinations of the variables and the values of z and z' appear to be unique. The reason for this data collapse, which is novel,

becomes clear only if one understands the similarities between asphalt and asphaltene formation and aggregation phenomena, which have scaling and universal properties; these are explained below where we analyze the scattering data, and provide a theoretical explanation for the values of z and z'.

The collapse of the precipitation data onto scaling curves also has two important implications and consequences. First, the scaling curve provides accurate predictions for those values of R, or those solvents, *for which no data are available*, or their measurement my be difficult. Secondly, the scaling representation of the data implies a universal property for the *onset of precipitation*, to be discussed below. To show that the data collapse is robust and a scaling curve can be obtained from far fewer data points with comparable accuracy which can then be used for predicting precipitation for other systems, and to also get some idea about the effect of fluctuations and uncertainties in the data on their collapse, we also collapsed onto a single curve the asphalt data only for n-C_5 and n-C_6, the lightest solvents used in our experiments, and again found that the same z and z' collapse the data. The resulting scaling curve shown in Figure 7 was then used for predicting the experimental data for n-C_7, n-C_8 and n-C_{10}. The results are shown in Figure 8, and it is seen that the accuracy of the predictions is very good. Similar results are obtained if we collapse the data for n-C_8 and n-C_{10}, the heaviest solvents used in our experiments, and then use the resulting scaling curve to predict the data for n-C_5, n-C_6 and n-C_7, or if we use the scaling curves shown in Figure 6 and predict the amount of precipitated asphaltene with n-C_6 and n-C_7. Thus, *any* two sets of data provide accurate predictions for all other data, i.e., *with limited amount of experimental data, one can make accurate predictions for other systems for which no data are available.*

We should point out that the collapse of the precipitation data is not restricted to our results and the crude oil that we used in our experiments. For example, we found that with *the same* values of z and z' we can collapse the data reported by Kokal *et al.*[20] onto scaling curves. The results are shown in Figure 9. Given that, as Kokal *et al.*[20] themselves pointed out, the fluctuations and uncertainties in their data are large, the collapse of their data is excellent. This confirms our assertion that *the collapse of the precipitation data onto scaling curves is independent of the type of crude oil, temperature and pressure.*

The Onset of Precipitation

From a practical point of view, an important quantity is R_c, the value of R at the onset of precipitation. For $R < R_c$ no precipitation occurs, whereas for $R \geq R_c$ one has asphalt or asphaltene precipitation. Currently, the only extensive experimental data for R_c that we are aware of are those of Hotier and Robin[23], which according to them are subject to great uncertainty. From the scaling curves shown in Figures 5, 6 and 9 we can derive a relation between R_c and M for the onset of precipitation for various solvents. To do this, we find the intercept of the scaling curves at $Y = 0$ and calculate the critical value X_c for the onset of precipitation. Since we have collapsed the data onto a single curve, the value of X_c *must be the same* for all the solvents. Indeed, Figure 5 predicts that for the asphalts $X_c = R/M^{1/4} \simeq 0.27$, and Figures 9 tell us that $X_c \simeq 0.3$, and therefore $R_c = cM^{1/4}$, where c is essentially independent of the type of the crude oil. Similarly, Figure 6 tells us that for the asphaltenes, $X_c \simeq 0.025$. These results tell us that *at the onset of precipitation, the critical ratio R_c depends mainly on the MW of the injected solvent*, at least for the solvents that we used in our experiments. More generally, we may write $R_c = c(T)M^{1/4}$, in which we believe that c is a temperature-dependent quantity. Estimating $c(T)$ requires experimental data at several temperatures.

ANALYSIS OF SMALL-ANGLE SCATTERING DATA

Asphalts and asphaltenes are molecular structures whose formation is the result of aggregation of the elementary particles in the crude oil solution. Thus, it would be useful to discuss briefly two important aggregation phenomena that are relevant to our paper. These are diffusion-limited particle (DLP) and diffusion-limited cluster-cluster (DLCC) aggregation. In the DLP aggregation model[24] the site at the center of a lattice (or a continuum) is occupied by a stationary particle. A new particle is then injected into the lattice, far from the center, which diffuses on the lattice until it reaches a surface site, i.e., an empty site which is a nearest-neighbor to the stationary particle, at which time the particle sticks to it and remains there permanently. Another diffusing particle is then injected into the lattice to reach another surface (empty) site and stick to it, and so on. If this process is continued for a long time, a large aggregate is formed, a typical two-dimensional (2D) example of which is shown in Figure 10. The most important property of the DLP aggregates is that, they are self-similar and fractal. This means that, if N_p is the number of the elementary particles in an aggregate of radius R_p, then one has $N_p \sim R_p^{D_f}$, where D_f is the fractal dimension of the aggregate. Computer simulations indicate that $D_f \simeq 2.5$, for 3D DLP aggregates.

In the DLCC aggregation model[25,26] one starts with an empty lattice (or a continuum). At time $t = 0$, a fraction p_0 of the lattice sites are selected at random and occupied by particles. Each occupied site can contain only one particle. If p_0 is small, the system will consist of a large number of isolated occupied sites and a few small clusters of particles. A cluster is a set of nearest-neighbor particles. One cluster, including a single particle, is then selected at random and is allowed to diffuse in a randomly-chosen direction. Then the perimeter sites of the cluster – the set of sites that are adjacent to the cluster – are examined to see whether they are occupied by other particles or clusters. If

so, the perimeter particles or clusters are attached to the cluster that was moved to form a larger cluster. Another randomly-selected cluster is moved again, its perimeter is examined for possible formation of a larger cluster, and so on. Figure 11 shows several stages of this process in 2D. The DLCC aggregates are also fractal objects, and extensive computer simulations suggest that for DLCC aggregates $D_f \simeq 1.8 \pm 0.05$ in 3D.

An important property of fractal aggregates is the roughness of their surface. Since the clusters that aggregate together have irregular shapes and sizes, their *active* surface area S_a, i.e., that part of their surface which is most likely to collide with the surface of another cluster, is different from the *total* surface area of the cluster, and constitutes only a small fraction of it. For a growing cluster during aggregation S_a scales with the total number of particles s in the cluster as

$$S_a \sim s^{\omega} , \tag{2}$$

where ω is a universal exponent, independent of many microscopic features of the cluster. As we discuss later, ω has a strong influence on the shape of the MW distribution of the aggregates.

An accurate probe of the structure of complex systems is small-angle scattering. In a scattering experiment the observed scattering intensity $I_s(q)$ by a single self-similar and fractal cluster or aggregate is given by[27]

$$I_s(q) \sim q^{-D_f} , \tag{3}$$

where q is the magnitude of the scattering vector given by

$$q = \frac{4\pi}{\lambda} \sin\left(\frac{\theta}{2}\right) . \tag{4}$$

Here λ is the wavelength of the radiation scattered by the sample through an angle θ. Thus, a logarithmic plot of $I_s(q)$ versus q should yield a straight line with the slope $-D_f$.

If the solution contains many aggregates or clusters of various sizes, as is the case with a crude oil that contains many asphalt or asphaltene aggregates, then the intensity $I(q)$ scattered is the average sum of the intensities scattered by all the aggregates. Suppose that $n_s(t)$ is the number of the clusters or aggregates of size s in the solution at time t, where s represents the number of the elementary particles in an aggregate. If the aggregates are fractal, then it has been shown that[28]

$$n_s = s^{-\tau} f(s/\langle s \rangle) , \tag{5}$$

where τ is a universal exponents, $\langle s \rangle$ is the mean aggregate size, and $f(x)$ is a *universal* scaling function. For a solution containing many aggregates of various sizes $I(q)$ is given by[29]

$$I(q) = \int s n_s I_s(q) ds , \tag{6}$$

which means that

$$I(q) \sim q^{-(3-\tau)D_f} . \tag{7}$$

We now analyze the small-angle scattering data to deduce the structure of the asphalt and asphaltene aggregates. The data that we analyze include both SANS and SAXS, which are known to have very different contrast mechanisms, especially for complex systems such as the asphalt and asphaltene aggregates. Despite this, both the SANS and SAXS data lead to the same conclusion regarding the structure of the asphalt and asphaltene aggregates.

We start with the analysis of the SANS data and give a brief description of such experiments[30]. The small-angle scattering spectrometer utilizes neutrons from a cold source containing liquid hydrogen at 1.5K. The outcoming neutrons are monochromatized by a single multilayered monochromator for selection of the wavelength. In the experiments the wavelength was 5.0Å with a wavelength spread of about 11%. The sample cell was a cylindrical quartz cuvette of 2-mm pathlength. The scattered neutrons, after passing through a helium-filled drift space, were detected by a ^{3}He area detector of 50×50 cm^2 containing 128×128 pixel elements. The sample-to-detector distance was 180cm, which corresponds to a q-range of 0.008 to 0.17Å^{-1}. Heptane was used as the solvent, and after the aggregates were formed, they were separated from the solution and were mixed with toluene. Then the system was allowed to equilibrate for 11 days. The experiments were carried out with the aggregate-toluene mixtures.

The logarithmic plot of the scattering intensity $I(q)$ versus q at 25°C and 5% aggregate concentration is shown in Figure 12. A power-law scattering is observed over about one order of magnitude in the length scale. The size of these aggregates appears to be very small, ranging from about 5Å to about 50Å. This is due to the fact that in these experiments the asphalt aggregates were dissolved in toluene, which is known to be a good solvent for asphalts and resin. Dissolution of the asphalt in toluene causes fragmentation of the aggregates into small pieces. As Figure 12 indicates, there are two distinct regimes. At large length scales (small q) one has a straight line with a slope of about 1.76 ± 0.11, whereas at small length scales (large q), the slope is about 2.6 ± 0.1. Hereafter, we use D_f and d_f to denote the fractal dimensions of the large and small aggregates, respectively. What is the interpretation of these results? From our experimental observations the following mechanisms for the formation of the aggregates emerge. After the solvent is added, the resin, that covers the surface of the small individual particles and the self-associates suspended in the oil, is partially dissolved. The particles and the resin are both electrically charged, albeit with opposite signs, and therefore dissolution of the resin creates electrical imbalance between the particles. The small clusters are then formed by diffusion of the charged solid particles in the oil, which stick together upon collision. But, this is precisely how the DLP aggregates are

formed. Their fractal dimension, which is about 2.5, is in agreement with the scattering data, $d_f \simeq 2.6 \pm 0.1$, obtained from Figure 12. After some time, one has a mixture of small aggregates of various sizes (which also carry a net electrical charge), as well as the individual charged particles. So, while the aggregation of the individual particles continues, aggregation of the clusters as well as the particles is also triggered. These clusters and particles also diffuse in the solution and stick to each other upon collision, which is precisely the mechanism by which the DLCC aggregates are formed. Indeed, if we take $\tau = 2$, the value for DLCC aggregates, Eq. (7) predicts a fractal dimension $D_f \simeq 1.76$ for large length scales, in excellent agreement with that of 3D DLCC aggregates.

Next, we consider SAXS data[31]. In these experiments 3 solution samples were used. Two of them were oil residues at atmospheric pressure and 350°C. After the solvent, which was n-C_7, was added and the asphalts were formed, they were separated and dispersed in benzene. The third sample was a vacuum residue *without* any separation with n-C_7. The solution used in the third scattering experiment contained 10% residue, containing the asphalt, dispersed in benzene. The wave length λ, selected by a variable-curvature monochromator, was 1.608$\mathring{A}$. The focal distance was 2m, with 1m between the sample and the linear sensitive detector.

The results are presented in Figure 13, which show power-law scattering over nearly two orders of magnitude variations in the aggregate size between 50$\mathring{A}$ and 1700$\mathring{A}$. Note that the size of these aggregates is much larger than those in the SANS experiments. The slope for the first two samples yields $D_f \simeq 1.8 \pm 0.03$, while the third sample yields a fractal dimension $D_f \simeq 1.75 \pm 0.05$, all of which are in excellent agreement with that of DLCC aggregates discussed above, and are also consistent with SANS data analyzed above, which were for a completely different oil. Note that, the range of length scales and the aggregate sizes that have been probed by SAXS in these experiments are much larger than those in the SANS experiments, but the results are completely consistent with each other. Note also that, unlike the SANS data, the results shown in Figure 13 do not indicate the presence in the solution of the DLP aggregates at small length scales. We attribute this to two important factors: One is the aging of the three solutions[32] for a very long time, which provides ample time for the small aggregates to diffuse in the solution and stick together as they collide. The second factor is the low concentration of the asphalt in the solution. If the concentration of the solid particles that constitute the asphalt particles is large enough, initially DLP aggregates are formed which cluster together later and form a DLCC aggregate. On the other hand, if the concentration is low enough and the system has reached equilibrium, it contains only one type of fractal aggregates. For example, if the asphalt-containing solution is aged for a long enough time, practically all the DLP aggregates as well as the individual charged particles cluster together and form one or more DLCC aggregates.

These results are also supported by the very recent experiments of Toulhoat *et al.*[33] Using atomic force microscopy, they obtained beautiful pictures of asphalt aggregates that are completely similar to those shown in Figures 10 and 11, thus providing strong support for our results. Thus, not only we estimate the fractal dimension of these aggregates, we also identify the mechanisms for their formation.

The effects of the temperature and pressure. As the temperature of the system rises, more resins are dissolved and thus the electrical charge imbalance between the particles or small clusters is much lower. Therefore, aggregates with much lower densities and effective fractal dimensions are formed. It is possible that the system will eventually contain DLCC and DLP aggregates with their three-dimensional fractal dimensions, but the time scale for reaching this state may be very long. This has been observed very clearly in several experiments[30]. The pressure of the system has an effect somewhat similar to that of the temperature. As the pressure rises, smaller aggregates with lower effective fractal dimensions are formed. However, as our results shown in Figure 2 indicate, once the pressure is large enough, the behavior of the system becomes independent of it. This is clearly seen in Figure 14 where we show the results[34] of SAXS experiments with a heavy oil at 25°C. In these experiments n-C_5 was the solvent, the volumetric ratio oil/solvent was about 3/2, and the pressure was about 5900 psia. At small length scales (large q) the slope of the line is about $d_f \simeq 1.3$, much smaller than $d_f \simeq 2.5$ for DLP aggregates, while at large length scales the slope is *less than one*, implying that there is no DLCC aggregate in the solution at all. These results indicate that at such high pressures only very small aggregates are formed, in agreement with our precipitation results (Figure 2) that indicate that with increasing pressure asphalt precipitation decreases.

We should mention that, in the past there has been some speculation about the possible fractal structure of asphalt and asphaltene aggregates[35–39]. However, none of these papers specified what kind of a fractal structure the asphalt and asphaltene aggregates may possess, or proposed any mechanism for their formation. In the absence of any mechanism for the formation of a fractal structure with a given fractal dimension, one can, in principle, have an infinite number of ways by which the fractal dimension may arise. In fact, Park and Mansoori[35], Crickmore and Hruska[36], and Lin *et al.*[37] all stated that, if the asphalt and asphaltene aggregates are fractal, *their fractal structures and fractal dimensions cannot be specified*, and Raghunathan[38] speculated that the fractal structure of these aggregates is similar to that of *linear polymers*. We must emphasize that a fractal dimension $D_f \simeq 1.8$

does *not* imply that the aggregates are nearly two dimensional. It only means that the number of the elementary solid particles in the aggregates is so low that, their fractal dimension is smaller than two.

If asphalt and asphaltene aggregates are of the DLCC and DLP types, then one can explain why the precipitation data can be collapsed onto a single scaling curve. Equation (5) tells us that, we can collapse all the aggregate-size distributions $n_s(t)$ obtained for fixed s or t onto a single curve, if we plot $s^\tau n_s(t)$ versus $s/\langle s\rangle$, since the scaling function $f(x)$ is *universal* and does not depend on the details of the system. Thus, if we take $\tau = 2$, the value for DLCC, we obtain

$$s^2 n_s(t) = f(s/\langle s\rangle) \ . \tag{8}$$

On the other hand, if the scaling functions shown in Figures 5, 6, 7 and 9 are written as $Y = h(X)$, where $h(X)$ is the collapsed curve, then the data collapse with $z = 1/4$ and $z' = 2$ implies that

$$R^2 W = h(R/M^{1/4}) \ , \tag{9}$$

which is completely similar to Eq. (8), explains the collapse of the precipitation data onto a single curve and the value $z' = 2$, and indicates that, as we argued above, the asphalt and asphaltene aggregates are of the DLCC type. Of course, the scaling functions $f(x)$ and $h(x)$ are not the same. Comparing Eqs. (8) and (9), one may infer that the *roles* of s and $n_s(t)$ in the dynamic aggregate-size distribution are played by R and W, respectively. It is not unreasonable to infer that the size of the asphalt aggregates may be proportional to the ratio R, and indeed as Figures 1, 3, and 4 indicate with increasing R the amount of precipitation, and thus the size of the aggregates, do increase. As a rough estimate, $W(t)$ is also proportional to $n_s(t)$, the number of clusters or aggregates of size s at time t for *all* $s \geq s_{min}$, where s_{min} is the minimum cluster size for precipitation, since only when a cluster is large enough, it can precipitate; otherwise it will remain suspended in the solution. We expect to have $s_{min} \sim \alpha\langle s\rangle$, where $\alpha > 1$. With these analogies, it becomes clear why the data collapse shown in Figures 5, 6, 7, and 9 is possible.

THE MOLECULAR WEIGHT DISTRIBUTION

Over the years, many authors have studied the MW distribution of asphalts and asphaltenes[40–47]. Most of them measured the average MW of the asphalts and asphaltenes from various oils, and provided some statistics of their measurements, but did not give the MW distribution itself. Trauth *et al.*[47] used a Monte Carlo method to determine the MW distribution. We now present new data for the MW distribution of asphalts and asphaltenes, and based on our results discussed above propose analytical equations to predict them.

We first describe briefly our experimental procedure for determining the MW distribution. The tank oil was diluted by several solvents including n-C_5, n-C_6, and n-C_{10}, and for R =1.5, 4.0, and 10.0 in cm^3 of solvent/gr of the tank oil. The samples were kept in a dark place in an inert gas to prevent oxidation, and they were stirred occasionally for 24 hours. In the next step, the samples were filtered using the Wattman No. 42 filter paper. The filter papers were then washed by excess amount of the solvents. The asphalt that remained on the filter was used for measuring its MW distribution and its average. Two average MWs were determined for the asphalts and asphaltenes. These were the weight-average molecular weight $\langle M_w\rangle$ and the number-average molecular weight $\langle M_n\rangle$. Also determined were the MW distributions using liquid size-exclusion chromatography, or gel permeation chromatography (GPC). The standard ASTM test method D3593–80 for determining the average MWs and the MW distributions of toluene-soluble macromolecules was used.

The GPC instrument consisted of a solvent reservoir, a pump, a sample injection device, 4 packed columns, a solute detector, a flow rate detector, and a recorder. It had 4 different columns filled with Styragel, and nominal exclusion limits of 500, 10^3, 1500, and 10^4Å were used in the measurement process. Each column had a length of 120cm and was 1cm in diameter. The columns of the GPC, at the specified temperature and solvent, were calibrated using the polystyrene standard. The resulting calibration curve was then transformed to give a relationship between the retention volume and the molecular weight M.

The asphalts or asphaltenes were dissolved in toluene at room temperature using a magnetic stirring device. The resulting solution was then injected into the chromatographic column packed with a solid and porous substrate, with a flow rate of 2 ml/min, in order to separate the various molecular aggregates according to their sizes. The concentrations of the separated aggregates were also determined and recorded. By using the MW calibration curve the MW averages and the MW distribution for each experiment were determined.

The MW averages and the MW distributions of the asphalt and asphaltene samples for all the solvents with R =1.5 and 4 were measured 2 weeks after forming the toluene-asphalt (or asphaltene) solutions, while for the solution with R = 10 the measurement were done after 3 weeks. To investigate non-equilibrium effects on the growth of the asphaltene or asphalt aggregates, a separate measurement was carried out for n-C_6 at R = 1.5 after 4 weeks.

Some typical MW distributions of the asphalts obtained with n-C_5 and n-C_{10} are shown in Figures 15 and 16. These distributions are bimodal, and thus consistent with the small-angle scattering data shown in Figure 12, because the existence of the two maxima is a strong indication that there are two different types of asphalt aggregates in the solution. One type are those that are formed by a DLP aggregation, while the other type are those that are formed by a DLCC process. We point out that, in general, the MW

distribution is a time-dependent quantity which evolves as the aggregation of the asphalt and asphaltene particles takes place. Thus, as discussed above, if the solution is aged for a long enough time, then the maximum that is due to the DLP aggregates should disappear, yielding a solution with only DLCC aggregates, and thus a unimodal MW distribution. This is clearly seen in Figure 17, where we show the results for an asphaltene solution obtained with n-C_6 and $R = 1.5$ after 4 weeks. More extensive data for several other solvents will be reported elsewhere[48].

Botet and Jullien[49] studied the cluster-size distribution during aggregation processes, and derived an analytical formula for the *most probable* cluster-size distribution. Suppose that at the beginning of the aggregation process there are N elementary particles, and that there are N_c clusters or aggregates in the system. Botet and Jullien[49] showed that, the most probable cluster-size distribution is given by $Nn_s/N_c^2 \sim f_\omega(N_c s/N)$, where ω is defined by Eq. (2). This equation tells us that $f_\omega(x)$ can be considered as a rescaled or reduced most probable cluster-size distribution. Botet and Jullien[49] also derived the following equation for $f_\omega(x)$

$$f_\omega(x) = cx^{-2\omega} \exp[-(1-2\omega)x] \,, \qquad (10)$$

where c is a renormalization constant obtained from $\int_0^\infty f_\omega(x)dx = 1$. This equation can have a maximum only if $\omega < 0$.

We now convert Eq. (10) to a MW distribution for the asphalt and asphaltene aggregates by assuming that, the MW of an aggregate is proportional to its size. Since the data shown in Figures 15-17 indicate that there can be a minimum molecular weight M_m at which the MW distribution is cutoff, Eq. (10) implies the following equation for the MW distribution for asphalts and asphaltenes:

$$f_\omega(M) = c(M-M_m)^{-2\omega} \exp[-a(M-M_m)] \,, \quad M \geq M_m \,, \qquad (11)$$

where a is a contant. In Eq. (11) we can treat ω as an adjustable parameter, but in what follows we provide evidence that ω may in fact be a *universal* exponent, and thus its value can be fixed. If so, all one has to do is specifying the minimum molecular weight M_m, which can be obtained by a simple measurement, and determining the constant c from the normalization condition. Then, the MW distribution is completely specified. However, Eq. (11) is appropriate if the MW distribution is unimodal, which is the case if the solution is aged for a long enough time. If it is bimodal, then we use the following equation which is a generalization of (11):

$$f_\omega(M) = \sum_{i=1}^{2} c_i(M-M_{mi})^{-2\omega} \exp[-a_i(M-M_{mi})] \,. \qquad (12)$$

In this equation subscripts 1 and 2 refer to the DLP and DLCC parts of the MW distribution, and thus $M_{m1} = 0$. Taken together, there are 6 parameters, which are c_i, a_i, ω, and M_{m2}, and are estimated by fitting the data to Eq. (12). However, for all the cases we found that $\omega \simeq -1/2$, indicating, as mentioned above, that it may be a universal parameter. The resulting fits of the data are also shown in Figures 15–17, and it can be seen that the agreement between the predictions and the data is generally very good. However, the significance of the proposed equations is not in the goodness of the fits, since there are 5 adjustable parameters. It is in the fact that Eqs. (11) and (12) have a firm theoretical foundation.

SUMMARY

In this paper we presented extensive new experimental data for the onset and amount of asphalt and asphaltene precipitation under various conditions and with different solvents, and their molecular weight distributions. We proposed a simple scaling equation that appears to be capable of providing accurate predictions for the precipitation data. Moreover, the scaling equation provides a particularly simple, and apparently universal, prediction for the onset of precipitation. We also analyzed small-angle scattering data for asphalt and asphaltene aggregates in solutions, and proposed the mechanisms that give rise to such aggregates. Based on these findings, we proposed new analytical equations for the MW distribution of the asphalt and asphaltene aggregates, which provide accurate predictions for the new data presented in this paper.

ACKNOWLEDGMENTS

Work at USC was supported in part by the Department of Energy. We would like to thank our past collaborators, especially M. Farhani, A.R. Mehrabi, and M. Nematy.

NOMENCLATURE

d_f, D_f	=	Fractal dimensions
f, h	=	Scaling functions
I	=	Scattering intensity
M	=	Molecular weight
M_m	=	Minimum molecular weight
n_s	=	Aggregate-size distribution
q	=	Scattering vector
R	=	Solvent/oil ratio
s	=	Aggregate size
S_a	=	Aggregate active surface
t	=	Time
W	=	Weight percent of percipitate
X, Y	=	Scaling variables
z, z'	=	Scaling exponents
θ	=	Scattering angle
λ	=	Wavelength
τ	=	Scaling exponent
ω	=	Active surface exponent

REFERENCES

1. Speight, J. G., *The Chemistry and Technology of Petroleum,* Marcel Dekker, New York (1991).
2. MacMillan, D.J., J.E. Tackett Jr., M.A. Jessee, and T.G. Monger-McClure, "A Unified Approach to Asphaltene Precipitation: Laboratory Measurement and Modeling," *JPT* (September 1995) 788.
3. Lichaa, P.M., and L. Herrera, "Electrical and other Effects Related to the Formation and Prevention of Asphaltenes Deposition," *SPE 5304* (1975).
4. Sahimi, M., *Flow and Transport in Porous Media and Fractured Rock,* VCH, Weinheim, Germany (1995).
5. Preckshot, G.W., N.G. DeLisle, C.E. Cottel, and D.L. Katz, "Asphaltic Substances in Crude Oils" *Trans. AIME* (1943) **151**, 188.
6. Katz, D.L., and K.E. Beu, "Nature of Asphaltic Substances," *Ind. Eng. Chem.* (1945) **37**, 195.
7. Dickie, J.P., M.N. Haller, and T.F. Yen, "Electron Microscopic Investigations on the Nature of Petroleum Asphaltics," *J. Colloid Interface Sci.* (1969) **29**, 475.
8. David, A., "Asphaltene Flocculation during Solvent Simulation of Heavy Oils," *AIChE Symposium Series* (1973) **69**, 56.
9. Yen, T.F., "Structure of Petroleum Asphaltene and its Significance," *Energy Sources* (1974) **1**, 447.
10. Koots, J.A., and J.G. Speight, "Relation of Petroleum Resins to Asphaltenes," *Fuels* (1975) **54**, 179.
11. Monger, T.G., "The Impact of Oil Aromaticity on Carbon Dioxide Flooding," *SPE/DOE Paper 12708* (1984).
12. Monger, T.G., and A. Khakoo, "The Phase Behavior of CO_2–Appalacian Oil Systems," *SPE 10269* (1981).
13. Hirschberg, A., L.N.J. deJong, B.A. Schipper, and J.G. Meijer, "Influence of Temperature and Pressure on Asphaltene Flocculation," *SPEJ* (1984) **24**, 283.
14. Monger, T.G., and J.C. Fu, "The Nature of CO_2–Induced Organic Deposition," *SPE 16713* (1987).
15. Boduszynski, M.M., " Composition of Heavy Petroleums. 1. Molecular Weight, Hydrogen Deficiency, and Heteroatom Concentration as a Function of Atmospheric Equivalent Boiling Point up to 1400°F," *Energy & Fuels* (1987) **1**, 2.
16. Lihoreau, C., J. Briant, and R. Tindy, "Influence de la Pression sur la Flocculation des Asphaltenes," *Revue Inst. Francais Pét.* (1967) **22**, 797.
17. Tuttle, R.M., "High-Pour-Point and Asphaltic Crude Oils and Condensates," *JPT* (1983) **35**, 1192.
18. Ravi-Kumar, V.S., T.T. Tsotsis, M. Sahimi, and I.A. Webster, "Studies of Transport of Asphaltenes Through Porous Membranes: Statistical Structural Models and Continuum Hydrodynamic Theories," *Chem. Eng. Sci.* (1994) **49**, 5789.
19. Rassamdana, H., B. Dabir, M. Nematy, M. Farhani, and M. Sahimi, "Asphalt Flocculation and Deposition: I. The Onset of Precipitation," *AIChE J.* (1996) **42**, 10.
20. Kokal, S.L., J. Najman, S.G. Sayegh, and A.E. George, "Measurement and Correlation of Asphaltene Precipitation from Heavy Oil by Gas Injection," *J. Can. Pet. Tech.* (1992) **31**, 24.
21. Burke, N.E., R.D. Hobbs, and S.F. Kashou, "Measurement and Modeling of Asphaltene Precipitation," *JPT* (Nov. 1990) 1440.
22. Kawanaka, S., S.J. Park, and G.A. Mansoori, "Organic Deposition from Reservoir Fluids: A Thermodynamic Predictive Technique," *SPE Reservoir Eng.* (1991) **6**, 185.
23. Hotier, G., and M. Robin, "Action de Divers Diluants sur les Produits Pétroliers Lourds: Mesure, Interprétation et Prévision de la Flocculation des Asphaltènes," *Rev. Institut Francais du Pet.* (1983) **38**, 101.
24. Witten, T.A., and L.M. Sander, "Diffusion-Limited Aggregation, a Kinetic Critical Phenomenon," *Phys. Rev. Lett.* (1981) **47**, 1400.
25. Meakin, P., "Formation of Fractal Clusters and Networks by Irreversible Diffusion-Limited Aggregation," *Phys. Rev. Lett.* (1983) **51**, 1119.
26. Kolb, M., R. Botet, and R. Jullien, "Scaling of Kinetically Growing Clusters," *Phys. Rev. Lett.* (1983) **51**, 1123.
27. Schaefer, D.W., J.E. Martin, P. Wiltzuis, and D.S. Cannel, "Fractal Geometry of Colloidal Aggregates," *Phys. Rev. Lett.* (1984) **52**, 2371.
28. Vicsek, T., and F. Family, "Dynamic Scaling for Aggregation of Clusters," *Phys. Rev. Lett.* (1984) **52**, 1669.
29. Bouchaud, E., M. Delsanti, M. Adam, M. Daoud, and M. Durand, "Gelation and Percolation: Swelling Effect," *J. Physique* (1986) **47**, 1273.
30. Sheu, E.Y., K.S. Liang, S.K. Sinha, and R.E. Overfield, "Polydispersity Analysis of Asphaltene Solutions in Toluene," *J. Colloid Interface Sci.* (1992) **153**, 399.

31. Herzog, P., D. Tchoubar, and D. Espinat, "Macrostructure of Asphaltene Dispersions by Small-Angle X-Ray Scattering," *Fuel* (1988) **67**, 245.

32. Rassamdana, H., and M. Sahimi, "Asphalt Flocculation and Deposition: II. Kinetic Growth and Formation of Fractal Aggregates," *AIChE J.* (1996) (in press).

33. Toulhoat, H., C. Prayer, and G. Rouquet, "Characterization by Atomic Force Microscopy of Adsorbed Asphaltenes," *Colloid. Surf.* (1994) **91**, 267.

34. Carnahan, N.F., *et al.*, "A Small Sngle X-ray Scattering Study of the Effect of Pressure on the Aggregation of Asphaltene Fractions in Petroleum Fluids under Near-Critical Solvent Conditions," *Langmuir* (1993) **9**, 2035.

35. Park, S.J., and G.A. Mansoori, "Aggregation and Deposition of Heavy Organics into Petroleum Crudes," *Energy Sources* (1988) **10**, 109.

36. Crickmore, P.J., and C. Hruska, "Fractal Geometry, the Korčak Law and Asphaltene Precipitation," *Fuel* (1989) **68**, 1488.

37. Lin, J.-R., H. Lian, K.M. Sadeghi, and T.F. Yen, "Asphalt Colloidal Types Differentiation by Korcak Distribution," *Fuel* (1991) **70**, 1439.

38. Raghunathan, P., "Evidence for Fractal Dimension in Asphalt Polymers from Electron-Spin-Relaxation Measurements," *Chem. Phys. Lett.* (1991) **182**, 331.

39. Liu, Y.C., E.Y. Sheu, S.H. Chen, and D.A. Storm, "Fractal Structure of Asphalt in Toluene," *Fuel* (1995) **74**, 1352.

40. Dickie, J.P., and T.F. Yen, "Macrostructure of the Asphaltic Fractions by Various Instrumental Methods," *Anal. Chem.* (1967) **39**, 1847.

41. Moschopedis, S.E., J.F. Fryer, and J.G. Speight, "Investigation of Asphaltene Molecular Weights," *Fuel* (1976) **55**, 227.

42. Speight, J.G., D.L. Wernick, K.A. Gould, R.E. Overfield, B.M.L. Rao, and D.W. Savage, "Molecular Weight and Association of Asphaltenes: A Critical Review," *Rev. Institut Francais Pet.* (1985) **40**, 52.

43. Boduszynski, M.M., "Composition of Heavy Petroleums. 2. Molecular Characterization," *Energy & Fuels* (1988) **2**, 597.

44. Acevedo, S., G. Escobar, L. Gutiérrez, and H. Rivas, "Isolation and Characterization of Natural Surfactants from extra Heavy Crude Oils, Asphaltenes and Maltenes," *Fuel* (1992) **71**, 619.

45. Strausz, O.P., T.W. Mojelsky, and E.M. Lown, "The Molecular Structure of Asphaltene: An Unfolding Story," *Fuel* (1992) **71**, 1355.

46. Taylor, S.E., "Use of Surface Tension Measurements to Evaluate Aggregation of Asphaltenes in Organic Solvents," *Fuel* (1992) **71**, 1338.

47. Trauth, D.M., S.M. Stark, T.F. Petti, M. Neurock, and M.T. Klein, "Representation of the Molecular Structure of Petroleum Resid through Characterization and Monte Carlo Modeling," *Energy & Fuels* (1994) **8**, 576.

48. Dabir, B., M. Nematy, A.R. Mehrabi, H. Rassamdana, and M. Sahimi, "Asphalt Flocculation and Deposition: III. The Molecular Weight Distribution," *Fuel* (to be published).

49. Botet, R., and R. Jullien, "Size Distribution of Clusters in Irreversible Kinetic Aggregation," *J. Phys. A* (1984) **17**, 2517.

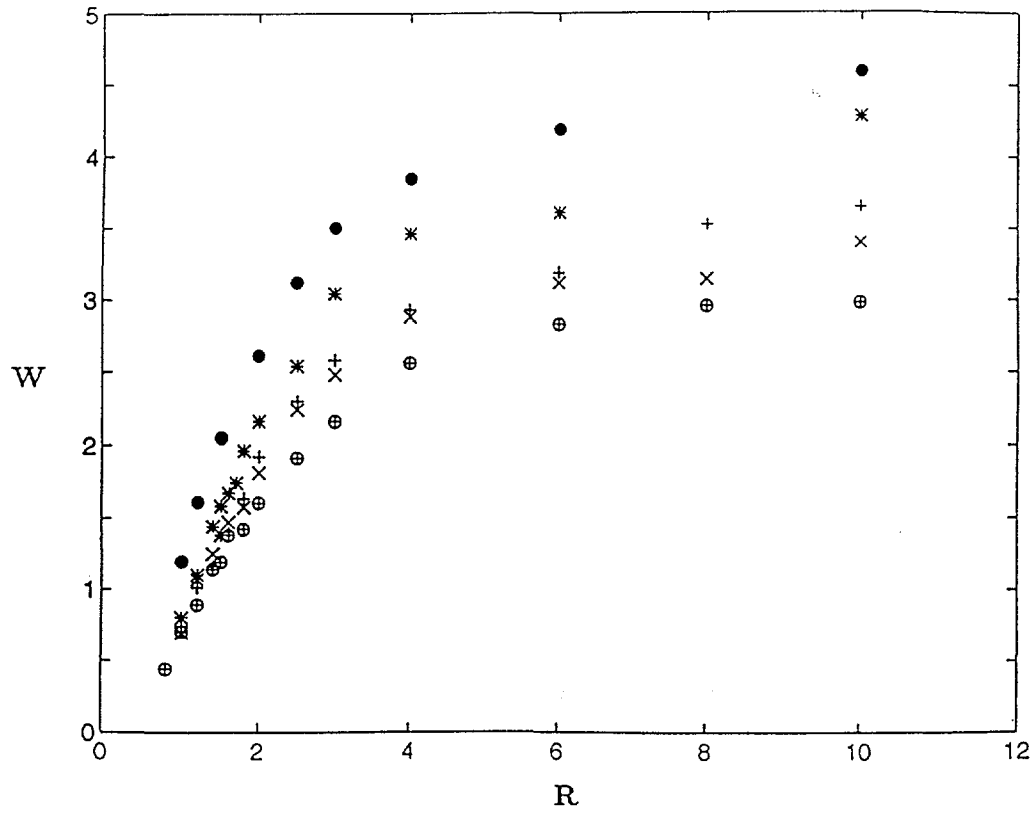

Figure 1. Experimental data for the weight percent W of precipitated asphalt as a function of the solvent/oil ratio R (in cm^3/gr). The results are, from top to bottom, for n-C_5, n-C_6, n-C_7, n-C_8, and n-C_{10} as the solvent.

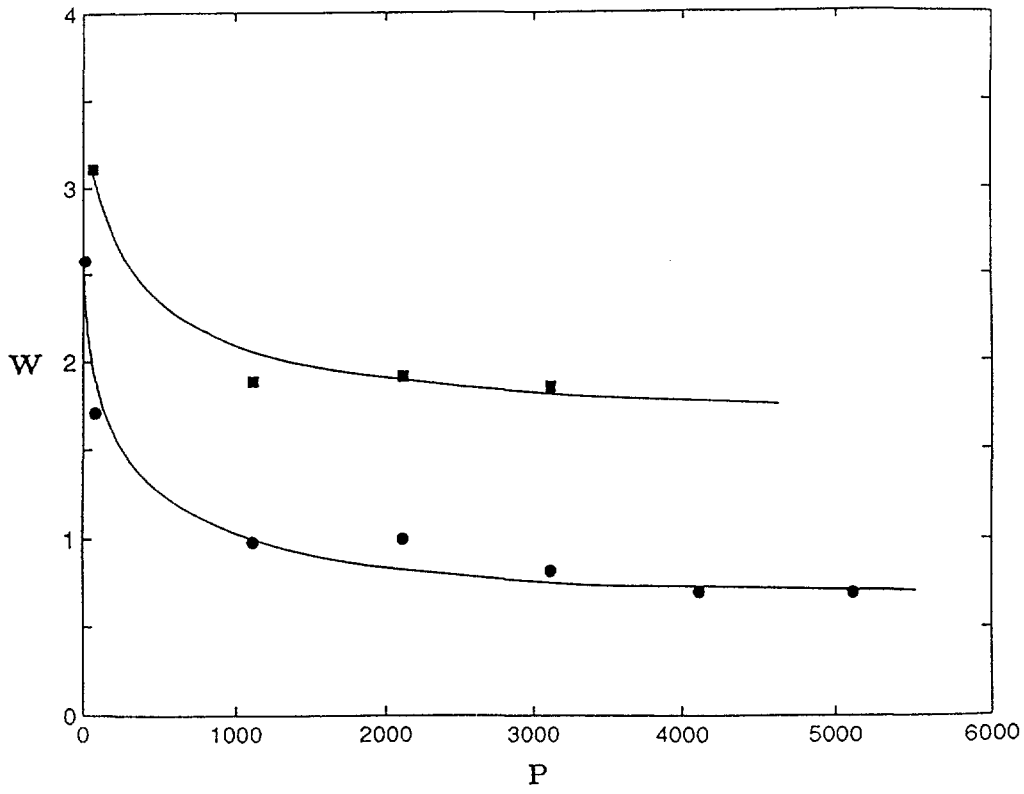

Figure 2. The weight percent W of precipitated asphalt as a function of the pressure P (in psia) at $T = 23°C$ and solvent/oil ratio $R = 3$ with n-C_6 (squares) and n-C_7 (circles) as the solvent.

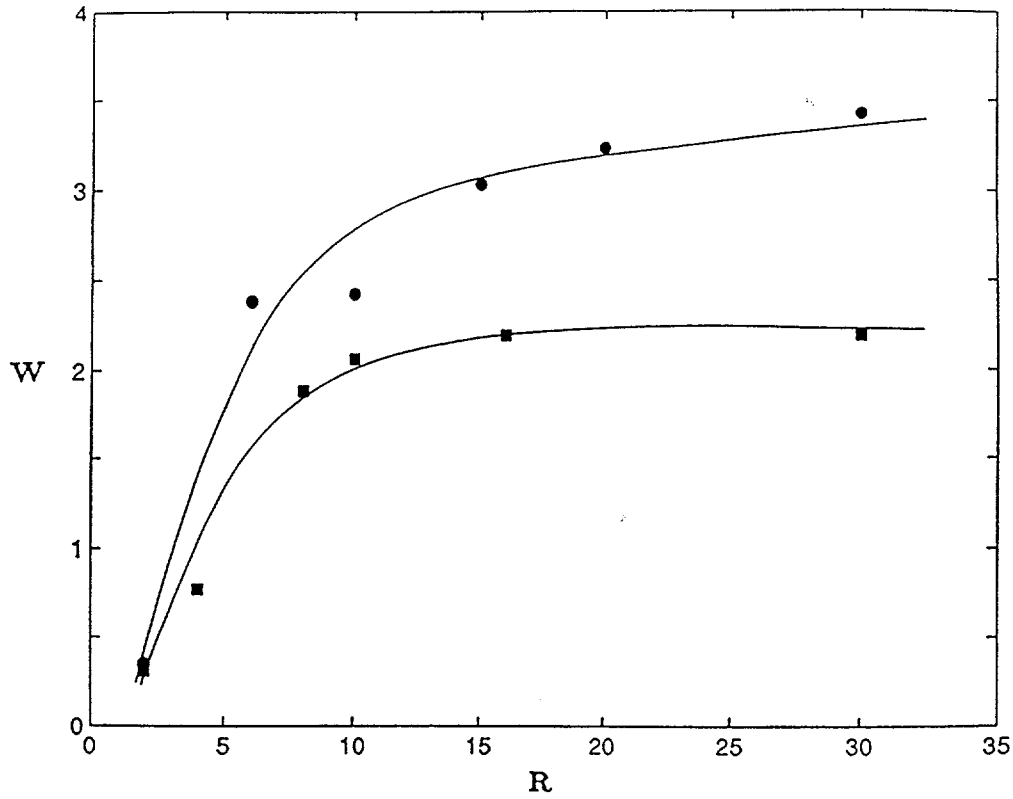

Figure 3. The weight percent W of precipitated asphaltene as a function of R with n-C_6 (circles) and n-C_7 (squares) as the solvent, at $T = 8°C$.

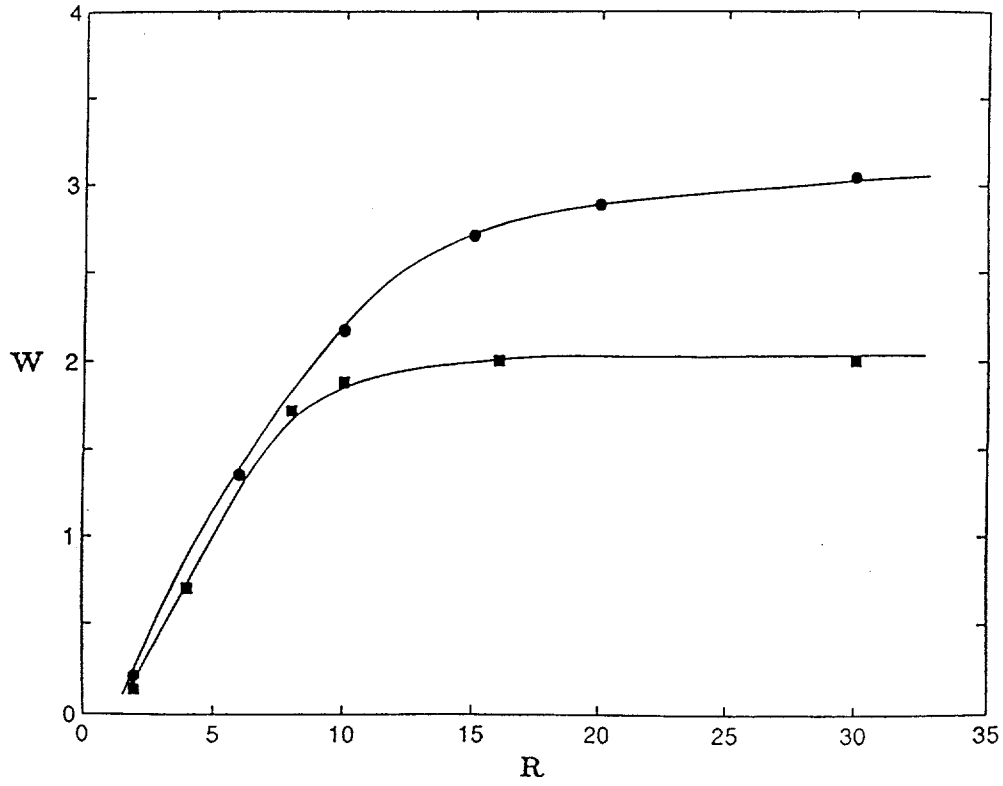

Figure 4. The same as in Figure 3, but at $T = 19°C$.

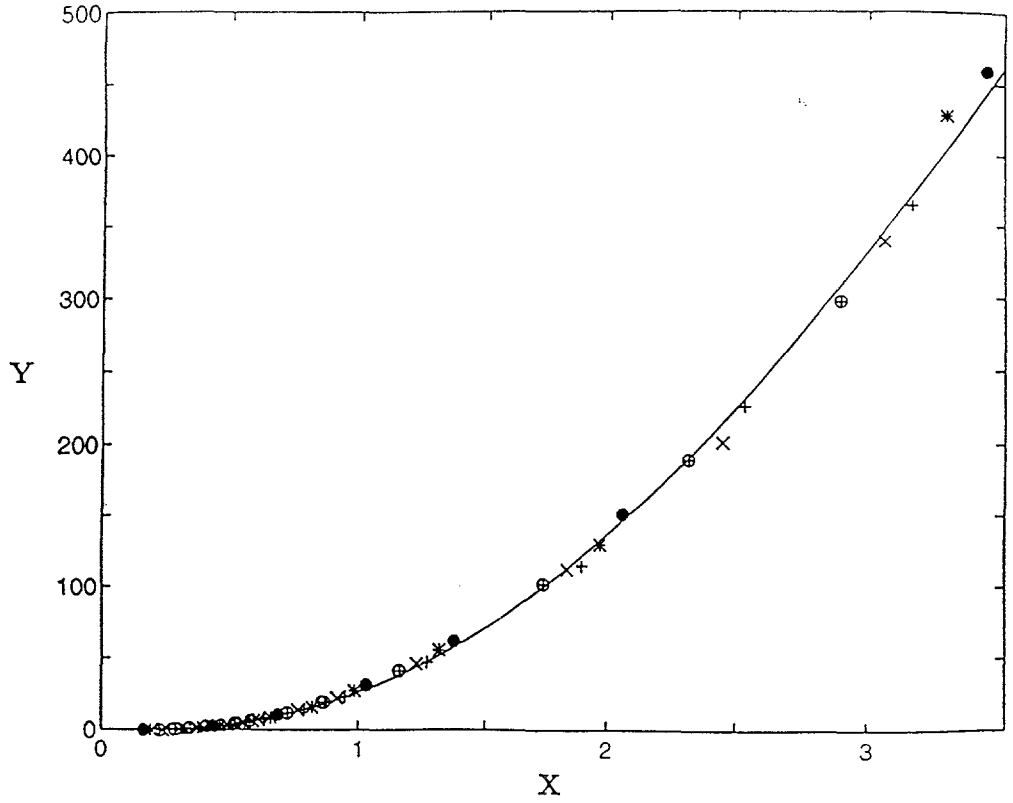

Figure 5. The collapse of the data shown in Figure 1 with $X = R/M^{1/4}$ and $Y = WR^2$.

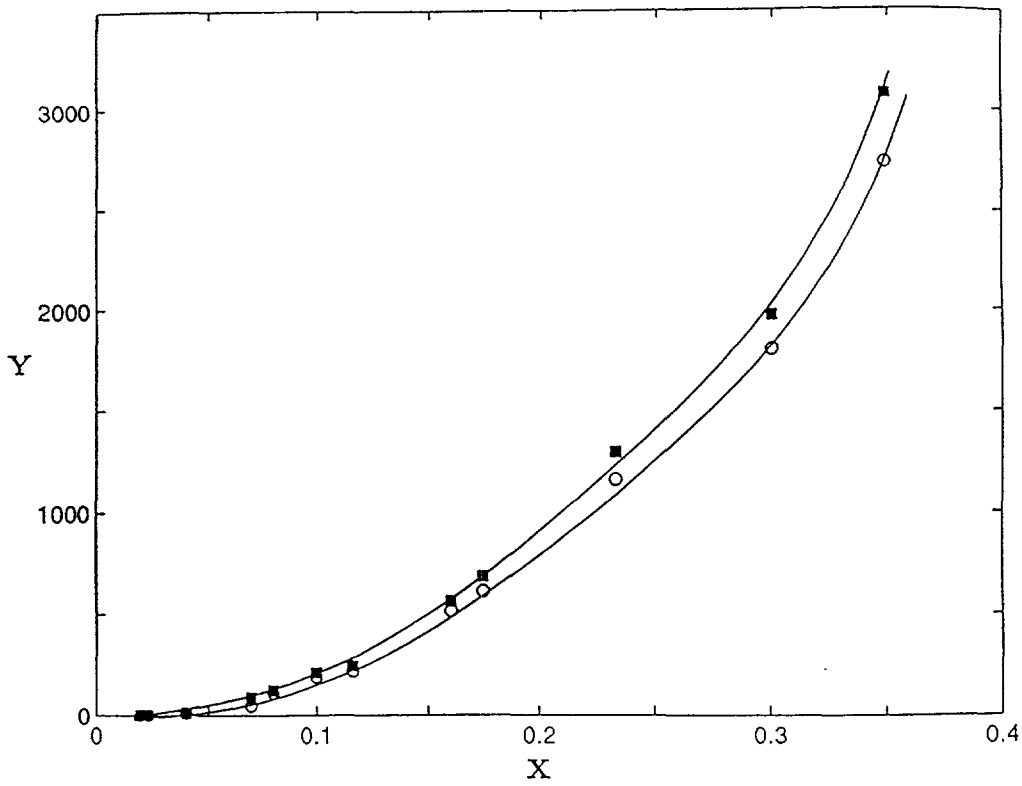

Figure 6. The collapse of the data shown in Figures 3 and 4 for $T = 8°C$ (squares) and $T = 19°C$ (circles).

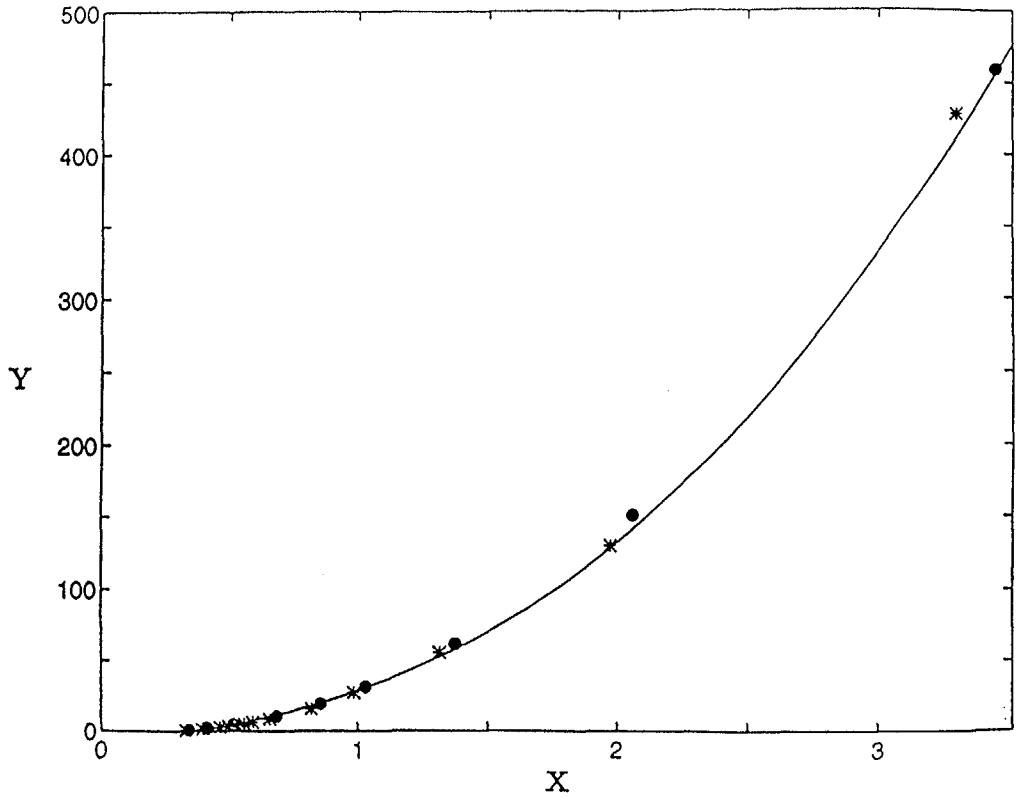

Figure 7. The collapse of the precipitation data for n-C_5 and n-C_{10} (see Figure 1).

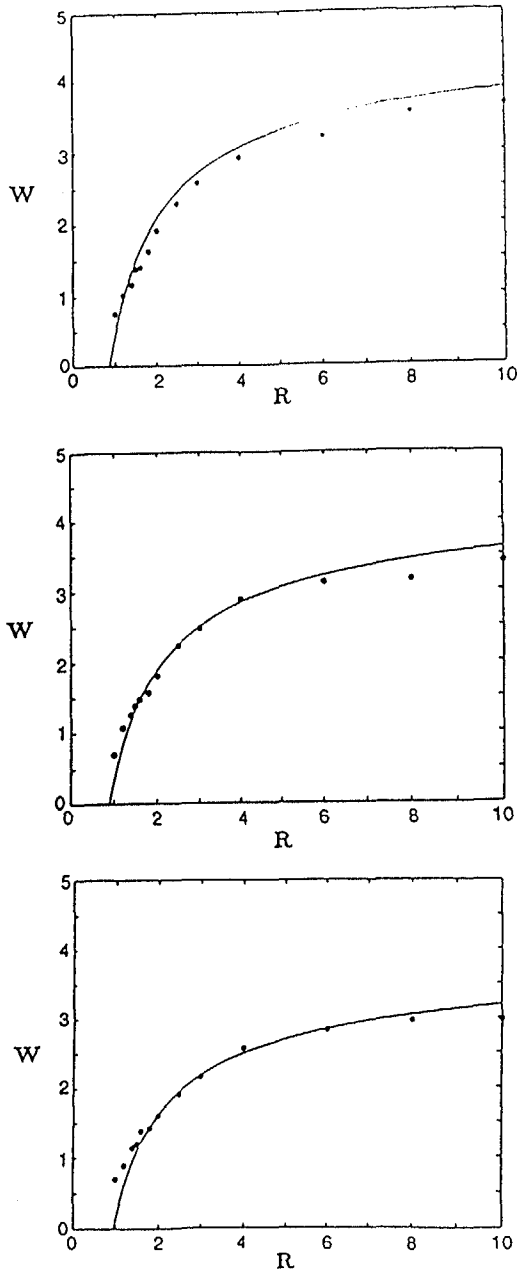

Figure 8. Comparison of the experimental data (symbols) and the predicted (curves) weight percent W of precipitated asphalt, as a function of the solvent/oil ratio R, using the scaling curve shown in Figure 7. The results are, from top to bottom, for n-C_7, n-C_8, and n-C_{10} as the solvent.

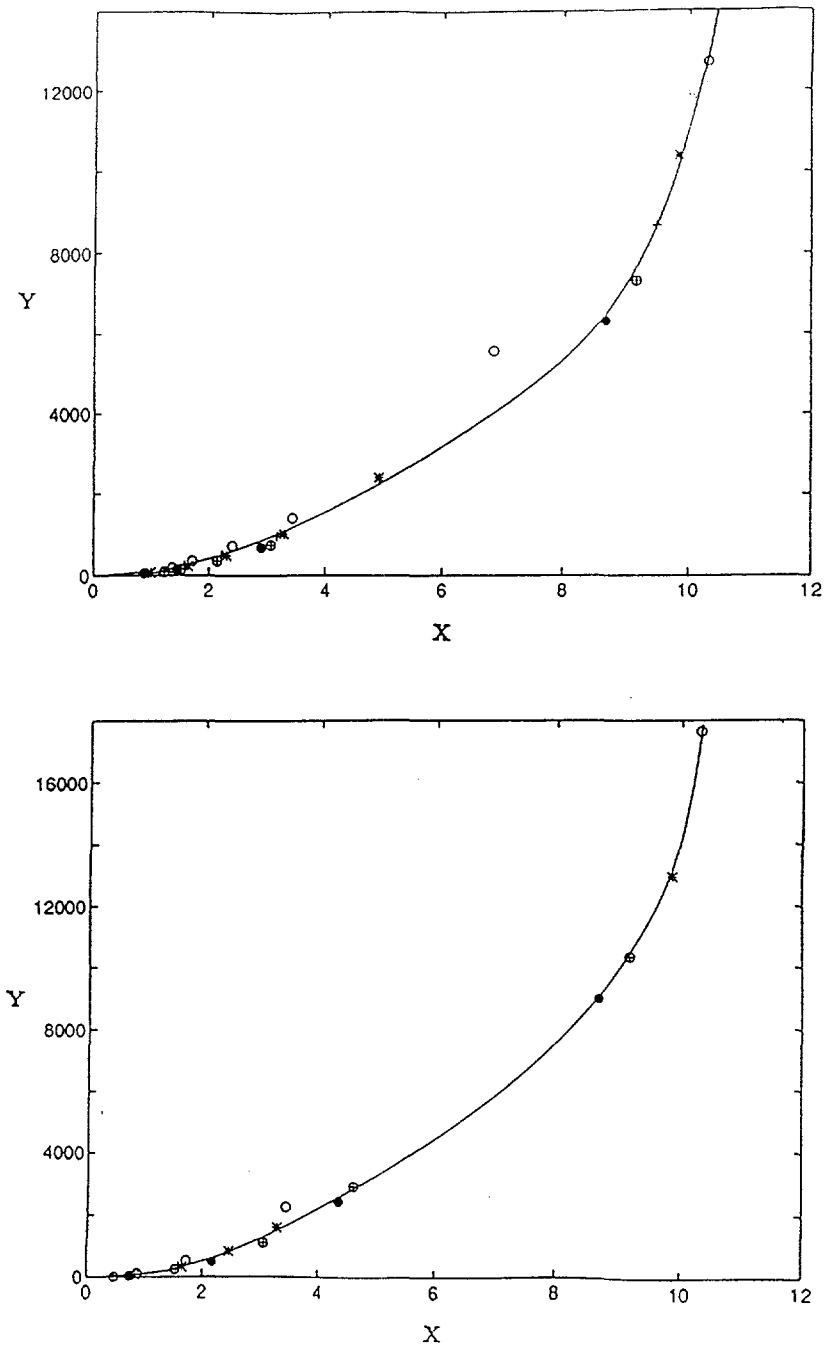

Figure 9. The collapse of the precipitation data of Kokal *et al.*[20] onto scaling curves for Suffield (top) and Lindberg (bottom) heavy oils.

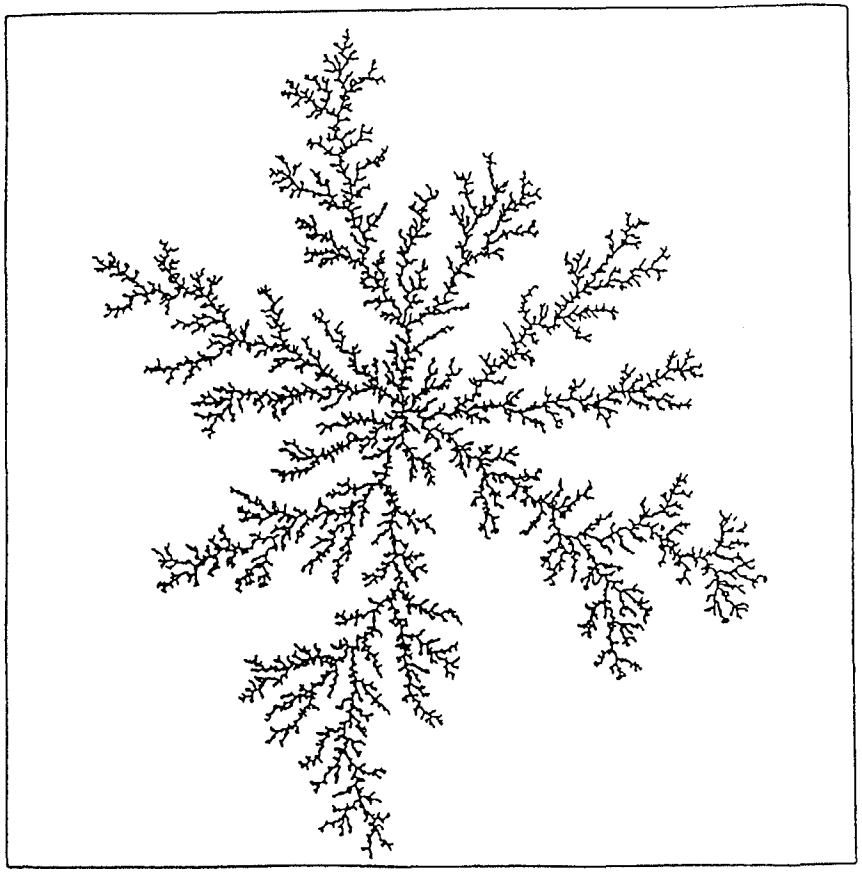

Figure 10. A typical two-dimensional diffusion-limited particle aggregate.

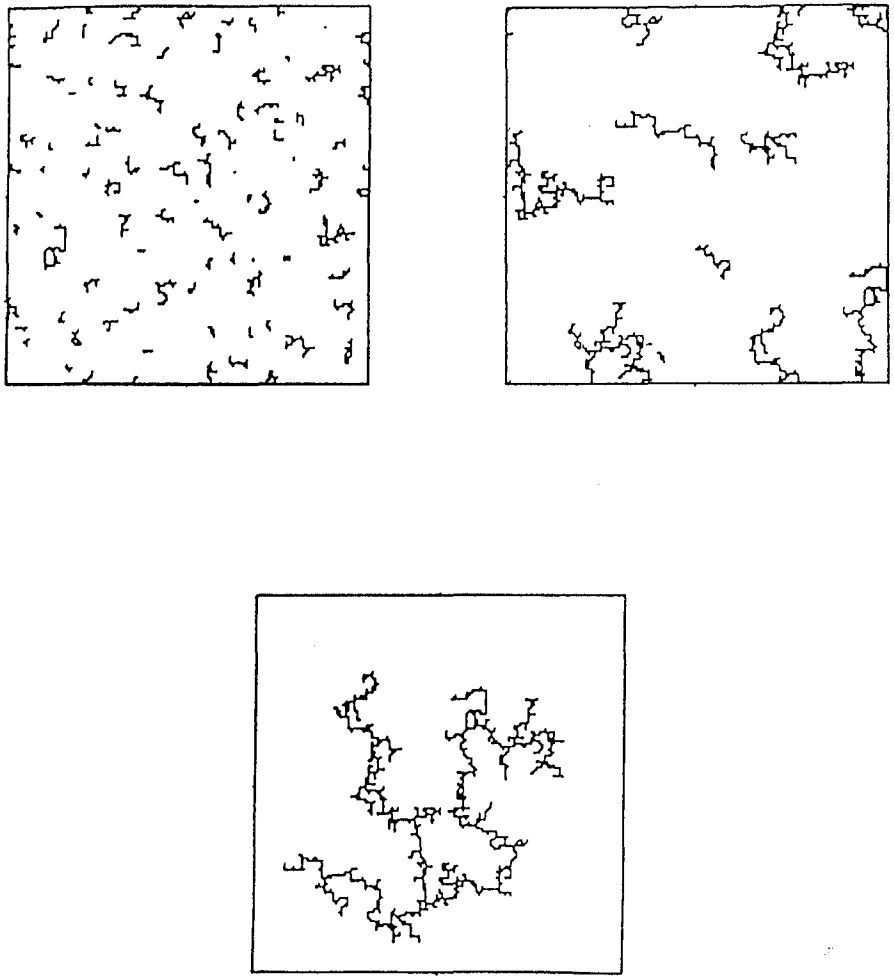

Figure 11. Three stages of the growth of a two-dimensional diffusion-limited cluster-cluster aggregate.

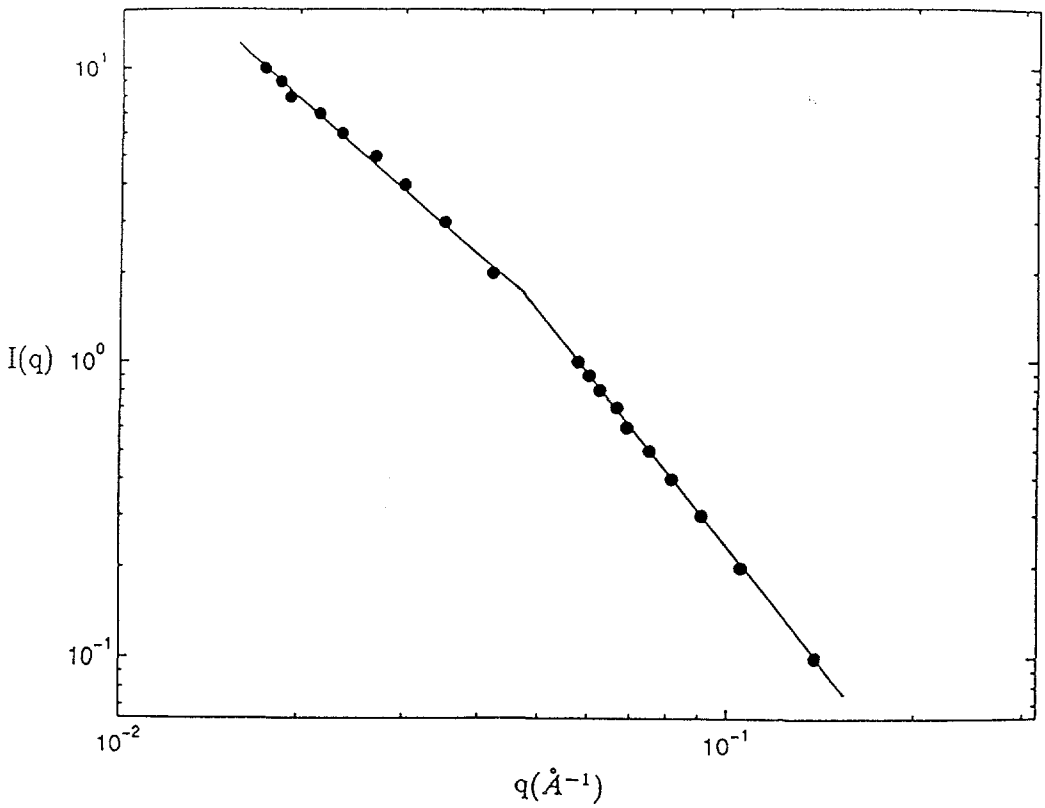

Figure 12. The SANS intensity $I(q)$ versus the scattering vector q at $P = 1$ atm.

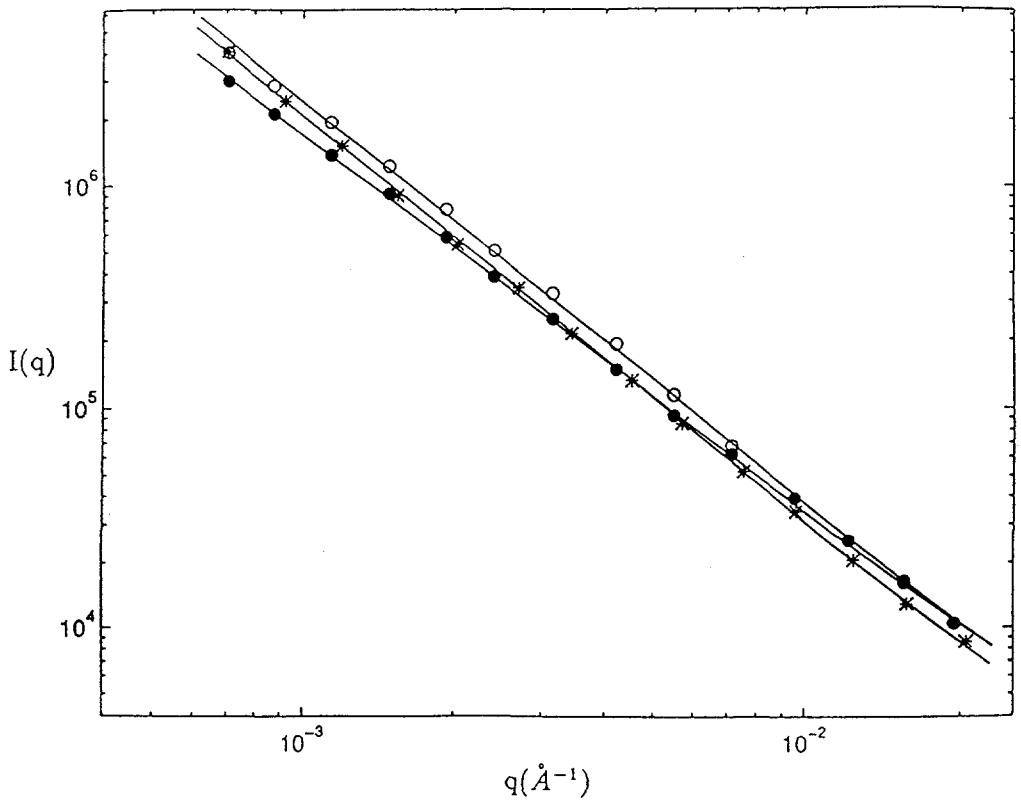

Figure 13. The SAXS intensity $I(q)$ versus the scattering vector q for three different oils at $P = 1$ atm.

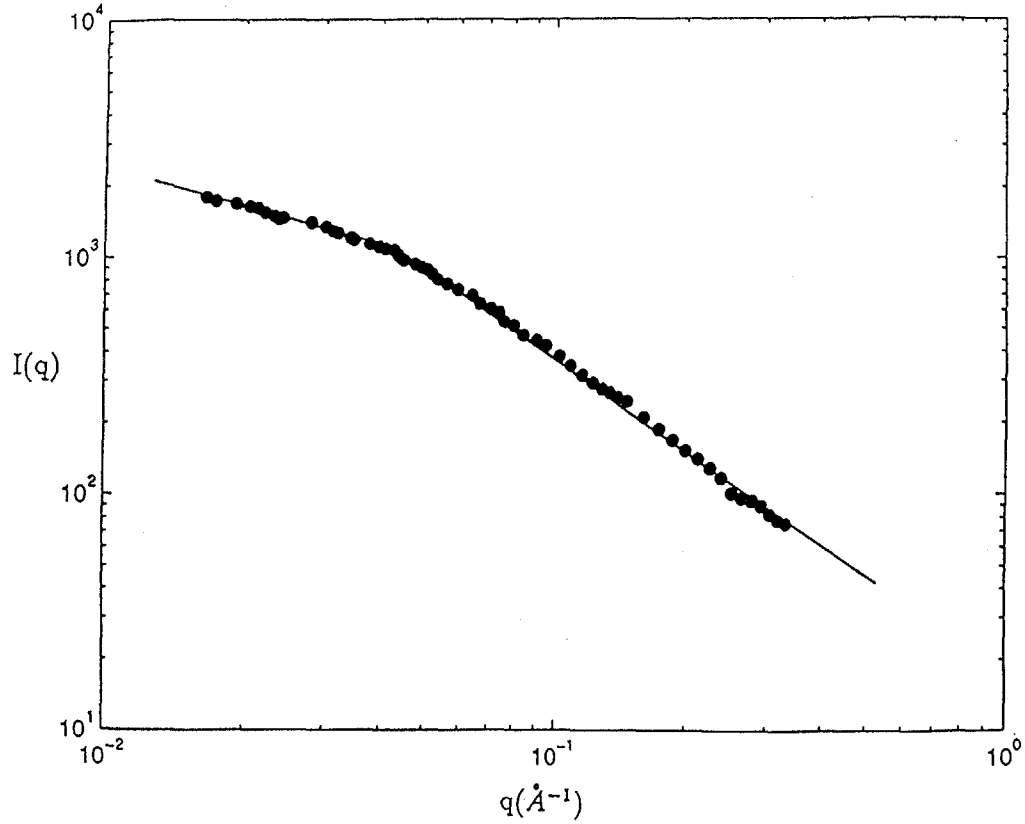

Figure 14. The SAXS intensity $I(q)$ versus the scattering vector q at $P = 400$ atm and $T = 25°C$.

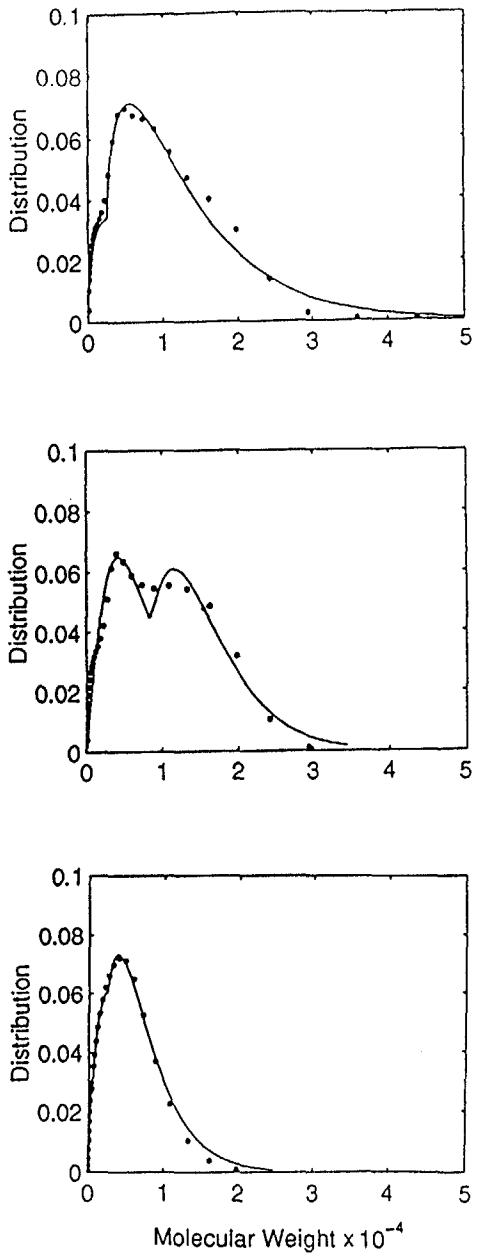

Figure 15. The molecular weight distributions of the asphalts obtained with n-C_5 as the solvent for $R = 1.5$ cm^3/gr (top), 4 (middle), and 10 (bottom).

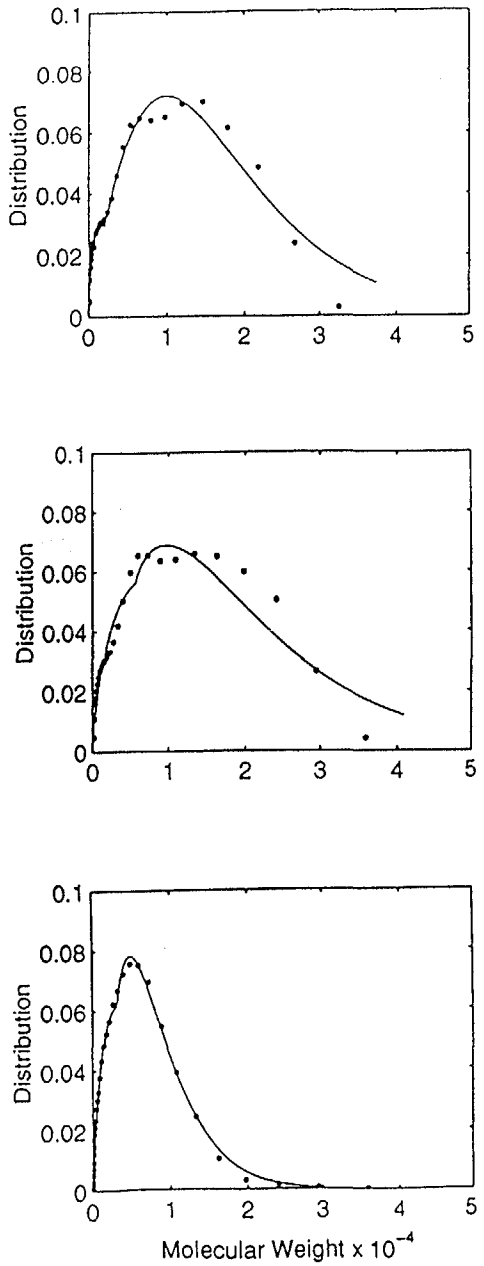

Figure 16. The same as in Figure 15, but with n-C_{10} as the solvent.

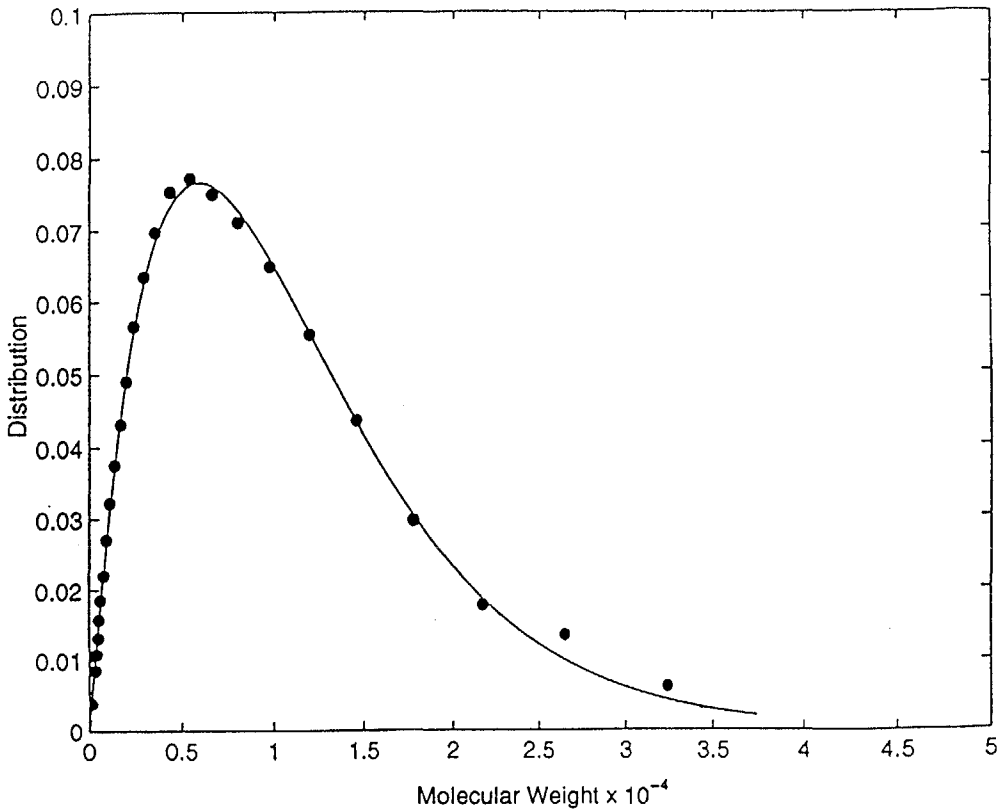

Figure 17. The molecular weight distribution of the asphaltene obtained with n-C_6 as the solvent and solvent/oil ratio $R = 1.5$ cm^3/gr, obtained after 4 weeks.

Theoretical and Experimental Investigations of Asphaltene Transport through Membranes

V. S. Ravi-Kumar, Theodore T. Tsotsis*, Muhammad Sahimi and Ian. A. Webster[1]

Department of Chemical Engineering
University of Southern California
Los Angeles, CA 90089-1211
and
[1]Unocal Corporation
1201 West 5th Street
Los Angeles, CA 90051

ABSTRACT

We present here an overview of our experimental and theoretical studies of asphaltene transport through membranes. Statistical Monte-Carlo models are utilized to model the structure of asphaltene molecules, and continuum hydrodynamic theory is used to calculate their transport coefficients.

INTRODUCTION

Due to the relative abundance of heavy crudes and the ongoing research activities in coal liquefaction and coal-liquid upgrading, the need to study the structure, reactivity and transport properties of heavy oils is ever increasing. Asphaltenes, which are a major component of heavy oils, create difficulties during upgrading. To increase the efficiency of the hydrotreating of heavy oils it would be helpful to have a better understanding of the asphaltene structure and the mechanism of asphaltene diffusion through restricted porous systems.

Membranes offer a number of advantages in fundamental investigations of transport and reaction. Microporous polymeric, mica and anodic membranes have straight, non-intersecting and fairly uniform pores; this eliminates the need for describing the tortuosity and the porous media topology. Sol-gel membranes with their fairly unimodal pore size distributions represent an intermediate step in the knowledge tree leading to a better understanding of the transport phenomena occuring in real catalyst systems. Inorganic membranes, in particular,

offer the oppurtunity for fundamental transport and reaction investigations at realistic process conditions (Nourbaksh *et al.*, 1990; Nourbaksh, 1991). These membranes, furthermore, show good potential for novel reactor applications in this area (Ravi-Kumar, 1995).

Several reviews on asphaltene structure have already been published (Yen, 1990; Speight, 1991; Sane *et al.*, 1994). A broadly accepted model for the asphaltenes molecular structure is beginning to emerge from these studies. Asphaltene molecules (particles) are thought to be stacked layers of condensed heterocyclic aromatic sheets with attached alkyl chains restricted to the plane of the sheet, typically 8.5-15Å in diameter. These particles are about 16-20Å in height. In asphaltenes the association and clustering do not stop at the particle level. Several molecular weight distribution studies have shown the presence of components (called "micelles" in the asphaltene literature) of very large molecular weight, which are thought to result from the agglomeration of individual particles. The clustering of the particles is affected by concentration and temperature. An important contribution in this area is by Klein and coworkers (Savage and Klein, 1989; Trauth *et al.*, 1994). They have taken the vast knowledge about the chemical structure of asphaltenes and have succeeded to instill in it a degree of mathematical formalism. They have developed numerical techniques which can be used to model representative molecular structures of asphaltenes and resids. Their work has significantly influenced our own studies in this field.

Considerably fewer studies have dealt with the subject of asphaltene transport through porous catalysts and membranes. In one of the earliest studies Thrash and Pildes (1981) studied the transport of asphaltenes through mica membranes. Shimura *et al.* (1982) studied asphaltene diffusion in porous catalysts by uptake-type experiments. A more detailed study of asphaltene transport was done by Baltus (1984) and Baltus and Anderson (1983, 1984), who used a Wicke-Kallenbach-type diffusion cell to measure the diffusivity, through mica membranes, of asphaltenes derived from Kuwaiti atmospheric bottoms. Their studies have been continued (Kyriakou *et al.*, 1988; Nortz *et al.*, 1990) with various fractionated samples of heavy oils using polycarbonate membranes and Taylor-dispersion-type experiments. Using models developed by Garcia de la Torre and Bloomfield (1978), Baltus and coworkers have also attempted to model the asphaltene structure as assemblages of interconnected spheres (Nortz *et al.*, 1990). Mieville *et al.* (1989) measured the diffusion of asphaltenes, by

uptake type experiments, through catalysts with both unimodal and bimodal pore size distributions. Hondo asphaltene was found to have the highest diffusivity, which was attributed to its smaller average aromatic cluster. Our group has also studied experimentally the transport of asphaltene for a number of years (Sane *et al.*, 1988, 1992, 1994). In our studies we have utilized model membranes which, as already pointed out, offer a number of advantages when it comes to fundamental investigations of transport and reaction.

Before describing our model of asphaltene diffusion, we first briefly review some of our experimental results. Further details are outlined in our prior publications (Sane, 1990; Sane *et al.*, 1988, 1992, 1994; Ravi-Kumar *et al.*, 1994).

EXPERIMENTAL

Most of our experiments desribed here were carried out in a stainless steel Wicke-Kallenbach-type diffusion cell (Sane, 1990) consisting of two half-cells separated by the microporous membrane, each equipped with an externally driven rotor shaft for good mixing to eliminate external mass transfer limitations. The temperature of each half-cell was individually controlled. During the experiments, samples were withdrawn from the high (HCS) and low concentration cell sides (LCS) and analyzed.

As outlined in the introduction, asphaltenes are thought to be mixtures of many compounds with a broad molecular weight (MW) distribution. The polydisperse nature of asphaltenes has implications for their transport. It implies, for example, (a fact overlooked until recently (Sane *et al.*, 1988)) that one cannot define a unique, time-independent effective diffusivity. Size exclusion chromatography (SEC) is a technique that can be used to study polydisperse compounds like asphaltenes. Using SEC, we have observed that the asphaltene in the LCS has initially different elution characteristics than the asphaltene in the HCS, but eventually approaches the behavior in the HCS. Furthermore, asphaltene components with nominal sizes exceeding those of the membrane pores diffuse across the membrane. This is consistent with the "dynamic nature" of the asphaltene molecule, which imparts on it the ability to generate itself from its fragments.

This dynamic nature of asphaltenes manifests itself in the effects of temperature and concentration on their transport properties. The measured activation energies for diffusion, for example, are typical of the association energies for individual asphaltene sheets and increase with decreasing pore size. Asphaltene

diffusivity also depends on initial HCS concentration, decreasing with increasing asphaltene concentration. The manner the concentration of metals and other heteroatoms change with time in the LCS and HCS during diffusion is an indicator of the relative abundance of these species in the asphaltene components during reaction and transport, and provides insight into the structural aspects of importance in asphaltene upgrading. The data (Sane *et al.* 1988,1992,1994; Sane, 1990) are again consistent with the overall asphaltene picture emerging from the structural investigations.

A MODEL OF ASPHALTENE DIFFUSION

There are a number of broad conceptual literature models of the asphaltene structure in the literature. A model which is consistent with both their tranport measurements and with the literature on their detailed chemistry and structure is, however, currently missing. In this paper we present such a model. The model uses Monte-Carlo techniques to describe the asphaltene structure and continuum hydrodynamic theory to describe the hindered diffusion. The model presently does not explicitly account for the agglomeration/delamination phenomena which characterize the dynamic nature of asphaltene molecules. The omission is deliberate since little concrete is known in this area (work is currently in progress in our group). The technique for generating the asphaltene structure is based on the mathematical formalism of Klein and coworkers (Savage and Klein, 1989; Trauth *et al.*, 1994). It requires knowledge of the probability distribution functions for the number of sheets in the asphaltene particles, the aromatic and saturated rings in each sheet and the number/length of paraffinic chains. Experimental techniques for identifying all these structural elements are available. For a given asphaltene, however, the approach requires a lot of resources and is time consuming. An alternate approach utilizing iterative stochastic modelling to determine the structural element probability distribution functions based on measured macroscopic properties like average MW, density, viscosity, etc. is gaining appeal.

In our studies, the structural element probability distributions of number of unit sheets, aromatic and saturated rings, and the length of alkyl chains were assumed to be 2-parameter log-normal distribution functions. Once these functions are defined, the program then determines the number of unit sheets in every asphaltene particle and the aromatic rings and saturated rings in every sheet. The rings in each sheet are stochastically arranged in a peri-condensed manner (packed as closely as possible). The peripheral rings are then arranged

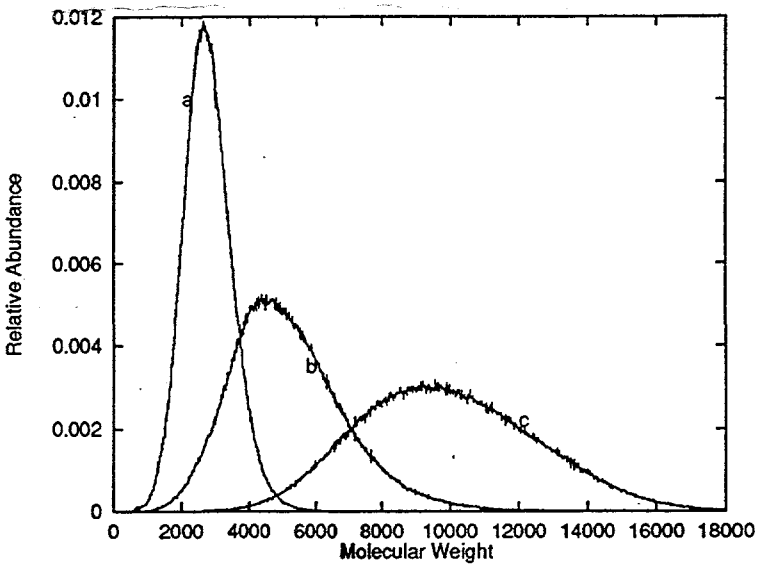

Figure 1: Molecular weight distributions of asphaltenes. a-Mean=0.90, b-Mean=3.58, c-Mean=7.16.

randomly so that the condensation index is close to the value of 0.8 reported by Savage and Klein (1989). The number of peripheral carbons and the number of peripheral carbons that can be substituted with aliphatic chains are then calculated. The peripheral carbons are randomly substituted with alkyl chains, whose lengths are determined from the cumulative distributions. The MW of each particle is calculated from the number of carbons and hydrogens in each molecule. Further details about the technique for generating the asphaltene structure can be found elsewhere (Ravi-Kumar *et al.*, 1994). Fig. 1, for example, shows the MW distribution of a number of generated asphaltenes. In this figure we vary the mean of the probability distribution for the number of sheets while maintaining the mean and standard deviation of the other probability distribution functions constant.

Calculation of the transport coefficients

We have used a continuum hydrodynamic theory to simulate the hindered resistance to the transport of asphaltenes (Deen, 1987). The transport coefficients of the asphaltene molecules are calculated by assuming that the molecules are rigid, neutrally buoyant and uncharged particles and the solvent is a contin-

uum. The porous membrane is assumed to consist of non-intersecting, straight, chemically inert, cylindrical pores. The diffusivity of the molecule through a pore is reduced as a result of the partitioning of the particles between the bulk phase and the porous medium, and as a consequence of the steric hindrance and the hydrodynamic viscous drag resistance due to the walls. The partitioning is described by the partition coefficient Φ, and the steric hindrance and hydrodynamic resistance by the hydrodynamic viscous drag coefficient K_d. The diffusivity through the pore, i.e., D_p is given as

$$D_p = D_\infty \Phi K_d \quad , \tag{1}$$

where D_∞ is the bulk diffusivity value. For the calculation of Φ and K_d the asphaltene particles have been approximated as spheroids.

The partition coefficient Φ, defined as the equilibrium ratio of the solute concentration in the pores to that in the bulk solution, is calculated using the corrected (Limbach *et al.*, 1989) statistical mechanics formulas of Giddings *et al.* (1968). For an axisymmetrically shaped particle Φ can be calculated as the fraction of the orientationally averaged pore volume accesible to the center of the molecule.

The averaged hydrodynamic viscous drag coefficient (K_d) is affected by steric and hydrodynamic viscous drag effects due to the presence of the pore wall. For nonspherical rigid molecules (with dimensions Λ) in cylindrical pores, K_d can be expressed (Anderson and Quinn, 1974) as an integral of the normalized hydrodynamic viscous drag coefficient $K_U(\Lambda, \beta, \Theta)$ over all radial positions β and all orientations Θ

$$K_d(\Lambda) = \frac{\int_\Theta \int_0^{\bar{\beta}(\Lambda,\Theta)} \beta K_U^{-1}(\Lambda, \beta, \Theta) d\beta d\Theta}{\int_\Theta \int_0^{\bar{\beta}(\Lambda,\Theta)} \beta d\beta d\Theta} \quad . \tag{2}$$

$\bar{\beta}(\Lambda, \Theta)$ is the radial position where the molecule first touches the pore wall for any given orientation. $K_U(\Lambda, \beta, \Theta)$ can be calculated by solving the Stokeś equation of motion and the equation of continuity, assuming a creeping flow of a Newtonian and incompressible viscous fluid.

Boundary-element methods (Tullock, 1992) can, in principle, be used for finding the solution of these equations, but the calculations are computationally intensive. The rigorous analytical calculation of $K_U(\Lambda, \beta, \Theta)$ for all β and Θ is also formidable for non-spherical particles. We have utilized here the centerline approximation (Deen, 1987; Anderson and Quinn, 1974), by assuming that

ecting, straight,
ecule through a
etween the bulk
c hindrance and
he partitioning
drance and hy-
ficient K_d. The

(1)

Φ and K_d the

o of the solute
lated using the
of Giddings *et*
lculated as the
o the center of

is affected by
ıce of the pore
lindrical pores,
of the normal-
adial positions

(2)

the pore wall
ing the Stokeś
eeping flow of

:, be used for
computation-
or all β and Θ
re the center-
ssuming that

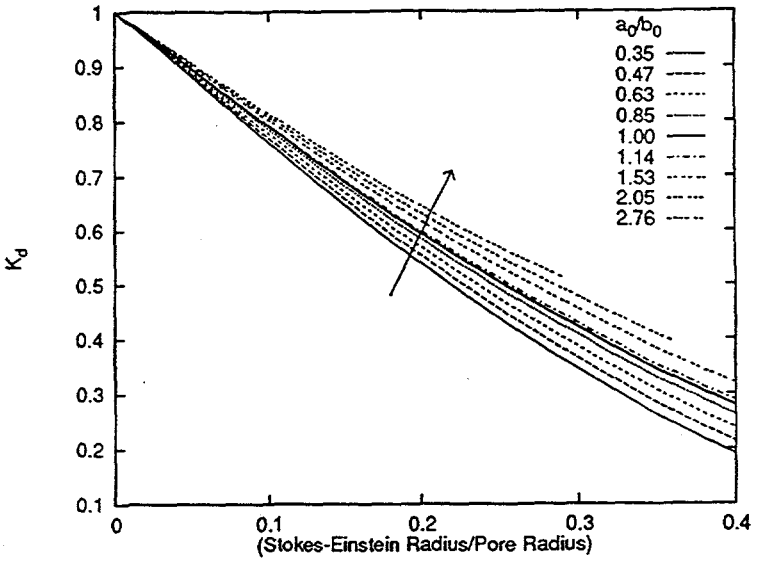

Figure 2: Hydrodynamic drag coefficient for various spheroidal sizes.

the asphaltene particles translate axisymmetrically along the center-line. The Stokeś flow problem in a cylindrical tube, containing a line of spheroidal particles located axisymmetrically along the center-line, was first addresed by Chen and Skalak (1970) using a singularity technique. The hydrodynamic viscous drag $\mathcal{D}$ for a particle, of spheroidal-diameter to pore-diameter ratio of b_0, and spheroidal-thickness to pore-thickness ratio of a_0, translating axisymmetrically with velocity U in a cylindrical pore filled with a stationary fluid of viscosity μ is

$$\mathcal{D} = 6\pi\mu b_0 K_U(a_0, b_0, 0, \bar{\Theta})U \tag{3}$$

where $\bar{\Theta}$ is the axisymmetrical orientation. Chen and Skalak (1970) have tabulated a limited number of $K_U(a_0, b_0, 0, \bar{\Theta})$ values.

To calculate the diffusivities for the broad size range of asphaltene particles we have recalculated the hydrodynamic coefficients for a much wider region of a_0 and b_0, in the range $0.0 \leq b_0 \leq 0.5$ and $0.4 \leq a_0/b_0 \leq 2.5$. The collocation points were spaced evenly along the surface of the spheroid. We used a system of 24 stream function terms and 32 equations and a modified boundary-element method to solve for the Stokeś stream function coefficients. Further details can be found elsewhere (Ravi-Kumar *et al.*, 1994). Once the Stokeś stream function is known, the hydrodynamic drag coefficient K_d can be calculated directly. K_d

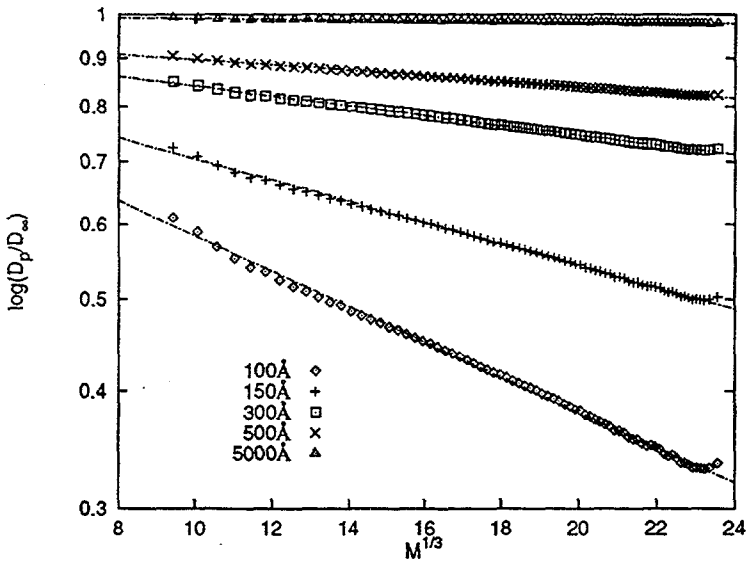

Figure 3: Distribution of hindered diffusion coefficients at different pore sizes.

as a function of the ratio of the Stokeś-Einstein radius of a spheroid to the pore-radius is shown in Fig. 2 for various values of a_0/b_0.

RESULTS AND DISCUSSION

Our model calculates the transport coefficients of asphaltene molecules as a function of the molecular weight and various other structural parameters. To generate the structures of a given asphaltene, the results are averaged over 5 simulation runs, each involving 200,000 particles. The molecular weight distributions of typical asphaltene molecules thus generated are shown in Fig. 1. The asphaltene molecules seem to follow a Schultz type distribution (Shue, 1990). Fig. 3 shows how the asphaltene diffusion coefficient scaled by its bulk value,i.e., (D_p/D_∞), changes with molecular weight and pore size. The diffusion coefficients were plotted versus molecular weight by averaging over all the molecules within a range of molecular weights. (D_p/D_∞) decreases with increasing molecular weight and decreasing pore diameter. Calculated asphaltene diffusivities are of the same order of magnitude as the experimental results of Baltus (1983) and Sane (1990). In the region of molecular weights shown in Fig. 3, a scaling relationship is observed between the (D_p/D_∞) and the molecular weight of the

24

ent pore sizes.

pheroid to the

molecules as a
arameters. To
veraged over 5
weight distri-
in Fig. 1. The
(Shue, 1990).
bulk value,i.e.,
iffusion coeffi-
the molecules
reasing molec-
ıe diffusivities
Baltus (1983)
g. 3, a scaling
weight of the

asphaltene particle, i.e.,

$$D_p/D_\infty \sim exp(-kM^{\frac{1}{3}}) \quad , \tag{4}$$

where k is a constant (which depends on the pore size) and M is the molecular weight of the asphaltene particles.

The validity of any model (and its further development) must eventually be judged by its agreement with experimental data. To critically evaluate the transport model presented here one must have structural information and diffusion data over a wide range of conditions. No such comprehensive data is available at this point and time that would allow meaningful comparisons. Work in this area is continuing in our group.

ACKNOWLEDGMENT

We wish to thank the National Science Foundation, the U.S. Department of Energy and the Unocal Corporation for their support.

REFERENCES

Anderson, J.L. and Quinn, J.A., 1974, *Biophys. J.* **14**, 131.

Baltus, R.E. and Anderson, J.L., 1983, *Chem. Eng. Sci.* **38(12)**, 1959.

Chen, T. C. and Skalak, R., 1970, *Appl. Sci. Res.* **22**, 403.

Deen, W.M., 1987, *AIChE J.* **24**, 1118.

Limbach, K. W., Nitsche, J. M., and Wei, J., 1989, *AIChE J.* **35(1)**, 42.

Mieville, R.L., Trauth, D.M. and Robinson, K.K., 1989, *ACS Preprints, Div. Pet. Chem.* **34(3)**, 635.

Nortz, R.L., Baltus, R.E., and Rahimi, P., 1990, *Ind. Eng. Chem. Res.* **29(9)**, 1968.

Nourbakhsh, N., Tsotsis, T.T., and Webster, I.A., 1989, *Appl. Catal.* **50**, 65.

Nourbakhsh, N., Smith, B. J., Webster, I. A., Wei, J., and Tsotsis, T. T., 1991, *J. Catalysis* **127**, 178.

Ravi-Kumar, V.S., Tsotsis, T.T., Sahimi, M. and Webster, I.A., 1994, *Chem. Eng. Sci.* **49**, 5789.

Ravi-Kumar, V. S., 1995, Experimental and Theoretical Studies of Transport and Reaction of Asphaltenes through Membranes, *Ph.D. Thesis*, University of Southern California.

Sane, R.C., Diffusion of Petroleum Asphaltenes in Porous Membranes, 1990, *Ph.D. Thesis*, University of Southern California.

Sane, R. C., Tsotsis, T. T., Webster, I. A., and Ravi-Kumar, V. S., 1992, *Chem. Eng. Sci.* **47(9-11)**, 2683.

Sane, R. C., Tsotsis, T. T., Webster, I. A. and Ravi-Kumar, V. S., 1994, in *Asphaltenes and Asphalts, 1. Developments in Petroleum Science* **40**, Elsevier Science (in press).

Savage, P.E. and Klein, M. T., 1989, *Chem. Engng. Sci.* **44**, 393.

Sheu, E. Y., Liang, K. S., Sinha, S. K., and Overfield, R.E., 1990, *ACS Preprints, Div. Pet. Chem.* **35**, 813.

Speight, J. G., 1991, *The Chemistry and Technology of Petroleum* (Marcel Dekker, New York).

Trauth, D.M., Stark, S.M., Petti, T.F., Neurock, M., and Klein, M.T., 1994, *Energy and Fuels* **8(3)**, 576.

Tullock, D.L., Phan-Thien, N., and Graham, A.L., 1992, *Rheo. Acta* **31**, 139.

Yen, T. F., 1990, *Ency. Polym. Sci. Engg.*, 1.

Yen, T.F., Erdman, J.L., and Pollack, S.P., 1961, *Anal. Chem.* **33(11)**, 1587.

Asphalt Flocculation and Deposition. II. Formation and Growth of Fractal Aggregates

Hossein Rassamdana[1,2] and Muhammad Sahimi[1,*]

[1]Department of Chemical Engineering, University of Southern California, Los Angeles, CA 90089-1211

[2]Improved Oil Recovery Research Center, National Iranian Oil Company, Taleghani Avenue, Tehran, Iran

Extensive small-angle X-ray and neutron scattering data, as well as the results of precipitation measurements, are analyzed to delineate the structure of the asphalt and asphaltene aggregates that are formed when a solvent is injected into a system containing crude oil. The two types of data suggest strongly that, both small and large aggregates have a fractal structure with well-defined fractal dimensions. If the system has been aged for a long enough time and its temperature is low enough, then large asphalt particles have the structure of diffusion-limited cluster-cluster aggregates with a fractal dimension $D_f \simeq 1.8$, while small asphalt particles are similar to diffusion-limited particle aggregates with a fractal dimension $d_f \simeq 2.5$. High temperatures increase the rotational motion of the particles, disturb the structure and mechanical stability of the aggregates, and decrease their fractal dimension. Aging effects, as well as the effects of the concentration of the asphalts in the solution, and the type of the solvent, on the structure of the aggregates are also investigated. The implications of these results for the structure, mechanical stability, and molecular weight distribution of asphalts and asphaltenes are discussed in detail. In particular, a new molecular weight distribution for the asphalt aggregates is proposed, and is shown to provide excellent predictions for the experimental data.

Key words: Small-angle scattering, fractal structures, diffusion-limited aggregation, asphalt precipitation.

---

* To whom all correspondence should be sent.

Introduction

Formation, flow and precipitation of particles or large aggregates in porous media is relevant to a wide variety of natural and industrial processes, such as deep-bed filtration, flow of dilute stable emulsions, migration of fines, and catalysis (for a review see Sahimi *et al.*, 1990), as well as ground water contamination and enhanced oil recovery (for reviews see Sahimi, 1993, 1995). The efficiency of these processes depends crucially on the availability of open pore space which provides transport paths for the fluid that carries the aggregates. In some cases, the particles or aggregates are formed when the fluid in the porous medium reacts with the solid matrix, resulting in solid products that are carried away by the flowing fluid. In other cases, the aggregates are formed when a fluid is injected into the pore space to react with, or displace, the in-place fluid. These aggregates have very unusual properties, and despite many years of research a definitive model of their structure has not emerged.

Consider a typical process in which such aggregates are formed, namely, catalytic coal liquefaction and coal liquid upgrading, during which large molecular saggregates, that are usually referred to as asphaltene, are formed whose precipitation on the pore surfaces of the catalyst decreases severely the efficiency of these processes. Over the years several studies have been undertaken (see, for example, Thrash and Pildes, 1981; Baltus and Anderson, 1983; Sakai *et al.*, 1983; Mieville *et al.*, 1989; Kyriacou *et al.*, 1988a,b; Nortz *et al.*, 1990; Sane *et al.*, 1988, 1992) by which the transport properties of asphaltenes derived from various types of heavy oil have been measured. However, in the absence of a reasonable structural model of the asphaltenes, such data cannot be interpreted and correlated accurately. Moreover, precipitation of the asphaltene aggregates on the pore surfaces of the catalyst causes severe problems for efficient operation of the process, and thus one also needs an accurate model for predicting the precipitation and its onset at which it is triggered. Despite some recent progress (see below), a generally-accepted model has not emerged yet.

Consider another industrial process in which such aggregates are formed, namely, enhanced oil recovery from an underground reservoir by a miscible displacement process in which an agent– a gas or a liquid– is injected into the reservoir to displace the oil. This often causes formation of large asphalt or asphaltene aggregates consisting of heavy organic compounds and their precipitation on the pore surfaces of the reservoir during the enhanced oil recovery process (Speight, 1991). For the sake of clarity we define (as do others; see, e.g., Speight, 1991)

asphalts as asphaltenes plus resin and wax. Formation of asphalt and asphaltene aggregates is a function of the composition of the crude oil and the displacing agents, and the pressure and temperature of the reservoir. Their deposition on the surface of the pores reduces the permeability of the pore space, leading to the eventual isolation of oil from the flowing fluid in the reservoir (see, for example, Lichaa and Herrera, 1975), a reduction in the efficiency of oil recovery processes, and an increase in their cost. Therefore, it is important to understand the mechanisms of formation of such aggregates under the reservoir conditions, the point at which their deposition on the pore surfaces is triggered, their thermodynamic and transport properties, and their effect on the properties of the pore space. Although over the past several decades such problems have been studied intensively (see, for example, Yen, 1990, and Speight, 1991, for comprehensive reviews), no general consensus has emerged.

In a previous paper (Rassamdana *et al.*, 1996; hereafter referred to as Part I), we presented the results of a systematic study of asphalt formation near the onset of precipitation which is particularly important to oil recovery, reported new experimental data for the amount of the precipitates, and presented two theoretical approaches for predicting them. In the present paper we study the kinetic growth of asphalt and asphaltene aggregates. We analyze two completely different classes of experimental data. One is our precipitation data reported in Part I which we analyze in order to gain insight into the structure of the asphalt aggregates. Small-angle scattering measurements, a highly accurate probe of the structure of molecular aggregates, constitute the second class of data which we analyze. We show that both types of data lead us to an unambiguous and novel model of the structure of the asphalt aggregates. The model has important implications for several structural and dynamical properties of the aggregates, which we discuss in detail. Effective diffusivities of asphalt aggregates in a pore have been reported elsewhere (Ravi-Kumar *et al.*, 1994).

The plan of this paper is as follows. In the next section we describe two models of formation and kinetic growth of molecular aggregates that are relevant to our discussion in this paper. We then describe the theory of small-angle scattering by fractal aggregates. Next, extensive small-angle X-ray and neutron scattering (SAXS and SANS, respectively) data are analyzed and are shown to be consistent with a fractal structure for the asphalt and asphaltene aggregates. The effects of the various factors that affect the structure of the aggregates, such as the temperature of the system and the composition of the crude oil and the solvent are discussed in detail. In

the next section, we analyze precipitation data and show that they are consistent with the scattering results, thus lending strong support to the fractality of the asphalt and asphaltene aggregates. We then discuss the implications of these results, including those for modelling aggregation of asphalts, their stability against temperature fluctuations, and their molecular weight distribution.

Particle and Cluster Aggregation

Two important aggregation processes that are relevant to our paper are diffusion-limited particle (DLP) and diffusion-limited cluster-cluster (DLCC) aggregation (see Meakin, 1988, for an excellent review). Here, we summarize briefly those aspects of these processes that are directly relevant to our discussion. In the DLP aggregation model (Witten and Sander, 1981) the site at the center of a lattice is occupied by a stationary particle. A particle is then injected into the lattice, far from the center, which diffuses (executes a random walk) on the lattice. If it reaches a surface site, i.e., an empty site which is a nearest-neighbor to the stationary particle, it sticks to that site and remains there permanently. Another particle is then injected into the lattice, which diffuses on the lattice until it reaches another surface (empty) site and sticks to it, and so on. If this process is continued for a long time, a large aggregate is formed, a typical two-dimensional (2D) example of which is shown in Figure 1. The DLP aggregates are self-similar and fractal, i.e., if their radius is R_p and they contain N_p elementary particles, then

$$N_p \sim R_p^{D_f} \ , \tag{1}$$

where D_f is their fractal dimension. Computer simulations (Meakin, 1988) indicate that $D_f \simeq$ 1.7 and 2.5, for 2D and 3D DLP aggregates, respectively.

In the DLCC aggregation model (Meakin, 1983; Kolb *et al.*, 1983) one starts with an empty lattice. At time $t = 0$, lattice sites are selected at random and occupied by particles, until a small fraction p_0 of the sites are occupied by the particles. Each occupied site can contain only one particle. A randomly-selected cluster of occupied sites, including a single site, is then selected and moved (allowed to diffuse) in a randomly-chosen direction. Then the perimeter sites of the cluster — the set of sites that are adjacent to the cluster — are examined to see whether they are occupied by other particles or clusters. If so, the perimeter particles or clusters are added (attached) to the cluster that was moved to form a larger cluster. Once a larger cluster

is formed, it is not allowed to break up again. (Later in this paper we investigate the stability of these aggregates, and the conditions under which the clusters may break up.) Another randomly-selected cluster is moved again, its perimeter is examined for possible formation of a larger cluster, and so on. Figure 2 shows 3 stages of this process in 2D. Similar to the DLP aggregates, the DLCC aggregates are also fractal objects with $D_f \simeq 1.45 \pm 0.05$ and 1.8 ± 0.05 in 2D and 3D, respectively. Observe that the fractal dimension of the DLCC aggregates is smaller than that of the DLP aggregates. The reason for this is clear: Aggregation of clusters creates larger holes in the final molecular structure than that of elementary particles. This is clearly seen in Figures 1 and 2. Note that, in this model it is assumed that the diffusivity $\mathcal{D}$ of a cluster is independent of its molecular weight M. In practice, one expects to have $\mathcal{D} \sim M^{-1/D_f}$ (since the radius R_p of the cluster is proportional to M^{1/D_f}), or more generally, $\mathcal{D} \sim M^{\zeta}$, where ζ is an exponent that may depend on the type of the solution in which the aggregation takes place. Computer simulations (Meakin, 1988) indicate that D_f is almost completely independent of ζ, provided that $\mathcal{D}$ decreases with increasing M.

Another important model is reaction-limited cluster-cluster (RLCC) aggregation process in which the clusters have to touch each other many times before joining. As a result, the clusters can penetrate more deeply into each other, leading to aggregates with a denser structure than that of the DLCC aggregates. For example, their fractal dimension in 3D is $D_f \simeq 2.05$, compared with $D_f \simeq 1.8$ for DLCC aggregates.

An important property of the DLCC aggregates is their surface roughness. Since the aggregating clusters have irregular shapes and sizes, their *active* surface area S_a, i.e., that part of their surface which is most likely to collide with the surface of another cluster, is different from their *total* surface area S, and in fact S_a constitutes only a small fraction of S. The active surface area S_a of an aggregate scales with the total number of particles s in it as

$$S_a \sim s^{\omega} , \tag{2}$$

where ω is a universal exponent, independent of many microscopic features of the aggregate. Obviously, $\omega < 1$, since the active surface area of a cluster cannot grow with its size faster than linearly.

An important property of both the DLCC and RLCC aggregates is their cluster-size distribution. Suppose that $n_s(t)$ is the number of clusters of size s at time t. Then, it has been

shown that (Vicsek and Family, 1984)

$$n_s = s^{-\tau} f(s/\langle s \rangle) \,, \tag{3}$$

where τ is a universal exponents, and $\langle s \rangle$ is the mean cluster (aggregate) size defined by

$$\langle s \rangle = \frac{\sum_{s=1}^{\infty} s^2 n_s(t)}{\sum_{s=1}^{\infty} s n_s(t)} \,. \tag{4}$$

Here $f(x)$ is a *universal* scaling function such that $f(x) \sim x^{\delta}$ for $x << 1$ and $f(x) << 1$ for $x >> 1$. For the DLCC aggregates $\tau = 2$ (Vicsek and Family, 1984), while for the RLCC aggregates $\tau = 3/2$ (Ball *et al.*, 1987). Thus, the value of τ can be used to distinguish between the DLCC and RLCC aggregates which, in fact, is what we do in our analysis of the scattering data discussed below. Obviously, the mean cluster size increases with the time t, and therefore

$$\langle s \rangle \sim t^{w} \,, \tag{5}$$

where w is a *dynamical* exponent which may depend on ζ, the exponent that relates the diffusivity of the clusters to their molecular weight.

Theory of Small-Angle Scattering by Fractal Aggregates

An accurate probe of the structure of fractal aggregates is small-angle scattering. We define the density-density autocorrelation function $C(r)$ at a distance $r = |\mathbf{r}|$ by

$$C(r) = \frac{1}{V} \sum_{r'} g(r') g(r + r') \quad , \tag{6}$$

where V is the volume of the system. The origin of the coordinate system is in the aggregate, $g(r) = 1$ if a given point at a distance r from the origin belongs to the aggregate, and $g(r) = 0$ otherwise. For a d-dimensional self-similar and fractal aggregate of s sites and large values of r we must have

$$C(r) \sim r^{D_f - d} \,. \tag{7}$$

In a scattering experiment the observed scattering intensity $I_s(\mathbf{q})$ by a single cluster is given by the Fourier transform of $C(\mathbf{r})$

$$I_s(\mathbf{q}) = \int_0^{\infty} C(\mathbf{r}) \exp(i\mathbf{q} \cdot \mathbf{r}) d^3\mathbf{r} \quad , \tag{8}$$

where $\mathbf{q}$ is the scattering vector whose magnitude q is given by

$$q = \frac{4\pi}{\lambda} \sin\left(\frac{\theta}{2}\right) \,. \tag{9}$$

Here λ is the wavelength of the radiation scattered by the sample through an angle θ. For a system with sufficiently low porosity, such as a fractal aggregate, it is not unreasonable to assume that, to a good approximation, there will be no interference scattering, and therefore the total scattering intensity is the sum of the scattering from all segments of the aggregate. For an isotropic medium, $C(\mathbf{r}) = C(r)$, where $r = |\mathbf{r}|$, and Eq. (8) becomes

$$I_s(q) = \int_0^\infty 4\pi r^2 \frac{\sin(qr)}{qr} C(r) dr \quad . \tag{10}$$

Using Eq. (7) in (10) with $d = 3$ yields

$$I_s(q) \sim q^{-D_f} \Gamma(D_f - 1) \sin[(D_f - 1)\pi/2] \quad , \tag{11}$$

where $\Gamma(x)$ is the Gamma function. Thus, a logarithmic plot of the scattering intensity $I_s(q)$ versus q (or the angle θ) should yield a straight line with the slope $-D_f$. Both light scattering and small-angle X-ray scattering from silica aggregation clusters have confirmed the validity of Eq. (11) (Schaefer *et al.*, 1984). In real systems the range of self-similarity and fractal behavior may be limited by lower and upper cutoff length scales R_ℓ and R_u (see below).

If the solution contains many aggregates or clusters of various sizes, then the intensity $I(q)$ scattered is the average sum of the intensities scattered by all the aggregates. Thus, $I(q)$ is given by (Bouchaud *et al.*, 1986)

$$I(q) = \int s n_s I_s(q) ds \, , \tag{12}$$

which, after using Eqs. (3) and (8), yields

$$I(q) \sim q^{-(3-\tau)D_f} \, . \tag{13}$$

Note that, since for the DLCC aggregates $\tau = 2$, Eqs. (11) and (13) are idential in this limit. We point out that power-law scattering, such as Eqs. (11) and (13), can also arise from scatterers that are not fractal, but their size distribution is of power-law type. Thus, later in this paper we also analyze the precipitation data which provide information about the asphalt cluster-size distribution.

We now analyze the small-angle scattering and precipitation data, from which we attempt to deduce the structure of the asphalt aggregates. We should point out that the small-angle scattering data that we analyze are not ours. However, their presentation and analysis in terms of fractal aggregates is novel and presented for the first time in this paper. In the original

papers mainly the asphalt particle size distribution was studied, but no attempt was made to deduce the structure of the aggregates. Moreover, the data that we analyze include both SANS and SAXS, which are known to have very different contrast mechanisms, especially for complex systems such as the asphalt aggregates. Despite this, both types of data lead to the same conclusion regarding the structure of the asphalt aggregates.

Analysis of the Small-Angle Scattering Data

We start with the analysis of the SANS data presented by Sheu *et al.* (1992), and give a brief description of their experiments. The small-angle scattering spectrometer utilizes neutrons from a cold source containing liquid hydrogen at 1.5K. The outcoming neutrons are monochromatized by a single multilayered monochromator for selection of the wavelength. In the experiments the wavelength was $5.0\mathring{A}$ with a wavelength spread of about 11%. The sample cell was a cylindrical quartz cuvette of 2-mm pathlength. The scattered neutrons, after passing through a helium-filled drift space, were detected by a ^{3}He area detector of 50×50 cm^2 containing 128×128 pixel elements. The sample-to-detector distance was 180cm, which corresponds to a q-range of 0.008 to $0.17\mathring{A}^{-1}$. Heptane was used as the solvent, and after the aggregates were formed, they were separated from the solution and were mixed with toluene and the scattering experiments were carried out after 11 days. The aggregate concentration in the toluene ranged from 0.5% to 5% (by weight), with a temperature range of 25 to 43°C.

The logarithmic plot of the scattering intensity $I(q)$ versus q at 25°C and 5% aggregate concentration is shown as the lower curves in Figure 3. A power-law scattering is observed over about one order of magnitude variation in the length scale. The size of these aggregates appears to be very small, ranging from about $5\mathring{A}$ to about $50\mathring{A}$. This is due to the fact that in these experiments the asphalt aggregates were dissolved in toluene, which is known to be a good solvent for asphalts and resins and causes fragmentation of the aggregates into small pieces. However, other data analyzed below are for much larger aggregates, and the results are still consistent with what we find from Figure 3. As Figure 3 indicates, there are two distinct regimes. At large length scales (small q) one has a straight line with a slope of about 1.76 ± 0.11, whereas at small length scales (large q), the slope is about 2.6 ± 0.1. Hereafter, we use D_f and d_f to denote the fractal dimensions of the large and small aggregates, respectively. What is the interpretation of these results? From our experimental observations (see Part I) the following mechanism for the formation of the aggregates is emerged. After the solvent is added, the resin,

that covers the surface of the small individual particles and the self-associates suspended in the oil, is partially dissolved. The particles and the resin are both electrically charged, albeit with opposite signs, and therefore dissolution of the resin creates electrical imbalance between the particles. The small clusters are then formed by diffusion of the charged solid particles in the oil, which stick together upon collision, precisely the way the DLP aggregates are formed. Their fractal dimension, which is about 2.5, is in agreement with the scattering data, $d_f \simeq 2.6 \pm 0.1$, obtained from Figure 3. After some time, one has a mixture of small clusters or aggregates of various sizes (which also carry a net electrical charge), as well as the individual charged particles. So, while the aggregation of the individual particles continues, aggregation of the clusters is also triggered. These clusters and particles also diffuse in the solution and stick to each other upon collision, precisely the mechanism by which the DLCC aggregates are formed. Indeed, with $\tau = 2$, the value for DLCC aggregates, Eq. (13) predicts $D_f \simeq 1.76$ for large length scales, in excellent agreement with that of 3D DLCC aggregates.

Next, we consider SAXS data reported by Herzog *et al.* (1988), who used 3 solution samples. Two of them were oil residues at atmospheric pressure and 350°C. After the solvent, which was *n*-heptane, was added and the asphalts were formed, they were separated and dispersed in benzene. The third sample was a 10% vacuum residue, containing the asphalt, *without* any separation with *n*-heptane and dispersed in benzene. The wave length λ was 1.608$\mathring{A}$.

The results presented in Figure 4 show power-law scattering over nearly two orders of magnitude variations in the aggregate size, $50\mathring{A} \leq \ell \leq 1700\mathring{A}$. Note that the size of these aggregates is much larger than those in the experiments of Sheu *et al.* (1992) discussed above. The slope for the first two samples is 1.8 ± 0.03, so that if we take $\tau = 2$, the value for the DLCC aggregates, the fractal dimension for the aggregates in the first two samples is $D_f \simeq 1.8 \pm 0.03$, while the third sample yields a fractal dimension $D_f \simeq 1.75 \pm 0.05$, all of which are in excellent agreement with that of 3D DLCC aggregates, and also consistent with the SANS data of Sheu *et al.* (1992) which were for a completely different oil. Note that, the ranges of length scales and the aggregate sizes that have been probed by SAXS in these experiments are much larger than those of Sheu *et al.*'s, but the results are completely consistent with each other. Note also that, unlike the data of Sheu *et al.*, the results shown in Figure 4 do not indicate the presence in the solution of the DLP aggregates at small length scales. We attribute this to two important factors: One is the aging of the three solutions for a very long time, which provides ample time

for the small aggregates to diffuse in the solution and stick together as they collide. The second factor can be the low concentration of the asphalt in the solution. Most fractal aggregates lose their mechanical stability if their mass exceeds some critical value, and have to restructure themselves (Kantor and Witten, 1984). Thus, if the concentration of the solid particles that constitute the asphalt particles is large enough, initially DLP aggregates are formed which cluster together later and form a DLCC aggregate. Once the mass of the DLCC aggregate exceeds the critical value for its mechanical stability, it can no longer absorb the small DLP aggregates, and they are left in the solution. On the other hand, if the concentration is low enough and the system has been aged for a long enough time, it will contain only one type of fractal aggregates. For example, if the asphalt-containing solution is aged for a long enough time, practically all the DLP aggregates as well as the individual charged particles cluster together and form one or more DLCC aggregates. Both of these factors result in virtually no small aggregate left in the solution that can be detected by small-angle scattering.

The next set of SAXS data that we analyze was reported by Dwiggins (1978). In his experiments oil was poured slowly into n-decane (the solvent), being stirred rapidly by a magnetic stirrer in a flask. The resulting solution, which contained 18.6% oil by weight, was then used for SAXS experiments at 25°C. The results are presented in Figure 5. The range of length scales probed in these experiments varies by only a factor of about 4.5, and therefore the results that are inferred from these data cannot by themselves be conclusive. But the size of the aggregates is very large, ranging from about 1600$\AA$ to about 7200$\AA$. Moreover, similar to the SANS data of Sheu *et al.* (1992), they indicate the existence of two distinct regimes. At large length scales (small q) the slope of the line is 1.85 ± 0.1, which together with $\tau = 2$ yield $D_f \simeq 1.85 \pm 0.1$, in agreement with the fractal dimension of the DLCC aggregates, whereas at small length scales (large q) we obtain $d_f \simeq 3$. This value of D_f is again in agreement with that of 3D DLCC aggregates. However, $d_f \simeq 3$ implies small compact aggregates, for which we have no explanation. Dwiggins (1978) also reported SAXS data for a whole (blank) oil, which is an oil to which no solvent has been added. The results for this solution are shown as the upper curve in Figure 6 which indicates that, over nearly one order of magnitude variations in the length scales, one only has large aggregates with $D_f \simeq 1.87 \pm 0.09$, if we take $\tau = 2$, again in excellent agreement with that of 3D DLCC aggregates. Dwiggins (1978) himself remarked that, "The curve for the whole oil further indicates the presence of very large particles," consistent with our assertion.

We point out that, if in interpreting the above results, we take $\tau = 3/2$, the value for the RLCC aggregates, all the scattering results for large length scales that were discussed above (and those that are discussed below) yield $D_f \simeq 1.2$, *inconsistent* with the fractal dimension of the RLCC aggregates. In other words, τ and D_f provide consistency checks on each other. Although there is no reason to believe that these aggregates can form by a percolation phenomenon, a process in which particles join randomly, we can also test whether percolation can be a plausible mechanism for the formation of the asphalt aggregates. For percolation in three dimensions, $\tau \simeq 2.18$. Thus, if in Eq. (13) we take this value of τ, since the slopes of all the scattering curves that were discussed above were about 1.8 at large length scales, we would obtain $D_f \simeq 2.2$, again inconsistent with the fractal dimension of percolation fractals $D_f \simeq 2.52$. Therefore, we believe that DLCC aggregation is the only sensible mechanism for the formation of the asphalt aggregates.

We must point out that the length scale (or the value of q) at which one has a crossover from the DLP aggregates to the DLCC ones depends on the composition of the oil, the type of the solvent, and the temperature and pressure of the system. This length scale is not a universal property, and thus cannot be estimated from a knowledge of D_f and d_f alone.

We now investigate the effect of three important factors on the structure of these aggregates, namely, the temperature of the system, the type of the solvent, and the aging of the asphalt-containing solution.

The effect of the temperature: In Figure 7 we present the logarithmic plots of $I(q)$ versus q for two systems that contain 1% (by weight) asphalt, at 25°C and 43°C, reported by Sheu *et al.* (1992). The other characteristics of the solutions were the same as those discussed above. As this figure indicates, these experiments probed over more than one order of magnitude variations in the length scales, and the results are indicative of two important effects. First, since the concentration of the asphalt is very low, at the time of the measurements aggregate formation had not been completed. Indeed, as the upper curve of Figure 7 (at 25°C) indicates, at large length scales (small q), the *effective* fractal dimension of the aggregates is only $D_f \simeq 1.42$, if we take $\tau = 2$, the value for the DLCC aggregates, and an even smaller D_f is we take $\tau = 3/2$, the value for the RLCC aggregates. At small length scales (large q), the slope is about 1.9 ± 0.1, indicating a d_f much lower than that of 3D DLP aggregates, $d_f \simeq 2.5$. These results should be compared with the lower curves shown in Figure 3, which are for a solution that contains

5% asphalt. Second, increasing the temperature of the system has two consequences. One is that more resins are dissolved and thus the electrical charge imbalance between the particles or small clusters is much lower. Thus, we expect to have aggregates with lower densities. The second, and the most important, consequence is that the rotational motion of the particles and clusters increases with rising temperature. It is known (Meakin, 1984) that, if during a DLCC aggregation process the clusters are allowed to rotate relatively fast, the fractal dimension of the DLCC aggregate *decreases*. For example, in 2D simulation of DLCC aggregation, the fractal dimension decreases from $D_f \simeq 1.45$ for aggregates with no cluster rotational motion, to $D_f \simeq 1$ with very fast rotations (Meakin, 1984), with a similar phenomenon happening in 3D. Therefore, at high temperatures we expect to have asphaltene aggregates with lower fractal dimensions. This is clearly confirmed by the lower curves of Figure 7, which show the data at 43°C. At large length scales the slope of the line is 1.0 ± 0.1, which even with $\tau = 2$ yields $D_f \simeq 1 \pm 0.1$ for the aggregates, and with $\tau = 3/2$ one finds $D_f < 1$, an unphysical result. Even at small length scales, the clusters also have much smaller masses, and have organized themselves into clusters with a lower effective fractal dimension, since the slope of the line is only 1.8. This assertion is also supported by the results of Dwiggins (1978). He carried out SAXS experiments with a whole oil at two different temperatures. One was at 25°C, the results of which are shown as the upper curves in Figure 6, and were already described. The second scattering experiments were at 80°C, the results of which are shown as the lower curves in Figure 6. In complete agreement with our assertion, and consistent with the data of Sheu *et al.* (1992) discussed above, at large length scales the aggregate has a fractal dimension $D_f \simeq 1$, while at small length scales the fractal dimension is $d_f \simeq 1.75 \pm 0.05$. A different set of SAXS data was reported by Storm *et al.* (1993) at 93°C. These authors used an oil residue with n-heptane as the solvent to form asphalt. The resulting asphalt was solved in an asphalt-free residue (synthetic residue), with which the scattering experiments were carried out. The results are presented in Figure 8 which indicate that, over one order of magnitude variations in the length scales, a power-law scattering is observed. This figure also indicates that between an upper and a lower cutoff length scales, the aggregates are fractal with a fractal dimension $D_f \simeq 1.1 \pm 0.1$, again in agreement with the results discussed above. Figure 8 also demonstrates nicely how a small-angle scattering experiment can provide estimates of the lower and upper length scales for the fractality of a system.

Aging effects: If the asphalt-containing solution is not aged for a long enough time, then one still obtains fractal aggregates, except that the formation of the aggregates is not complete and thus the fractal dimensions of the aggregates represent *effective values* that may be *smaller* than their long-time values. For example, if the asphalt-containing solution that results in the lower curves of Figure 3 is not aged for 11 days, and the scattering experiment is carried out immediately after mixing of the asphalt-containing solution with toluene, one obtains the results that are shown as the upper curves in Figure 3. In this case, at large length scales the slope is about 1.66, which together with $\tau = 2$ yields $D_f \simeq 1.66$, smaller than that of 3D aggregates, $D_f \simeq 1.8$ (see above), whereas at small length scales we have $d_f \simeq 1.94$, smaller than that of 3D DLP aggregates, $d_f \simeq 2.5$. The reason for these values may be that the solution has not yet been aged for a long enoungh time, and thus aggregate formation has not been completed. Figure 9 also shows the effect of aging on the resulting aggregates. All the characteristics of the system are similar to those shown in Figure 3, except that the concentration of the asphalt particles in the solution is only 1%. The results indicate power-law scattering over one order of magnitude variations in the length scales. The upper curve in Figure 9 corresponds to the scattering results immediately after dispersion of the asphalt-containing solution in toluene, and indicates the existence of fractal aggregates with $D_f \simeq 1.14 \pm 0.07$. The lower curve is for a scattering experiment 11 days after the mixing and yields a fractal dimension $D_f \simeq 1.94 \pm 0.13$, consistent with $D_f \simeq 1.8$ for 3D DLCC aggregates. Note that, as we discussed above, when the concentration of the solid particles is low, only one type of fractal aggregates is formed, and Figure 9 confirms this again.

The effect of the solvent: Most of the above results were obtained with n-heptane as the solvent. The only exception was the case with n-decane. All the results were also consistent with each other. We now discuss the scattering results with a completely different solvent, and then *speculate* on the possible effect of the solvent on the structure of the asphalt aggregates. Figure 10 presents the logarithmic plot of a SAXS experiment reported by Dwiggins (1978). In this experiment, n-propanol was used as the solvent at room temperature. The solution that was used for the scattering experiment contained about 50% (by weight) crude oil. Figure 10 indicates that there is only one type of fractal aggregate in the solution. The slope of the line is about 2.7 ± 0.06, inconsistent with a DLCC structure for which $D_f(3-\tau) \simeq 1.8$ [see Eq. (13)], and with a RLCC structure for which $D_f(3-\tau) \simeq 3.07$. Thus, what is the interpretation of this

result? At this point we can only speculate, since we do not have enough information about the experiments, nor do we have any data for any other type of solvent other than what we are discussing here. Moreover, the range of the length scales probed in these experiments is not broad enough to draw any definitive conclusion from the results. However, we note that Jullien and Hasmy (1995) have argued that, if in the DLCC aggregation model the initial concentration of the particles is larger than a critical value, then instead of the usual DLCC aggregate one may obtain a gel network with a fractal structure. The fractal dimension of the gel network (at the gel point) is about $D_f \simeq 2.52$ (for a review of gelation models and their fractal structures see Sahimi, 1992, 1994). If we assume that the solution essentially contains one large aggregate, so that, instead of Eq. (13), Eq. (11) is applicable, then one has an aggregate with a fractal dimension $D_f \simeq 2.7$, only 7% larger than that of gels. Since the concentration of the crude oil in the propanol was very high, it is possible that the concentration of the asphalt particles was above the critical value for gel formation, and therefore a gel network was formed. One may also speculate that, the presence of propanol in the solution created hydrogen bonds that bridged the small clusters, which otherwise would not have been attached to each other. As a result, a much denser fractal aggregate with higher D_f was formed.

Scaling Analysis of the Precipitation Data

We now consider the problem from a completely different angle, namely, the precipitation of the asphalt aggregates, and show that the *amount* of the precipitated aggregates also provides insight into their structure, and that the results are in agreement with the small-angle scattering data. To measure the amount of the precipitated aggregates we used a crude oil which we filtered to remove its solid contents, such as sand. We then diluted the oil by a solvent, which was a n-alkane with a carbon number ranging from 5 to 10. Several different dilution ratios R, measured in terms of the cm^3 of the agent/gr of the oil, were used. The diluted oil was then agitated in a tube, which caused the formation and precipitation of the aggregates. After one day the solid content of the oil, i.e., the precipitated aggregates, was measured. During the entire experiment the temperature was kept at about 25°C. Complete details of the experiments are given in Part I.

Figure 11 shows our experimental results for the weight percent of the precipitated asphalt W, in weight of the asphalt/gr of the crude oil, for 5 different solvents (n-alkanes) and various solvent to crude ratios R. (Some of these data were reported in Part I, and are presented here

only for the following discussion.) These results are strongly suggestive of the possibility that a scaling equation may be developed for predicting them, since all the curves start at about the same point and at large values of R they become more or less parallel. As a result, it may be possible to collapse the data onto a single scaling curve. This is in fact typical of aggregation processes. For example, one can calculate the cluster-size distribution $n_s(t)$, discussed above, as a function of either the cluster size s at a fixed time t, or as a function of t at a fixed s. This has been studied in detail by Meakin *et al.* (1985). However, Eq. (3) also tells us that we can collapse all the cluster-size distributions onto a single curve, if we plot $s^\tau n_s(t)$ versus $s/\langle s\rangle$ (with $\langle s\rangle \sim t^w$), since the scaling function $f(s/\langle s\rangle)$ is *universal* and does not depend on the details of the system. Figure 12 shows the results of this collapse which confirms Eq. (3) with $\tau = 2$.

Since the small-angle scattering data analyzed above already suggest that, asphalts and asphaltenes are fractal aggregates with well-defined scaling properties, the data collapse should be possible, and this is indeed the case. The variables in Figure 11 are R, W, and M, the molecular weight of the solvent. We find that, if let $X = R/M^z$ and $Y = WR^{z'}$, then all the experimental data shown in Figure 11 can be collapsed onto a single curve with

$$z = \frac{1}{4}\,, \quad z' = 2\,, \tag{14}$$

where the estimated error bars are about $\pm 5\%$. The resulting data collapse is shown in Figure 13. Note that, we could not find any other values for z and z' that could collapse the precipitation data onto a single curve with the same accuracy, nor could we find any other combinations of the three variables that collapse the data onto a single curve. Thus, these combinations of the variables and the values of z and z' appear to be unique.

In Part I the exponents z and z' were given without providing any theoretical explanation for their values, nor could we explain why the precipitation data can be collapsed onto a single curve. However, based on the dynamic cluster-size distribution for the DLCC aggregates, we can now provide a theoretical explanation for both of these. If we combine Eqs. (3) and (5), and take $\tau = 2$, the value for the DLCC aggregates, we obtain

$$s^2 n_s(t) = f(s/t^w)\,, \tag{15}$$

which implies that the universal scaling function $f(x)$ can be expressed only in terms of $s^2 n_s(t)$. On the other hand, if the scaling function shown in Figure 13 is written as $Y = h(X)$, where

$h(X)$ is the curve representing the collapsed data, then the data collapse shown in Figure 13 implies that

$$R^2 W = h(R/M^z) \,, \tag{16}$$

which is completely similar to Eq. (15), offers a plausible explanation for the collapse of the precipitation data onto a single curve and the value $z' = 2$, and indicates that, as we argued above, the clusters have the structure of the DLCC aggregates. Of course, the scaling functions $f(x)$ and $h(x)$ are not the same. Comparing Eqs. (15) and (16), one may infer that the *roles* of s and $n_s(t)$ in the dynamic cluster-size distribution are played by R and $W(t)$, respectively. It is not unreasonable to infer that the size of the asphalt aggregates may be proportional to the ratio R, and indeed as Figure 11 indicates with increasing R the amount of precipitation, and thus the size of the aggregates, do increase. As a rough estimate, $W(t)$ is also proportional to $n_s(t)$, the number of clusters or aggregates of size s at time t for *all* $s \geq s_{min}$. Here s_{min} is the minimum cluster size for precipitation, since only when a cluster is large enough, it can precipitate; otherwise it will remain suspended in the solution. We expect to have $s_{min} \sim \alpha\langle s\rangle$, where $\alpha > 1$. With these analogies, it becomes clear why the data collapse shown in Figure 13 is possible. However, one has to be careful with such analogies, since although we expect $W(t)$ to be related to $n_s(t)$, the relation between them is more complex than a simple proportionality. In fact, we expect that the weight percent of precipitated asphalt $W(t)$ to be related to $n_s(t)$ by the following equation

$$W(t) \sim \int_{\alpha\langle s\rangle}^{\infty} s n_s(t) ds \,, \tag{17}$$

that is, $W(t)$ is simply proportional to the sum of the sizes of all the clusters that are larger than $s_{min} \sim \alpha\langle s\rangle$. The analogy between Eqs. (15) and (16) also implies that the *role* of the mean cluster size $\langle s\rangle \sim t^w$ in the dynamic cluster-size distribution, Eq. (15), is played by M^z in the scaling equation for the precipitation data, Eq. (16). That is, the mean size of the asphalt aggregates is proportional to the molecular weight M of the solvent, raised to some power z. Since Eq. (5) tells that the exponent w depends on ζ, the exponent that relates the diffusivity of an aggregate to its molecular weight, $\mathcal{D} \sim M^{\zeta}$, we also conclude that the exponent z, the analog of w, may also be non-universal and presumably depend on the type of the solvent and/or the asphalt-containing oil, whereas the exponent $z' = 2$ is universal and does not depend on the solvent or the oil type. This universality is the result of mass conservation in the system, which also results in Eq. (3) with $\tau = 2$.

We now make another quantitative connection between the scattering results and the precipitation data, and show that the latter also indicate that $D_f \simeq 1.8$ and $d_f \simeq 2.5$. To do this, we assume that the distribution of the asphalt aggregates does obey Eq. (3), derive an expression for the mass of the aggregates in the solution, and show that the results are consistent with the precipitation data only if $\tau = 2$, $d_f \simeq 2.5$, and $D_f \simeq 1.8$. For a cluster of size s the redius is $R_p(s) \sim s^{1/D_f}$, and its volume is $v \sim s^{3/D_f}$. Thus the volume of the clusters or aggregates in the solution is

$$V \sim \int_0^{\alpha\langle s\rangle} v n_s(t) ds \tag{18}$$

which, when combined with Eq. (3), yields

$$V \sim \int_0^{\alpha\langle s\rangle} s^{3/D_f} s^{-\tau} f(s/\langle s\rangle) ds = \langle s\rangle^{3/D_f-\tau+1} \int_0^{\alpha} x^{3/D_f-\tau} f(x) dx \sim \langle s\rangle^{3/D_f-\tau+1} . \tag{19}$$

Note that, the limits of the integrals in Eqs. (17)–(19) are different. Equation (17) is for the large aggregates that have precipitated (whose minimum size is about $\alpha\langle s\rangle$), while Eqs. (18) and (19) are for those that have remained in the solution. If v_t is the volume of a *typical* cluster or aggregate in the solution, then Eq. (19) is written as $V \sim v_t^{[3+D_f(1-\tau)]/3}$. In a solution that contains one or a few large aggregates with a fractal dimension D_f and a large number of small aggregates with a fractal dimension d_f, the typical or average aggregate size is dominated by those of the small aggregates. That is, the mean size of the aggregates *remaining in the solution* is dominated by the small aggregates (since if they had been large enough, they would have precipitated). Therefore, we can write $v_t \sim \ell^{d_f}$, where ℓ is the radius of the typical aggregates. Combining this equation with Eq. (19), and noticing that the mass m of the aggregates in the solution is $m = \rho V$, where ρ is the aggregate density, we obtain

$$m \sim \rho \ell^{d_f[3+D_f(1-\tau)]/3} . \tag{20}$$

Equation (20) tells us that a logarithmic plot of m versus ℓ should yield a straight line with a slope $p = d_f[3 + D_f(1 - \tau)]/3$. If our interpretation of the small-angle scattering results is correct, then $\tau = 2$, $d_f \simeq 2.5$ and $D_f \simeq 1.8$, which means that slope of the line should be $p \simeq 1.0$. The only quantity to be specified is ℓ, which is very difficult to measure directly. Since asphalt and asphaltene aggregates are fractal with complex shapes, one can estimate ℓ only if the fractal aggregate is approximated by a simple shape. For example, Herzog *et al.* (1988) and Acevedo *et al.* (1994) suggested that one may represent asphalts roughly as relatively thin

discs, whose thickness was estimated to be in the range $3.6 - 8.0\mathring{A}$, while the density of asphalt aggregates is typically about $1.1 - 1.3$ gr/cm^3. Thus, if, as a rough estimate, we assume ℓ to be the radius of the discs, given the weight and density of the asphalts in the solution and the thickness of the discs, which we took it to be $5.8\mathring{A}$, ℓ can be estimated. We found that for a fixed dilution ratio R a plot of $\ln m$ versus $\ln \ell$ does reproduce straight lines whose slopes vary between 0.9 and 1.13, with an average of about 1.03, in agreement with the theoretical prediction $p \simeq 1.0$.

Our recent measurements of the MW distributions of asphalts and asphaltenes with various solvents and dilution ratios R (Dabir *et al.*, 1996) suggest that heavier solvents with larger molecular diameters also generate larger aggregates, resulting in broader MW distributions. As pointed out above, the analogy between Eqs. (15) and (16) also implies that the mean aggregate size is directly related to the molecular weight of the solvent. Thus, we may also assume ℓ to be proportional to some characteristic length scale of the solvent molecules, such as their effective molecular diameter or, since we used n-alkanes as the solvent, their linear dimension. However, for n-alkanes the effective molecular diameter is directly proportional to their linear dimension, and therefore any one of them can be used. For the n-alkanes the values of ℓ, taken as the effective molecular diameter, are available in standard handbooks. Figure 14 shows the plot of $\ln m$ (calculated from Figure 11) versus $\ln \ell$ for various n-alkanes and values of the dilution ratio R, where on each line R is constant. As can be seen, all the lines for the various n-alkanes and Rs are parallel to one another as they should be, since their slope depends only on the universal quantities τ, d_f, and D_f. Moreover, we find that $p \simeq 1.05$, in excellent agreement with both the theoretical expectation $p \simeq 1.0$ and $p \simeq 1.03$ obtained by assuming that the aggregates can be represented as thin discs. Therefore, not only the precipitation data are consistent with a dynamic cluster-size distribution for fractal diffusion-limited aggregates, they also indicate that the fractal dimensions of the aggregates are the same as those that we infer from the scattering data. Note that, only if we take $\tau = 2$ and have two types of aggregates in the solution with two different fractal dimensions d_f and D_f, do the predictions of Eq. (20) agree with the data, thus supporting our interpretation of the scattering data. All other plausible values of τ, d_f and D_f yield slopes that do agree with the experimental value, $p \simeq 1.05$.

We should point out that an equation similar to Eq. (20) with $\tau = 2$ was given previously

by Crickmore and Hruska (1989) (CH) using a completely different derivation. However, in their derivation they made a *wrong* assumption, but still obtained the same result as ours! They assumed that d_f (whose origin they did not specify) is the fractal dimension of the *largest* asphalt aggregate (which is in fact D_f), whereas as our discussion here makes it clear, d_f is the fractal dimension of the *typical* or average-size aggregates, which are dominated by the small DLP clusters. Janardhan and Mansoori (1993) attempted to derive the equation given by CH, made the same error as them, and applied the equation erroneously to some precipitation data at *the onset of the precipitation.* At this point, the dilution ratio R_c is different for various solvents, and therefore there is no way of obtaining the type of straight lines shown in Figure 14, since on each line the dilution ratio is constant for all the solvents. It is not clear to us how they obtained the results that they present in their paper.

Summarizing the results of the last two sections, almost all the different sets of small-angle scattering data as well as the precipitation results, *for completely different oils* and aggregate sizes ranging from 50$\AA$ to over 7000$\AA$, yield the *same result*: The largest asphalt particles are DLCC aggregates with a *universal* fractal dimension $D_f \simeq 1.8$ (independent of the type of the oil), whereas the small asphalt particles are DLP aggregates with a *universal* $d_f \simeq 2.5$. As discussed above, high temperatures can generate low density aggregates with lower *effective* fractal dimensions, because they increase rotational motion of the diffusing clusters in the solution. Moreover, if the concentration of the solid particles in the oil is low, eventually only the DLCC aggregates will form. Thus, we can identify both the fractal dimension of these aggregates and the mechanisms of their formation. These results are also supported by the recent experiments of Toulhoat *et al.* (1994). Using atomic force microscopy, they obtained beautiful pictures of asphalt aggregates that are completely similar to those shown in Figure 1, and thus providing strong support for our results.

We should mention that, in the past there has been some speculation about the possibility of asphalts and asphaltenes having a fractal structure (Park and Mansoori, 1988; Crickmore and Hruska, 1989; Lin *et al.*, 1991; Kuzeev *et al.*, 1991; Mukhametzyanov and Kuzeev, 1991; Raghunathan, 1991; Liu *et al.*, 1995). However, aside from Liu *et al.* (1995), none of these authors specified what kind of a fractal structure the asphalt and asphaltene aggregates may possess, or proposed any mechanism for their formation. In the absence of any mechanism for the formation of a fractal structure with a given fractal dimension, one can, in principle,

have an infinite number of ways by which the fractal structure may form. In fact, Park and Mansoori (1988), Crickmore and Hruska (1989), and Lin *et al.* (1991) all stated that, if the asphalt and asphaltene aggregates are fractal, *their fractal structures and fractal dimensions cannot be specified*, and Raghunathan (1991) speculated that the fractal structure of these aggregates is similar to that of *linear polymers* whose fractal dimension is $D_f \simeq 5/3$. Liu *et al.* (1995) proposed that if the concentration of the asphalt aggregates in the solution is high or low, then one has non-fractal aggregates, whereas in the intermediate regime one has the RLCC aggregates. However, their own data suggest that $\tau \simeq 1.8 \pm 0.2$, much closer to $\tau = 2$ for the DLCC aggregates, than to $\tau = 3/2$ for the RLCC aggregates. While we agree with them regarding non-fractality (and compactness) of the aggregates if their concentration in the solution is very high (see above), we disagree with them about the low concentration regime. We must also emphasize that a fractal dimension $D_f \simeq 1.8$ does *not* imply that the aggregates are nearly two dimensional. It only means that the number of the elementary solid particles in the aggregates is so low that their fractal dimension is smaller than two. But, such aggregates still have a 3D structure, i.e., they cannot be placed on a plane, or even on a few planes.

Finally, we point out that, there is no shortage of broad conceptual models of asphalts and asphaltenes structure in the literature. Over the years, many models have been proposed, beginning perhaps with the work of Dickie and co-workers (1967, 1969), in which an analogy to polymers was proposed. Many other conceptual models have been proposed (see, for example, Yen, 1974; Ignasiak *et al.*, 1977; Speight and Moschopedis, 1980; Sakai *et al.*, 1983; Boduszynski, 1987, 1988; Sane *et al.*, 1988; Nortz *et al.*, 1990; Strausz *et al.*, 1992). In particular, an interesting model has been proposed by Klein and co-workers (Savage and Klein, 1989; Truath *et al.*, 1994), in which the experimental knowledge about the chemical structure of asphaltenes has been used for developing a model that combines experimental data and an iterative stochastic method for generating a model of asphaltenes. However, it is not clear to us that their model can yield molecular structures similar to what we propose here.

Implications of the Results

The discovery that asphalt particles are fractal aggregates implies that the vast knowledge already available for such aggregates can be used immediately to study in detail the structure of the asphalts and the kinetics of their formation. Here we discuss three important consequences of our results, which are modelling aggregation and flocculation of the asphalt particles, their

mechanical stability, and their molecular weight distribution.

Modelling Kinetics of Aggregation of the Asphalt Particles

The kinetics of aggregation of many colloidal particles can be described in terms of the Smoluchowski equation

$$\frac{dn_k}{dt} = \frac{1}{2}\sum_{i+j=k}^{k-1} K(i,j)n_i n_j - n_k \sum_{i=1}^{\infty} K(k,i)n_i \ , \tag{21}$$

where n_i is the number of clusters or aggregates of size i, and $K(i,j)$ is a collision matrix or kernel, which is a function of both the collision of the clusters and the aggregation processes. The first term of the right hand side of Eq. (21) represents the formation of clusters of size k from the two smaller clusters of sizes i and $j = k - i$, while the second term represents the loss of the clusters of size k by reaction with other clusters to form larger clusters. This equation is based on the assumption that the collision between the clusters or aggregates, or the asphalt particles in our problem, is random and binary. The assumption of randomness is valid if the fluctuations in the density of the particles is small. Such an assumption makes the equation a mean-field approximation, and mean-field approximations are valid only above a certain spatial dimension d which, in our case, is $d = 2$. Thus, the Smoluchowski equation is valid for describing aggregation of the asphalt and asphaltene particles.

The most important parameter of the Smoluchowski equation is the kernel $K(i,j)$ and its functional form. For many processes to which the Smoluchowski equation may be applicable, it is *not* clear *a priori* what functional form one should use for the kernel. Ziff *et al.* (1985) carried out extensive computer simulations of DLCC aggregation in three dimensions, and showed that

$$K(i,j) \sim \left(i^{\zeta} + j^{\zeta}\right)\left(i^{1/D_f} + j^{1/D_f}\right) \ , \tag{22}$$

where ζ is the exponent that relates the diffusivity of the cluster to its molecular weight, $\mathcal{D} \sim M^{\zeta}$, defined earlier. Thus, Eq. (22) can be used immediately to study the kinetics of asphalt and asphaltene aggregation by the Smoluchowski equation.

Mechanical Stability of the Asphalt Aggregates and an Upper Bound to Their Molecular Weight

One of the most interesting aspects of fractal aggregates is that, their density can be much smaller than that of their constituent particles, and it decreases as their size increases. But,

at the same time, fractal aggregates can preserve their mechanical stability and support deformation. Therefore, it is sensible to ask, how large fractal aggregates can become before losing their mechanical stability, which would force them to reorganize themselves into a more stable structure.

Consider first a non-fractal object. Suppose that the system is at a temperature T, and that the material at a distance r from the origin is displaced by an amount u, which produces a strain $\epsilon \sim u/r$. Suppose also that the shear modulus of the system is μ. Thus, the displacement of the system costs an elastic energy per unit volume of the system which is about $\mu\epsilon^2$. With thermal fluctuations in the system we must have $k_B T \sim \mu\epsilon^2 r^d$, where r^d is the volume of the system, and k_B is the Boltzmann constant, and thus $\epsilon^2 \sim r^{-d}$.

Consider now fractal aggregates. We must distinguish between fractal aggregates with many closed loops of particles at any length scale, such as gel networks at the gelation point, and those that contain small and insignificant (in a macroscopic sense) loops, such as the DLCC and DLP aggregates (see Figures 1 and 2). In loopless fractals there is essentially only one path connecting two widely-separated points in the system, which is called the *minimum path.* Suppose that we fix one of the points at the origin, and displace the other one by an amount u. Since the fractal is loopless, displacement of the particle strains only the essentially one-dimensional path between the displaced particle and the one at the origin (the same argument *cannot* be used for fractals with large loops, since there are more than one path between the two points). Suppose that the number of the elementary particles in the path is n_p, and that their effective size is a. If r is large, then

$$n_p \sim r^{D_{min}} , \tag{23}$$

where D_{min} is called the fractal dimension of the minimum path. In general, $D_{min} > 1$, but for the DLP aggregates $D_{min} \simeq 1$, while for the DLCC aggregates in 3D $D_{min} \simeq 1.25$. Kantor and Witten (1984) showed that

$$\epsilon^2 \sim \frac{k_B T}{\mu b^d n_a} \left(\frac{r}{a}\right)^{D_{min}} . \tag{24}$$

In this equation, b^d is the volume of the atoms that constitute the particles, and n_a is the number of atoms in a particle. Thus, the average strain *increases* with the length scale r, $\epsilon \sim r^{D_{min}}$, in contrast with non-fractal objects for which $\epsilon \sim r^{-d}$. If r and n_p are larger than some critical values r_c and n_{pc}, ϵ becomes of the order of unity. If an aggregate is larger than

this critical size n_{pc}, it becomes flexible and is free to respond to internal forces in the same way as polymers do. If the forces are attractive, then the aggregate attains a *collapsed* state. For colloidal particles, such as asphalt and asphaltene aggregates, n_a is typically about 10^3, μb^d is about 10 eV, while $k_B T$ is about 1/40 eV at room temperature. Thus, the maximum value that n_p can take is about 10^4, before thermal fluctuations distort the aggregate and force it to reorganize itself into another more stable structure. Thus, fractal structures, such as the asphalt and asphaltene aggregates, *cannot* become too large. This restriction places an upper bound on the largest molecular weight that an asphalt or asphaltene aggregate can attain, which is about $6000 - 8000$. In the literature, one finds estimates of the average molecular weight of the asphalt or asphaltene aggregates that are as large as $10^5 - 10^6$. In the light of what we discuss here, such claims are wrong.

The Molecular Weight Distribution of the Asphalt Aggregates

The MW distribution is, in general, a time-dependent quantity which evolves as the aggregation of the asphalt and asphaltene particles takes place. Since the asphalt and asphaltene aggregates are of the DLP and DLCC type, a measure of their MW distribution is provided by their cluster-size distribution, Eq. (3). Because the Smoluchowski equation can be used to determine the cluster-size distribution, one can, in principle, also use the same equation to study the time-evolution of the MW distribution. However, what we are interested in here is the MW distribution of the aggregates after a long time. Over the years, many authors have studied this problem (Dickie and Yen, 1967; Moschopedis and Speight, 1976; Moschopedis *et al.*, 1976; Boduszynski *et al.*, 1977; Ignasiak *et al.*, 1977; Speight and Moschopedis, 1977; Schwager and Yen, 1978; Snape and Bartle, 1984; Speight *et al.*, 1985; Boduszynski 1987, 1988; Acevedo *et al.*, 1992; Strausz *et al.*, 1992; Taylor, 1992; Trauth *et al.*, 1994). Aside from Trauth *et al.* (1994), these authors measured mainly the average MW of asphalts and asphaltenes from various oils, and provided some statistics of their measurements, but none proposed an analytical formula for the MW distribution, and in fact they did not even give the full MW distribution itself. Trauth *et al.* (1994) used a Monte Carlo method to determine the MW distribution, based on their own model described above.

Botet and Jullien (1984) studied the cluster-size distribution during DLCC aggregation processes. They derived an analytical formula for the *most probable* cluster-size distribution, and also determined numerically the *average* cluster-size distribution (since it cannot be calculated

analytically in closed form), where the averaging was taken with respect to the process time. Suppose that at the beginning of the aggregation process there are N particles, and that there are N_c clusters or aggregates in the system. Botet and Jullien (1984) showed that, the most probable cluster-size distribution is given by

$$\frac{Nn_s}{N_c^2} \sim f_\omega(N_c s/N) \,, \tag{25}$$

where ω is defined by Eq. (2). Equation (25) tells us that $f_\omega(x)$ can be considered as a rescaled *or reduced* most probable cluster-size distribution. Subject to certain assumptions, Botet and Jullien (1984) also derived the following equation for $f_\omega(x)$

$$f_\omega(x) = \frac{(1-2\omega)^{1-2\omega}}{\Gamma(1-2\omega)} x^{-2\omega} \exp[-(1-2\omega)x] \,. \tag{26}$$

This equation can have a maximum only if $\omega < 0$. Botet and Jullien compared Eq. (26) with their numerical simulations and showed that, except around the maximum of the distribution where Eq. (26) does not always estimate the magnitude of the maximum very accurately, it provides a very accurate description of the cluster-size distribution.

We now convert Eq. (26) to a MW distribution for the asphalt and asphaltene aggregates by assuming that, the molecular weight of an aggregate is proportional to its size. Experimental measurements also show that there is usually a minimum molecular weight M_m at which the MW distribution is cutoff. Therefore, Eq. (26) implies the following equation for the MW distribution for asphalts and asphaltenes:

$$f_\omega(M) = c_1(M - M_m)^{-2\omega} \exp[-c_2(M - M_m)] \,, \quad M \geq M_m \,, \tag{27}$$

where c_1 and c_2 are constant. The normalization condition, $\int_0^\infty f_\omega(M)dM = 1$, gives one relation between c_1 and c_2, so that Eq. (27) has one free parameter to adjust. In Eq. (27) we can treat ω as an adjustable parameter, but in what follows we provide evidence that ω may in fact be a *universal* exponent, and thus its value can be fixed.

We used Eq. (27) to fit the experimental data presented by Park and Mansoori (1988). The data are for the asphalt MW distributions in Brookhaven oil, obtained with three different n-alkanes. For all three cases we obtained

$$\omega \simeq -0.14 \pm 0.03 \,, \tag{28}$$

indicating that, at least for n-alkanes, the value of ω is universal. That ω is found to be negative is expected, since, as mentioned above, Eqs. (26) and (27) can have a maximum only

if ω is negative. Figure 15 compares our fits with the data. As can be seen, except around the maximum of the distributions, the agreement between the predictions and the data is excellent. The slight disagreement between the predictions and the data around the maximum is expected, since, as discussed above, Botet and Jullien (1984) had already shown that Eq. (26) may underestimate the magnitude of the maximum of the cluster-size distribution, consistent with Figure 15. The small value of ω also has two implications for the structure of the asphalt and asphaltene aggregates. First, it implies that the active surface area of the aggregates that actually participates in the process is very small. This is partly due to the rough and irregular, and possibly fractal, nature of the aggregates' surface, and partly due to the fact that no solvent can dissolve all the resins that cover the surface of the solid particles that are suspended in the oil, which are the building blocks of the aggregates. Second, $\omega < 0$ implies that as the size of the aggregates increases, their active surface area *decreases*, since an increase in the aggregate size also increases the roughness of its surface.

As mentioned earlier, some authors have suggested an analogy between the structure of the asphalt and asphaltene aggregates, and polymers. In the polymer literature, use of a log-normal distribution for representing the MW distribution of polymers is popular. Therefore, we thought it may be useful to also use a log-normal distribution for predicting the above data, and compare the results with the predictions of Eq. (27). Hence we used

$$f(M) = \frac{1}{\sqrt{2\pi}\sigma(M - M_m)} \exp\left\{-[\ln(M - M_m) - \ln\langle M\rangle]^2/2\sigma^2\right\} , \qquad (29)$$

where $\langle M\rangle$ and σ are the mean and standard deviation of the distribution, respectively, which we treated as adjustable parameters. The resulting fits of the data are shown in Figure 16, and it is clear that they do not agree with the data. Elsewhere (Dabir *et al.*, 1996) we present new and extensive data for the MW distribution of asphalts and asphaltenes, and discuss their theoretical prediction using the ideas discussed here.

Summary and Conclusions

We have analyzed extensive small-angle scattering and precipitation data in order to delineate the structure of asphalt and asphaltene aggregates. Almost all the data, with various oils and solvents, provide compelling evidence that the asphalt and asphaltene aggregates are fractal objects with well-defined structures and fractal dimensions. Moreover, the *mechanisms* of their formation also become clear: At short length scales, the aggregates are formed by a

diffusion-limited *particle* aggregation process, while at large length scales they are due to a diffusion-limited *cluster-cluster* aggregation process. We have also shown that the type of the solvent and the temperature of the system both have a strong influence on the structure of the aggregates, and that the fractal structure of the aggregates places an upper bound on their size and average molecular weight. Finally, we have proposed a new molecular weight distribution for the asphalt and asphaltene aggregates, which provides very good predictions for the experimental data.

Acknowledgments

This work was supported in part by the Department of Energy. We would like to thank Ali R. Mehrabi for his expert help in computing the molecular weight distributions.

Literature cited

Acevedo, S., G. Escobar, M.A. Ranaudo, and L. Gutiérrez, "Discotic Shape of Asphaltenes Obtained from g.p.c. Data," *Fuel* **73**, 1807 (1994).

Acevedo, S., G. Escobar, L. Gutiérrez, and H. Rivas, "Isolation and Characterization of Natural Surfactants from extra Heavy Crude Oils, Asphaltenes and Maltenes," *Fuel* **71**, 619 (1992).

Ball, R. C., D. A. Weitz, T. A. Witten, and F. Leyvraz, "Universal Kinetics in Reaction-Limited Aggregation," *Phys. Rev. Lett.* **58**, 274 (1987).

Baltus, R. E., and J. L. Anderson, "Asphaltene Characterization and Diffusion Measurements," *Chem. Eng. Sci.* **38**, 1959 (1983).

Boduszynski, M. M., " Composition of Heavy Petroleums. 1. Molecular Weight, Hydrogen Deficiency, and Heteroatom Concentration as a Function of Atmospheric Equivalent Boiling Point up to 1400°F," *Energy & Fuels* **1**, 2 (1987).

Boduszynski, M. M., "Composition of Heavy Petroleums. 2. Molecular Characterization," *Energy & Fuels* **2**, 597 (1988).

Boduszynski, M. M., B. Raj Chadha, and T. Szkutta-Pochopien, "Investigations on Romashkino Asphaltic Bitumen. 3. Fractionation of Asphaltenes Using Ion-Exchange Chromatography," *Fuel* **56**, 434 (1977).

Botet, R., and R. Jullien, "Size Distribution of Clusters in Irreversible Kinetic Aggregation," *J. Phys. A* **17**, 2517 (1984).

Bouchaud, E., M. Delsanti, M. Adam, M. Daoud, and M. Durand, "Gelation and Percolation: Swelling Effect," *J. Physique* **47**, 1273 (1986).

Crickmore, P. J., and C. Hruska, "Fractal Geometry, the Korčak Law and Asphaltene Precipitation," *Fuel* **68**, 1488 (1989).

Dabir, B., M. Nematy, A. R. Mehrabi, H. Rassamdana, and M. Sahimi, "Asphalt Flocculation and Deposition. III. The Molecular Weight Distribution," *Fuel* (to be published).

Dickie, J. P., M. N. Haller, and T. F. Yen, "Electron Microscopic Investigations on the Nature of Petroleum Asphaltics," *J. Colloid Interface Sci.* **29**, 475 (1969).

Dickie, J. P. and T. F. Yen, "Macrostructures of the Asphaltic Fractions by Various Instrumental Methods," *Anal. Chem.* **39**, 1847 (1967).

Dwinggins, C. W., "Study of the Colloidal Nature of Petroleum with an Automated Bonse-Hart X-Ray Small-Angle Scattering Unit," *J. Appl. Cryst.* **11**, 615 (1978).

Herzog, P., D. Tchoubar, and D. Espinat, "Macrostructure of Asphaltene Dispersions by Small-Angle X-Ray Scattering," *Fuel* **67**, 245 (1988).

Ignasiak, T., A. V. Kemp-Jones, and O. P. Strausz, "The Molecular Structure of Athabasca Asphaltene. Cleavage of the Carbon-Sulfur Bonds by Radical Ion Electron Transfer Reactions," *J. Org. Chem.* **42**, 312 (1977).

Ignasiak, T., O. P. Strausz, and D. S. Montgomery, "Oxygen Distribution and Hydrogen Bonding in Athabasca Asphaltene," *Fuel* **56**, 359 (1977).

Janardhan, A. S., and G. A. Mansoori, "Fractal Nature of Asphaltene Aggregation," *J. Pet. Sci. Eng.* **9**, 17 (1993).

Jullien, R., and A. Hasmy, "Fluctuating Bond Aggregation: A Model for Chemical Gel Formation," *Phys. Rev. Lett.* **74**, 4003 (1995).

Kantor, Y., and T. A. Witten, "Mechanical Stability of Tenuous Objects," *J. Physique Lett.* **45**, L-675 (1984).

Kolb, M., R. Botet, and R. Jullien, "Scaling of Kinetically Growing Clusters," *Phys. Rev. Lett.* **51**, 1123 (1983).

Kyriacou, K. C., R. E. Baltus, and P. Rahimi, "Characterization of Oil Residual Fractions Using Intrinsic Viscosity Measurements," *Fuels* **67**, 109 (1988a).

Kyriacou, K. C., V. V. Sivaramakrishna, R. E. Baltus, and P. Rahimi, "Measurement of Diffusion Coefficient of Oil Residual Fractions Using Porous Membranes," *Fuels* **67**, 15 (1988b).

Kuzeev, I. R., I. Z. Mukhametzyanov, and Yu. M. Abyzgil'din, "Macroscopic Structures of Petroleum Pitches in the Course of Solidification," *Kolloid. Zhur.* **53**, 434 (1991).

Lichaa, P. M., and L. Herrera, "Electrical and other Effects Related to the Formation and Prevention of Asphaltenes Deposition," *Society of Petroleum Engineers Paper 5304* (1975).

Lin, J.-R., H. Lian, K. M. Sadeghi, and T. F. Yen, "Asphalt Colloidal Types Differentiation by Korcak Distribution," *Fuel* **70**, 1439 (1991).

Liu, Y. C., E. Y. Sheu, S. H. Chen, and D. A. Storm, "Fractal Structure of Asphalt in Toluene," *Fuel* **74**, 1352 (1995).

Meakin, P., "Formation of Fractal Clusters and Networks by Irreversible Diffusion-Limited Aggregation," *Phys. Rev. Lett.* **51**, 1119 (1983)

Meakin, P., "The Effects of Rotational Diffusion on the Fractal Dimensionality of Structures Formed by Cluster-Cluster Aggregation," *J. Chem. Phys.* **81**, 4637 (1984).

Meakin, P., in *Phase Transitions and Critical Phenomena,* edited by C. Domb and J. L. Lebowitz, Vol. 12 , Academic Press, London (1988).

Meakin, P., T. Vicsek, and F. Family, "Dynamic Cluster-Size Distribution in Cluster-Cluster Aggregation: Effects of Cluster Diffusivity," *Phys. Rev. B* **31**, 564 (1985).

Moschopedis, S. E., J. F. Fryer, and J. G. Speight, "Investigation of Asphaltene Molecular Weights," *Fuel* **55**, 227 (1976).

Moschopedis, S. E., and J. G. Speight, "Investigation of Hydrogen Bonding by Oxygen Functions in Athabasca Bitumen," *Fuel* **55**, 187 (1976).

Mieville, R. L., D. M. Trauth, and K. K. Robinson, "Asphaltene Characterization and Diffusion Measurements," *ACS Preprints, Div. Pet. Chem.* **34**, 635 (1989).

Mukhametzyanov, I. Z., and I. R. Kuzeev, "Fractal Structures of Paramagnetic Aggregates of Petroleum Pitches," *Kolloid. Zhur.* **53**, 644 (191).

Nortz, R. L., R. E. Baltus, and P. Rahimi, "Determination of the Macroscopic Structure of Heavy Oil by Measuring Hydrodynamic Properties," *Ind. Eng. Chem. Res.* **29**, 1968 (1990).

Park, S. J., and G. A. Mansoori, "Aggregation and Deposition of Heavy Organics into Petroleum Crudes," *Energy Sources* **10**, 109 (1988).

Raghunathan, P., "Evidence for Fractal Dimension in Asphalt Polymers from Electron-Spin-Relaxation Measurements," *Chem. Phys. Lett.* **182**, 331 (1991).

Rassamdana, H., B. Dabir, M. Nematy, M. Farhani, and M. Sahimi, "Asphalt Flocculation and Deposition. I. The Onset of Precipitation," *AIChE J.* **42**, 10 (1996).

Ravi-Kumar, V. S., T. T. Tsotsis, M. Sahimi, and I. A. Webster, "Studies of Transport of Asphaltenes Through Porous Membranes: Statistical Structural Models and Continuum Hydrodynamic Theories," *Chem. Eng. Sci.* **49**, 5789 (1994).

Sahimi, M., "Structural and Dynamical Properties of Branched Polymers and Gels and Their Relation with Elastic Percolation Networks," *Mod. Phys. Lett. B* **6**, 507 (1992).

Sahimi, M., "Flow Phenomena in Rocks: From Continuum Models to Fractals, Percolation, Cellular Automata, and Simulated Annealing," *Rev. Mod. Phys.* **65**, 1393 (1993).

Sahimi, M., *Applications of Percolation Theory*, Taylor and Francis, London (1994).

Sahimi, M., *Flow and Transport in Porous Media and Fractured Rock*, VCH, Weinheim, Germany (1995).

Sahimi, M., G. R. Gavalas, and T. T. Tsotsis, "Statistical and Continuum Models of Fluid-Solid Reactions in Porous Media," *Chem. Eng. Sci.* **45**, 1443 (1990).

Sakai, M., K. Sasaki, and M. Inagaki, "Hydrodynamic Studies of Dilute Pitch Solutions: The Shape and Size of Pitch Molecules," *Carbon* **21**, 593 (1983).

Sane, R. C., I. A. Webster, and T. T. Tsotsis, "Study of Asphaltene Diffusion Through Unimodal Porous Membrane," *Stud. Surf. Sci. Catal.* **38**, 705 (1988).

Sane, R. C., I. A. Webster, T. T. Tsotsis, and V. S. Ravi-Kumar, in *Asphalts and Asphaltenes,* edited by T. F. Yen, Elsevier, New York (1992).

Savage, P. E., and M. T. Klein, "Asphaltene Reaction Pathways - V. Chemical and Mathematical Modeling," *Chem. Eng. Sci.* **44**, 393 (1989).

Schaefer, D. W., J. E. Martin, P. Wiltzuis, and D. S. Cannel, "Fractal Geometry of Colloidal Aggregates," *Phys. Rev. Lett.* **52**, 2371 (1984).

Schwager, I., and T. F. Yen, "Coal-Liquefaction Products from Major Demonstration Processes. 1. Separation and Analysis," *Fuel* **57**, 100 (1978).

Sheu, E. Y., K. S. Liang, S. K. Sinha, and R. E. Overfield, "Polydispersity Analysis of Asphaltene Solutions in Toluene," *J. Colloid Interface Sci.* **153**, 399 (1992).

Snape, C. E., and K. D. Bartle, "Definition of Fossil Fuel-Derived Asphaltenes in Terms of Average Structural Properties," *Fuel* **63**, 883 (1984).

Speight, J. G., *The Chemistry and Technology of Petroleum,* Marcel Dekker, New York (1991).

Speight, J. G., and S. E. Moschopedis, "Asphaltene Molecular Weights by a Cryoscopic Method," *Fuel* **56**, 344 (1977).

Speight, J. G., and S. E. Moschopedis, "On the Polymeric Nature of Petroleum Asphaltenes," *Fuel* **59**, 440 (1980).

Speight, J. G., D. L. Wernick, K. A. Gould, R. E. Overfield, B. M. L. Rao, and D. W. Savage, "Molecular Weight and Association of Asphaltenes: A Critical Review," *Rev. Institut Francais Pet.* **40**, 52-62 (1985).

Storm, D. A., E. Y. Sheu, and M. DeTar, "Macrostructure of Asphaltenes in Vacuum Residue by Small-Angle X-Ray Scattering," *Fuel* **72**, 977 (1993).

Strausz, O. P., T. W. Mojelsky, and E. M. Lown, "The Molecular Structure of Asphaltene: An Unfolding Story," *Fuel* **71**, 1355 (1992).

Taylor, S. E., "Use of Surface Tension Measurements to Evaluate Aggregation of Asphaltenes in Organic Solvents," *Fuel* **71**, 1338 (1992).

Thrash, R. J., and R. H. Pildes, "The Diffusion of Petroleum Asphaltenes Through well Characterized Porous Membranes," *ACS Preprints, Div. Pet. Chem.* **26**, 515 (1981).

Toulhoat, H., C. Prayer, and G. Rouquet, "Characterization by Atomic Force Microscopy of Adsorbed Asphaltenes," *Colloid. Surf.* **91**, 267 (1994).

Trauth, D. M., S. M. Stark, T. F. Petti, M. Neurock, and M. T. Klein, "Representation of the Molecular Structure of Petroleum Resid through Characterization and Monte Carlo Modeling," *Energy & Fuels* **8**, 576 (1994).

Vicsek, T., and F. Family, "Dynamic Scaling for Aggregation of Clusters," *Phys. Rev. Lett.* **52**, 1669 (1984).

Witten, T. A., and L. M. Sander, "Diffusion-Limited Aggregation, a Kinetic Critical Phenomenon," *Phys. Rev. Lett.* **47**, 1400 (1981).

Yen, T. F., "Structure of Petroleum Asphaltene and its Significance," *Energy Sources* **1**, 447 (1974).

Yen, T. F., in *Encyclopedia of Polymer Science and Engineering*, edited by H. F. Mark, N. M. Bikales, C. G. Overberger, and G. Menges, 2nd edition, Wiley, New York (1990), p. 1.

Ziff, R. M., E. D. McGrady, and P. Meakin, "On the Validity of Smoluchowski's Equation for Cluster-Cluster Aggregation Kinetics," *J. Chem. Phys.* **82**, 5269 (1985).

Captions

Figure 1. A two-dimensional diffusion-limited particle aggregate.

Figure 2. Various stages of formation of a two-dimensional diffusion-limited cluster-cluster aggregate.

Figure 3. Logarithmic plot of the scattering intensity $I(q)$ versus the magnitude of the scattering vector q for the data of Sheu *et al.* (1992). The results are for immediately after mixing of the asphalt with toluene (top), and 11 days after the mixing (bottom). The concentration of the asphalt in the solution is 5% at 25°C.

Figure 4. Logarithmic plot of the scattering intensity $I(q)$ versus the magnitude of the scattering vector q for the data of Herzog *et al.* (1988). The results are for two different oil residues at atmospheric pressure and 350°C (top two), and for a vacuum residue (circles).

Figure 5. Logarithmic plot of the scattering intensity $I(q)$ versus the magnitude of the scattering vector q for the data of Dwinggins (1978).

Figure 6. Logarithmic plot of the scattering intensity $I(q)$ versus the magnitude of the scattering vector q for the data of Dwinggins (1978) for whole oil, showing the effect of the temperature. The results are for 25°C (top) and 80°C (bottom).

Figure 7. Logarithmic plot of the scattering intensity $I(q)$ versus the magnitude of the scattering vector q for the data of Sheu *et al.* (1992), showing the effect of the temperature. The results are for 25°C (top) and 43°C (bottom).

Figure 8. Logarithmic plot of the scattering intensity $I(q)$ versus the magnitude of the scattering vector q for the data of Storm *et al.* (1993). The results are for 93°C.

Figure 9. Logarithmic plot of the scattering intensity $I(q)$ versus the magnitude of the scattering vector q for the data of Sheu *et al.* (1992) at 25°C , showing the effect of aging of the sample. The results are for immediately after mixing of the asphalt with toluene (top), and 11 days after the mixing (bottom). The concentration of the asphalt in the solution is 1%.

Figure 10. Logarithmic plot of the scattering intensity $I(q)$ versus the magnitude of the scattering vector q for the data of Dwinggins (1978), with propanol as the solvent.

Figure 11. Experimental precipitation data for the weight percent W of the asphalt aggregates, as a function of the solvent to crude ration R. The results are, from top to bottom, for $n-C_5$, $n-C_6$, $n-C_7$, $n-C_8$, and $n-C_{10}$ as the solvent.

Figure 12. The collapse of the cluster-size distribution $n_s(t)$ of DLCC aggregates onto a

single curve (adopted from Meakin *et al.*, 1985).

Figure 13. The collapse of the experimental precipitation data of Figure 11, where $X = R/M^z$ and $Y = WR^{z'}$, with $z = 1/4$ and $z' = 2$.

Figure 14. Logarithmic plot of the weight m of the asphalt aggregates remaining in the solution versus the molecular diameter ℓ. Symbols are the same as in Figure 11, and on each line the symbols show the data at a fixed ratio R. The results are, from top to bottom, for $R = 2, 4, 6, 10$, and 20.

Figure 15. Comparison of the predictions of Eq. (27) (curves) with the experimental data of Park and Mansoori (1988) for the molecular weight M of the asphalt aggregates. The results are for $n{-}C_5$ (top left), $n{-}C_6$ (top right), and $n{-}C_7$ (bottom) as the solvent.

Figure 16. Comparison of the predictions of Eq. (29) (curves) with the experimental data of Park and Mansoori (1988) for the molecular weight M of the asphalt aggregates. Symbols are the same as those in Figure 15.

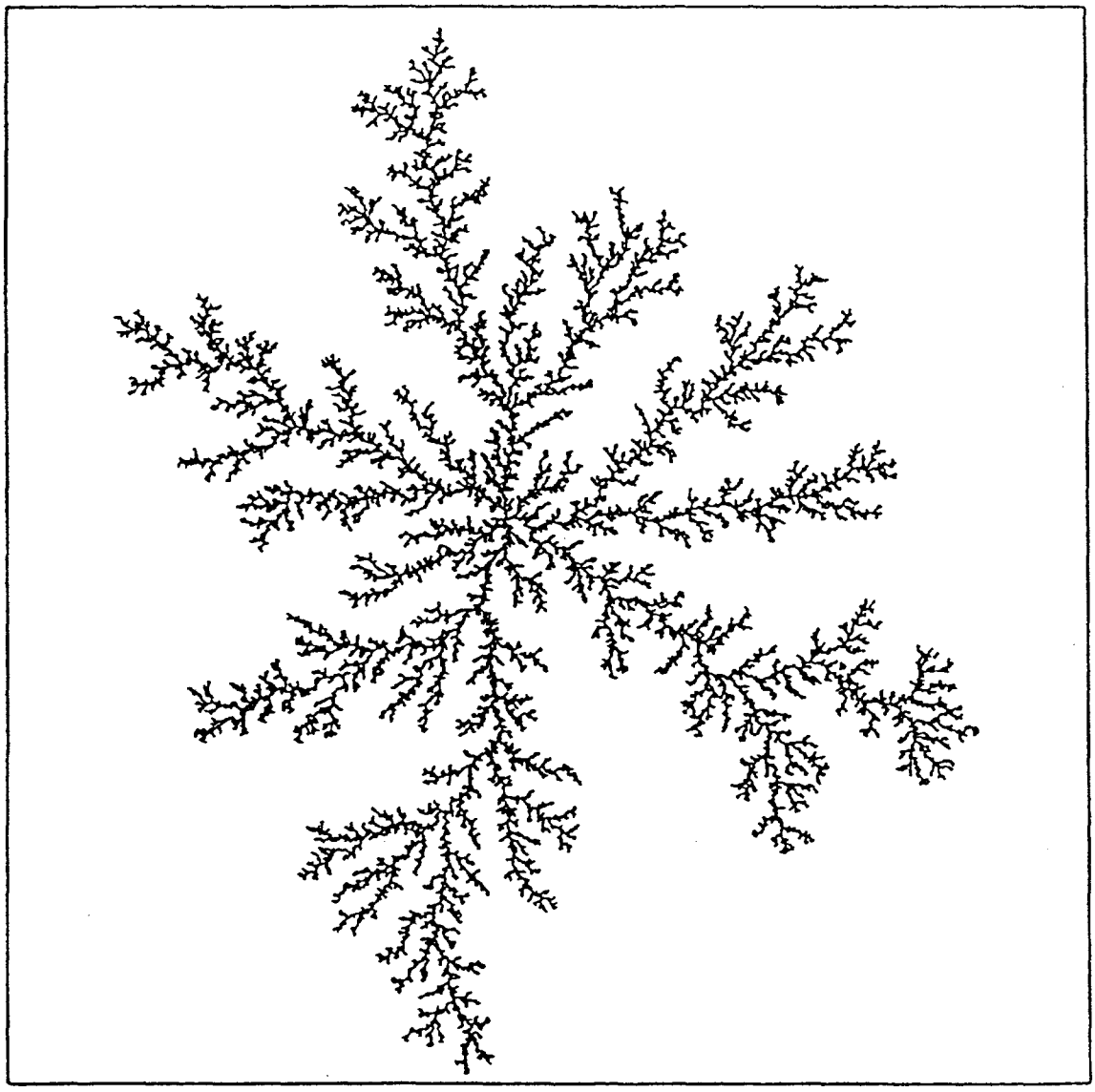

F1

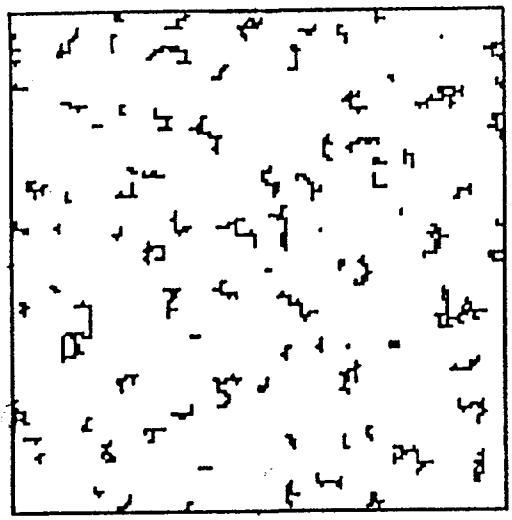

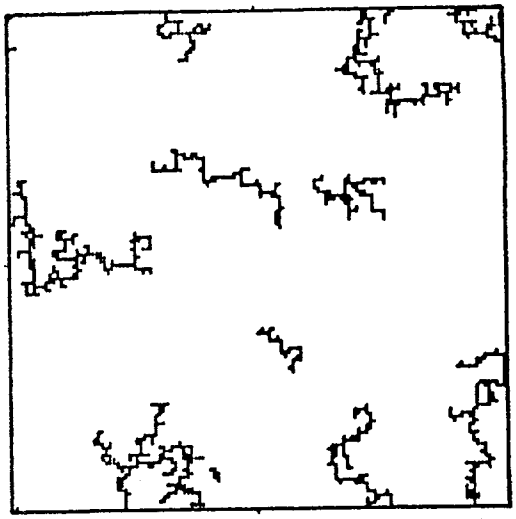

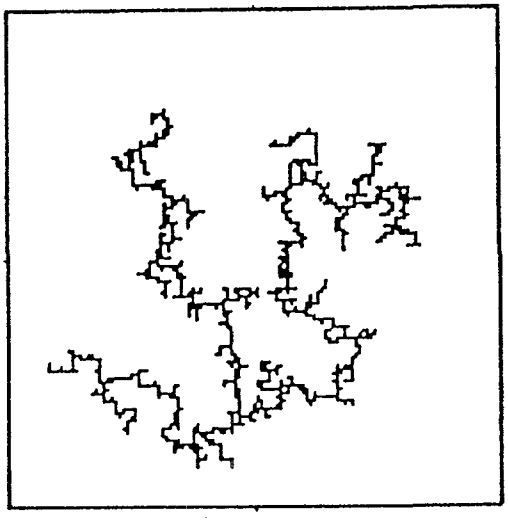

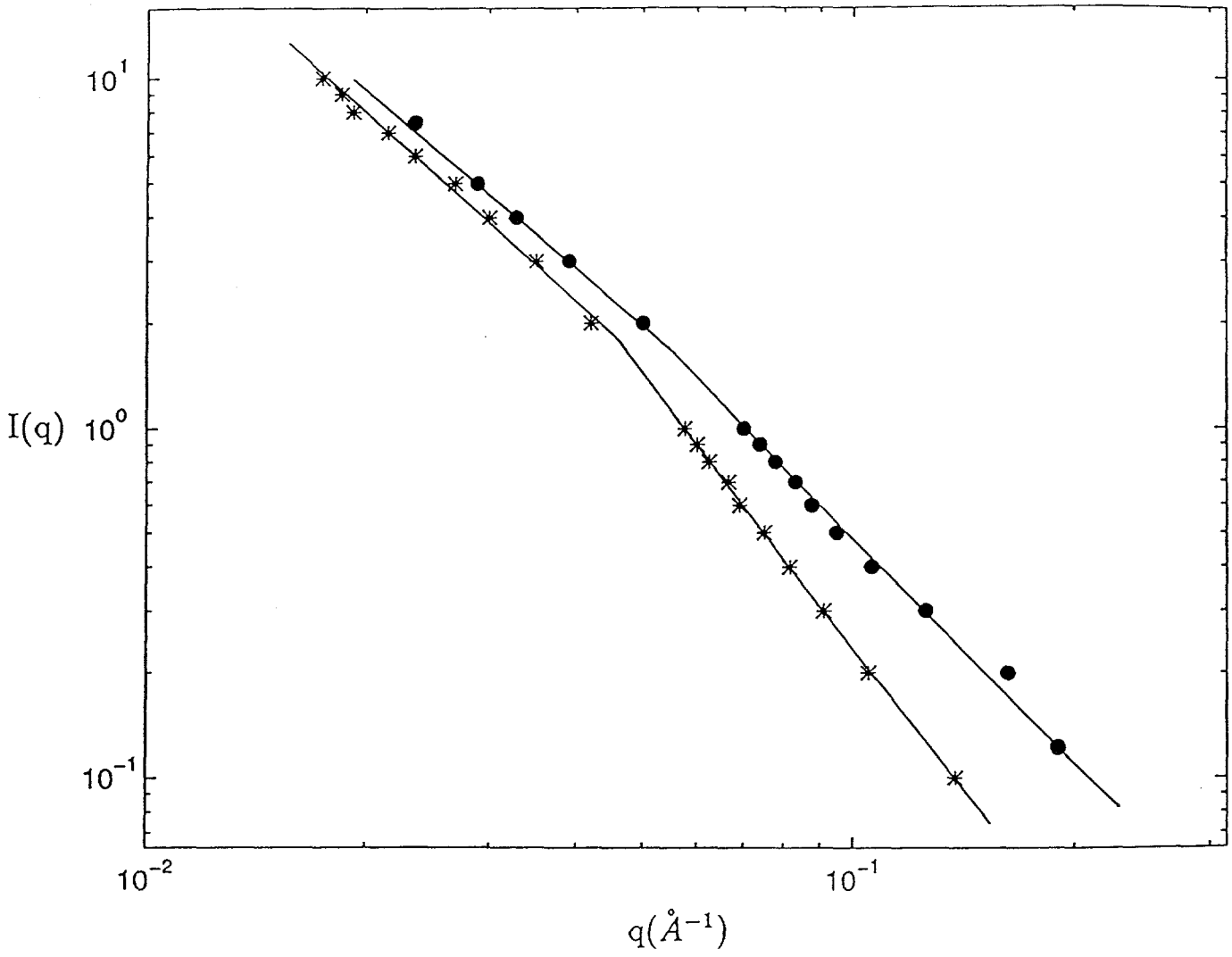

ED

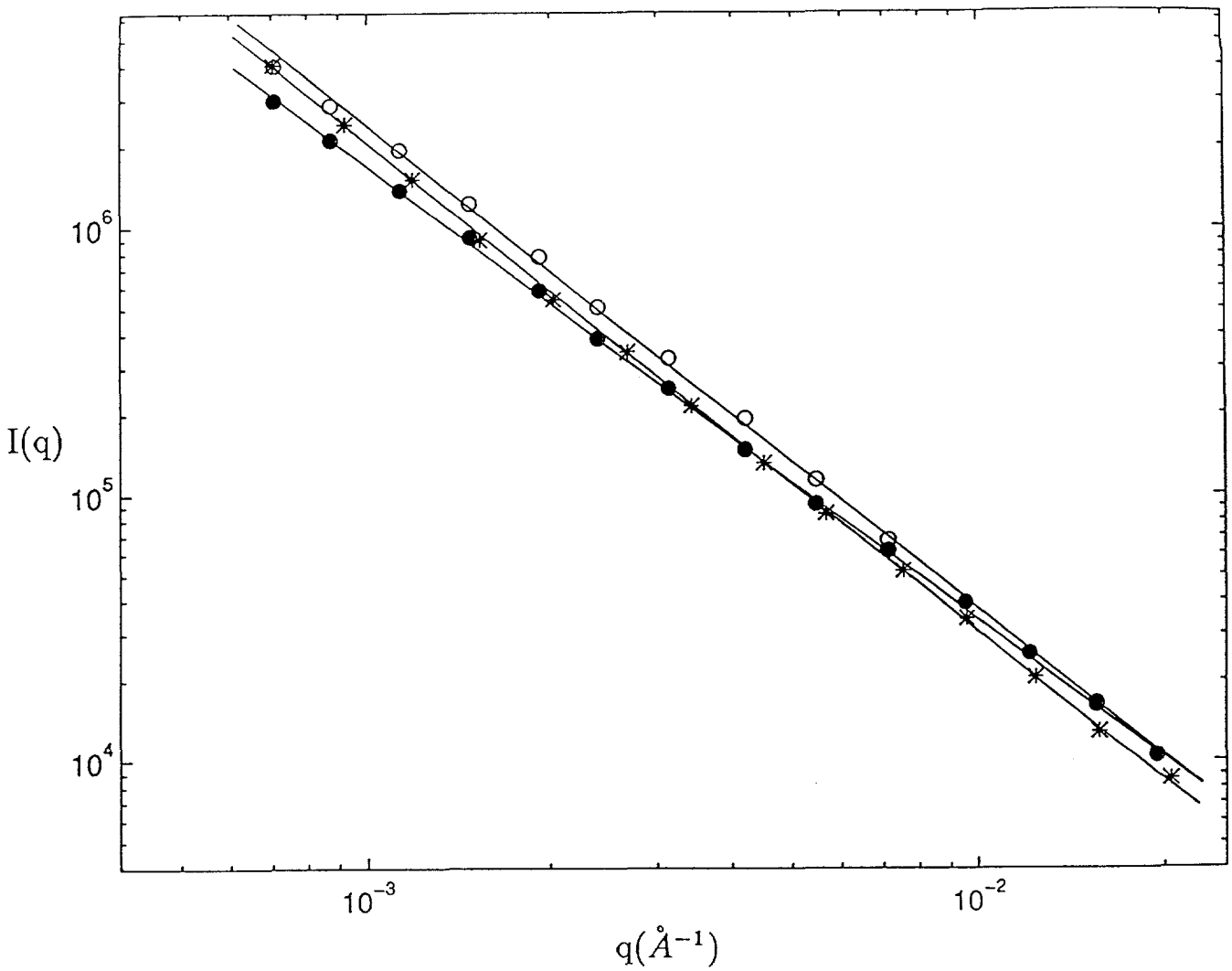

FIL

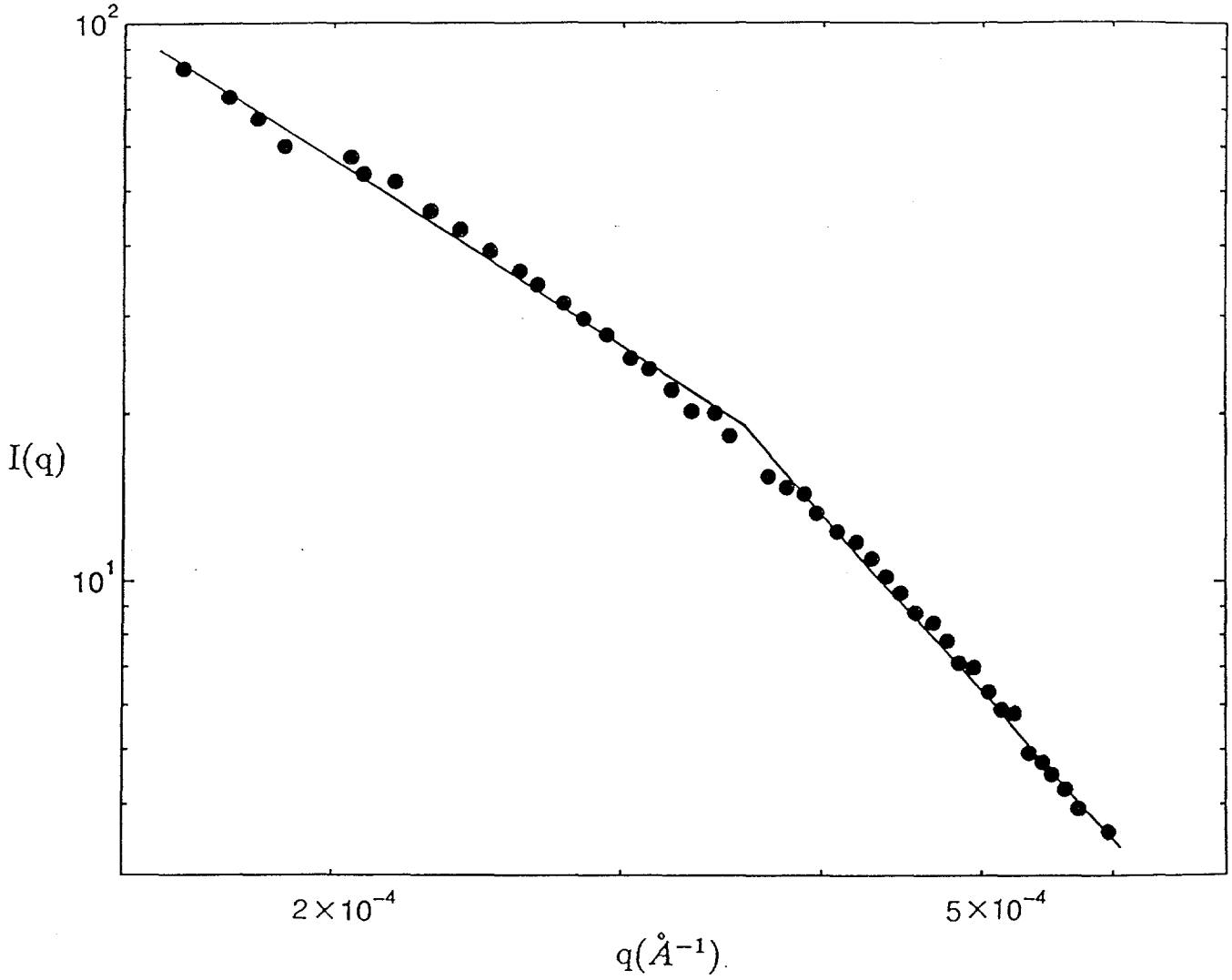
10^2
10^1
I(q)
2×10^{-4}
5×10^{-4}
$q(\AA^{-1})$

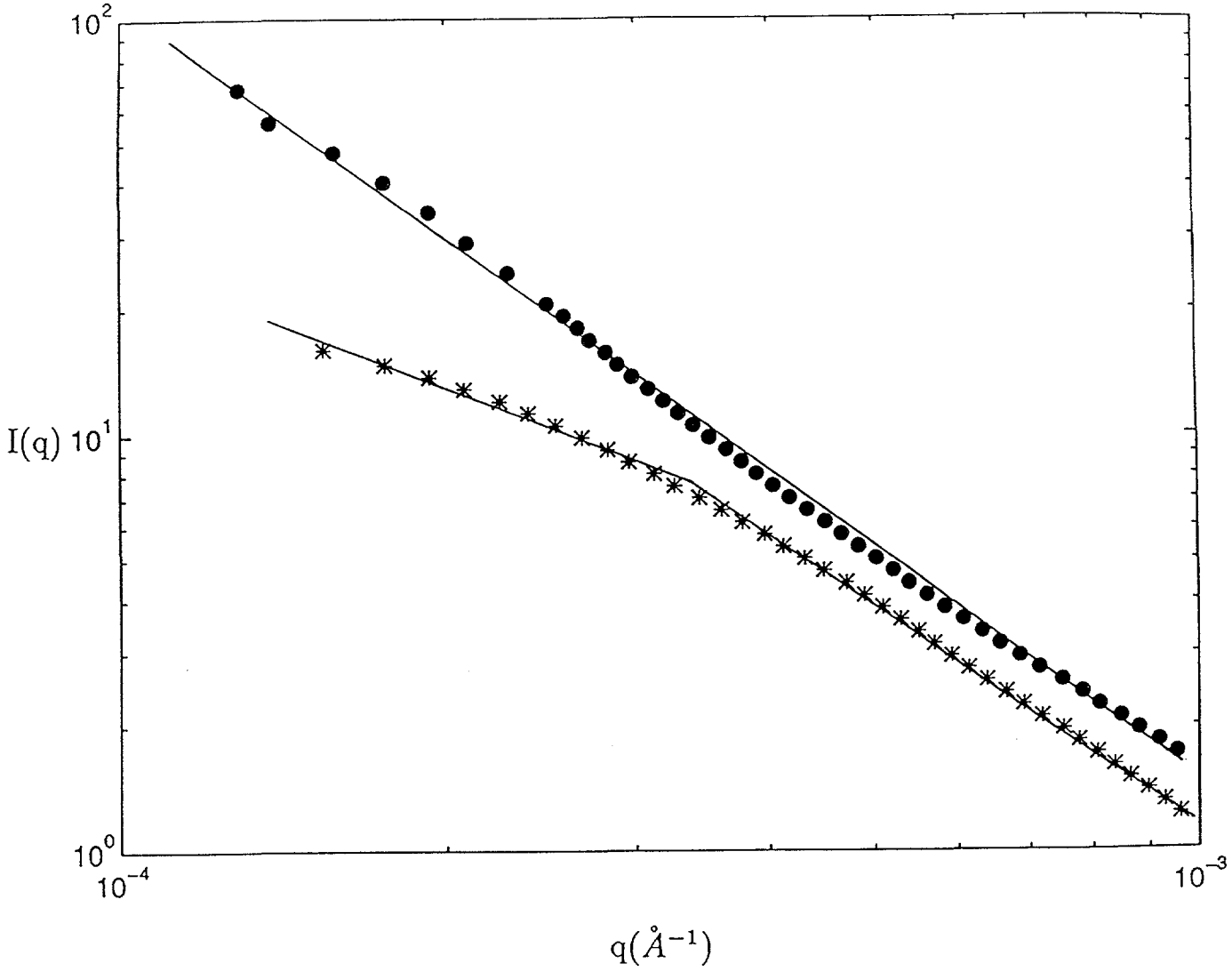
10^2
I(q) 10^1
10^0
10^{-4}
10^{-3}
q($\AA^{-1}$)

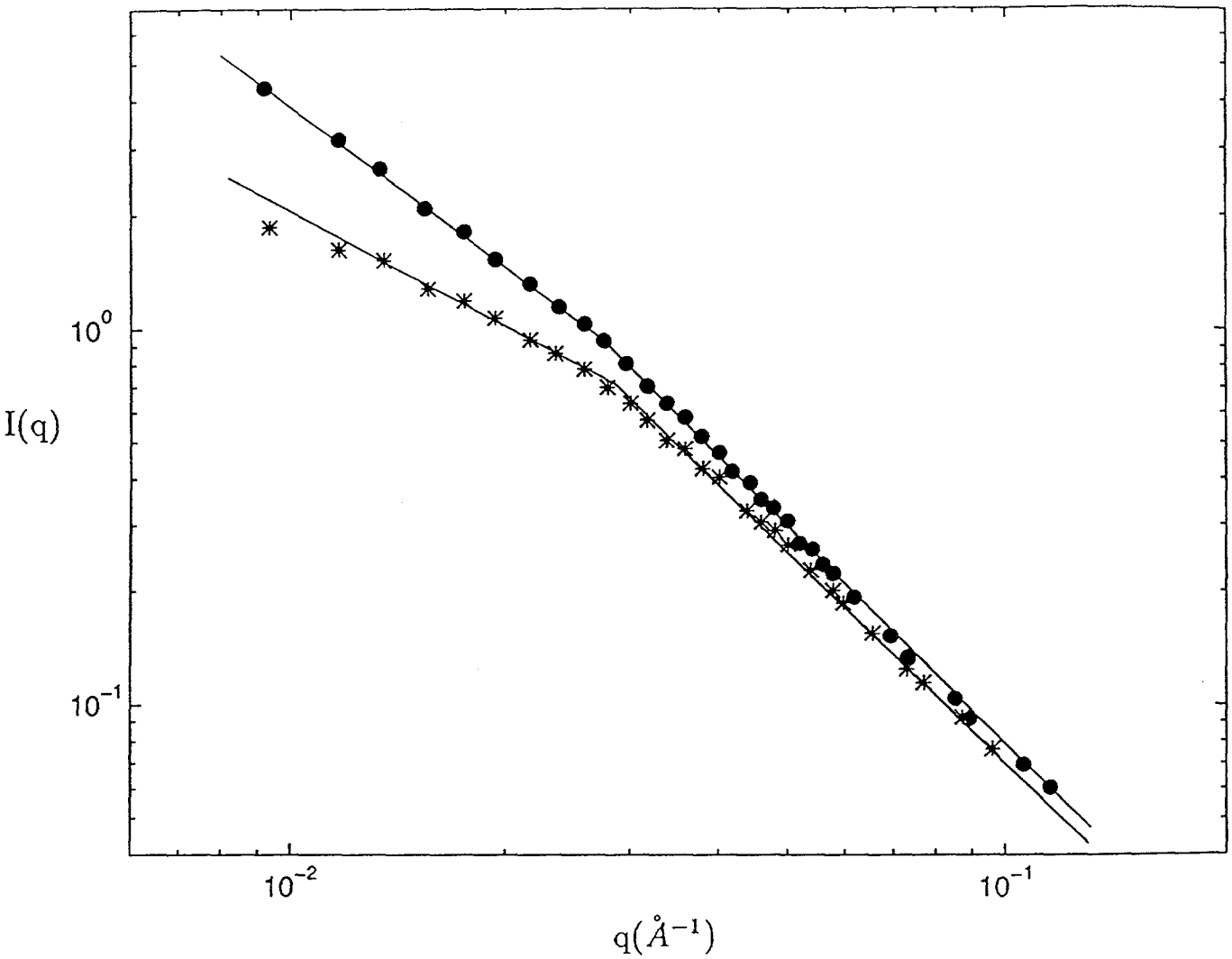
I(q)
10^0
10^{-1}
10^{-2}
10^{-1}
$q(\AA^{-1})$

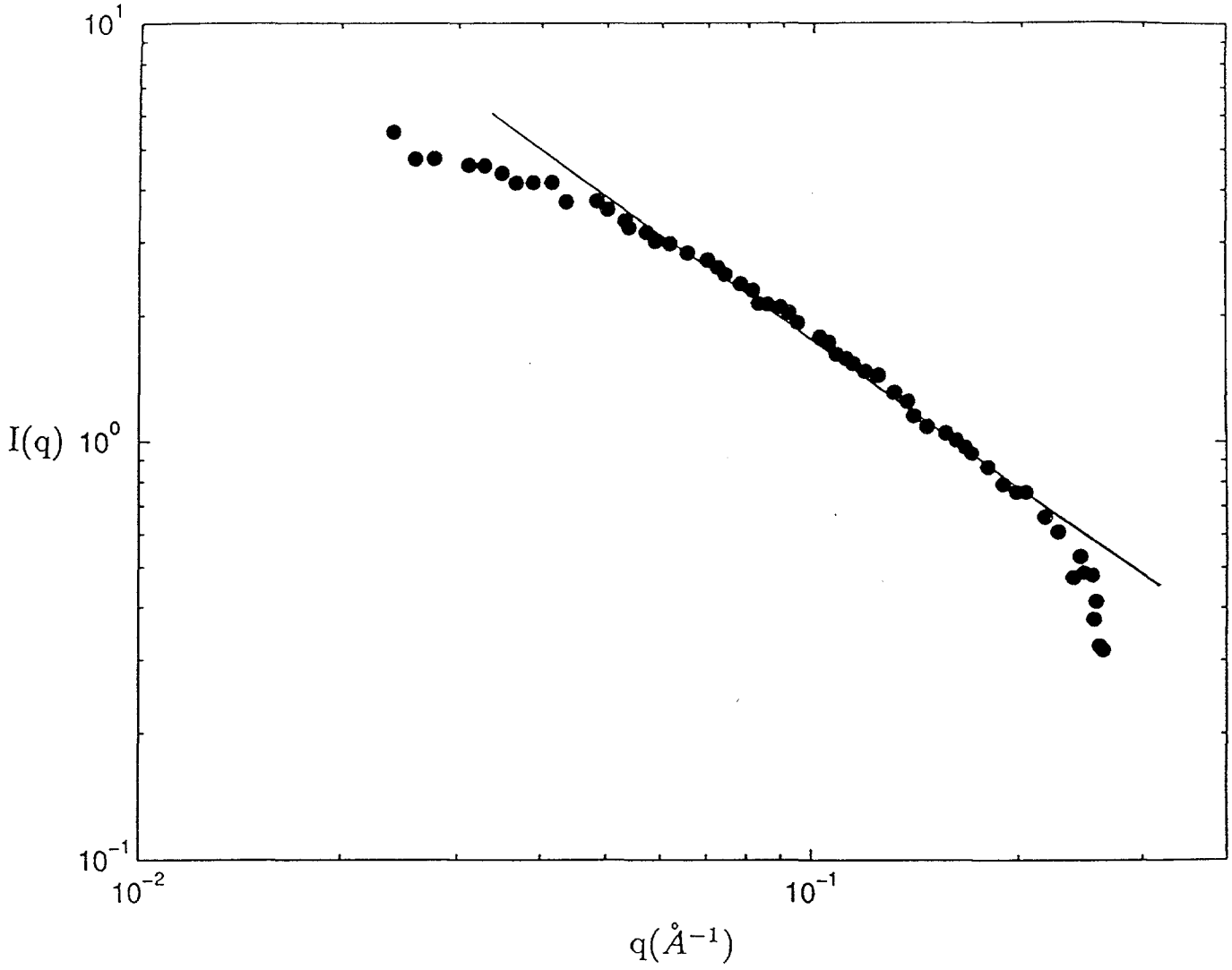
10^1
I(q) 10^0
10^{-1}
10^{-2}
10^{-1}
q($\AA^{-1}$)

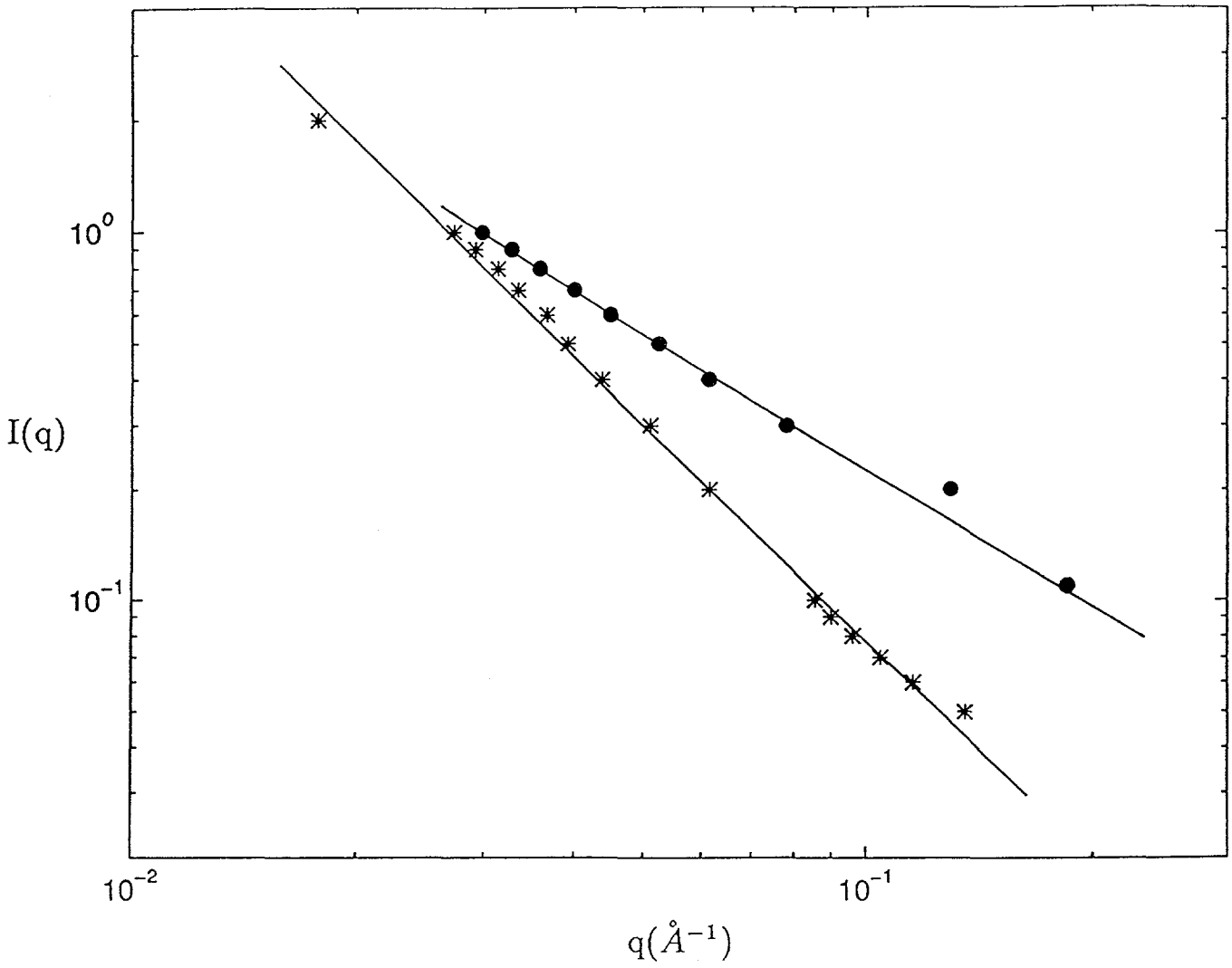
10^0
10^{-1}
I(q)
10^{-2}
10^{-1}
$q(\AA^{-1})$

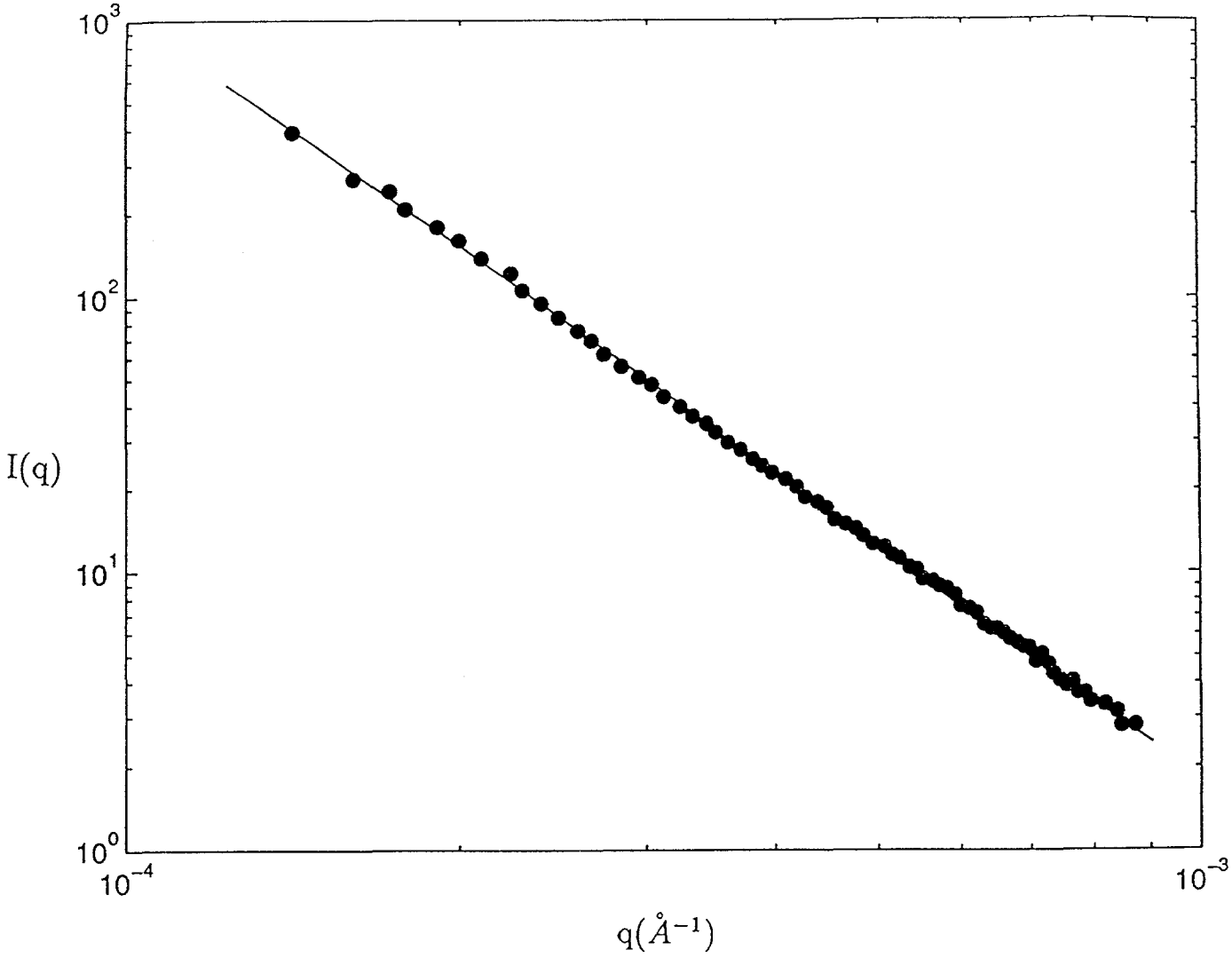
10^3
10^2
10^1
10^0
I(q)
10^{-4}
10^{-3}
$q(\AA^{-1})$

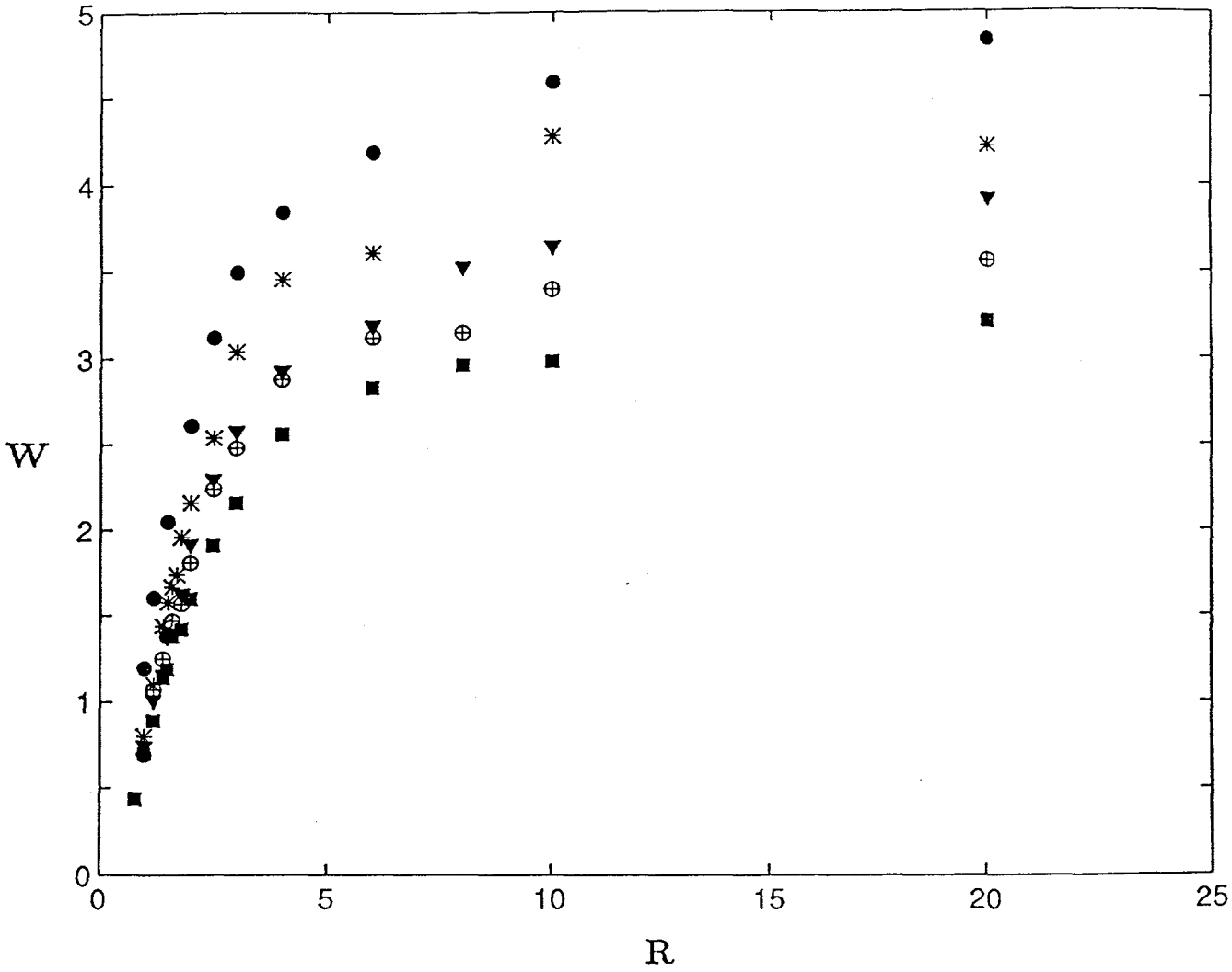

Fig

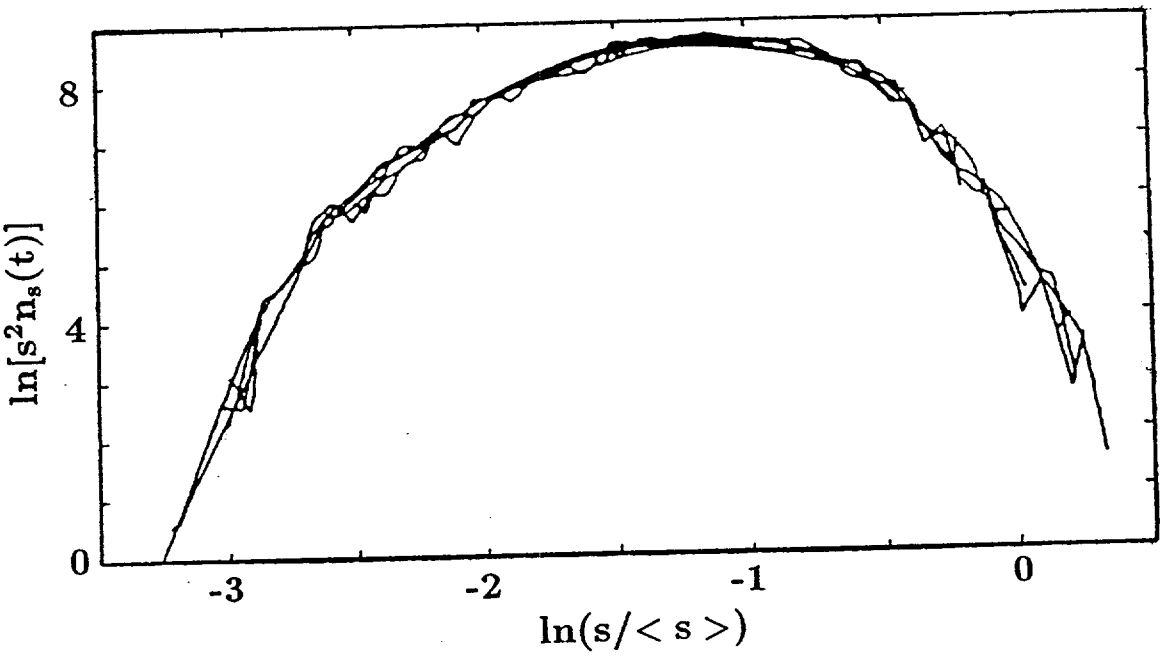

FIG 2

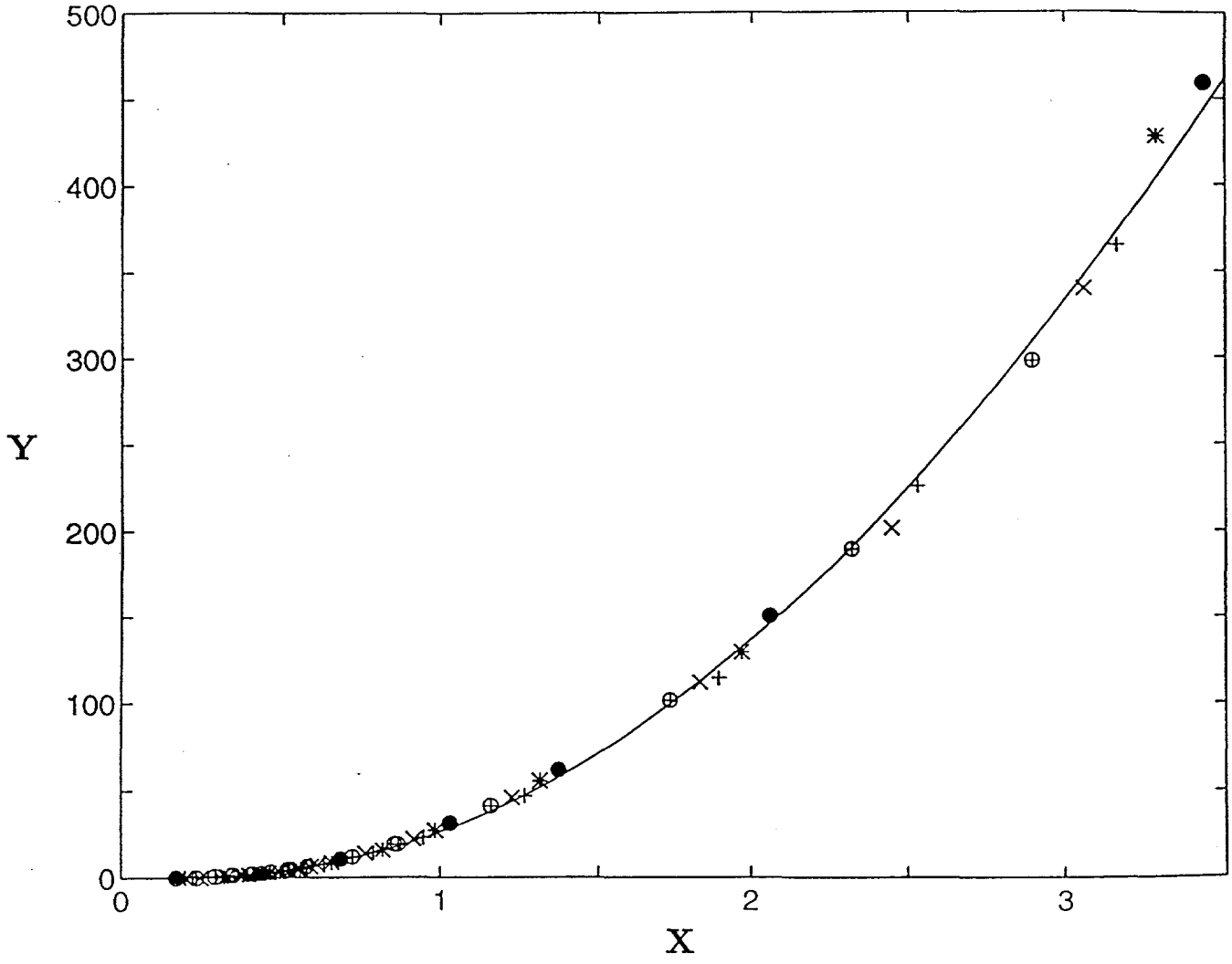

FB

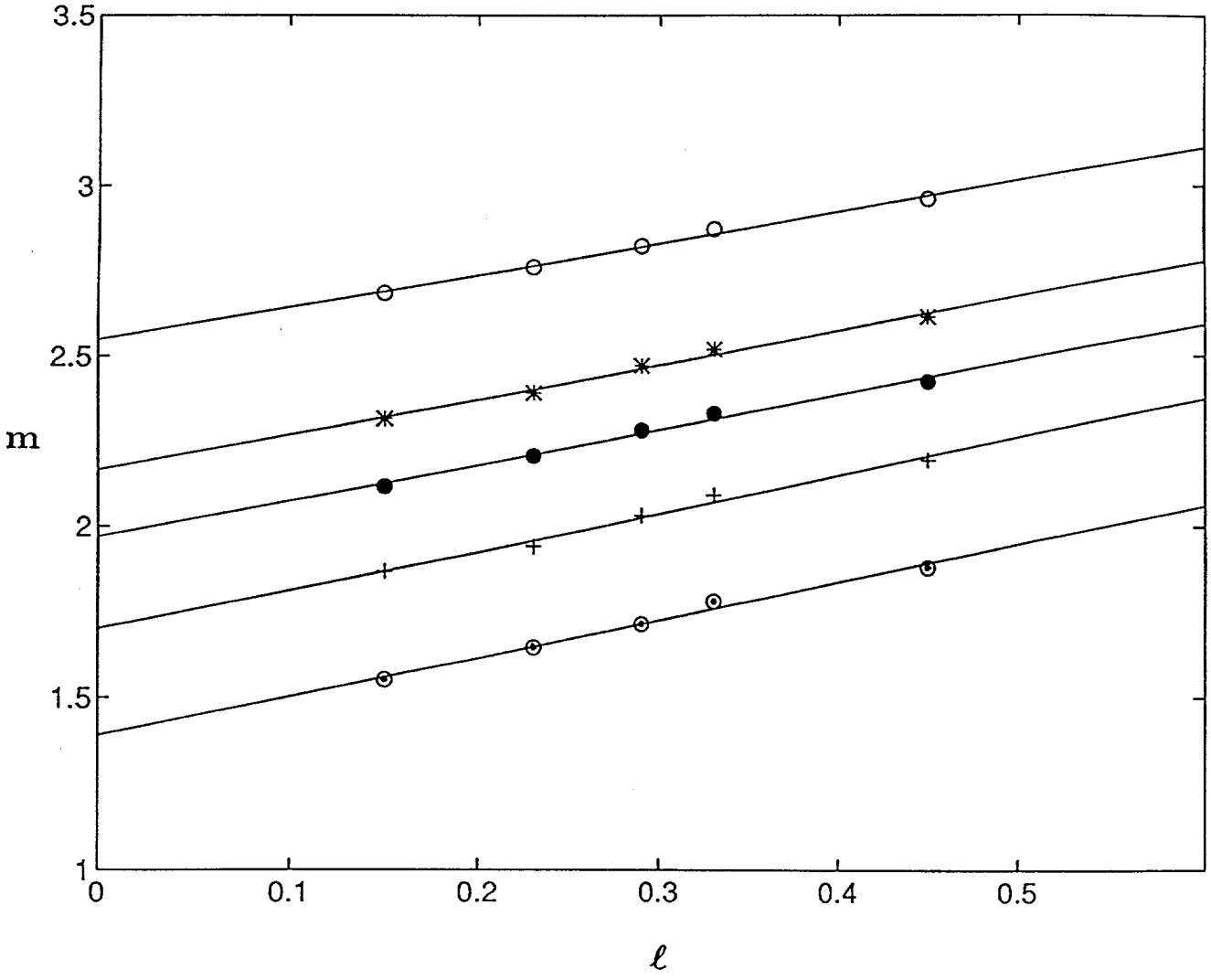

F14

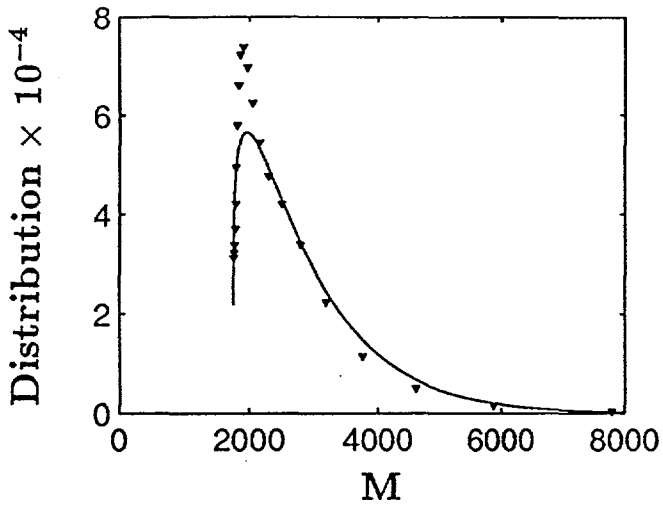
Distribution × 10^-4
8
6
4
2
0
0
2000
4000
6000
8000
M

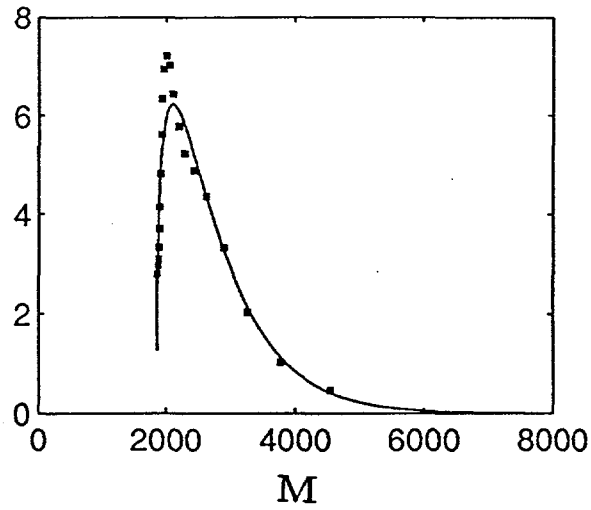
8
6
4
2
0
0
2000
4000
6000
8000
M

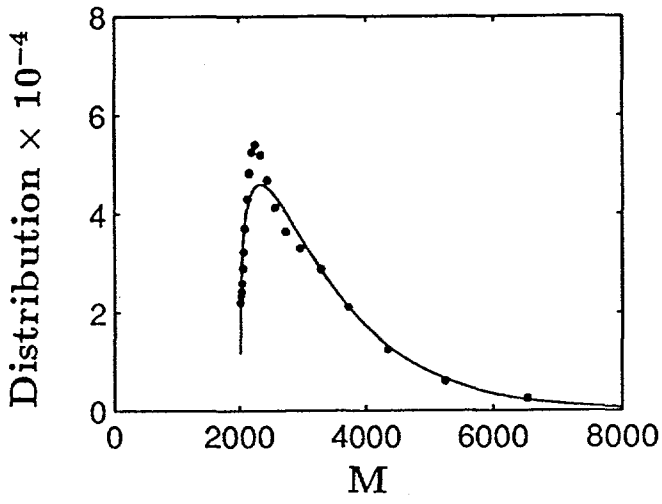
Distribution × 10^-4
8
6
4
2
0
0
2000
4000
6000
8000
M

Fig 5

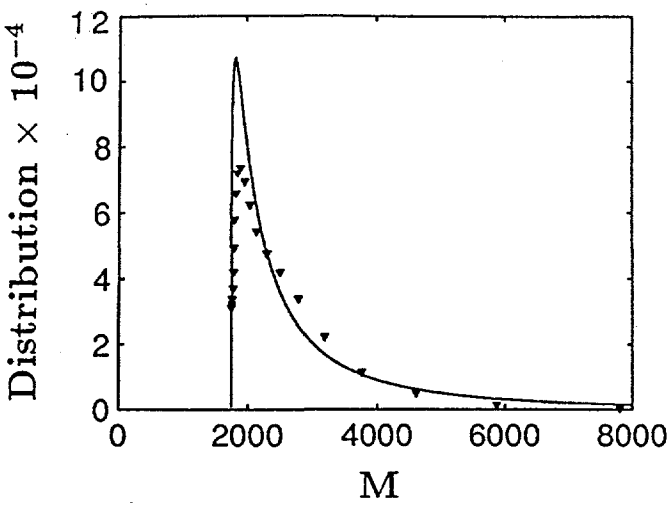
Distribution × 10^-4
12
10
8
6
4
2
0
0
2000
4000
6000
8000
M

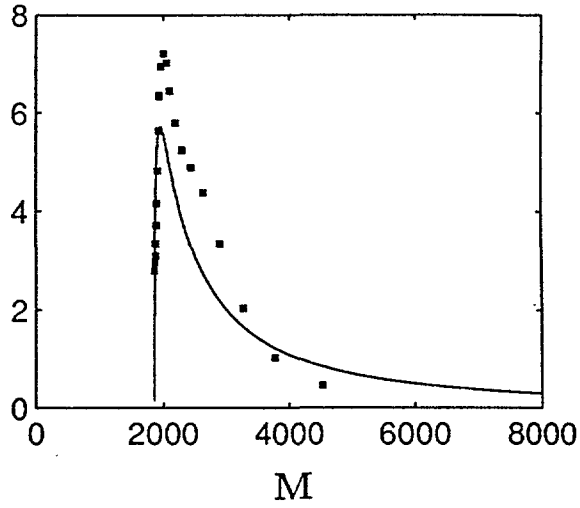
8
6
4
2
0
0
2000
4000
6000
8000
M

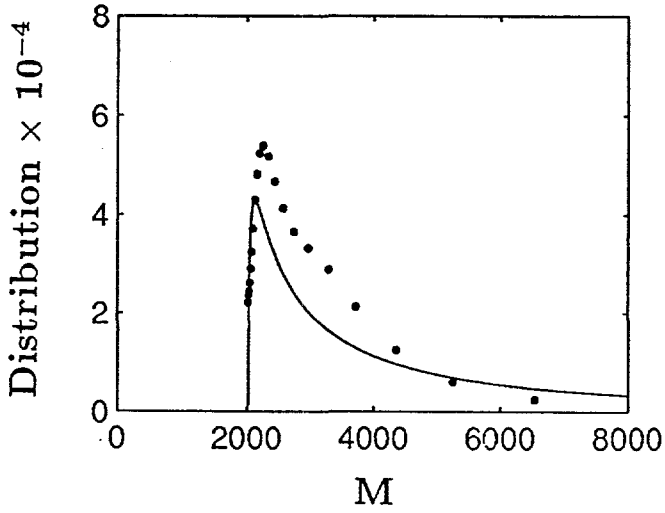
Distribution × 10^-4
8
6
4
2
0
0
2000
4000
6000
8000
M

FIG

Full, in press

Asphalt Flocculation and Deposition: III. The Molecular Weight Distribution

Bahram Dabir[1], Mehdi Nematy[1], Ali Reza Mehrabi[2], Hossein Rassamdana[2,3], and Muhammad Sahimi[2,*]

[1]Department of Chemical Engineering, Amir Kabir University of Technology, Hafez Avenue, Tehran, Iran

[2]Department of Chemical Engineering, University of Southern California, Los Angeles, CA 90089-1211, USA

[3]Improved Oil Recovery Research Center, National Iranian Oil Company, Taleghani Avenue, Tehran, Iran

We present extensive new experimental data for the molecular weight (MW) distributions of the asphalt and asphaltene aggregates, which are formed when a solvent is injected into a crude oil. The effects of various factors, such as the solvent, the solvent-to-oil volumetric ratio, and aging of the solution are all investigated. It is shown that if the asphalt- or asphaltene-containing solution has not reached equilibrium, one always obtains a bimodal MW distribution, which is due to the existence of two different types of aggregates with distinct structures and mechanisms of formation. However, after a long enough time the MW distribution will be unimodal. Based on the models that we have proposed for the formation the structure of the asphalt and asphaltene aggregates, which are based on the analysis of small-angle scattering and precipitation data, we propose analytical equations for the MW distribution of the aggregates which provide accurate predictions for our data.

---

*Corresponding author.

An important problem in the petroleum industry is enhanced recovery of oil by a miscible displacement process[1]. For example, miscible displacement of oil by carbon dioxide or natural gas is considered one of the most efficient methods of increasing oil production. However, this process often causes some changes in the fluid flow behavior and the equilibrium properties of the fluids. Under certain conditions such changes lead to the formation of heavy organic compounds on the pore surfaces of oil reservoirs, such as [2] asphaltenes and asphalts which are large molecular aggregates with complex structure and properties. Although many authors do not distinguish between asphalt and asphaltene, we define[2] the former as the latter plus resin, and use this terminology throughout this paper. Asphalts and asphaltenes are essentially amorphous solids that contain, in addition to carbon and hydrogen, nitrogen, oxygen, sulfur, and metals. Their formation is a function of the composition of the crude oil and the displacing agents, and the pressure and temperature of the reservoir. Their deposition on the surface of the pores reduces the permeability of the pore space, leading to the eventual isolation of oil from the flowing fluid in the reservoir[3] and reduction of the efficiency of the oil recovery process. Because of the practical importance of miscible displacements, it has been of great interest to understand the mechanisms that give rise to the formation of asphalt and asphaltene aggregates, their thermodynamic and transport properties, the point at which their precipitation on the pore surfaces is triggered, and its effect on the properties of the pore space. Although over the past several decades the nature of asphalts and asphaltenes and the mechanism of their precipitation on the pore surfaces of a porous medium have been studied intensively[2,4–14], no general consensus has emerged. One important reason for the lack of consensus is that most of these studies were not systematic in that, rather than investigating several important and related aspects of the problem, all in one study with similar compounds and under similar conditions, they considered only one aspect of the problem. The complexity of the structure of the asphalt and asphaltenes aggregates has also hindered progress.

In two previous papers[15,16] (hereafter referred to as Part I and Part II) we presented extensive new experimental data for the onset and amount of asphalt and asphaltene precipitation under a variety of conditions. In Part I we presented a new scaling approach to predicting such data, based on the similarities between asphalt and asphaltene formation and non-equilibrium aggregation phenomena. In Part II we presented an analysis of small-angle X-ray and neutron

scattering (SAXS and SANS, respectively) data, showing that they provide key insights into the structure of the asphalt and asphaltene aggregates, based on which we proposed the mechanisms that form them.

An important characteristic of the asphalt and asphaltene aggregates is their molecular weight (MW) distribution. In the past, there have been many studies of the MW distribution of the asphalts. Early studies[17–20] indicated that the MW of the asphalts can vary between 80,000 and 300,000. However, other studies[21–33] have provided evidence for much smaller MWs, ranging from 600 to 9,000. A wide variety of measurement techniques have also been used, especially in the more recent investigations[34–51], including light absorption coefficients, viscosity determination, vapour-pressure osmometry, and several others. With a few exceptions[39,44,46–48,50], these studies reported the *average* MW of the asphalts from various oils, and provided some statistics of their measurements, rather than giving the full distributions themselves. Theoretical investigations of the MW distribution of the asphalts are also rare[52,53]. Transport properties of the asphalts, such as their effective diffusivity in a pore, and how they vary with the MW distribution, have also been reported[54].

The purpose of this paper is to present the results of a systematic study of the MW distributions of the asphalt and asphaltene aggregates. We first present our new and extensive experimental data for the MW distributions of these aggregates, followed by their theoretical modelling. Our modelling is based on the results reported in Parts I and II. We show that those results lead us to new analytical equations for the MW distribution of the asphalt and asphaltene aggregates, which provide accurate predictions for the new data presented here.

EXPERIMENTAL PROCEDURE

We first describe briefly the experimental procedure for determining the MW distribution. The crude oil under study was a light tank oil with an API° 29.7, that was obtained from an oil field in southwest Iran. Table 1 shows its chemical composition and some PVT properties. We did not analyze the elemental composition of the oil, as it was not crucial to our results discussed in this paper. The tank oil was diluted by several solvents which were n-C_5, n-C_6, n-C_7, and n-C_{10}, and for several values of solvent to oil ratio R, measured in terms of cm^3 of the solvent/gr of the oil; we used R =1.5, 4.0, and 10.0. The samples were kept in a dark place in an inert gas to prevent oxidation, and they were stirred occasionally for 24 hours. In

the next step, the samples were filtered using the Wattman No. 42 filter paper. The filter papers were then washed by excess amount of the solvents. The asphalt that remained on the filter was used for measuring its MW distribution and its average. The asphaltene content was separated and measured by the standard IP-143 procedure. All the experiments were done at 18°C. Two average MWs were determined for the asphalts and asphaltenes, which were the weight-averaged molecular weight $\langle M_w \rangle$ and the number-averaged molecular weight $\langle M_n \rangle$. Also determined were the MW distributions using liquid size-exclusion chromatography, or gel permeation chromatography (GPC). The standard ASTM test method D3593–80 for determining the average MWs and the MW distributions of toluene-soluble aggregates was used.

The GPC instrument consisted of a solvent reservoir, a pump, a sample injection device, 4 packed columns, a solute detector, a flow rate detector, and a recorder. It had 4 different columns filled with Styragel, and nominal exclusion limits of 500, 10^3, 1500, and $10^4 \mathring{A}$ were used in the measurement process. Each column had a length of 120cm and a diameter of 1 cm. For each solvent, the columns of the GPC were calibrated using the polystyrene standard. The resulting calibration curve was then transformed to give a relationship between the retention volume and the molecular weight M.

The asphalts or asphaltenes were dissolved in toluene using a magnetic stirring device. The resulting solution was then injected into the chromatographic column packed with a solid and porous substrate, with a flow rate of 2 ml/min, in order to separate the various molecular aggregates according to their sizes. The concentrations of the separated aggregates were also determined and recorded. By using the MW calibration curves, the MW averages and the MW distribution for each experiment were determined. For R =1.5 and 4 they were measured 2 weeks after the solutions with toluene and the asphalts or asphaltenes were formed, while for $R = 10$ the measurements were done after 3 weeks. To investigate non-equilibrium (aging) effects on the growth of the aggregates, a separate measurement was carried out with n-C_6 and $R = 1.5$ after 4 weeks.

EXPERIMENTAL RESULTS AND DISCUSSION

Figure 1 shows the resulting MW distributions for the asphalts obtained with n-C_5. As can be seen, for all values of R the MW distributions have two maxima. The two maxima provide

strong evidence for the existence of *two* distinct types of asphalt aggregates in the solution. One type are those that are formed by the aggregation of the small elementary particles that are suspended in the oil. The size of such aggregates is relatively small, and thus the left-side maximum in the MW distribution is due to such aggregates. The other type of the asphalt aggregates are those that are formed by the aggregation of the first type of the aggregates and also the elementary particles still residing in the solution. The fact that there are two maxima in the MW distribution indicates that, not only the mechanisms of the formation of the two types of aggregates are different, their structures must also be very different. This distinction between the two types of the aggregates becomes clearer in the next section, where we discuss theoretical modelling of our data.

Figures 2-4 show the results for the asphalts obtained with n-C_6, n-C_7, and n-C_{10}. The qualitative features of these distributions are similar to those shown in Figure 1. A comparison of all the data indicates that, heavier solvents give rise to heavier, and thus larger, asphalt aggregates. Moreover, as the solvent becomes heavier, the MW distributions become broader. Note that, even the results for $R = 10$, which were measured 3 weeks after forming the asphalt-containing solutions, show a small but distinct maximum to the left of the main one. This indicates that, even after 3 weeks the asphalt-containing solutions still contained the small aggregates that are formed by the aggregation of the elementary particles.

Figures 5-8 show the results for the asphaltenes obtained with the same solvents. All the qualitative features of these results are similar to those of the asphalts, shown in Figures 1-4. There are, however, two differences between the two sets of MW distributions. If we compare the results that were obtained with $R = 1.5$ and 4, we find that, compared with the asphalts, a larger number of asphaltene aggregates with relatively large MWs have been formed. This difference is clearly seen in Figures 4 and 8. Moreover, the MW distributions of the asphaltenes are generally broader than those of the asphalts. Both differences can be attributed to the fact that, in order to form the asphaltene-containing solutions, the resins, which have smaller MWs than the asphaltenes, are removed from the asphalt solutions. To make this point clearer, we present in Tables 2-5 the averages of all the MW distributions, which confirm our assertion.

We point out that, in general, the MW distribution evolves with time as the aggregation of the asphalt and asphaltene particles proceeds. Thus, if the asphalt- or asphaltene-containing

solution is aged for a long enough time, the maximum that is due to the existence of the small aggregates should disappear, since there would be ample time for such aggregates to join together and form larger aggregates, and thus one should obtain only a unimodal MW distribution. This is clearly seen in Figure 9, where we show the results for the asphaltenes obtained with n-C_6 and $R = 1.5$ after 4 weeks. The distribution is unimodal, thus confirming our assertion. We shall come back to this point in the next section.

THEORETICAL MODELLING

In Part II we analyzed extensive small-angle X-ray and neutron scattering (SAXS and SANS, respectively) data, based on which we proposed the mechanisms for the formation of the asphalt and asphaltene aggregates. We proposed that two important and much studied[55] aggregation phenomena, namely, diffusion-limited particle (DLP) and diffusion-limited cluster-cluster (DLCC) aggregation are the basic mechanisms that give rise to the molecular structures of the asphalts and asphaltenes. Since these are directly related to our discussion in this paper, let us first briefly summarize the essential ideas behind the DLP and DLCC aggregation phenomena and models, and how discuss SAXS and SANS data lead us to the identification of the structure of the asphalts and asphaltenes.

In the DLP aggregation model[56] the site at the center of a lattice (or a continuum) is occupied by an stationary particle. Another new particle is then injected into the lattice, far from the center, which diffuses on the lattice until it reaches a surface site, i.e., an empty site which is a nearest-neighbor to the stationary particle, at which time the particle sticks to it and remains there permanently. Another diffusing particle is then injected into the lattice to reach another surface (empty) site and stick to it, and so on. If this process is continued for a long time, a large aggregate is formed, a typical three-dimensional (3D) example of which is shown in Figure 10. One of the most important properties of the DLP aggregates is that, they are self-similar and fractal. This means that if s is the number of the elementary particles in an aggregate of radius R_a, then one has

$$s \sim R_a^{D_f} \ , \tag{1}$$

where D_f is the fractal dimension of the aggregate. Computer simulations indicate[55] that $D_f \simeq 2.5$ for 3D DLP aggregates. A fractal dimension less than the Euclidean dimension of

the space implies that the aggregate cannot fill the space, and has a sparse structure.

In the DLCC aggregation model[57,58] one starts with an empty lattice (or a continuum). At time $t = 0$, a fraction p_0 of the lattice sites are selected at random and occupied by elementary particles. Each occupied site contains only one particle. If p_0 is small, the system will consist of a large number of isolated occupied sites and a few small clusters of particles. A cluster is a set of nearest-neighbor particles. One cluster, including a single particle, is then selected at random and is allowed to diffuse in a randomly-chosen direction. Then the perimeter sites of the cluster – the set of sites that are adjacent to the cluster – are examined to see whether they are occupied by other particles or clusters. If so, the perimeter particles or clusters are attached to the cluster that was moved to form a larger cluster. Another randomly-selected cluster is moved again, its perimeter is examined for possible formation of a larger cluster, and so on. Figure 11 shows several stages of this process in 2D. The DLCC aggregates are also fractal objects, and extensive computer simulations suggest[55] that for DLCC aggregates $D_f \simeq 1.8$ in 3D, which is smaller than that of the DLP aggregates, since aggregation of clusters creates larger holes in the final molecular structure than that of elementary particles (compare Figures 10 and 11).

An important property of fractal aggregates, which is relevant to our paper, is the roughness of their surface. Since the clusters that aggregate together have irregular shapes and sizes, their *active* surface area S_a, i.e., that part of their surface which is most likely to collide with the surface of another cluster, is different from the *total* surface area of the cluster, and in fact it constitutes only a small fraction of it. For a growing cluster during aggregation S_a scales with the total number of particles s in the cluster as[55]

$$S_a \sim s^{\omega} , \tag{2}$$

where ω is a universal exponent, independent of many microscopic features of the cluster. As we discuss later, ω has a strong influence on the shape of the MW distribution of the aggregates. Obviously, $\omega < 1$, since the active surface area of a cluster cannot grow with its size faster than linearly.

An accurate probe of the structure of complex systems is small-angle scattering. In a scattering experiment the observed scattering intensity $I_s(q)$ by a single self-similar and fractal

cluster or aggregate is given by[59]

$$I_s(q) \sim q^{-D_f} \ , \tag{3}$$

where q is the magnitude of the scattering vector given by

$$q = \frac{4\pi}{\lambda} \sin\left(\frac{\theta}{2}\right) \ . \tag{4}$$

Here λ is the wavelength of the radiation scattered by the sample through an angle θ. Thus, a logarithmic plot of the scattering intensity $I_s(q)$ versus q (or the angle θ) should yield a straight line with the slope $-D_f$.

If the solution, with which the scattering experiment is carried out, contains many aggregates or clusters of various sizes, as is the case with a crude oil that contains many asphalt or asphaltene aggregates, then the intensity $I(q)$ scattered is the average sum of the intensities scattered by all the aggregates. Suppose that $n_s(t)$ is the number of the clusters or aggregates of size s in the solution at time t, where s represents the number of the elementary particles in an aggregate. If the aggregates are fractal, then it has been shown that[60]

$$n_s = s^{-\tau} f(s/\langle s \rangle) \ , \tag{5}$$

where τ is a universal exponents, $\langle s \rangle$ is the mean aggregate size, and $f(x)$ is a universal scaling function; for DLCC aggregates[60] $\tau = 2$. For a solution containing many aggregates of various sizes $I(q)$ is given by[61]

$$I(q) = \int s n_s I_s(q) ds \ , \tag{6}$$

which means that

$$I(q) \sim q^{-(3-\tau)D_f} \ . \tag{7}$$

Since for DLCC aggregates $\tau = 2$, Eqs. (3) and (7) are identical for this case. We point out that power-law scattering, such as Eqs. (3) and (7) can also arise from scatterers that are not fractal, but the distribution of their sizes is of power-law type. However, such is not the case with the asphalt and asphaltene particles.

Small-angle scattering data have been presented by several research groups[62–67]. In Part II we analyzed most of such data using the Eqs. (3) and (7), an analysis that had not been performed by most of authors[62–66] reporting the data. The data included both SANS and SAXS

which are known to have very different contrast mechanisms, especially for complex systems such as the asphalt and asphaltene aggregates. Despite this, both the SANS and SAXS data led us to the same conclusion regarding the structure of the asphalt and asphaltene aggregates: at large length scales (corresponding to small values of q) the asphalt and asphaltene aggregates are fractal with a fractal dimension $D_f \simeq 1.8$, whereas at small length scales (large q) the fractal dimension is $d_f \simeq 2.5$. Hereafter, we use D_f and d_f to denote the fractal dimensions of the large and small aggregates, respectively. To interpret these values of D_f and d_f, we proposed the following mechanisms for the formation of the aggregates which are based on our experimental observations. After the solvent is added, the resin, that covers the surface of the small individual particles and the self-associates suspended in the oil, is partially dissolved. The particles and the resin are both electrically charged, albeit with opposite signs, and therefore dissolution of the resin creates electrical imbalance between the particles. The small clusters are then formed by diffusion of the charged solid particles in the oil, which stick together upon collision. But, this is precisely how the DLP aggregates are formed. Their fractal dimension, which is about 2.5, is in agreement with the scattering results, $d_f \simeq 2.5$. After some time, one has a mixture of small clusters or aggregates of various sizes (which also carry a net electrical charge), as well as the individual charged particles. So, while the aggregation of the individual particles continues, aggregation of the clusters as well as the particles is also triggered. These clusters and particles also diffuse in the solution and stick to each other upon collision, which is precisely the mechanism by which the DLCC aggregates with a fractal dimension $D_f \simeq 1.8$ are formed. We showed in Part II that this picture of formation of the asphalt and asphaltene aggregates is completely consistent with our precipitation data presented in Part I.

If the asphalt- or asphaltene-containing solution is aged for a long time, then there would be ample time for the small aggregates to diffuse in the solution and stick together as they collide. As a result, one will have only one type of aggregate which is of DLCC type. This is also confirmed by the small-angle scattering data[16,63], and by our MW distribution data discussed above. High temperatures or pressures can distort the structure of the aggregates. As the temperature of the system rises, more resins are dissolved and thus the electrical charge imbalance between the particles or small clusters is much lower. Therefore, aggregates with much lower densities and effective fractal dimensions are formed. It is possible that the solution

will eventually contain DLCC and DLP aggregates with their effective fractal dimensions given above, but the time scale for reaching this state may be very long. This has been observed very clearly in several scattering experiments. The pressure of the system has an effect somewhat similar to that of the temperature. As the pressure rises, smaller aggregates with lower fractal dimensions are formed, and small-angle scattering experiments confirm this[66,68]. These experiments indicate that at small length scales (large q) one has $d_f \simeq 1.3$, much smaller than $d_f \simeq 2.5$ for DLP aggregates, while at large length scales D_f is *less than one*, implying that there is no DLCC aggregate in the solution at all, and one only has very small aggregates, in agreement with recent experiments[68] that indicate that with increasing pressure asphalt precipitation decreases. Thus, not only we identified[16] the fractal dimension of these aggregates, we also proposed the mechanisms for their formation. Our proposal is also supported by the very recent experiments of Toulhoat *et al.*[69] Using atomic force microscopy, they obtained beautiful pictures of asphalt aggregates that are completely similar to those shown in Figures 10 and 11, thus providing strong experimental evidence for our proposed mechanisms.

We should mention that, in the past there has been some speculation[67,70–73] about the possibility that asphalt and asphaltene aggregates may have a fractal structure. However, aside from Liu *et al.*[67], none of these authors specified what kind of a fractal structure the asphalt and asphaltene aggregates may possess, or proposed any mechanism for their formation. In the absence of any mechanism for the formation of a fractal structure with a given fractal dimension, one can, in principle, have an infinite number of ways by which the fractal dimension may arise. In fact, Park and Mansoori[70], Crickmore and Hruska[71], and Lin *et al.*[72] all stated that, if the asphalt and asphaltene aggregates are fractal, *their fractal structures and fractal dimensions cannot be specified*, and Raghunathan[73] speculated that the fractal structure of these aggregates is similar to that of *linear polymers*! Liu *et al.*[67] suggested that the asphalt aggregates are similar to those formed by a *reaction-limited* cluster-cluster aggregation process (as opposed to a *diffusion-limited* process proposed by us). In this phenomenon[55], two clusters do not stick to each other before many collisions between them take place. As a result, diffusion plays no role in the formation of such aggregates. For such fractal aggregates one has $D_f \simeq 2$ and $\tau = 3/2$. However, as we discussed in Part II, both the precipitation and small-angle scattering data indicate that DLP and DLCC aggregation processes are the most plausible

mechanisms of formation of the asphalt and asphaltene aggregates.

Based on these results, we can propose an analytical equation for the MW distribution of the asphalt and asphaltene aggregates. Botet and Jullien[74] studied the aggregate (cluster)-size distribution during aggregation processes, and derived an analytical formula for the *most probable* aggregate-size distribution. Suppose that at the beginning of the aggregation process there are N elementary particles, and that there are N_c clusters or aggregates in the system. Botet and Jullien[74] showed that, the most probable cluster-size distribution is given by $Nn_s/N_c^2 \sim f_\omega(N_c s/N)$, where ω is defined by Eq. (2). This equation tells us that $f_\omega(x)$ is simply a rescaled or reduced most probable aggregate-size distribution. Subject to certain assumptions, Botet and Jullien[74] also derived the following equation for $f_\omega(x)$

$$f_\omega(x) = cx^{-2\omega} \exp[-(1-2\omega)x] \,, \tag{8}$$

where c is a normalization constant obtained from $\int_0^\infty f_\omega(x)dx = 1$. Equation (8) can have a maximum only if $\omega < 0$, and is not expected to be very accurate if x is very small.

As discussed in Part II, we can convert Eq. (8) to a MW distribution for the asphalt and asphaltene aggregates by assuming that, the MW of an aggregate is proportional to its size. Since the data shown in Figures 1-9 indicate that there is a minimum molecular weight M_m at which the MW distribution is cutoff, Eq. (8) implies the following equation for the MW distribution for the asphalts and asphaltenes:

$$f_\omega(M) = c(M-M_m)^{-2\omega} \exp[-a(M-M_m)] \,, \quad M \geq M_m \,, \tag{9}$$

where a is a constant. However, Eq. (9) is appropriate if the MW distribution is unimodal which, as we discussed above, is the case if the solution is aged for a long enough time. If the MW distribution is bimodal, then we propose the following equation which is a generalization of (9) that allows for more than one maximum in the distribution:

$$f_\omega(M) = \sum_{i=1}^{2} c_i(M-M_{mi})^{-2\omega} \exp[-a_i(M-M_{mi})] \,. \tag{10}$$

The idea is that, each maximum is caused by an aggregation process which gives rise to a MW distribution given by Eq. (9), and Eq. (10) simply superposes the two distributions and maxima. In Eq. (10) subscripts 1 and 2 refer to the DLP and DLCC parts of the MW

distribution. Thus $M_{m1} = 0$, and M_{m2} represents the MW of the smallest asphalt or asphaltene aggregates that are of DLCC type. Since it is very difficult to directly measure M_{m2}, it has to be determined by fitting the data to Eq. (10). Taken together, there are 6 parameters in Eq. (10), which are c_i, a_i, ω, and M_{m2}, and are estimated by fitting the data to Eq. (10). However, although we can treat ω as an adjustable parameter, we provide evidence that ω may in fact take on a *universal* value. If so, and if the MW distribution has only one maximum (i.e., if there is only one type of the aggregate in the solution), all one has to do is specifying the minimum molecular weight M_m and determining the constant c from the normalization condition. Then, the MW distribution is completely specified.

The resulting fits of the data are also shown in Figures 1-9, and it can be seen that the agreement between the predictions and the data is generally very good. Shown in Tables 6 and 7 are the estimated values of ω for both the asphalts and asphaltenes, obtained by fitting the MW distribution data to Eq. (10). There are two notable features in these results. One is that the estimated values of ω for the asphaltenes are generally larger than the corresponding values for the asphalts. That is, the asphaltenes have a smaller active surface area than the asphalts. This is undoubtedly due to the fact that, to obtain the asphaltenes the resins have to be removed from the asphalt-containing solutions. The absence of the resins generates smaller electric charge imbalance in the aggregates, and thus smaller active surface area. However, this may be a non-equilibrium effect, since the second notable feature of the results presented in Tables 6 and 7 is that, the results for $R = 10$, for which the measurements were done 3 weeks after the asphalt- or asphaltene containing solutions were formed, indicate that as the solutions reach equilibrium, ω appears to approach $-1/2$. Indeed, for the MW distribution shown in Figure 9, for which the measurements were done after 4 weeks, we estimate that $\omega \simeq -0.52$.

The result $\omega = -1/2$ for the DLCC aggregates can actually be derived. Suppose that $\mathcal{D}$ is the diffusivity of an asphalt or asphaltene aggregate diffusing in the solution. From the Stokes-Einstein relation we know that $\mathcal{D}$ is roughly proportional to R_a^{-1}, where R_a is the radius of the aggregate. Using Eq. (1) we obtain $\mathcal{D} \sim s^{-1/D_f}$ for an aggregate of s particles. Diffusion of the aggregates in the solution generates friction with a friction coefficient $C_f \sim 1/\mathcal{D} \sim s^{1/D_f}$, and a friction force $F \sim sC_f \sim s^{1+1/D_f}$. From the theory of diffusion processes we know that the velocity v of the diffusing aggregates is proportional to F^{-1}, implying that $v \sim s^{-(1+1/D_f)}$.

Thus, if we write $v \sim s^{\alpha}$, we obtain

$$\alpha = -\left(1 + \frac{1}{D_f}\right) . \tag{11}$$

On the other hand, Botet and Jullien[74] have derived the following relation between α and ω for a 3D DLCC aggregate

$$2\omega = \alpha + \frac{1}{D_f} . \tag{12}$$

If we substitute (11) into (12) we obtain $\omega = -1/2$. This agreement between the theory and our results is another confirmation of our proposed mechanisms of formation of the asphalt and asphaltene aggregates and their fractal structure. Therefore, it is not unreasonable to assume that $\omega = -1/2$ for all cases if the solutions reach equilibrium. A universal value of ω is also appealing, since it puts Eqs. (9) and (10) on an even firmer theoretical foundation. Finally, we note that for all the cases ω varies in a relatively narrow range which, given the wide spread in the data, is quite remarkable.

We point out that Eq. (10) is very robust. To see this, consider Figure 9 which indicates that there is only one maximum in the MW distribution. Despite this, we fitted the data to Eq. (10) rather than Eq. (9), and found that $c_1 = c_2$, $a_1 = a_2$, and $M_{m1} = M_{m2} = 0$. The significance of Eqs. (9) and (10) is *not* in the fact that they provide accurate representation of our data. In fact, Trauth *et al.*[52] suggested an empirical MW distribution which is very similar to Eq. (9). The most significant aspect of Eqs. (9) and (10) is that, these equations *can be derived*, with no empiricism involved, if we accept the mechanisms that we have proposed for the formation of the asphalt and asphaltene aggregates. We believe that in Part II and in the present paper we have presented ample evidence for the validity of these mechanisms, which is reinforced by the fact that the evidence comes from three *different* types of experimental data, namely, the precipitation, small-angle scattering, and the MW distributions data.

SUMMARY

We have presented extensive new experimental data for the MW distributions of the asphalt and asphaltene aggregates. We have shown that the type and amount of the solvent, and non-equilibrium (aging) effects have a strong influence on the shape and broadness of the MW distribution. Based on the mechanisms of formation and the structure of the aggregates that we proposed in Part II, we have also proposed new analytical equations for the MW distributions

of the asphalt and asphaltene aggregates, which not only provide accurate predictions for the new data presented in this paper, but also confirm our proposed mechanisms and structures.

ACKNOWLEDGMENTS

Work at USC was supported in part by the Department of Energy. We would like to thank K. P. Dowlati, M. H. Hazin, and S. Mashhadi Rafiee for helping us with the measurements.

REFERENCES

1. Sahimi, M., *Flow and Transport in Porous Media and Fractured Rock*, VCH, Weinheim, Germany, 1995

2. Speight, J. G., *The Chemistry and Technology of Petroleum,* Marcel Dekker, New York, 1991

3. Lichaa, P. M., and Herrera, L., *Society of Petroleum Engineers Paper 5304*, 1975

4. Preckshot, G. W., DeLisle, N. G., Cottel, C. E., and Katz, D. L., *Trans. AIME* 1943, **151**, 188

5. Katz, D. L., and Beu, K. E., *Ind. Engng. Chem.* 1945, **37**, 195

6. Dickie, J. P., Haller, M. N., and T. F. Yen, *J. Colloid Interface Sci.* 1969, **29**, 475

7. David, A., *AIChE Symp. Series* 1973, **69**, 56

8. Yen, T. F., *Energy Sources* 1974, **1**, 447

9. Tuttle, R. M., *J. Pet. Tech.* 1983, **35**, 1192

10. Monger, T. G., *Society of Petroleum Engineers/Department of Energy Paper 12708*, 1984

11. Monger, T. G., and Khakoo, A., *Society of Petroleum Enginners 10269*, 1981

12. Hirschberg, A., deJong, L. N. J., Schipper, B. A., and Meijer, J. G., *Soc. Pet. Eng. J.* 1984, **24**, 283

13. Monger, T. G., and Fu, J. C., *Society of Petroleum Enginners 16713*, 1987

14. Lihoreau, C., Briant, J., and Tindy, R. *Revue Inst. Francais Pét.* 1967, **22**, 797

15. Rassamdana, H., Dabir, B., Nematy, M., Farhani, M., and Sahimi, M., *AIChE J.* 1996, **42**, 10

16. Rassamdana, H., and Sahimi, M., *AIChE J.* 1996 (in press)

17. Pfeiffer, J. P., and Saal, R. N., *J. Phys. Chem.* 1940, **44**, 139

18. Labout, J. W., in *Properties of Asphaltic Bitumen* (Ed. J.P. Pfeiffer), Elsevier, New York, 1950, p 35

19. Ray, R. B., Witherspoon, P. A., and Gorin, R. E. J., *J. Phys. Chem.* 1957, **61**, 1296

20. Winniford, R. S., *J. Inst. Petrol.* 1963, **49**, 215

21. Sakhanov, A., and Vassiliev, N., *Petrol. Z.* 1927, **23**, 1618

22. Katz, M., *Can. J. Research* 1934, **10**, 435

23. Hillman, E. S., and Barnett, B., *Proc. Am. Soc. Test. Mat.* 1937, **37**, 558

24. Mack, C. J., *J. Phys. Chem.* 1932, **36**, 2901

25. Eckert, G. W., and Weetman, B., *Ind. Engng. Chem.* 1947, **39**, 1514

26. Fischer, K. A., and Schram, A., *Proc. 5th World Petrol. Congr.* 1959, Section V, Paper 20

27. Reerink, H., *Ind. Engng. Chem. Prod. Res. Dev.* 1973, **12**, 82

28. Markhasin, I. L., Svirskaya, O. D., and Strads, L. N., *Kolloid. Z.* 1969, **31**, 299

29. Altgelt, K. H., *Preprints, Am. Chem. Soc., Div. Petrol. Chem.* 1968, **13**(3), 37

30. Dickson, F. E., Davis, B. E., and Wirkkala, R. A., *Analyt. Chem.* 1969, **41**, 1335

31. Koots, J. A., and Speight, J. G., *Fuels* 1975, **54**, 179

32. Kirby, W. J., *J. Soc. Chem. Ind.* 1943, **62**, 58

33. Lever, M., *Ann. Conbust. Liquides* 1934, **9**, 511

34. Dickie, J. P., and Yen, T. F., *Analyt. Chem.* 1967, **39**, 1847

35. Moschopedis, S. E., Fryer, J. F., and Speight, J. G., *Fuel* 1976, **55**, 227

36. Moschopedis, S. E., and Speight, J. G., *Fuel* 1976, **55**, 187

37. Speight, J. G., Wernick, D. L., Gould, K. A., Overfield, R. E., Rao, B. M. L., and Savage, D. W., *Rev. Institut Francais Pet.* 1985, **40**, 52

38. Boduszynski, M. M., Raj Chadha, B., and Szkutta-Pochopien, T., *Fuel* 1977, **56**, 434

39. Boduszynski, M. M., *Energy & Fuels* 1987, **1**, 2.

40. Boduszynski, M. M., *Energy & Fuels* 1988, **2**, 597

41. Ignasiak, T., Kemp-Jones, A. V., and Strausz, O. P., *J. Org. Chem.* 1977, **42**, 312

42. Speight, J. G., and Moschopedis, S. E., *Fuel* 1980, **59**, 440

43. Schwager, I., and Yen, T. F., *Fuel* 1978, **57**, 100

44. McKay, J. F., Harnsberger, P. M., Erickson, R. B., Cogswell, T. E., and Latham, D. R., *Fuel* 1981, **60**, 17

45. McKay, J. F., Latham, D. R., and Haines, W. E., *Fuel* 1981, **60**, 27

46. Snape, C. E., and Bartle, K. D., *Fuel* 1984, **63**, 883

47. Acevedo, S., Méndez, B., Rojas, A., Layrisse, I., and Rivas, H., *Fuel* 1985, **64**, 1741

48. Acevedo, S., Escobar, G., Gutiérrez, L., and Rivas, H., *Fuel* 1992 **71**, 619

49. Strausz, O. P., Mojelsky, T. W., and Lown, E. M., *Fuel* 1992 **71**, 1355

50. Taylor, S.E., *Fuel* 1992, **71**, 1338

51. Senglet, N., Williams, C., Faure, D., Des Couriéres, T., and Guilard, R., *Fuel* 1990, **72**, 72

52. Trauth, D. M., Stark, S. M., Petti, T. F., Neurock, M., and Klein, M. T., *Energy & Fuels* 1994, **8**, 576

53. Storm, D. A., DeCanio, S. J., DeTar, M. M., and Nero, V. P., *Fuel* 1990, **69**, 735

54. Ravi-Kumar, V. S., Tsotsis, T. T., Sahimi, M., and Webster, I. A., *Chem. Eng. Sci.* 1994, **49**, 5789

55. Meakin, P., in *Phase Transitions and Critical Phenomena* (Eds. C. Domb and J. L. Lebowitz), Vol. 12, 1988, Academic Press, London, p 335

56. Witten, T. A., and Sander, L. M., *Phys. Rev. Lett.* 1981, **47**, 1400

57. Meakin, P., *Phys. Rev. Lett.* 1983, **51**, 1119

58. Kolb, M., Botet, R., and Jullien, R., *Phys. Rev. Lett.* 1983, **51**, 1123

59. Schaefer, D. W., Martin, J. E., Wiltzuis, P., and Cannel, D. S., *Phys. Rev. Lett.* 1984, **52**, 2371

60. Vicsek, T., and Family, F., *Phys. Rev. Lett.* 1984, **52**, 1669

61. Bouchaud, E., Delsanti, M., Adam, M., Daoud, M., and Durand, M., *J. Physique* 1986, **47**, 1273

62. Sheu, E. Y., Liang, K. S., Sinha, S. K., and Overfield, R. E., *J. Colloid Interface Sci.* 1992, **153**, 399

63. Herzog, P., Tchoubar, D., and Espinat, D., *Fuel* 1988, **67**, 245

64. Dwinggins, C. W., *J. Appl. Cryst.* 1978, **11**, 615

65. Storm, D. A., Sheu, E. Y., and DeTar, M. M., *Fuel* 1993, **72**, 977

66. Carnahan, N. F., Quintero, L., Pfund, D. M., Fulton, J. L., Smith, R. D., Capel, M., and Leontaritis, K., *Langmuir* 1993, **9**, 2035

67. Liu, Y. C., Sheu, E. Y., Chen, S. H., and Storm, D. A., *Fuel* 1995, **74**, 1352

68. Sahimi, M., Rassamdana, H., and Dabir, B., *Society of Petroleum Engineers Paper 35707*, 1996

69. Toulhoat, H., Prayer, C., and Rouquet, G., *Colloid. Surf.* 1994, **91**, 267

70. Park, S. J., and Mansoori, G. A., *Energy Sources* 1988, **10**, 109

71. Crickmore, P. J., and Hruska, C., *Fuel* 1989, **68**, 1488

72. Lin, J.-R., Lian, H., Sadeghi, K. M., and Yen, T. F., *Fuel* 1991, **70**, 1439

73. Raghunathan, P., *Chem. Phys. Lett.* 1991, **182**, 331

74. Botet, R., and Jullien, R., *J. Phys. A* 1984, **17**, 2517

Table 1

Tank oil PVT data

Component	Mole percent
C_1	0.0
C_2	0.0
C_3	0.0
i-C_4	0.05
n-C_4	0.64
i-C_5	1.69
n-C_5	2.21
n-C_6	4.23
C_7^+	91.18

C_3-asphalt weight percent = 11; n-C_7-asphalt weight percent = 2.2; molecular weight of the oil (measured by vapor pressure osmometer) = 200; specific gravity of the oil (at 60/60°F) = 0.8778 gr/cm^3; weight percent of C_{33}^+ fractions = 12.66; specific gravity of C_{33}^+ fractions (at 60/60°F) = 1.0186 gr/cm^3; normal boiling point of C_{33}^+ fractions = 468°C.

Table 2

The weight-averaged molecular weights $\langle M_w \rangle$ of the asphalts obtained with various solvents, and solvent to oil ratio R.

R	1.5	4.0	10.0
n-C_5	5694	5539	3138
n-C_6	8410	7946	3122
n-C_7	9085	7843	4337
n-C_{10}	7550	8373	3978

Table 3

The number-averaged molecular weights $\langle M_n \rangle$ of the asphalts obtained with various solvents, and solvent to oil ratio R.

R	1.5	4.0	10.0
n-C_5	1330	1180	876
n-C_6	2019	1897	852
n-C_7	2013	1705	1268
n-C_{10}	1719	1987	1089

Table 4

The weight-averaged molecular weights $\langle M_w \rangle$ of the asphaltenes obtained with various solvents, and solvent to oil ratios R.

R	1.5	4.0	10.0
n-C_5	5951	5680	4191
n-C_6	7422	9835	4727
n-C_7	11202	8582	4864
n-C_{10}	11427	11840	4707

Table 5

The number-averaged molecular weights $\langle M_n \rangle$ of the asphaltenes obtained with various solvents, and solvent to oil ratios R.

R	1.5	4.0	10.0
n-C_5	1553	1608	1437
n-C_6	1821	3095	1662
n-C_7	3108	2591	1622
n-C_{10}	3022	4629	1097

Table 6

Estimated values of the MW distribution parameter ω for the asphalts obtained with various solvents, and solvent to oil ratios R.

R	1.5	4.0	10.0
n-C_5	-0.28	-0.65	-0.44
n-C_6	-0.41	-0.37	-0.41
n-C_7	-0.37	-0.49	-0.50
n-C_{10}	-0.50	-0.37	-0.45

Table 7

Estimated values of the MW distribution parameter ω for the asphaltenes obtained with various solvents, and solvent to oil ratios R.

R	1.5	4.0	10.0
n-C_5	-0.43	-0.55	-0.50
n-C_6	-0.45	-0.58	-0.59
n-C_7	-0.52	-0.49	-0.62
n-C_{10}	-0.48	-0.69	-0.41

Captions

Figure 1. The molecular weight distributions of the asphalts obtained with n-C_5 and solvent to oil ratio (in cm^3 of the solvent/gr of oil) $R = 1.5$ (top left), 4 (top right), and 10 (bottom). Symbols represent the data, while the curves are the predictions of Eq. (10).

Figure 2. The same as in Figure 1, but with n-C_6 as the solvent.

Figure 3. The same as in Figure 1, but with n-C_7 as the solvent.

Figure 4. The same as in Figure 1, but with n-C_{10} as the solvent.

Figure 5. The molecular weight distributions of the asphaltenes obtained with n-C_5 and solvent to oil ratio (in cm^3 of the solvent/gr of oil) $R = 1.5$ (top left), 4 (top right), and 10 (bottom). Symbols represent the data, while the curves are the predictions of Eq. (10).

Figure 6. The same as in Figure 5, but with n-C_6 as the solvent.

Figure 7. The same as in Figure 5, but with n-C_7 as the solvent.

Figure 8. The same as in Figure 5, but with n-C_{10} as the solvent.

Figure 9. The molecular weight distribution of the asphaltenes obtained with n-C_6 and solvent to oil ratio $R = 1.5$ cm^3/gr of oil. The measurements were done 4 weeks after the asphaltene-containing solution was formed. Symbols represent the data, while the curve is the predictions of Eq. (10).

Figure 10. A typical three-dimensional diffusion-limited particle aggregate.

Figure 11. Three stages of formation of a two-dimensional diffusion-limited cluster-cluster aggregate.

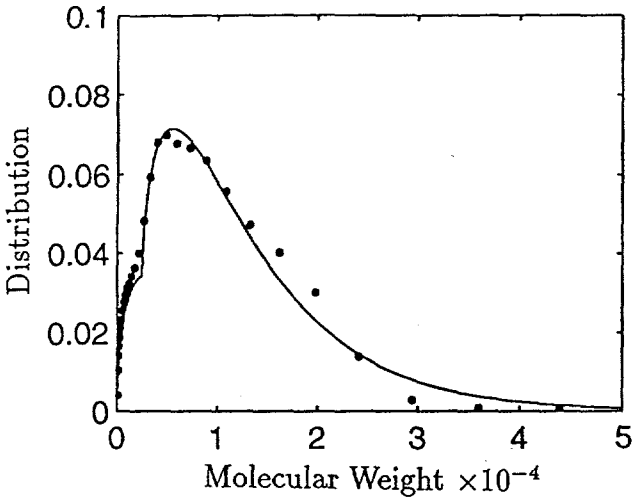
0.1
0.08
0.06
0.04
0.02
0
Distribution
0
1
2
3
4
5
Molecular Weight $\times 10^{-4}$

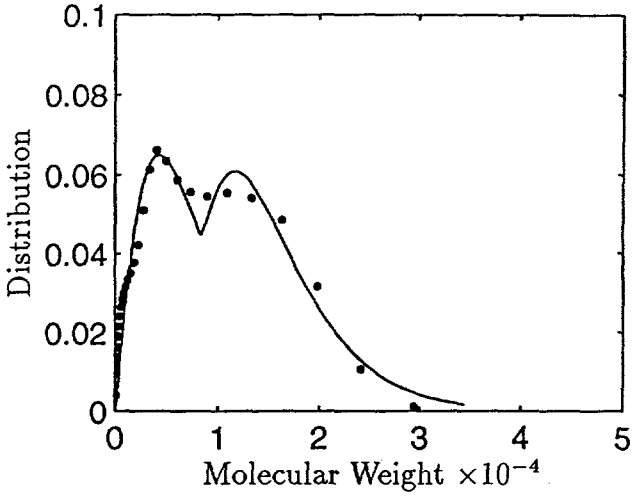
0.1
0.08
0.06
0.04
0.02
0
Distribution
0
1
2
3
4
5
Molecular Weight $\times 10^{-4}$

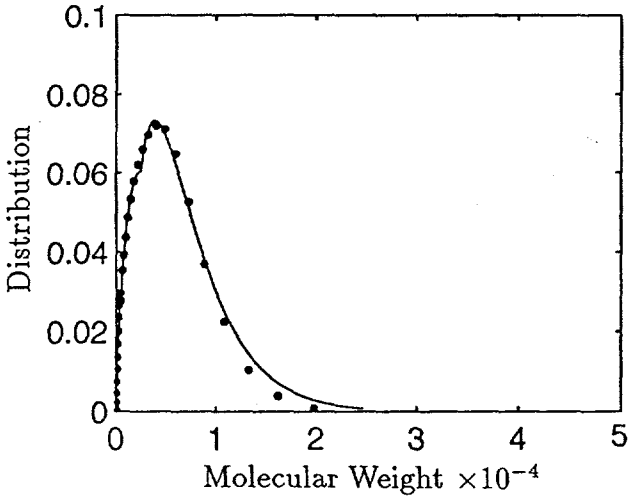
0.1
0.08
0.06
0.04
0.02
0
Distribution
0
1
2
3
4
5
Molecular Weight $\times 10^{-4}$

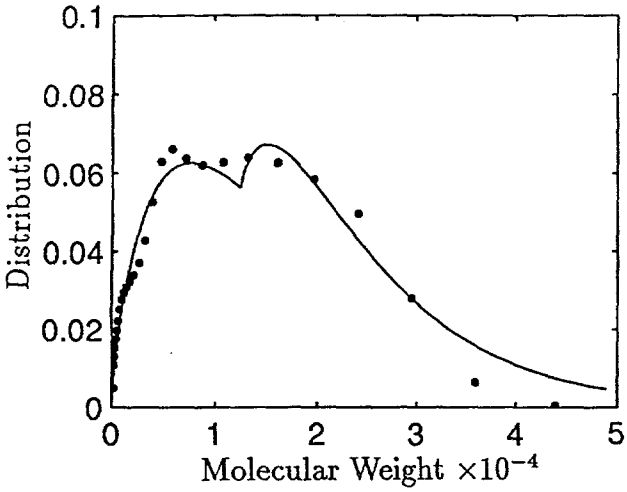
0.1
0.08
0.06
0.04
0.02
0
Distribution
0
1
2
3
4
5
Molecular Weight $\times 10^{-4}$

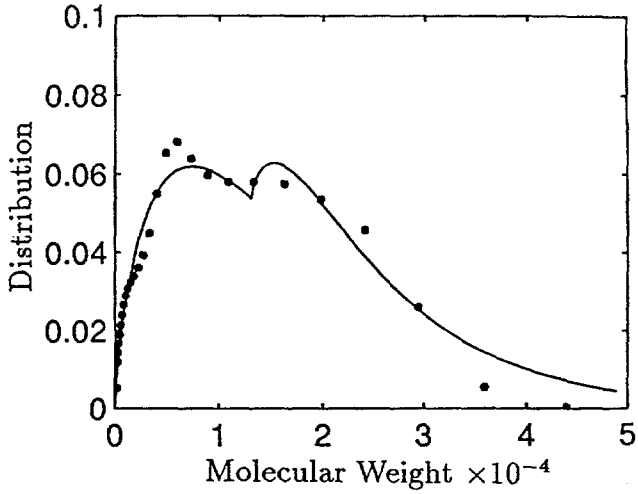
0.1
0.08
0.06
0.04
0.02
0
Distribution
0
1
2
3
4
5
Molecular Weight $\times 10^{-4}$

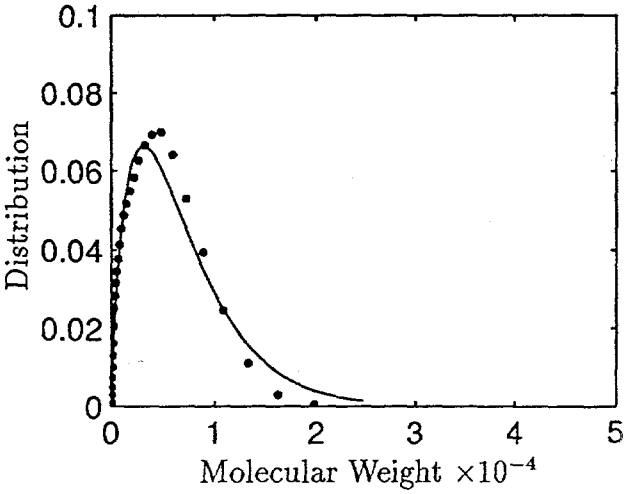
0.1
0.08
0.06
0.04
0.02
0
Distribution
0
1
2
3
4
5
Molecular Weight $\times 10^{-4}$

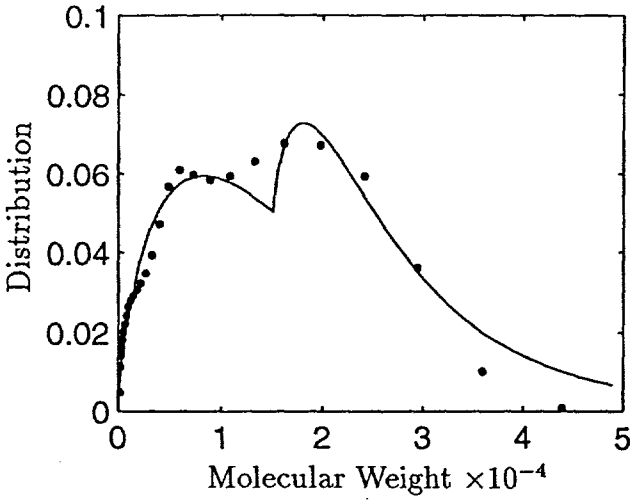
0.1
0.08
0.06
0.04
0.02
0
Distribution
0
1
2
3
4
5
Molecular Weight $\times 10^{-4}$

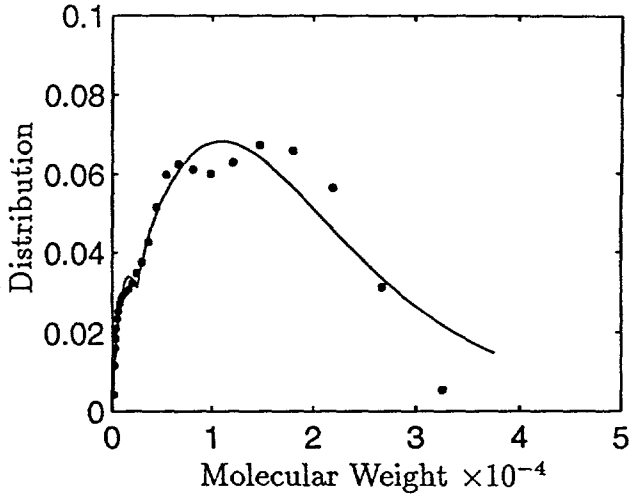
0.1
0.08
0.06
0.04
0.02
0
Distribution
0
1
2
3
4
5
Molecular Weight $\times 10^{-4}$

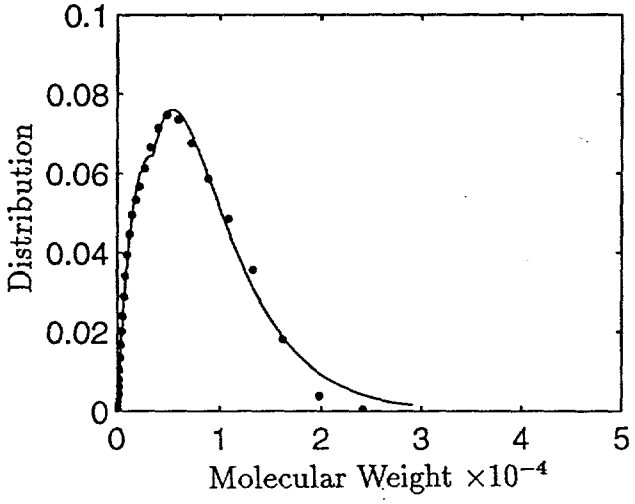
0.1
0.08
0.06
0.04
0.02
0
Distribution
0
1
2
3
4
5
Molecular Weight $\times 10^{-4}$

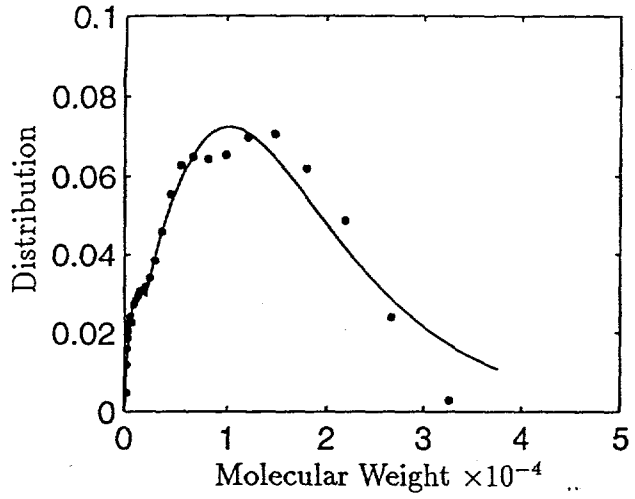
0.1
0.08
0.06
0.04
0.02
0
Distribution
0
1
2
3
4
5
Molecular Weight $\times 10^{-4}$

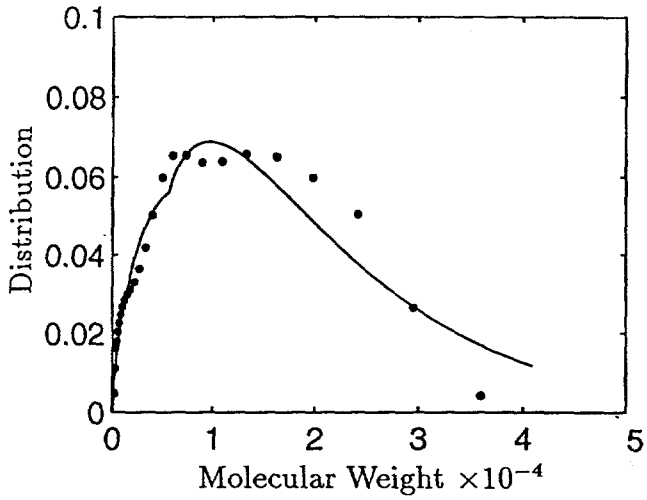
0.1
0.08
0.06
0.04
0.02
0
Distribution
0
1
2
3
4
5
Molecular Weight $\times 10^{-4}$

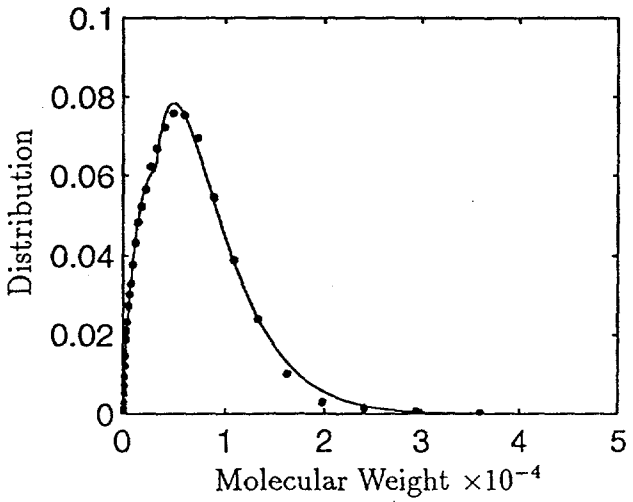
0.1
0.08
0.06
0.04
0.02
0
Distribution
0
1
2
3
4
5
Molecular Weight $\times 10^{-4}$

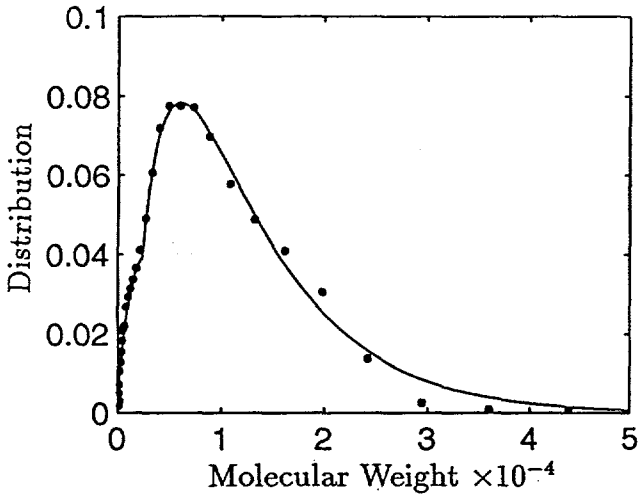
0.1
0.08
0.06
0.04
0.02
0
Distribution
0
1
2
3
4
5
Molecular Weight $\times 10^{-4}$

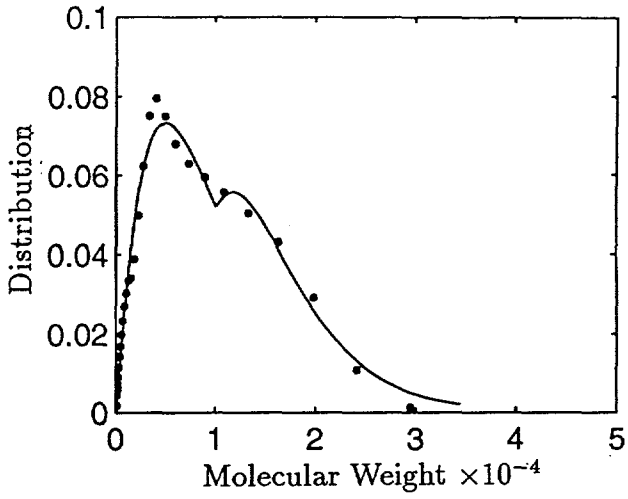
0.1
0.08
0.06
0.04
0.02
0
Distribution
0
1
2
3
4
5
Molecular Weight $\times 10^{-4}$

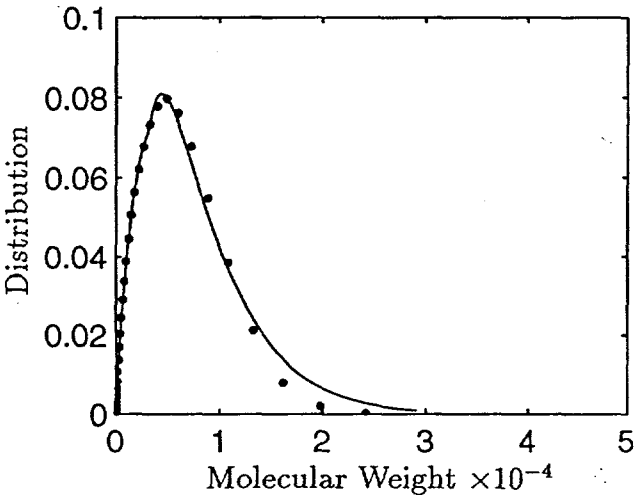
0.1
0.08
0.06
0.04
0.02
0
Distribution
0
1
2
3
4
5
Molecular Weight $\times 10^{-4}$

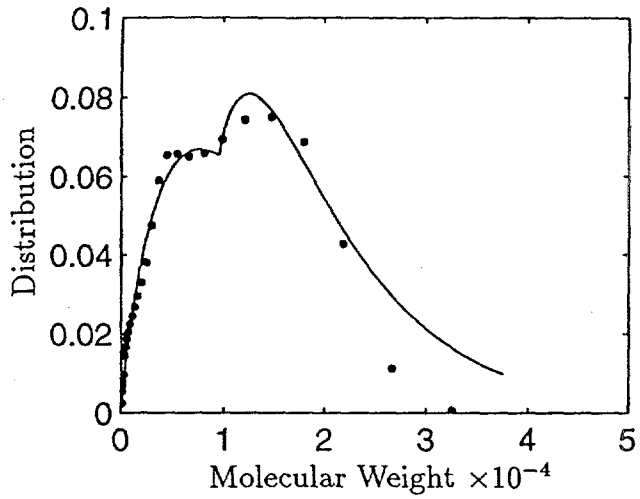
0.1
0.08
0.06
0.04
0.02
0
Distribution
0
1
2
3
4
5
Molecular Weight $\times 10^{-4}$

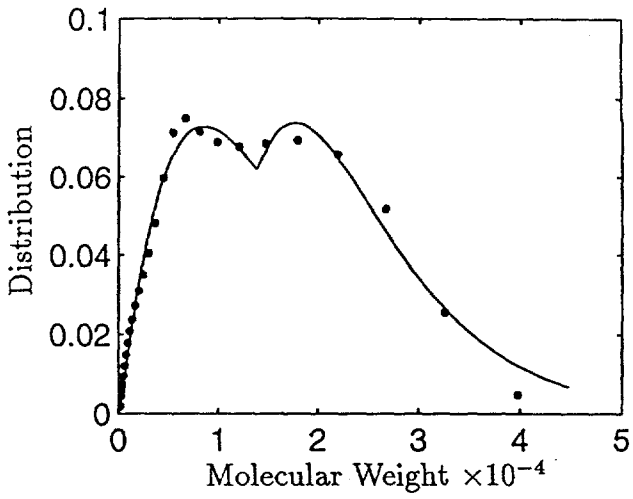
0.1
0.08
0.06
0.04
0.02
0
Distribution
0
1
2
3
4
5
Molecular Weight $\times 10^{-4}$

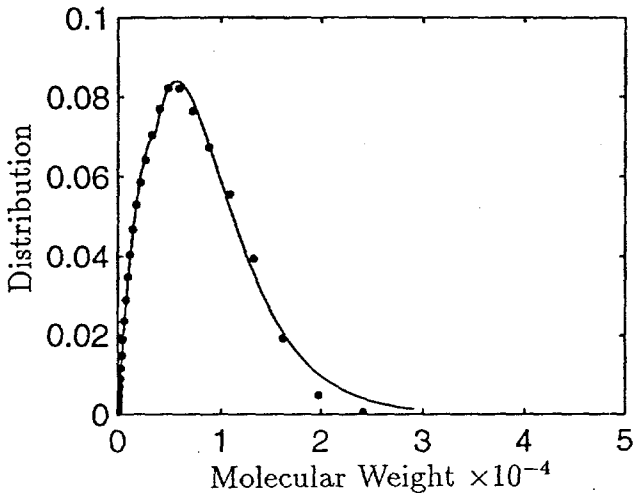
0.1
0.08
0.06
0.04
0.02
0
Distribution
0
1
2
3
4
5
Molecular Weight $\times 10^{-4}$

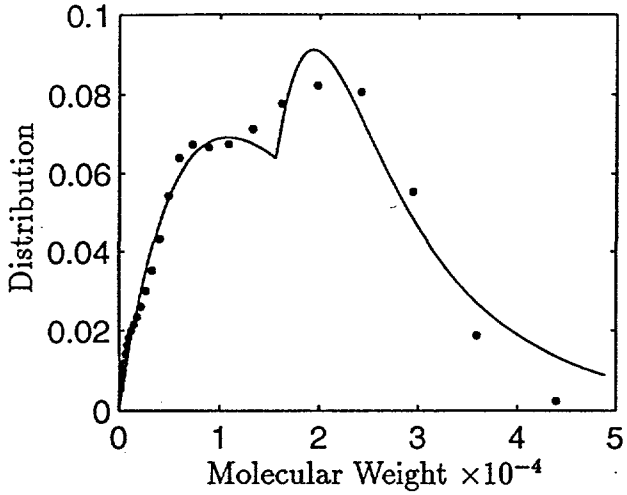
0.1
0.08
0.06
0.04
0.02
0
Distribution
0
1
2
3
4
5
Molecular Weight $\times 10^{-4}$

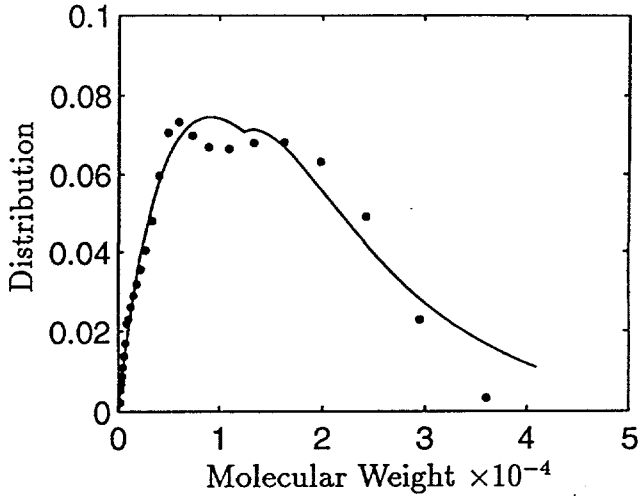
0.1
0.08
0.06
0.04
0.02
0
Distribution
0
1
2
3
4
5
Molecular Weight $\times 10^{-4}$

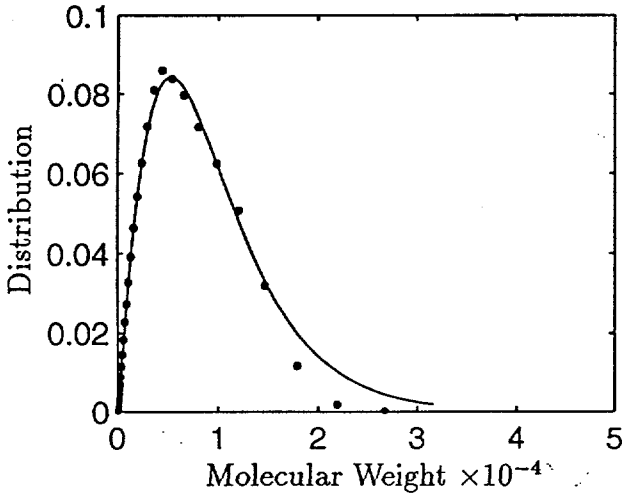
0.1
0.08
0.06
0.04
0.02
0
Distribution
0
1
2
3
4
5
Molecular Weight $\times 10^{-4}$

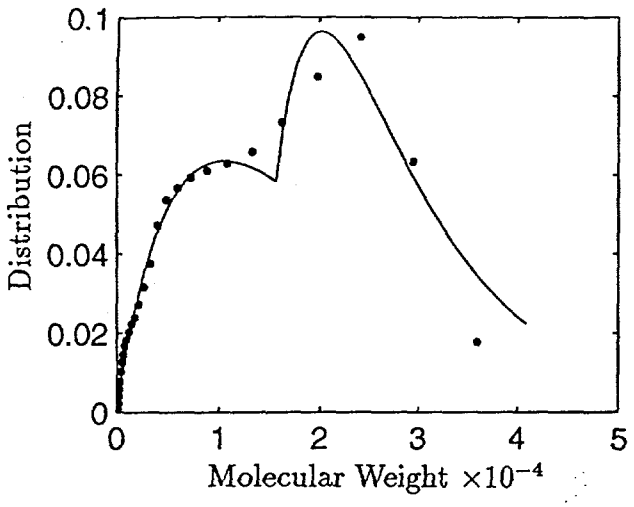
0.1
0.08
0.06
0.04
0.02
0
Distribution
0
1
2
3
4
5
Molecular Weight $\times 10^{-4}$

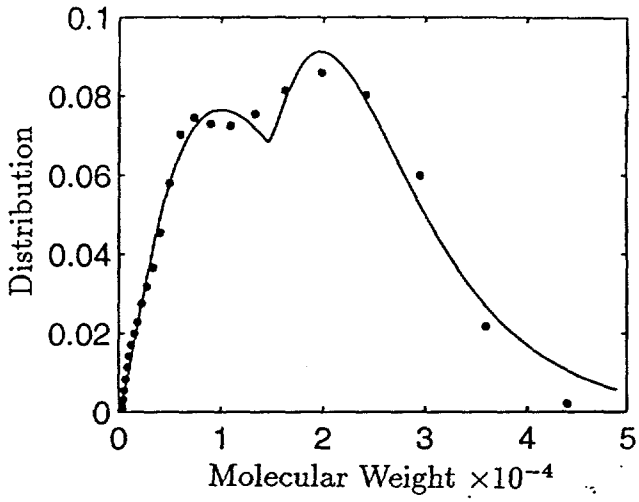
0.1
0.08
0.06
0.04
0.02
0
Distribution
0
1
2
3
4
5
Molecular Weight $\times 10^{-4}$

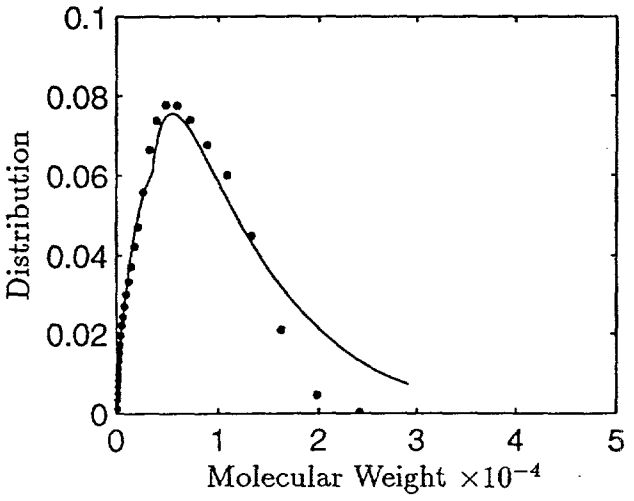
0.1
0.08
0.06
0.04
0.02
0
Distribution
0
1
2
3
4
5
Molecular Weight $\times 10^{-4}$

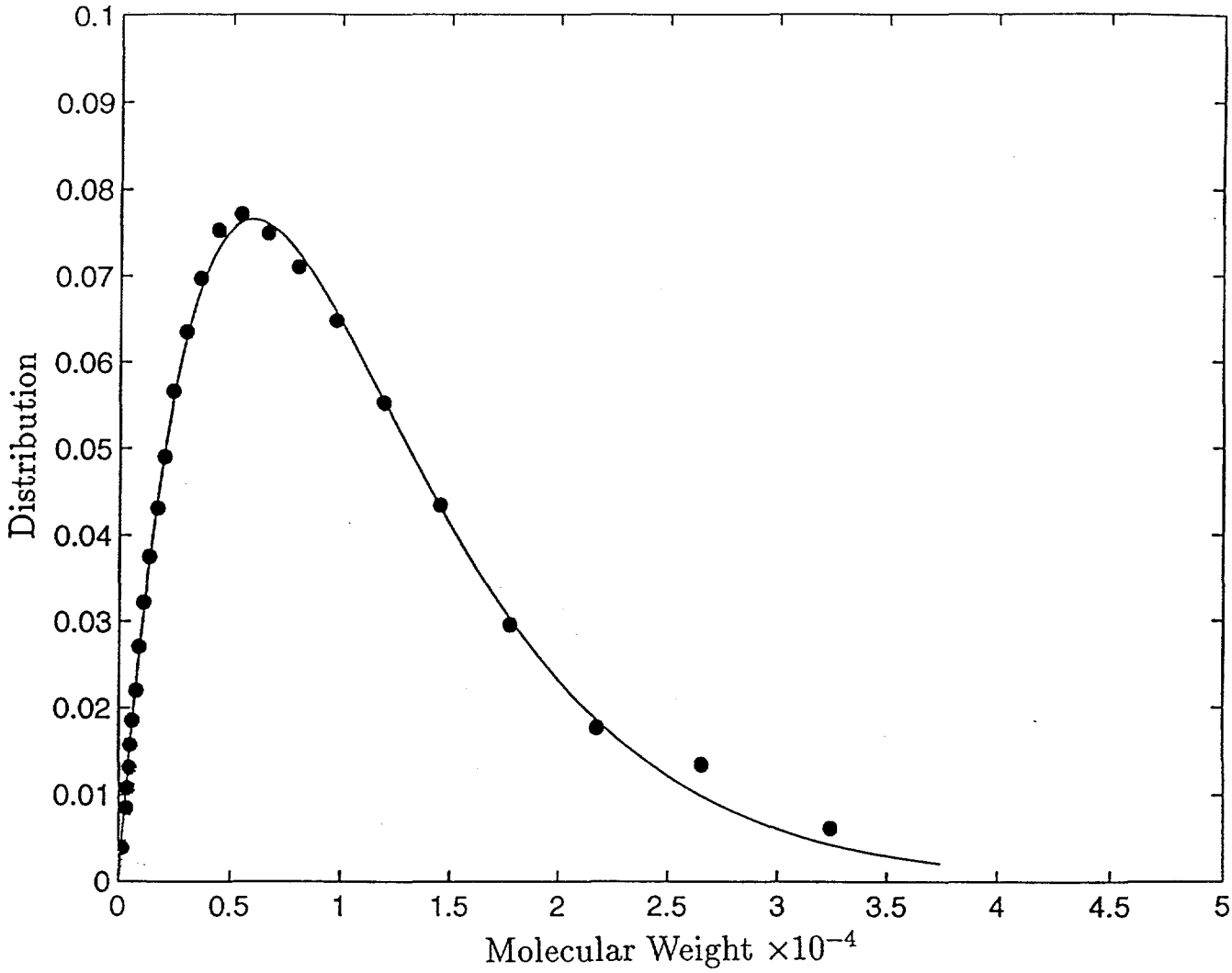
0.1
0.09
0.08
0.07
0.06
0.05
0.04
0.03
0.02
0.01
0
Distribution
0
0.5
1
1.5
2
2.5
3
3.5
4
4.5
5
Molecular Weight $\times 10^{-4}$

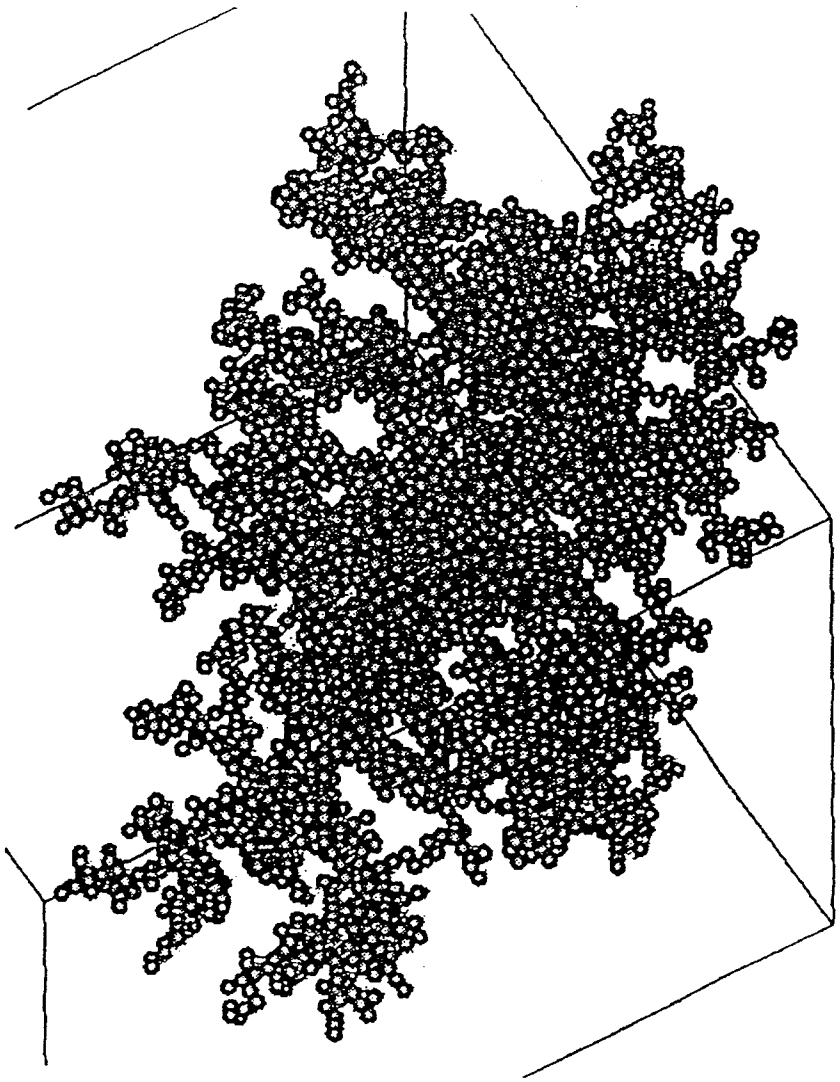

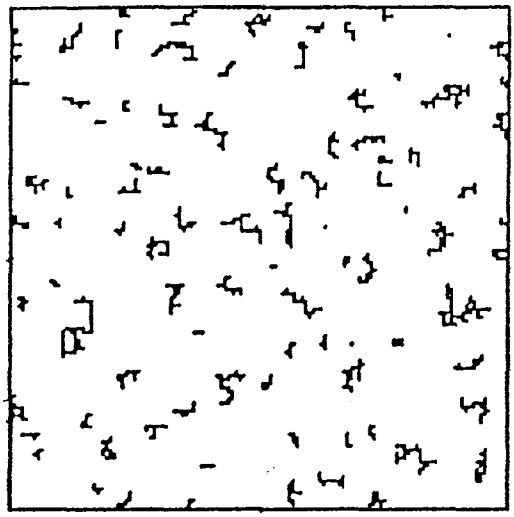

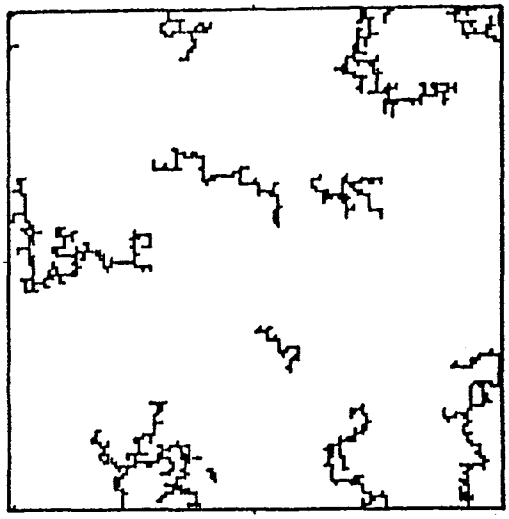

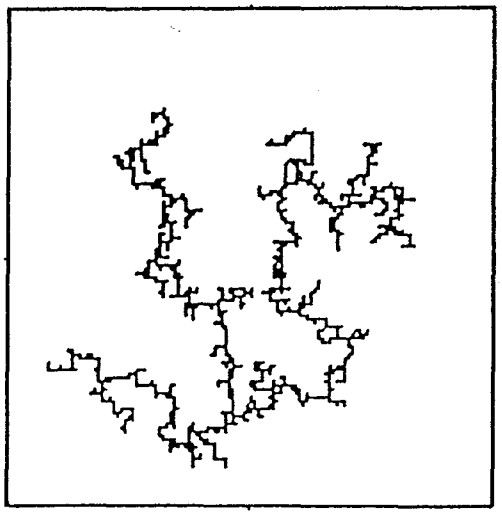

PREFACE

A significant portion of the experimental work on this grant (DE-FG22-92PC92527) was performed with coal-derived materials. However, much of the data from this work was part of an unfinished doctoral thesis that has been lost due to circumstances beyond the control of the authors and the Department of Energy. Readers are cautioned to view the Final Report and Addendum accordingly. A publication resulting from this work (Yang, L., Zhu, Y. and Tsotsis, T. T., 1996,"The Use of Inorganic Membranes in Reactive Liquid Phase Applications" *Proceedings of the Fourth International Conference on Inorganic Membranes*, D. G. Fain, ed., 128-142) contains the following reference which is not available: Yang, L., "The Use of Membranes in the Study of Coal Liquids," 1996, Ph.D. Thesis, University of Southern California.

Addendum to the Final Report

DE-FG22-92PC92527 "Hindered Diffusion of Coal Liquids"

Theodore T. Tsotsis, Professor
Department of Chemical Engineering
University of Southern California
Los Angeles, CA 90089-1211

Muhammad Sahimi, Professor
Department of Chemical Engineering
University of Southern California
Los Angeles, CA 90089-1211

Dr. Ian Webster, President
Pronav Engineering
10530 Floral Dr.
Whittier, CA 90606

TABLE OF CONTENTS **Page**

1. INTRODUCTION AND BACKGROUND INFORMATION

This document is an addendum to the Final Report document for DOE contract DE-FG22-92PC92527 which was submitted on 7/02/96. This document was prepared in response to the request by the DOE program manager Mr. Robert Warzinski. This document contains unpublished experimental "raw" data on the transport/separation of coal liquids through membranes. These data were not included in the original report because they were deemed at that point not to be, for various reasons, of "archival journal" publication quality. The original goal of our University Coal Research program project was to further the fundamental understanding of the transport/separation of oil macromolecules through porous systems. Most of our experiments were carried out utilizing a variety of inorganic membranes; an extensive program of research focusing on the agglomeration/delamination behavior of such systems involved sorption/precipitation studies utilizing a variety of other model systems. All of this prior work has been published in archival journals and has been included in the Final Report submitted on 7/02/96. Further details about the literature on the state of the art in the field and the modeling part of the work can be found in the original Final Report.

In this document we will first briefly describe the experimental system used in the transport/separation investigations. Then we will concisely describe the data analysis techniques that were utilized. Subsequently we will detail the experimental data generated in this system that were not included in the final report previously submitted.

- **Background on Membrane Transport/Separation and Data Analysis Techniques**

A membrane is defined as a semipermeable barrier between two phases. This barrier, in order to be of value, must be permselective which means that it restricts the movement of molecules through it. Permselectivity can be obtained by many mechanisms. These include but are not limited to:

1) Size exclusion or molecular sieving;

2) Differences in diffusion coefficients (bulk as well as surface);
3) Differences in electrical charge;
4) Differences in solubility in sorption and/or reactivity within the membrane pores.

There are different types of membranes available. Of interest in this study were primarily inorganic membranes, which, because of their chemical and physical stability, have attracted research attention recently. Inorganic membranes can be categorized as dense and porous membranes. The dense inorganic membranes consist of solid layers of metal (Pd, Ag, various Ag alloys) or (oxidic) solid electrolytes which allow diffusion of hydrogen (or oxygen)in the form of ionic species. Another category of dense membranes consists of a porous support on which a "liquid" is immobilized. This liquid fills the pores completely and is itself semipermeable. Interesting examples of such membranes are molten salts immobilized in porous steel or ceramic supports and semipermeable to oxygen. Sometimes this liquid can be formed in situ as for example during the use of ceramic membranes in the decomposition of H_2S where liquid S is condensed in the pores and blocks hydrogen diffusion. Another example is the group of the so-called dynamic membranes where a hydroxide (gel) is precipitated in or on a porous support. Of interest in this study will be porous membranes consisting of a porous ceramic support with porous top-layers which can have different morphologies and microstructures.

The available ceramic membranes are characterized by two distinctly different pore systems. The first type of membranes (track-etch or anodic) are characterized by straight, nonintersecting pores either cylindrical or conical in shape running from one side of the membrane to the other. The membranes utilized mostly here are characterized by a porous structure, which consists of a percolating system of pores with more or less regular shapes or with a spongy structure. This is associated with the packing of particles resulting during the preparation of such membranes. In composite membranes the top layer is modified further by precipitation of a new phase followed by further treatment. This results in a decrease of the pore size or in a change in the chemical character of the internal pore

surface.

The principle of separation through membranes of liquid macromolecular mixtures of interest in this study is by ultrafiltration, based on the concept of size exclusion or sieving. During separation of such a mixture the ultrafiltration membrane is characterized by its permeability and selectivity. Permeability is defined as the flux of permeate per unit transmembrane pressure (the average pressure difference across the membrane structure from the feed to the permeate side). Selectivity is defined as the ratio of the solute concentrations in permeate and feed. These two characteristic parameters of an ultrafiltration process are affected by many operating conditions. The following discussion presents the theory utilized in analyzing the experimental data in order to calculate the permeability and selectivity of the membranes towards the various liquids investigated.

- **Permeability**

The pore structure of an ultrafiltration membrane can be modeled by various techniques. For the purposes of this study a simple "parallel bundle of pores" model will be utilized which considers the pore structure to consist of n parallel straight cylindrical capillaries of length L and radius of r_p. The flux of fluid through a single-layer membrane can be expressed by the Hagen-Poiseuille[i] equation:

$$< Q >= \pi r_0^4 (P_1 - P_2)\left(\frac{n}{8\mu L}\right) \qquad (1)$$

Where

$<Q>$ – average flux ($m^3/m^2 \cdot s$);

r_0 – membrane pore size (m);

P_1, P_2 – upstream and downstream pressures, respectively (Pa);

n – area pore density (m^{-2});

μ – fluid viscosity (Pa·s);

L – membrane layer thickness (m).

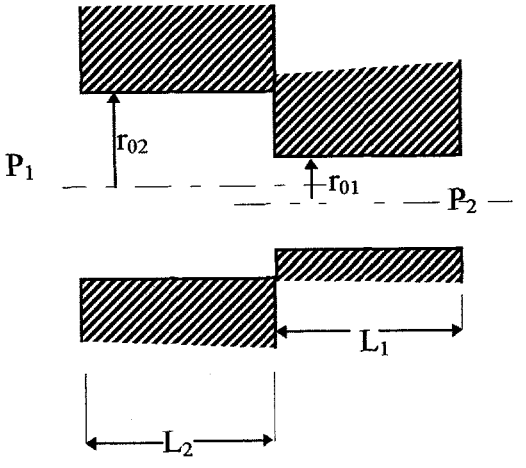

Figure 1.1. A Schematic of A Two-layer Membrane

For a two-layer membrane as demonstrated in Figure , the flux can be found as:

$$< Q >= \frac{(P_1 - P_2)}{\frac{8\mu L_1}{\pi r_{01}^4 n_1} + \frac{8\mu L_2}{\pi r_{02}^4 n_2}} \tag{2}$$

or

$$< Q >= \frac{(P_1 - P_2)}{\frac{8\mu L_1}{\pi r_{01}^4 n_1}\left(1 + \frac{r_{01}^4 n_1 L_2}{r_{02}^4 n_2 L_1}\right)} \tag{3}$$

For a multiple-layer membrane,

$$< Q >= \frac{(P_1 - P_2)}{\frac{8\mu L_1}{\pi r_{01}^4 n_1}\sum_{k=1}^{i}\left(\frac{r_{01}^4 n_1 L_k}{r_{0k}^4 n_k L_1}\right)} \tag{4}$$

where

$$R_i \equiv \frac{r_{01}^4 n_1 L_i}{r_{0i}^4 n_i L_1} \tag{5}$$

is defined as the flow resistance factor for each membrane layer i. When $R_i \ll 1$, the contribution of this layer to total flow resistance can be ignored.

- **Selectivity**

The transport and separation properties of ultrafitration membranes are most often characterized by determination of the volume permeate flux and the retention coefficient of selected macromolecules. The experimental retention coefficent is defined as

$$R_0=1-C_p/C_f \tag{6}$$

where

C_p -- solution concentration downstream of the membrane

C_f -- solution concentration upstream of the membrane

According to Deen,[ii] the solute flux in a single layer membrane, assuming that the membrane layer is described by the bundle of uniform, parallel (e.g. nonintersecting) pores model, can be described by the following equation:

$$< N >= W < V > C_0 \frac{[1-(C_L / C_0)e^{-Pe}]}{[1-e^{-Pe}]} \tag{7}$$

where

$$Pe = \frac{W < V > L}{HD_\infty}$$

$$H = \Phi K_d$$

$$W = \Phi K_c$$

$$\Phi = (1-\lambda)^2$$

$$K_d = \frac{6\pi}{K_t}$$

$$Kc = \frac{(2-\Phi)K_s}{2K_t}$$

$$\left(\frac{Kt}{Ks}\right) = \frac{9}{4}\pi^2\sqrt{2}(1-\lambda)^{-5/2}\left[1+\sum_{n=1}^{2}\left(\frac{a_n}{b_n}\right)(1-\lambda)^n\right]+\sum_{n=0}^{4}\left(\frac{a_n}{b_n}\right)\lambda^n$$

Table 1.1. Constants a_n and b_n in Deen's Equation

n	a_n	B_n
1	-73/60	7/60
2	77293/50400	-2227/50400
3	-22.5083	4.0180
4	-5.6117	-3.9788
5	-0.3363	-1.9215
6	1.216	4.392
7	1.647	5.006

The constants a_n and b_n were given by Bungay[iii] as in Table 1.

The above model was based on the following assumptions:

1. the radius of the pore r_0 and that of the solute molecules r_s (see Figure 1.2) greatly exceed that of the solvent, which is treated as a continuum;
2. At the low Reynolds numbers of interest to this study, flow is fully developed within about one pore radius downstream from the entrance;
3. the pore length L is much larger than its radius.

Equation 7 can be rearranged as:

$$\frac{<N>}{W<V>C_0} = \frac{[1-(C_L/C_0)e^{-Pe}]}{[1-e^{-Pe}]} \qquad (8)$$

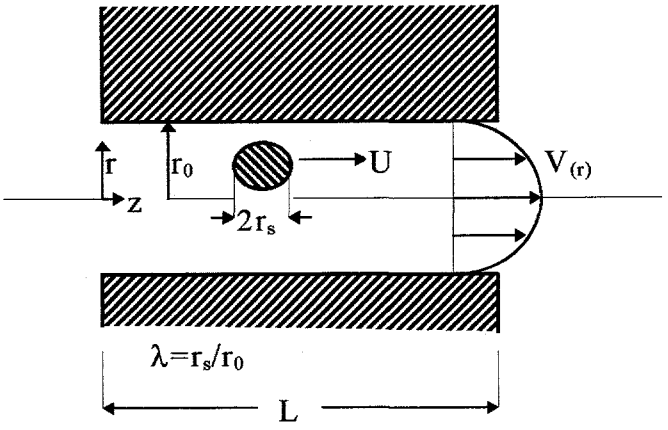

Figure 1.2. Capillary Model for Flow through Membrane Pores.

The relations described by equation 8 is illustrated in Figure 1.3.

From Figure 3 we can find that when *Pe* is larger than *1*,

$$\frac{<N>}{W<V>C_0} \approx 1 \tag{9}$$

Since $<N> = <V>C_L$, equation 9 becomes

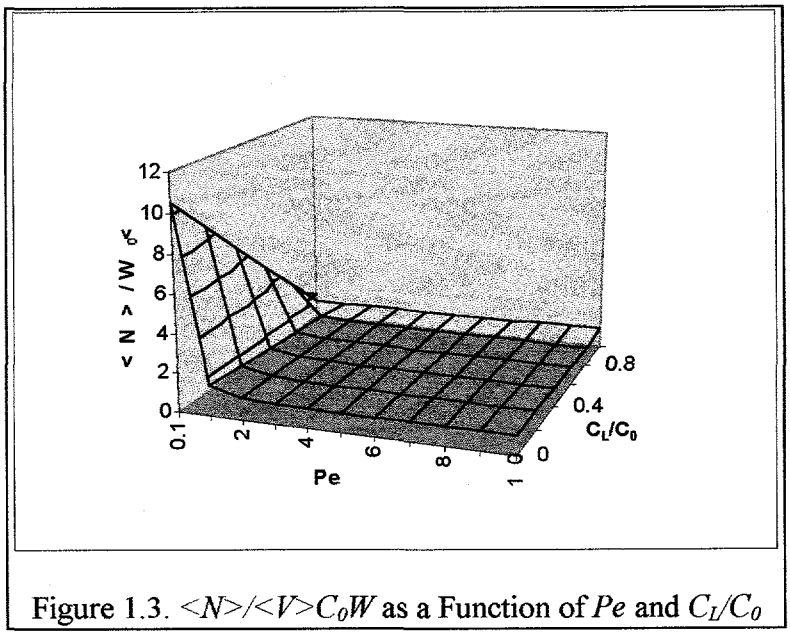

Figure 1.3. $<N>/<V>C_0W$ as a Function of *Pe* and C_L/C_0

$$s \equiv \frac{C_L}{C_0} = W \tag{10}$$

where

s – sieving factor

From the above discussion one can see that when Pe is larger than 1, the sieving factor, or selectivity of membrane is independent of any other variables such as the membrane thickness, but is a sole function of λ, which is the ratio of solute hydrodynamic radius to membrane pore geometric radius. The change of C_L/C_0 as a function of λ, when Pe is larger than 1, is given in Figure 1.4

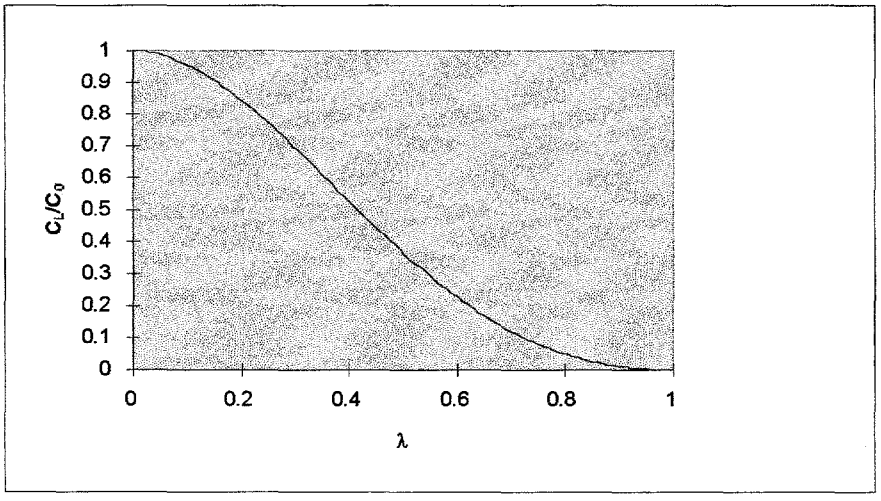

Figure 1.4. Sieving Coefficient $s \equiv C_L/C_0$ as a Function of λ

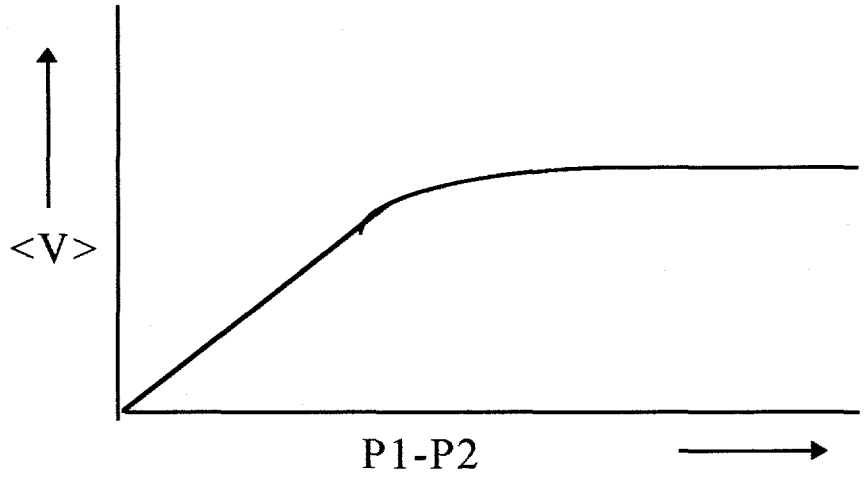

Figure 1.5. Typical Dependence of Permeate Flux on Transmembrane Pressure.

During the course of a typical permeation and separation experiment using membranes a variety of phenomena such as concentration polarization, adsorption and internal pore fouling might influence the permeate rate. In the membrane transport investigations involving oil liquid macromolecules one expects to encounter most if not all these phenomena. This makes model analysis a very complex undertaking.

According to Hagen-Poiseuille equation previously discussed, $\langle V \rangle$ should be proportional to (P_1-P_2). However, in reality, this is not observed when (P_1-P_2) is high. A typical dependence of permeate flux on the transmembrane pressure is demonstrated in Figure 1.5. These phenomena are generally modeled as solute concentration polarization as demonstrated in Figure 1.6.

At a given operating condition, the permeate crossing the surface carries with it a certain amount of solute. This can be represented by the product of total flow rate per unit area and solute concentration. As a result of solute transport across the membrane structure, the concentration of solute near the membrane surface can be higher than in the bulk. However, due to the higher solute concentration near the wall, there will be back diffusion of solute from near the wall into the bulk liquid phase. This can be expressed as *D(dC/dz)*. Thus at steady-state

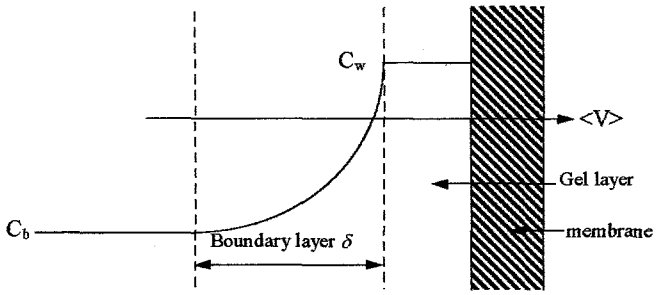

Figure 1.6. A Scheme Describing the Concentration Polarization Phenomena.

$$< V > C = D\frac{dC}{dz} \tag{11}$$

By integrating,

$$\frac{C_w}{C_b} = \exp\left(< V > \frac{\delta}{D}\right) \tag{12}$$

where $k \equiv \frac{D}{\delta}$.

In the case of low mass transfer rates, Brites and de Pinho[iv] developed a laminar boundary layer model to determine an average thickness, $<\delta>$, that is used to calculate k and to relate *Sh* with *Re* and *Sc*:

$$k = D_{SW}\,\mathrm{Re}^{1/2}\,\frac{(0.25Sc^{2/3} - 0.025)^{1/2}}{0.567R_m}\left(\frac{Sc}{Sc_m}\right)^{0.14} \tag{13}$$

where R_m is the membrane tube radius and Reynolds number is defined with a

characteristic velocity, which is the stirrer linear speed and with the membrane tube radius as the characteristic length.

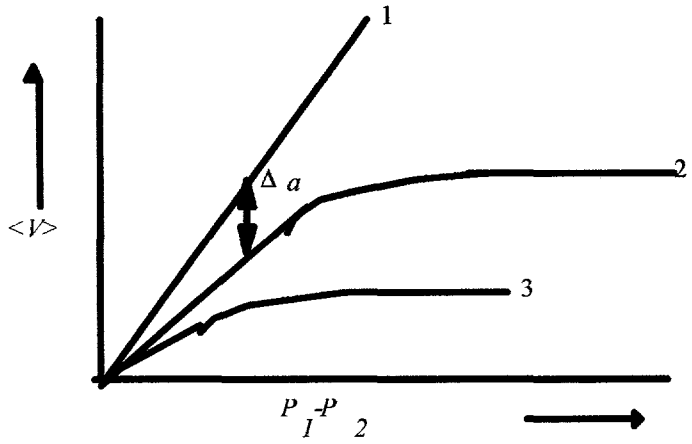

Figure 1.7. Typical Flux vs. Transmembrane Pressure Dependence[v]

Macromolecules also often interact with surfaces they come in contact with. This phenomenon, commonly described as fouling is due to adsorption; it is often difficult to understand and predict its influence on flux and selectivity. To simplify the analysis, a monomolecular adsorption layer is assumed to be formed covering the membrane pore surface during contact with the feed solution (with or without permeation across the membrane surface area). A significant flux reduction (20-35%) can occur even with a monomolecular adsorption layer. The tendency to form an adsorbed layer on the membrane pore surface may be a function of the nature of the membrane surface. For example, it is commonly observed that hydrophilic surfaces adsorb less strongly than hydrophobic surfaces especially when organics are involved.

It is known that the presence of adsorption layer can modify the linear relationship between the flux and transmembrane pressure. This is illustrated in Figure 1.7. In these situations, the difference, Δa, in the linear portions of the two $<V>$ vs. $(P_1 - P_2)$ relationships shown in Figure 1.7 may be attributed to the adsorption phenomenon

occurring on the pore walls. In general, the smaller the pore size the larger will be the value of Δa.

At high solute concentrations, however, a number of layers progressively build-up on the membrane surface in contact. These secondary layers are responsible for further flux reduction which can be quite pronounced, and up to 90% of the original flux can be lost. Adsorption and fouling phenomena can also change the selectivity of membranes. as commonly observed for example with filtration membranes utilized for the ultrafiltration of milk.[vi]

- **Coal Liquids**

During liquefaction coal is reacted under high hydrogen pressures and elevated temperatures in the presence of hydrogen donor solvents and catalysts to produce complex mixtures of countless organic aliphatic, aromatic and heterocyclic compounds. Traditionally coal liquefaction has been studied utilizing four solubility classes of compounds:[vii]

1) oil – soluble in aliphatic solvents (e.g. pentane or hexane).
2) asphaltenes – soluble in aromatic solvents (e.g. benzene or toluene) but insoluble in aliphatic solvents (e.g. pentane or hexane).
3) preasphaltenes – soluble in THF but insoluble in aromatic solvents (e.g. benzene or toluene).
5) unreacted coal and char – THF insoluble.

Among these four solubility classes of components, oil is the most desirable product while obviously unreacted coal and char are the least desired ones. When one's interest is in transport investigations one must always be reminded that though the solubility of individual components of a coal liquid will to a large extent depend on the molecular weight the number and the nature of the polar substituents and the aromaticity

together with the size and condensation index of the aromatic units also play an important role.[viii] In the literature coal liquid molecular size (in terms of the radius of the equivalent hydrodynamic sphere r_H) has been correlated to its molecular weight $\overline{M}_W$ [ix] according to the following equation

$$r_H = \xi r_G \tag{14}$$

$$r_G = \left[\frac{\overline{M}_W[\eta]}{\Phi'}\right]^{1/3}$$

$$[\eta] = K(\overline{M}_W)^a$$

where

r_H - radius of the equivalent hydrodynamic sphere

r_G - radius of gyration

$[\eta]$ - intrinsic viscosity (cm^3/g)

$\overline{M}_W$ - weight-average molecular weight (g/mol)

$[\ \eta\ ]$ - constants

a - positive constant

When $\overline{M}_W < 10^5$, $[\eta] = 5.2 \times 10^{-2}(\overline{M}_W)^{0.56}$.

- **The Transport Experimental Apparatus**

The experimental system utilized in the transport investigations is shown in Figure 1.8. This system has the capability of being operated in a batch, CSTR and membrane CSTR mode. The residence time for the CSTR and the membrane CSTR can be varied over a range of 20 to 80 *min*. Built within a protective barricade of metal construction, the unit can be safely controlled, operated and products sampled from outside the barricade. The overall unit is divided into the following different sections: (a) a gas delivery system; (b) a slurry feed system; (c) a preheater; (d) the transport vessel; (e) a solid sample basket;

(f) liquid sampling system; and (g) a gas sampling system.

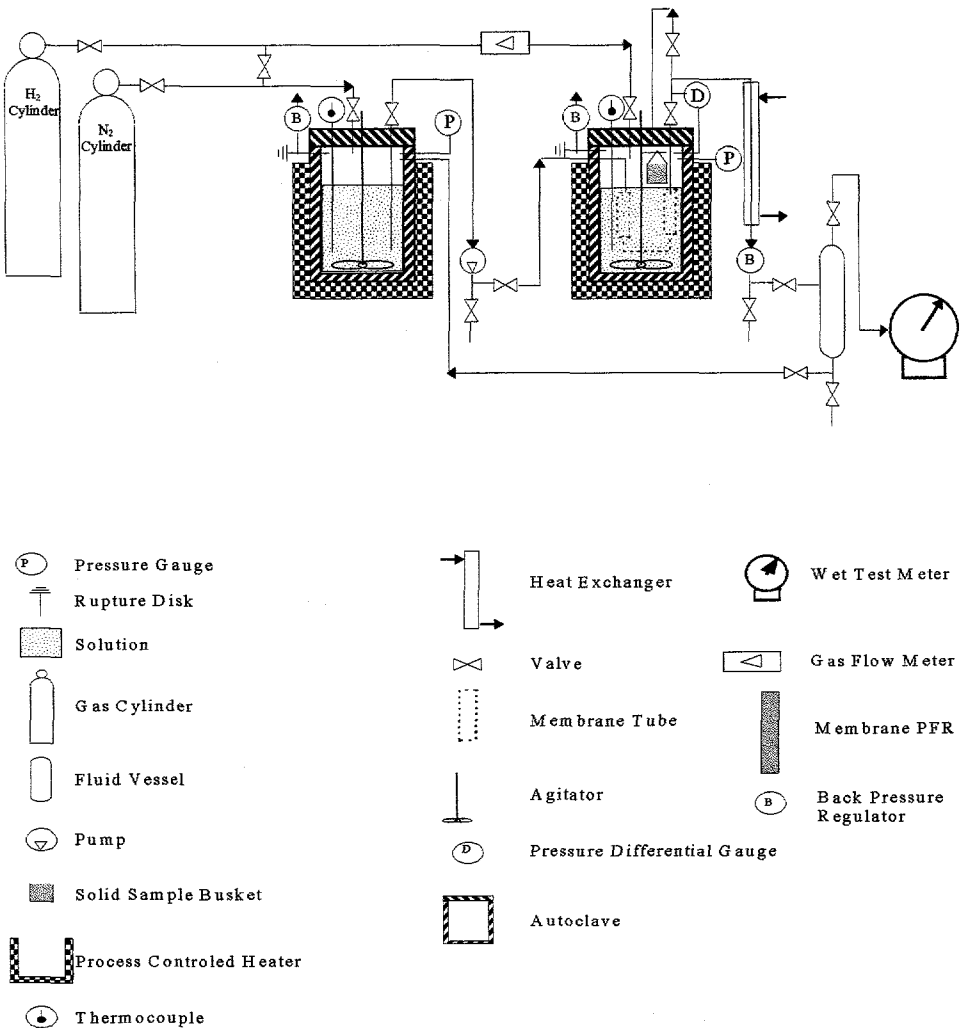

Figure 1.8. Schematic of a Membrane Reactor System

The gas delivery system which consists of 1/4" tubing and valves, supplies a constant flow of gas to the unit at pressures ranging from atmospheric to 5000 psi. The gases are supplied from regulated gas cylinders. Gas flow rate is measured by a mass flow meter and the gas pressures to other parts of the unit are controlled by accurate pressure regulators.

To deliver either solvent, a coal liquid or a coal-solvent slurry to the transport apparatus at system pressure a feed tank (a 300 *ml* autoclave) is provided to store the feed. Slurry is mixed in the feed tank with a variable speed stirrer and heated with a preheater. Feed flows by gravity to a Beckman HPLC pump through 1/8" stainless steel tubing. The feed flow rate, ranging from 0-10ml/min is controlled by the HPLC pump. The preheater consists of a process controlled heater. It can be used to preheat the feed to the transport vessel to about 250 °C. Higher temperatures can be attained within the transport system itself. A 300 ml Autoclave Engineers magnetdrive autoclave of custom design is used to carry out the transport experiments. The pressure of the system is controlled by a back pressure regulator and the temperature is controlled by a temperature controller. When the system is operating in its CSTR reactor mode, a dip tube is used to serve as the exit port. The total volume of solution (hence the CSTR residence time), is controlled by the position of the dip tube. The other end of the dip tube is connected to a jacket water cooler where cold water is run through the shell-side of the cooler while the effluent of the transport system goes through the tube-side. The effluent is cooled down in the cooler. A piston pump, which is attached to the tube side of the water cooler is used to control the effluent flow rate.

When the reactor is operating at its membrane CSTR transport mode, the dip tube is replaced by a membrane tube assembly and the piston pump for flow control is replaced by a back-pressure regulator. The membrane tube assembly consists of several pieces of 1cm O.D. ceramic membrane tubes which are connected in series by Swagelok tube fittings. The liquids are driven by the pressure in the system through the membrane pores into the inner side of the membrane tube. One end of the membrane tube assembly is blinded by a Swagelok blank fitting and the other end is connected to a back-pressure regulator. Since the effluent flow rate is determined by the pressure difference between the autoclave and the pressure inside the membrane tube, the back pressure regulator is used to control the effluent flow rate and hence the liquid volume (or the residence time). The autoclave stirrer is typically operated at 1500 rpm to ensure constant concentrations throughout the transport volume external to the membrane and to minimize mass transport

limitations due to interfacial resistance.

For transport investigations under reactive conditions a vapor-liquid separator consisting of a 1000 ml high pressure vessel is used to separate gaseous and liquid products. The vapor from the separator is directed to a wet-test meter where the vapor flow rate is measured while the liquid collected in the high-pressure separator is periodically drained to a liquid sampling system. In the membrane CSTR operation mode, pressure-reduced liquid from the effluent pump is collected in the high pressure separator and is periodically drained to collect liquid samples. Liquid samples inside the transport apparatus are collected through a dip tube, one end of which is emerged in the system and the other end connected with a metering valve. Gas samples are withdrawn from the top of the high pressure separator. System product gas flow is measured through a mass flow-meter.

2. GENERAL EXPERIMENTAL PROCEDURES

The experimental system described above has been used for all the permeation experiments of both pure compounds as well as mixtures. To ensure a clean system for each experiment, all tubing and valves were flushed for 48 hr prior to each experimental run with the solvent, which is to be used during the permeation and separation experiment. The feed-tank was a glass vessel, and the wetted parts of the piston pump and centrifugal pump were made of Teflon. The piston pump feeds the solution from the permeant feed tank from the tube side of the membrane back to the shell side of the membrane tube, which is the space between the autoclave and the membrane tube, while the centrifugal pump provided the recirculation flow rate to prevent any concentration stagnancy on the membrane tube side. A back-pressure regulator was used to maintain the tube side at a constant positive pressure, which is important to minimize any liquid flashing at high temperature. The permeant is cooled down by a jacketed water cooler before going back into the feed tank. A magnetic stirrer was used on the shell side to minimize concentration polarization. N_2 gas was used to pressurize the system on the shell-side (autoclave side). A temperature-controlled heater was used to control the temperature. The configuration of the system allows varying the pressure and temperature while maintaining a constant cross-flow rate through the bore of the membrane. Effective operation necessitates that the piston pump flow rate be almost the same as the permeate's flow rate through the membrane so that when running with a mixture, a build-up of solute would not occur in the shell side. In all experimental cases reported here, piston pump feed rate to the permeate flow rate ration was ≈ 1. For all experiments reported, the temperature and the pressure of the membrane separation system were maintained at constant desired points. The piston pump flow rate was manually adjusted throughout each experiment to maintain the liquid level in the feed tank constant.

The coal asphaltenes and preasphaltenes utilized in our experiments have been generated by direct coal liquefaction carried-out in our laboratories. Coal samples were

obtained through The Penn State Coal Sample Bank and subsequently liquefied by thermal hydrogenation in the presence of tetrahydronapthalene. Typically a liquefaction run involved weighing 40 g of a coal sample and then subsequently drying overnight at 100 °C to ensure a low moisture content. The sample was then added to the autoclave together with 215 ml of tetrahydronapthalene. Coal cracking was carried out at 350 °C and under 1000 psig of H_2 for a period of 2 hr. Isolation of the resulting products was done following a conventional isolation procedure. Extraction of products was done sequentially in the order of oils, asphaltenes, and preasphaltenes. Heptane was first used to extract the oils (these are liquids with a low M_n of 200 soluble in alkanes) by mixing it with the liquefaction products at a 40:1 solvent to products ratio. The resulting solution was vigorously stirred for 24 hr and then filtered with 5 μm filters by gravimetric filtration. The filtrate solution was then distilled for heptane recovery and oil isolation. Xylenes, at a 40:1 mixing ratio, were then mixed with the solid filter cake to extract asphaltenes (solid materials with a M_n of 750 soluble in aromatic solvents). The solution was stirred and isolated in a similar procedure followed for the oil isolation. Finally, tetrahydrofuran (THF) was used to extract preasphaltenes (high molecular weight species with a M_n of 1200) with the same procedure as oils and asphaltenes. The leftover solids containing unbreakable aromatic structures not subject to hydrogenation are described as "unreacted" coal.

Gas chromatography, thermogravimetric weight measurements and Gel Permeation Chromatography were the main analytical techniques utilized in our experiments. For the transport experiments with asphaltenes and preasphaltenes Gel Permeation Chromatography proved to be the most accurate technique for analysis because of the very dilute concentrations being utilized. With GPC one is able to analyze both for concentration and molecular weight distribution. Due to the high gas solubility of THF, the refractometer proved to be inaccurate and as a result, the absorbance detector was used for all preasphaltene and asphaltene analysis. For the dilute concentrations utilized in the transport experiments under nonreactive conditions a linear relationship between absorbance and concentration was observed as noted in Figures 2.1, 2.2, and 2.3.

GPC molecular weight distributions are shown in Figure set 2.4 for a single sample at different material concentration values. Most of the defining characteristics are noticeable in each of the responses regardless of the concentration. However, the higher concentrations allow for higher precision and accuracy and may have a few small additional defining characteristics that are not observed at lower concentrations. In either case, these slight deviations are small in consideration to the type of data that are expected from this type of analysis. The linear trend displayed in Figure sets 2.1, 2.2, and 2.3 can be expected as a result of the nature of the GPC requirement for dilute solution injections. In this study we have assumed that the molecules are in a relaxed state and do not individually differ in absorbance properties to any great extent that can easily be differentiated by the GPC system. This is a necessary assumption if one is to utilize the GPC device for concentration analysis since the present computer software makes no attempt and cannot correct for possible differences in absorbance responses for each individual molecular weight. On the basis of the aforementioned assumption the GPC system responds much like a gas chromatograph. The column, carrier fluid, material(s) injected, amount of material injected, and detector determine the type and size of response observed. The absorbance response for each individual molecular weight increases linearly with respect to overall concentrations as noted in the figures and according to the following form

$$A_{MW} = \varepsilon X_{MW} C_{Total} \qquad (15)$$

where A is the absorbance, X_{MW} mass fraction of a particular molecular weight, C_{total} overall solute concentration, and ε the absorbance constant. Since the individual molecules are assumed to have similar absorbance properties one, therefore, can infer that the overall area reflects the total amount of solute injected and since sample injections always took place at a specific, known volume, the total material reflected in the peaks also reflects the concentration. The GPC column separates the THF injected from the solid material as it passes through the column. Therefore, the response for the first peak(s) reflect the amount of solid material without regard for how much solvent had been

originally used to dilute the material. With this in mind, the concentration of the original sample can be determined providing consistent injections into the GPC system are made. Obviously, a response of zero is expected for a zero amount of material entering the column. This is not always observed according to the extrapolated data in Figures 2.1-2.3. These small errors, however, are the result of the inherent imprecision of the GPC system and in the preparation of dilute standard concentration asphaltene/preasphaltene solutions .

Figure 2.1a. Asphaltene Concentration Determinations through GPC.

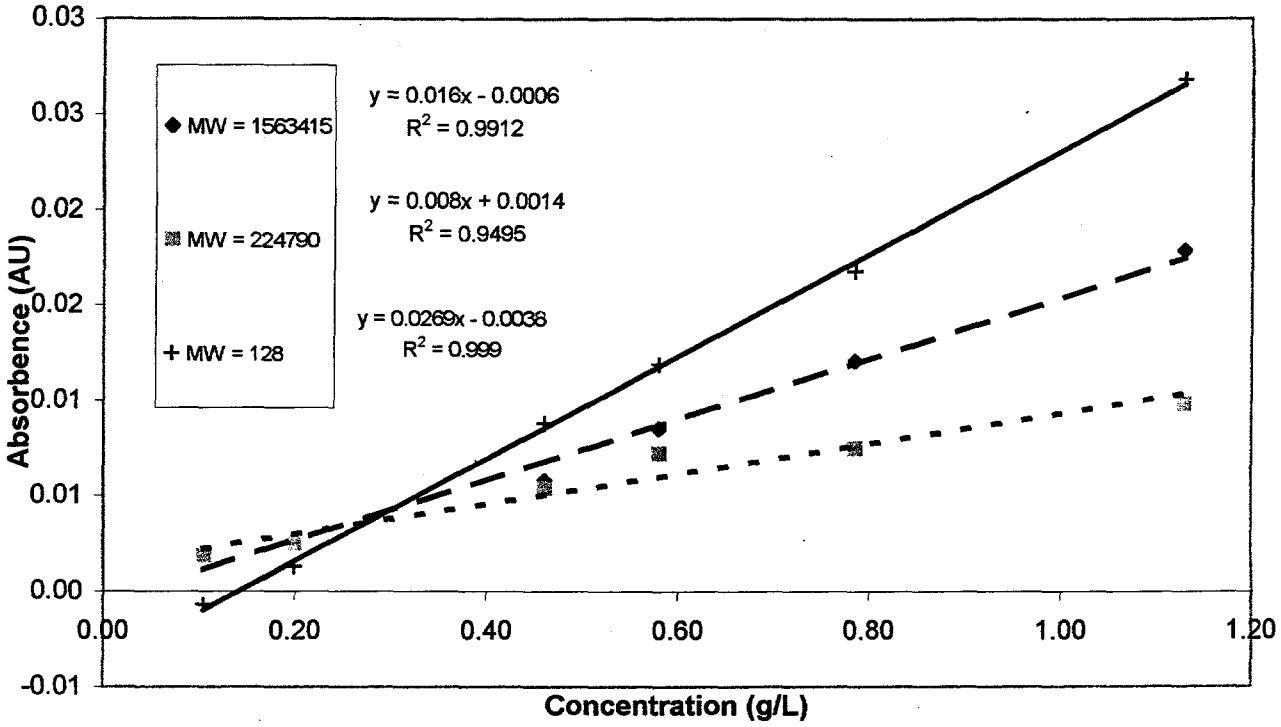

Figure 2.1b. Asphaltene Concentration Determinations through GPC.

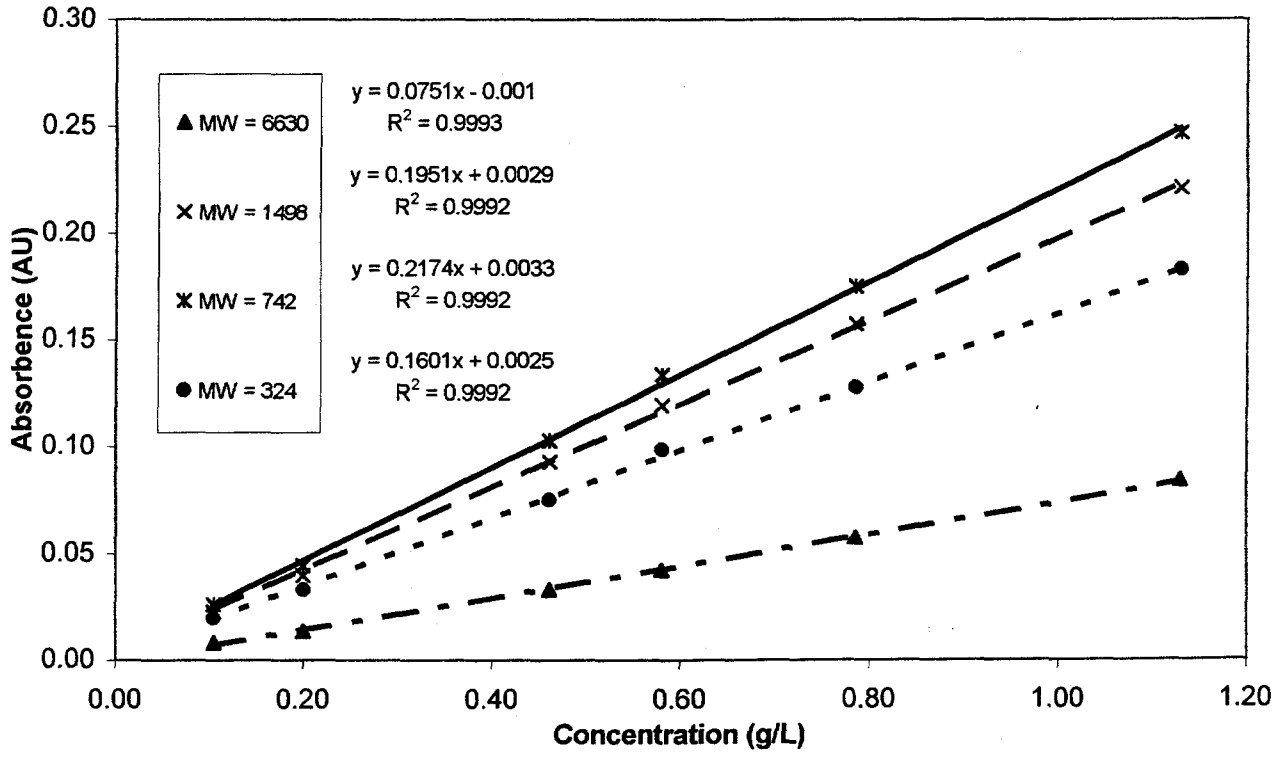

Figure 2.2a. Preasphaltene Concentration Determinations through GPC.

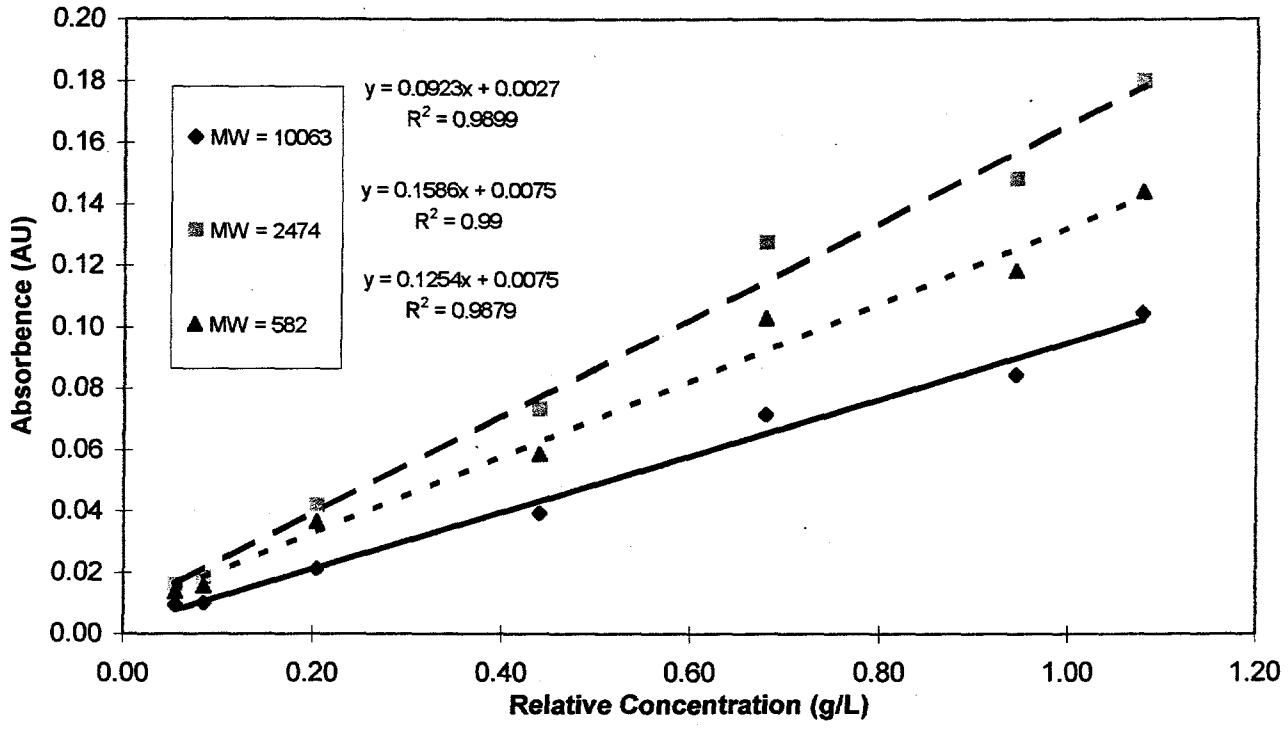

Figure 2.2b. Preasphaltene Concentration Determinations through GPC.

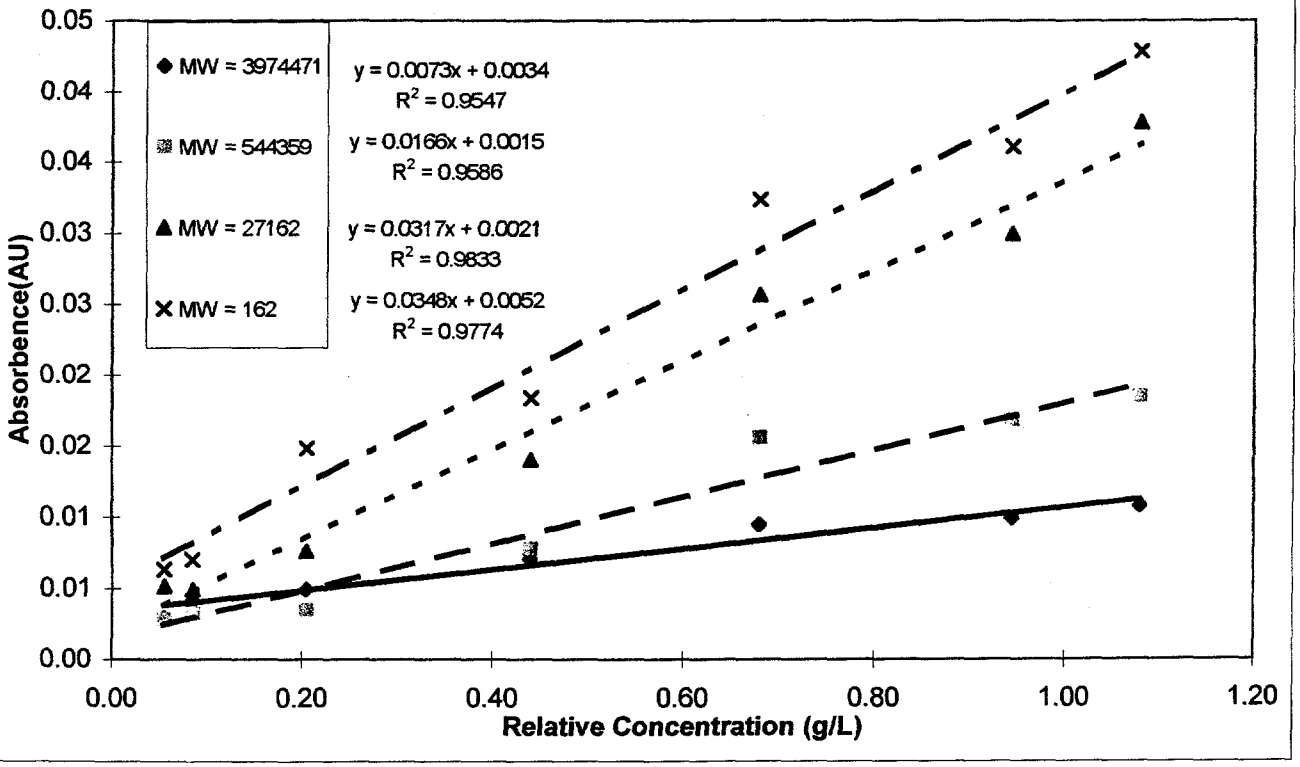

Figure 2.3a. Total Area Normalization Parameter Determination.

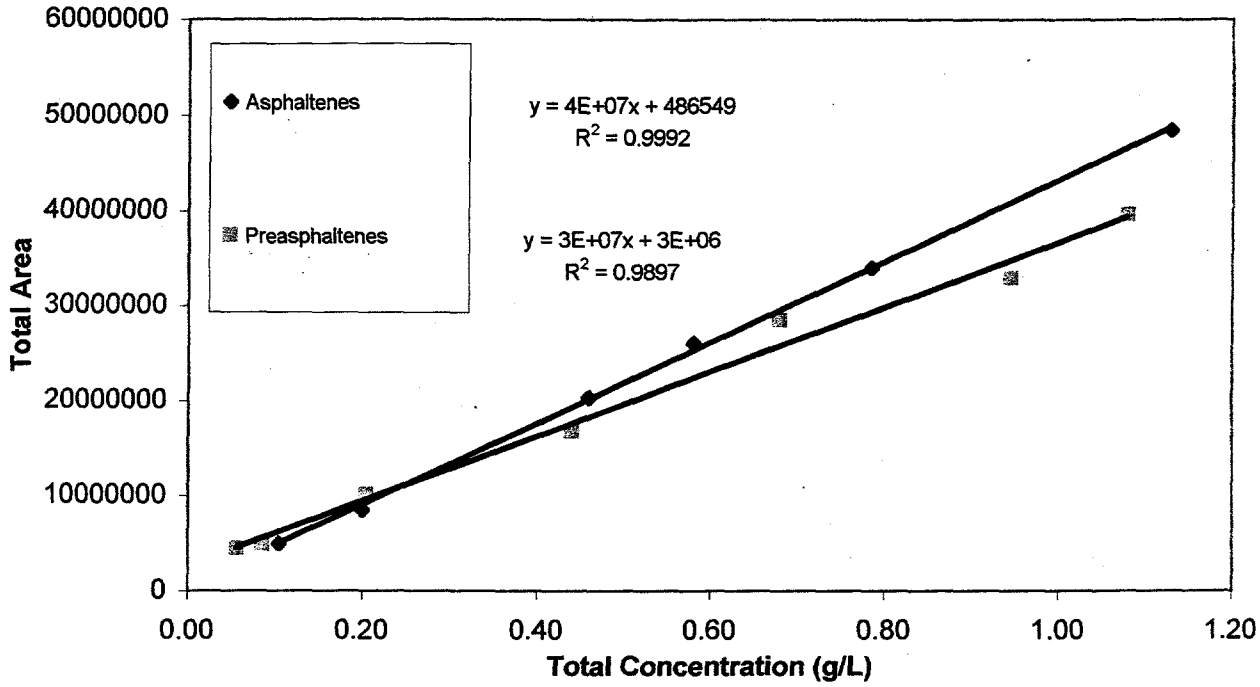

Figure 2.3b. Preasphaltene Concentration Determination.

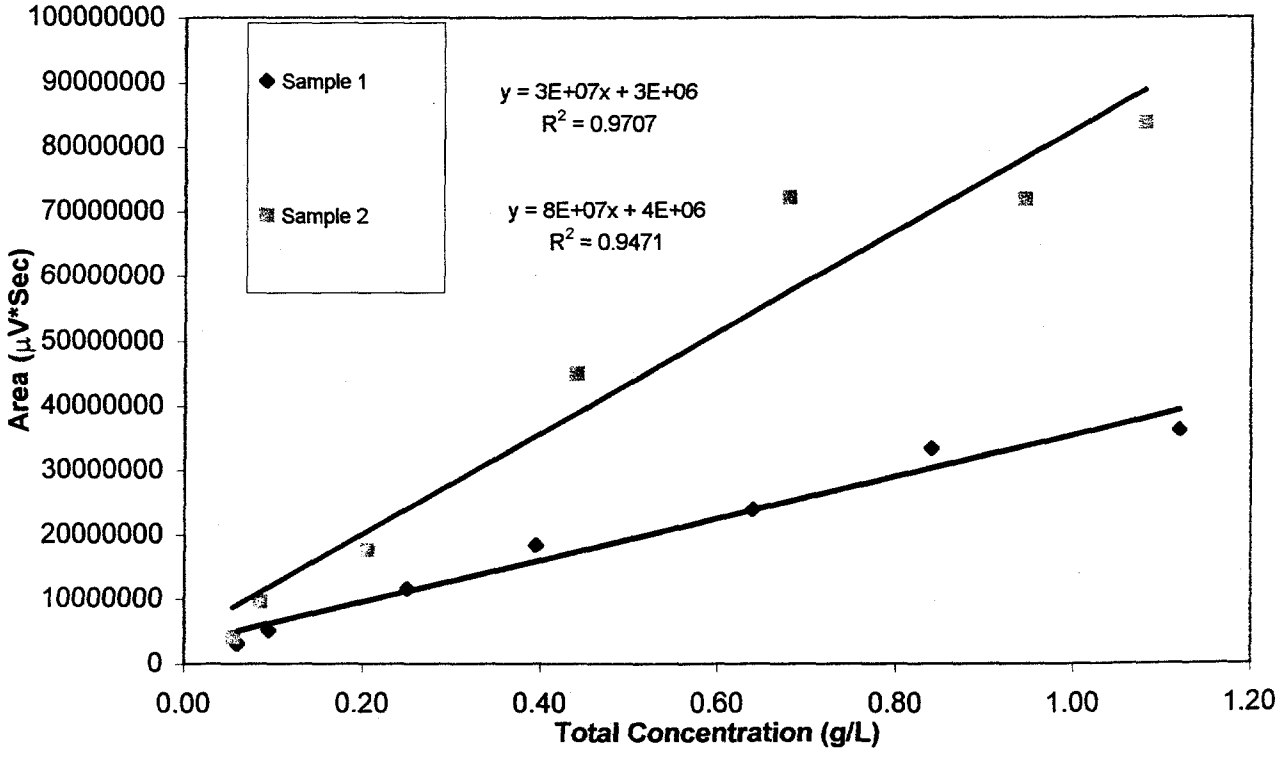

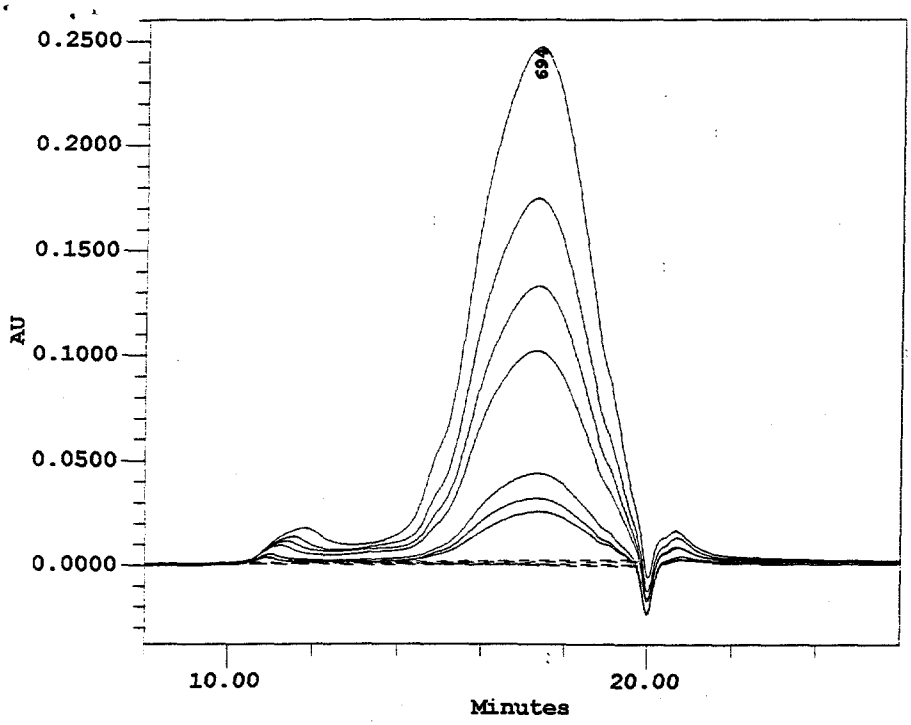

#	Mn (Daltons)	MP (Daltons)	Mw (Daltons)
1	554	694	12380
2	553	683	18716
3	551	706	16973
4	554	717	19537
5	551	694	21007
6	557	717	22188
7	553	694	22910

Figure 2.4a.

GPC Absorbance response to Asphaltene-THF Solutions. Concentration values increase with absolute absorbance magnitude.

1 - 0.05 g/L 2 - 0.1 g/L 3 - 0.2 g/L 4 - 0.4 g/L

5 - 0.6 g/L 6 - 0.8 g/L 7 - 1.0 g/L

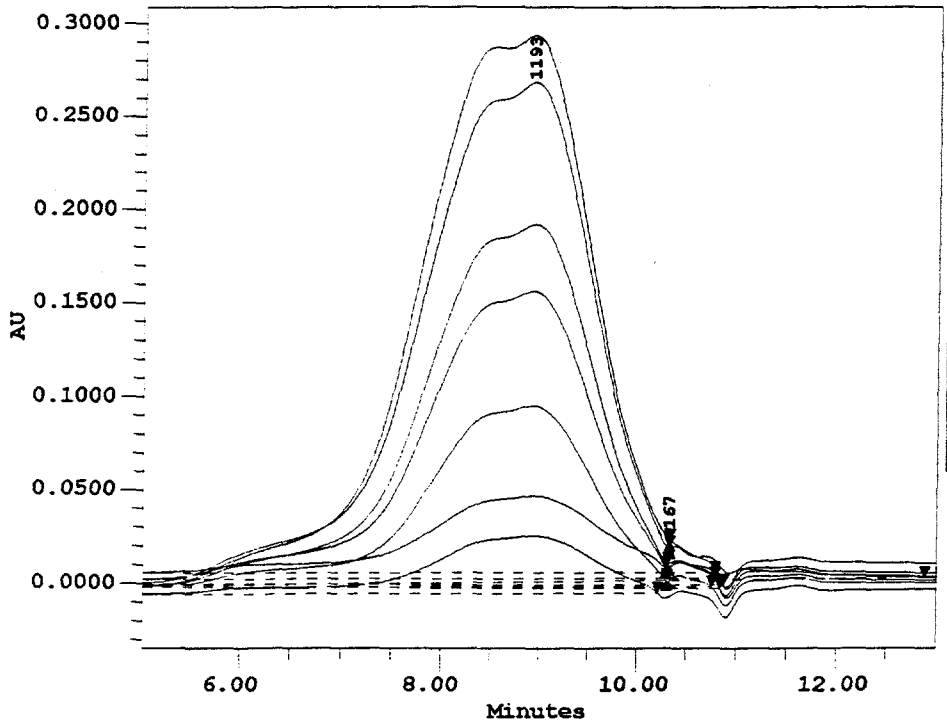

#	Mn (Daltons)	MP (Daltons)	Mw (Daltons)
1	1041	1135	11453
2	1121	1164	8868
3	1127	1164	11311
4	1130	1193	9757
5	1132	1193	8439
6	1135	1193	8776
7	1152	1193	7771
8		145	
9		151	
10		151	
11		151	
12		154	
13		167	

Figure 2.4b.

GPC absorbance responses to Preasphaltene-THF solutions. Concentration values increase with absolute absorbance magnitude.

1 - 0.05 g/L 2 - 0.1 g/L 3 - 0.2 g/L 4- 0.4 g/L

5 - 0.6 g/L 6 - 0.8 g/L 7 - 1.0 g/L

3. TRANSPORT INVESTIGATIONS OF COAL ASPHALTENES AND PREASPHALTENES IN γ-AL_2O_3 MEMBRANES

These alumina membranes have been prepared by deposition of γ-Al_2O_3 films on Coors and US Filter porous substrates. We have found both the Coors and US Filter macroporous substrates having surfaces that cause problems in forming crack-free alumina films. The average pore size of the substrates is of the order of 2000 angstroms. For the preparation of the γ-Al_2O_3 films we utilized a 20 wt.% alumina boehmite sol (Dispal 23N4-20), which was supplied by the Vista Chemical Company. The sol was diluted to 6 wt.% in distilled water and then heated and rigorously stirred at 90° C. Typically, 15g of the Boehmite was prepared with 35g of water. Meanwhile, a polyvinyl alcohol (PVA) solution was prepared by adding 0.5g of PVA to 5 ml of a 1M HCl solution diluted with 50g of water. While the boehmite solution was being heated, 1.5 ml of the PVA solution thus prepared was added to it to provide a 0.03 wt.% PVA content. The solution was allowed to stir at 90 °C for 2 hr. The solution was then cooled to room temperature and filtered through 5 μm syringe filters.

Before applying the alumina coatings to the substrates, the substrates were first sonicated in isopropyl alcohol in an ultrasonic bath for 1 hr and subsequently allowed to dry for 24 hr. The outside tube surface was then wrapped in teflon tape to prevent the alumina coating from spreading on the outer surface of the substrates. Depending on whether the substrates already had γ-alumina films previously deposited on them or not, the membranes were subject to dip-coating from 2 to 4 min. After the allotted time frame, the membranes were drawn from the solution at a rate of 2 cm/min and allowed to dry for 48 hr under ambient conditions. After 2 days, the membranes were calcined in air within an oven. The first temperature profile raised the temperature at a heating rate of 0.2 °C/min up to100 °C and then held it there for 4 hr. The secondary temperature profile varied depending on the type of substrate. US Filter substrates were heated at the same heating rate up to 500 °C and held there for 6 hr. COORS membranes required multiple

films at slightly different temperatures for each film (see further discussion below). The membranes were tested for argon permeation and maximum transmembrane pressure drops. All membranes were expected to be capable of a minimum transmembrane pressure drop of at least 40 psi and a permeation of near or under 1.0 ml/min/cm^2/psi.

As mentioned previously during film deposition we have utilized polyvinyl alcohol which acts as a binder for the alumina films to prevent film cracking during calcination. However, care must be taken not to add too much or too little of the binder. Not enough binder will cause extensive cracking especially with the COORS substrates. Too much binder on the other hand will create a thick film on the surface of the substrate and prevent pore penetration of the Boehmite. In addition, only calcining at 500 °C was not always successful for the COORS substrates. The material structure resulting was rather weak. As a result a calcination procedure was devised which resulted in converting some of the earlier γ-Al_2O_3 films into α-alumina layers before the final γ-alumina layer was deposited. This calcination procedure involved heating the substrates at 900 °C, 700 °C, and followed by a final 500 °C γ-alumina film deposition. This calcination procedure proved successful in providing good mesoporous alumina films. Of course much more remains to be learned in this area, since deposition of smooth and crack-free γ-alumina films still remains mostly an art.

We report here experiments with both asphaltene and preasphaltene solutions. γ-alumina films are stable to THF which made it possible to carry-out investigations with preasphaltenes dissolved in a THF solvent. The experiments with coal pre-asphaltenes are presented in Tables 3a-3c and in Figures 3a-3c. The experiments at 298 K are shown in Tables and the corresponding Figures 3a. As can be seen in Figure 3a.2 the rejection factors vary between 0.1 to 0.0.65 and seem to be increasing with molecular weight as one would have expected. The membrane for the first few hours or so is undergoing a conditioning process which is likely to involve adsorption within the pore structure of the preasphaltenes themselves and narrowing of the pore structure. The transport behavior at two other temperatures is shown in Tables and the corresponding Figures 3b and 3c. The

behavior in terms of rejection coefficients and separation factors is again similar except from the fact that the membrane appears to condition itself faster as one would expect it to happen at these higher temperatures where molecular mobility is higher and sorption/desorption equilibria are attained faster.

Transport investigations with asphaltenes dissolved in THF are shown in Tables and Figures 3d to 3f. Asphaltenes generally behave similarly with preasphaltenes with the membrane taking a few hours to condition itself into a steady-state and the rejection factors increasing with molecular weight. The behavior in Figures 3d.2 -3f.2 can be compared directly with the behavior in Figures 3a.2-3c.2 since the same molecular weights were monitored in both figures (one needs to be cautious here, however since these are equivalent polystyrene molecular weights; it is unlikely, for example, that a 1030 MW asphaltene component will be similar in chemical or molecular structure with the equivalent MW preasphaltene component). It is interesting to know that the lower molecular weight asphaltene components show lower rejection coefficients than the corresponding preasphaltene components. On the other hand the reverse is true for the medium to higher molecular weights. It is interesting to see that the γ-alumina films (after conditioning) are even capable of separating asphaltenes and preasphaltenes given the nominal pore diameter of the "clean" alumina film. One has to be cautioned also that that the higher rejection factors observed at the highest temperature of 373 k might be due to the fact that higher shell side pressure (approaching the critical pressure of THF) had to be maintained (for the same transmembrane pressure drop) since this temperature is above the THF standard boiling temperature of 339 K.

Table 3a.1 Preasphaltene-THF Filtration Experiments for a γ-Alumina Film.
Nominal Shell Pressure: 0 psig Temperature: 298 K

Trial Number & Description	ΔP	Membrane Condition Time	Equil. Time	Total Area	Estimat. Conc.	Flow Rate
	(PSID)	(Min)	(Min)	(μV*Sec)	(g/L)	(ml/min)
(1.) Shell Side	41.1	120	120	67881405	0.8127	-
Tube Side		120	120	55801486	0.6580	0.2293
(2.) Shell Side	54.4	510	390	73756978	0.8879	-
Tube Side		510	390	46438192	0.5381	0.1498
(3.) Shell Side	40.1	1260	750	70774777	0.8497	-
Tube Side		1260	750	43538376	0.5010	0.1173
(4.) Shell Side	43.8	1380	120	70172383	0.8420	-
Tube Side		1380	120	41752041	0.4781	0.1091

Table 3a.2 Rejection Factors of Preasphaltenes-THF for a γ-Alumina Film.
Temperature: 298 K

	GPC Time/*Molecular Weight*				
Trial Number	6.50 ***56721***	8.50 ***2073***	9.00 ***1030***	9.80 ***344***	**Permeability (ml/min/PSID/cm^2)**
1	0.2929	0.2052	0.2300	0.2741	0.00072502
2	0.3391	0.4034	0.3288	0.2446	0.00035788
3	0.6296	0.4260	0.2374	0.1397	0.00037999
4	0.6404	0.4451	0.2711	0.1674	0.00032363

Table 3a.3 MW-MW Separation Factors of Preasphaltenes-THF for a γ-Alumina Film.
Temperature: 298 K

Trial	***56721-344***	***2073-344***	***1030-344***
1	0.97	1.12	1.08
2	0.85	0.76	0.87
3	0.37	0.61	0.86
4	0.38	0.61	0.85

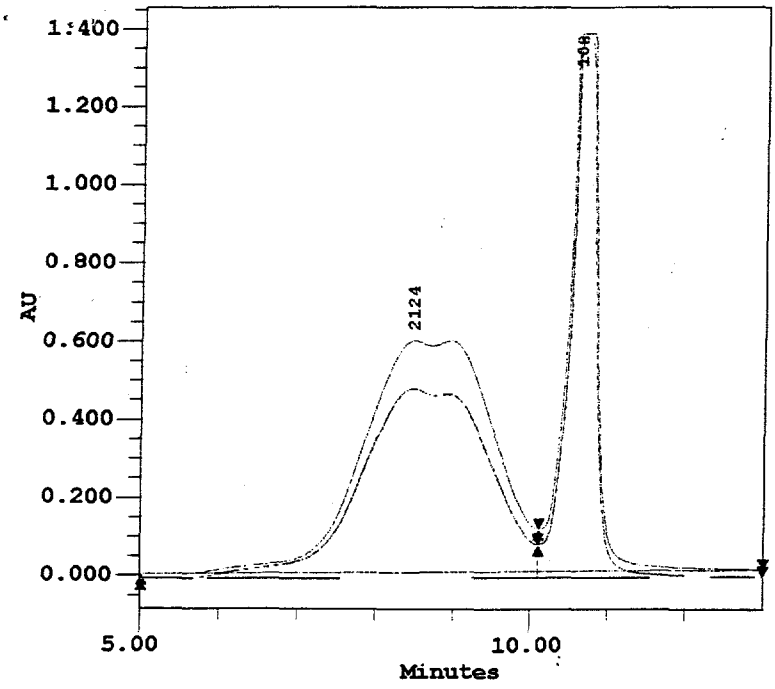

Figure 3a.1a.
GPC Analysis of Preasphaltene Separation by a Gamma-Alumina Film in a THF Medium (T = 293K).
Time = 120 Minutes.
Pressure Drop: 45 PSID
1 - Downstream - Tube Side.
2 - Upstream - Shell Side.

#	Mn (Daltons)	MP (Daltons)	Mw (Daltons)
1	1110	2124	3857
2	1146	2175	4590
3		103	
4		108	

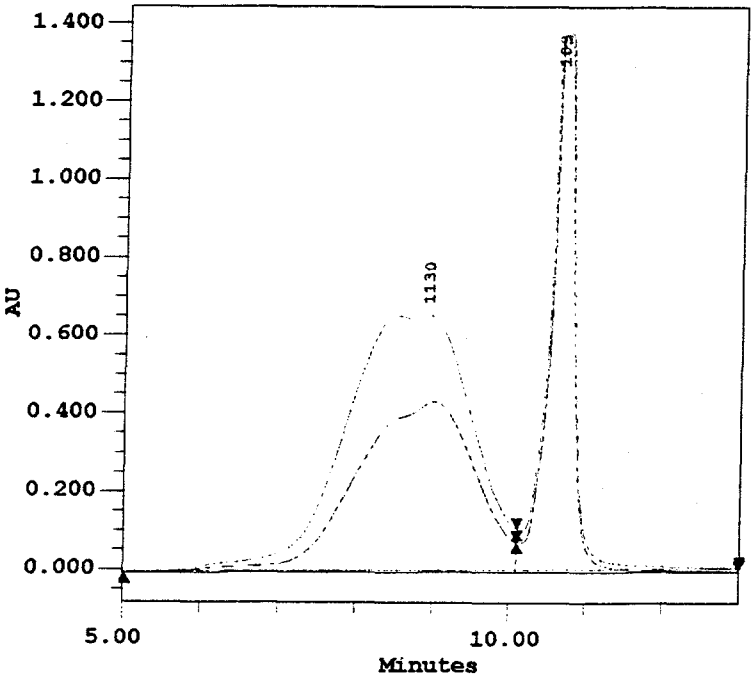

Figure 3a.1b.
GPC Analysis of Preasphaltene Separation by a Gamma-Alumina Film in a THF Medium (T = 293K).
Time = 510 Minutes.
Pressure Drop: 45 PSID
1 - Downstream - Tube Side.
2 - Upstream - Shell Side.

#	Mn (Daltons)	MP (Daltons)	Mw (Daltons)
1	1030	1007	3867
2	1133	1130	4031
3		98	
4		103	

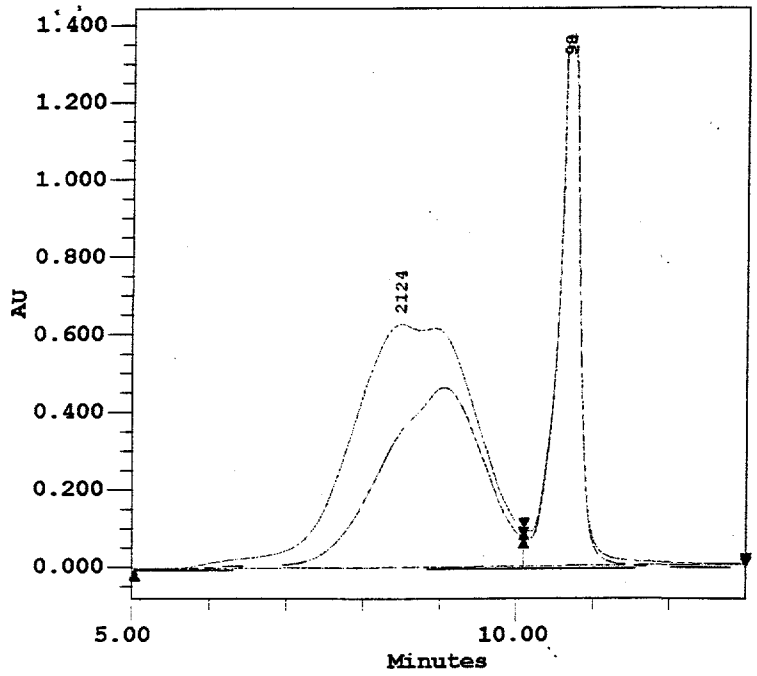

Figure 3a.1c.
GPC Analysis of Preasphaltene Separation by a Gamma-Alumina Film in a THF Medium (T = 293K).
Time = 1260 Minutes.
Pressure Drop: 45 PSID
1 - Downstream - Tube Side.
2 - Upstream - Shell Side.

#	Mn (Daltons)	MP (Daltons)	Mw (Daltons)
1	926	962	2963
2	1148	2124	4215
3		98	
4		98	

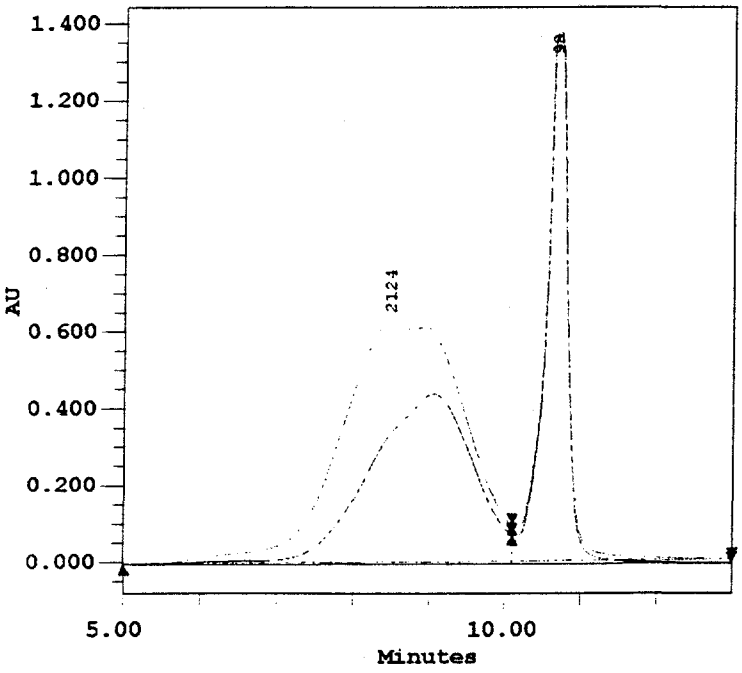

Figure 3a.1d.
GPC Analysis of Preasphaltene Separation by a Gamma-Alumina Film in a THF Medium (T = 293K).
Time = 1380 Minutes.
Pressure Drop: 45 PSID
1 - Downstream - Tube Side.
2 - Upstream - Shell Side.

#	Mn (Daltons)	MP (Daltons)	Mw (Daltons)
1	935	962	3143
2	1154	2124	4339
3		98	
4		98	

Figure 3a.2 Rejection Factors for a γ-Alumina Film with Preasphaltene-THF Solution (ΔP = 45 PSID), (T = 298 K).

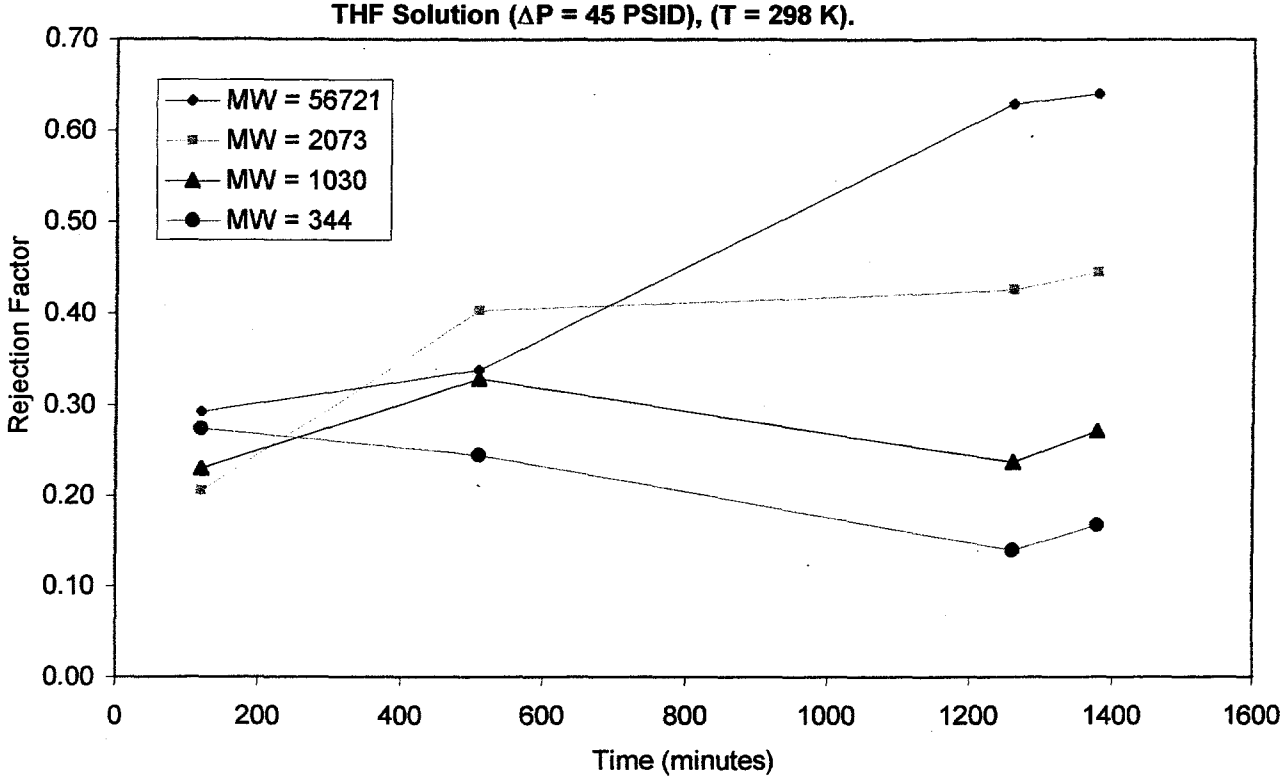

Figure 3a.3 Separation Factors for a γ-Alumina Filmwith Preasphaltene-THF Solution (ΔP = 45), (T = 298 K).

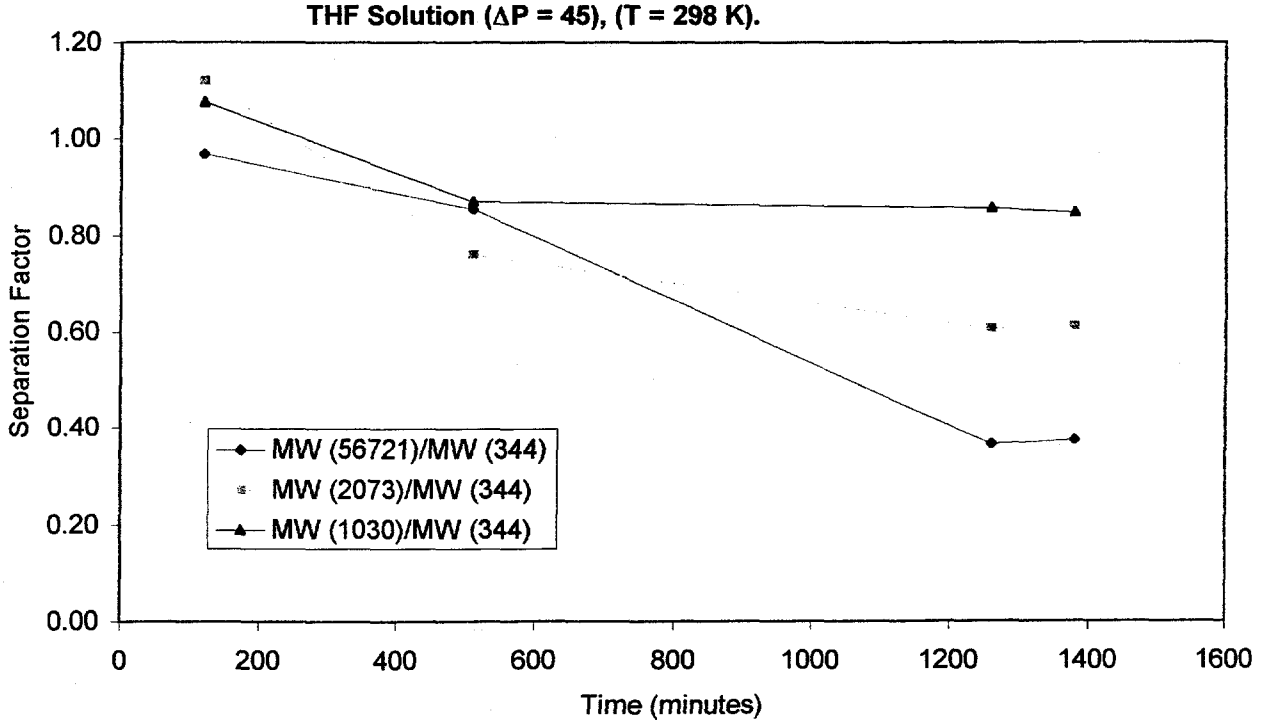

Table 3b.1 Preasphaltene-THF Filtration Experiments for a γ-Alumina Film.
Nominal Shell Pressure: 400 psig Temperature: 323 K

Trial Number & Description	ΔP	Membrane Condition Time	Equil. Time	Total Area	Estimat. Conc.	Flow Rate
	(PSID)	(Min)	(Min)	(μV*Sec)	(g/L)	(ml/min)
(1.) Shell Side	42.5	30	30	89444693	1.0888	-
Tube Side		30	30	65959410	0.7881	0.0716
(2.) Shell Side	41.2	390	360	90609565	1.1037	-
Tube Side		390	360	51786903	0.6066	0.0438
(3.) Shell Side	36.2	990	600	69448503	0.8328	-
Tube Side		990	600	43293776	0.4978	0.0341
(4.) Shell Side	34.2	1290	300	68409375	0.8194	-
Tube Side		1290	300	45747732	0.5293	0.0318

Table 3b.2 Rejection Factors of Preasphaltenes-THF for a γ-Alumina Film.
Temperature: 323 K

	GPC Time/*Molecular Weight*				
Trial Number	6.50 ***56721***	8.50 ***2073***	9.00 ***1030***	9.80 ***344***	**Permeability (ml/min/PSID/cm^2)**
1	0.3352	0.2640	0.1990	0.1959	0.00021896
2	0.4217	0.3975	0.2561	0.1711	0.00013803
3	0.4781	0.4488	0.2964	0.0613	0.00012263
4	0.5817	0.4446	0.2090	-0.0591	0.00012086

Table 3b.3 MW-MW Separation Factors of Preasphaltenes-THF for a γ-Alumina Film.
Temperature: 323 K

Trial	*56721-344*	*2073-344*	*1030-344*
1	0.79	0.90	1.00
2	0.64	0.68	0.87
3	0.48	0.51	0.69
4	0.31	0.43	0.67

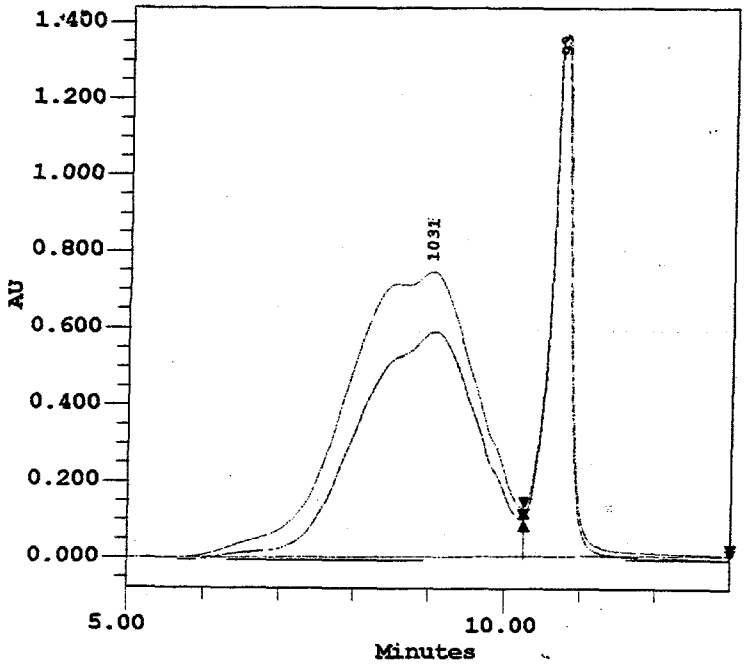

Figure 3b.1a.
GPC Analysis of Preasphaltene Separation by a Gamma-Alumina Film in a THF Medium (T = 323K).
Time = 30 Minutes.
Pressure Drop: 40 PSID
1 - Downstream - Tube Side.
2 - Upstream - Shell Side.

#	Mn (Daltons)	MP (Daltons)	Mw (Daltons)
1	925	962	3171
2	1002	1031	3849
3		93	
4		93	

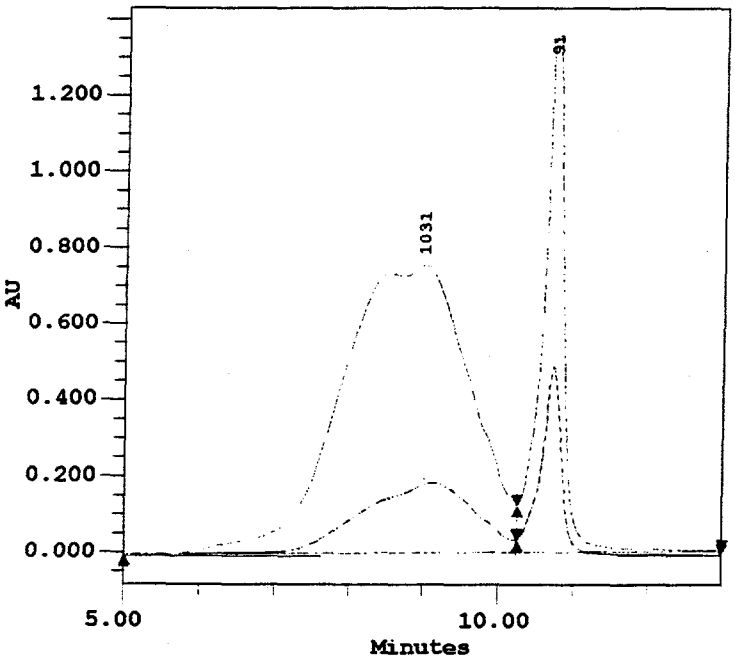

Figure 3b.1b.
GPC Analysis of Preasphaltene Separation by a Gamma-Alumina Film in a THF Medium (T = 323K).
Time = 390 Minutes.
Pressure Drop: 40 PSID
1 - Downstream - Tube Side.
2 - Upstream - Shell Side.

#	Mn (Daltons)	MP (Daltons)	Mw (Daltons)
1	840	878	3456
2	995	1031	3770
3		91	
4		91	

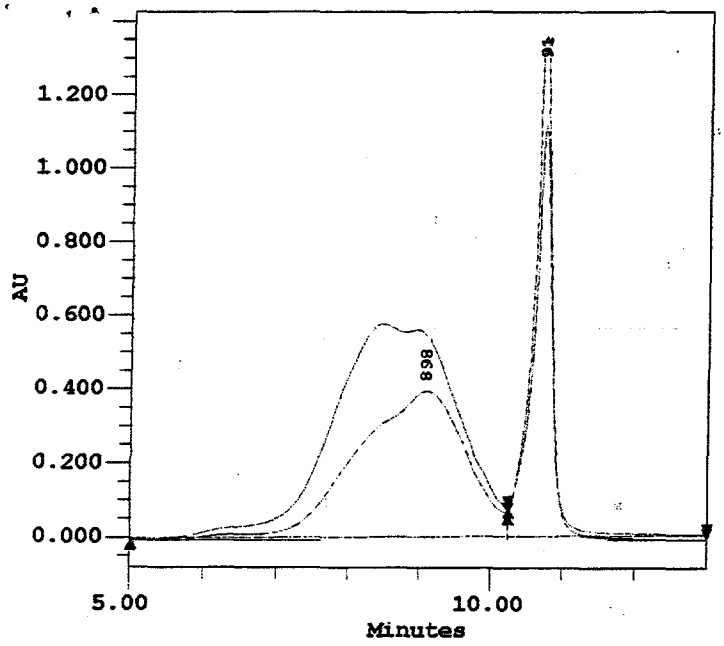

Figure 3b.1c.
GPC Analysis of Preasphaltene Separation by a Gamma-Alumina Film in a THF Medium (T = 323K).
Time = 990 Minutes.
Pressure Drop: 40 PSID
1 - Downstream - Tube Side.
2 - Upstream - Shell Side.

#	Mn (Daltons)	MP (Daltons)	Mw (Daltons)
1	900	898	3728
2	1082	2124	4526
3		91	
4		91	

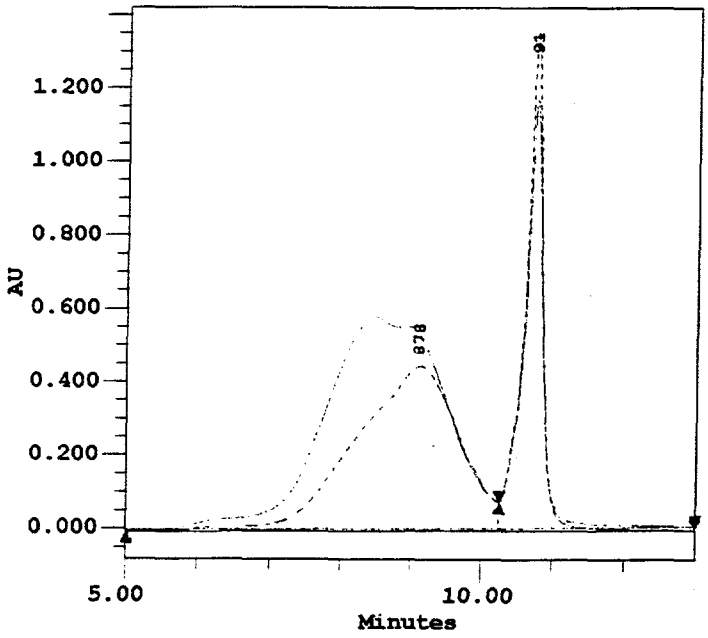

Figure 3b.1d.
GPC Analysis of Preasphaltene Separation by a Gamma-Alumina Film in a THF Medium (T = 323K).
Time = 1290 Minutes.
Pressure Drop: 40 PSID
1 - Downstream - Tube Side.
2 - Upstream - Shell Side.

#	Mn (Daltons)	MP (Daltons)	Mw (Daltons)
1	847	878	3338
2	1115	2175	4684
3		91	
4		91	

Figure 3b.2 Rejection Factors for a γ-Alumina Film with Preasphaltene-THF Solution (ΔP = 40 PSID), (T = 323 K).

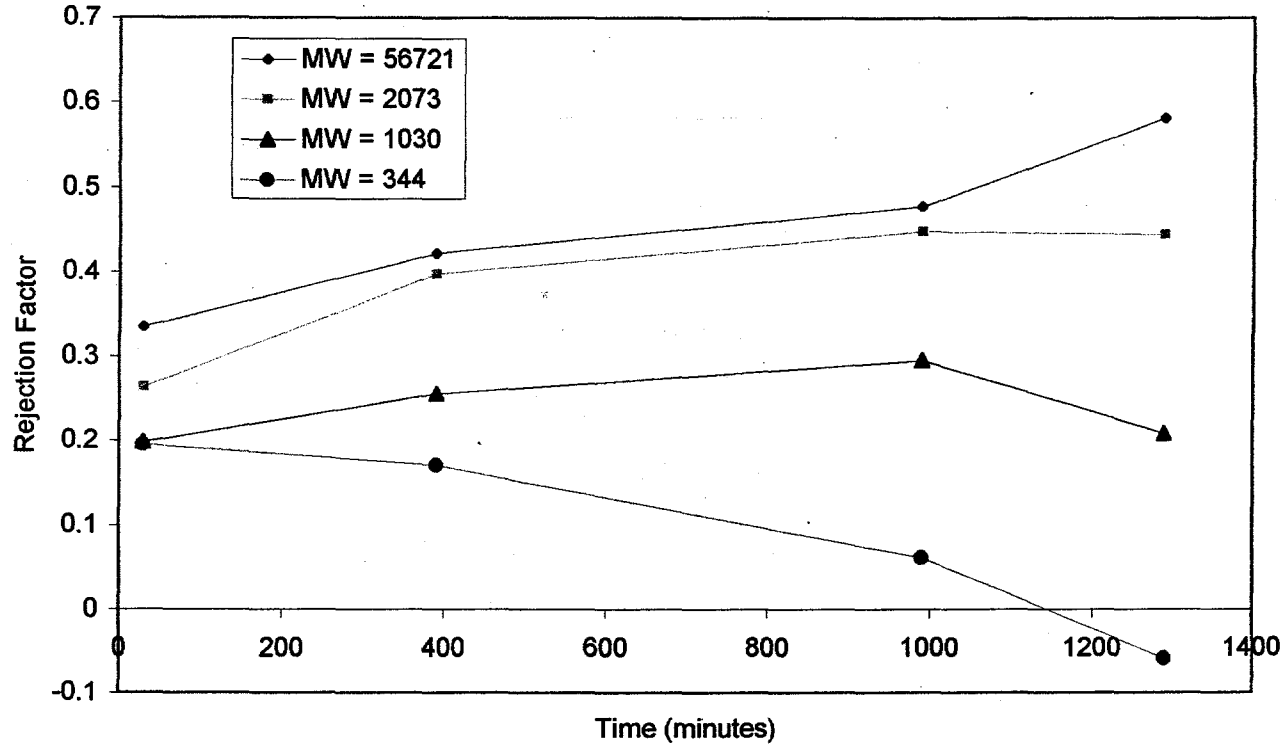

Figure 3b.3 Separation Factors for a γ-Alumina Film with Preasphaltene-THF Solution (ΔP = 40), (T = 323 K).

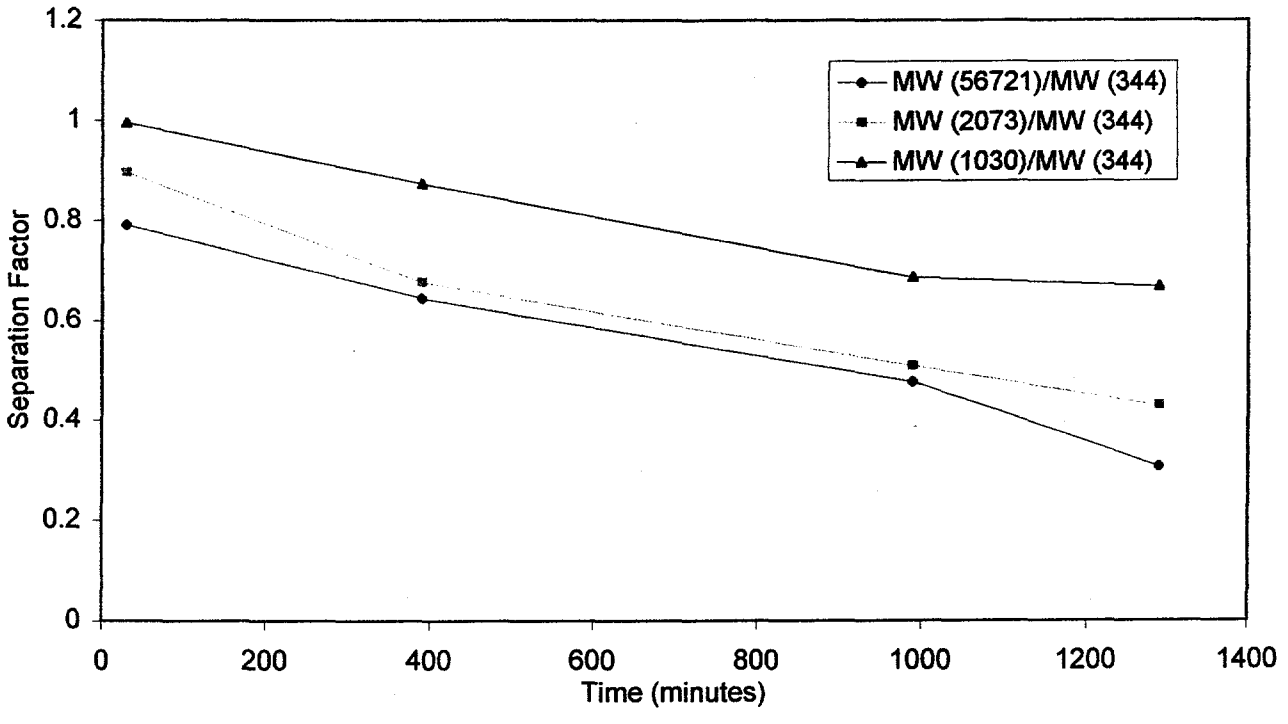

Table 3c.1 Preasphaltene-THF Filtration Experiments for a γ-Alumina Film.
Nominal Shell Pressure: 600 psig Temperature: 373 K

Trial Number & Description	ΔP	Membrane Condition Time	Equil. Time	Total Area	Estimat. Conc.	Flow Rate
	(PSID)	(Min)	(Min)	(μV*Sec)	(g/L)	(ml/min)
(1.) Shell Side	25.0	510	510	78914299	0.9540	-
Tube Side		510	510	43850516	0.5050	0.0716
(2.) Shell Side	41.1	1050	540	84106536	1.0204	-
Tube Side		1050	540	36942731	0.4165	0.0438
(3.) Shell Side	39.7	1410	360	80467288	0.9738	-
Tube Side		1410	360	36914298	0.4162	0.0341

Table 3c.2 Rejection Factors of Preasphaltenes-THF for a γ-Alumina Film.
Temperature: 373 K

	GPC Time/*Molecular Weight*				
Trial Number	6.50 ***56721***	8.50 ***2073***	9.00 ***1030***	9.80 ***344***	**Permeability (ml/min/PSID/cm^2)**
1	0.6479	0.5302	0.3364	0.1848	0.00037223
2	0.6832	0.6389	0.5010	0.2859	0.00013836
3	0.7282	0.6469	0.4425	0.1762	0.00011173

Table 3c.3 MW-MW Separation Factors of Preasphaltenes-THF for a γ-Alumina Film.
Temperature: 373 K

Trial	*56721-344*	*2073-344*	*1030-344*
1	0.35	0.49	0.75
2	0.39	0.45	0.65
3	0.28	0.37	0.62

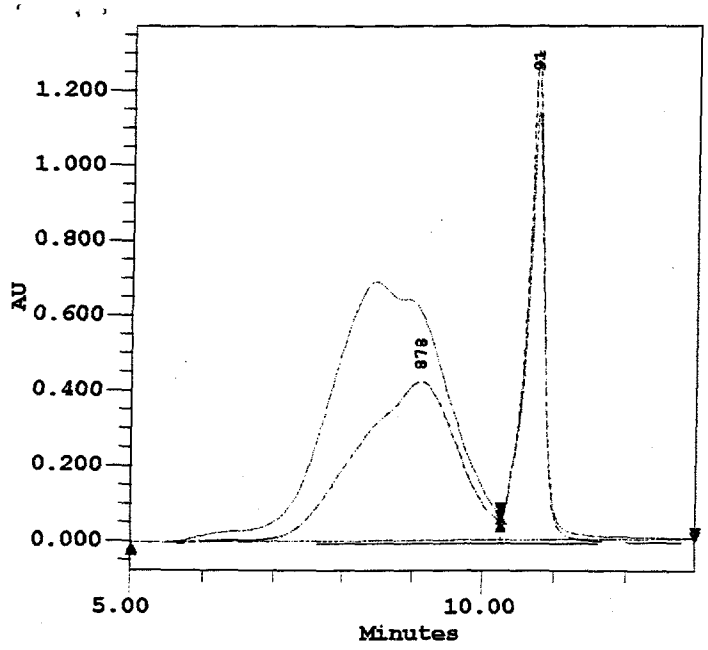

Figure 3c.1a.

GPC Analysis of Preasphaltene Separation by a Gamma-Alumina Film in a THF Medium (T = 373K).
Time = 510 Minutes.
Pressure Drop: 40 PSID
1 - Downstream - Tube Side.
2 - Upstream - Shell Side.

#	Mn (Daltons)	MP (Daltons)	Mw (Daltons)
1	889	878	3426
2	1124	2175	4479
3		91	
4		91	

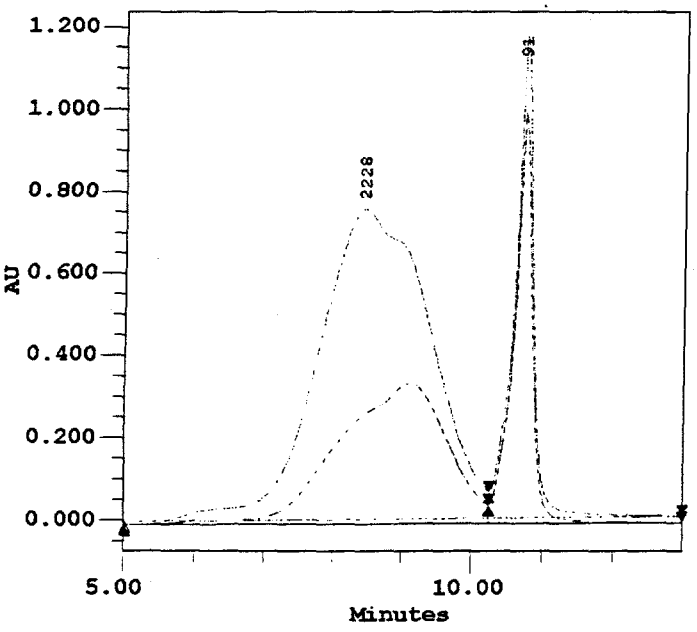

Figure 3c.1b.

GPC Analysis of Preasphaltene Separation by a Gamma-Alumina Film in a THF Medium (T = 373K).
Time = 1050 Minutes.
Pressure Drop: 40 PSID
1 - Downstream - Tube Side.
2 - Upstream - Shell Side.

#	Mn (Daltons)	MP (Daltons)	Mw (Daltons)
1	919	878	3975
2	1185	2228	4754
3		91	
4		91	

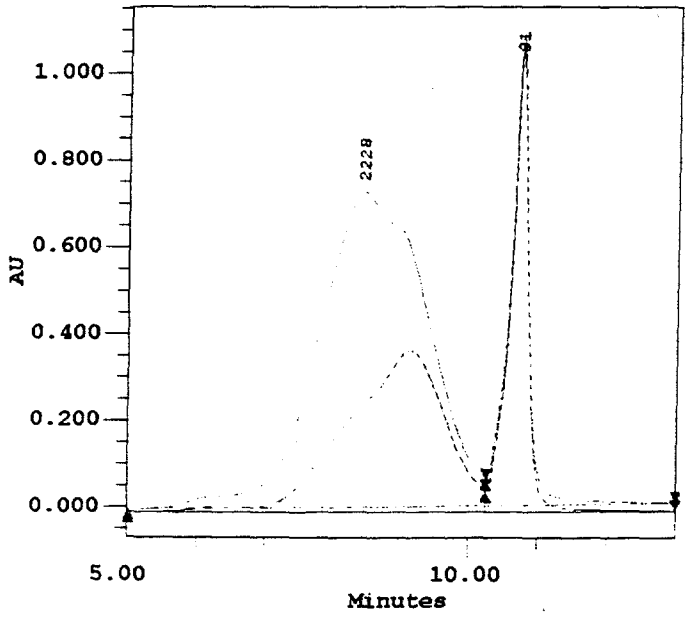

Figure 3c.1c.

GPC Analysis of Preasphaltene Separation by a Gamma-Alumina Film in a THF Medium (T = 373K).
Time = 1410 Minutes.
Pressure Drop: 40 PSID
1 - Downstream - Tube Side.
2 - Upstream - Shell Side.

#	Mn (Daltons)	MP (Daltons)	Mw (Daltons)
1	870	858	3528
2	1197	2228	4877
3		88	
4		91	

Figure 3c.2 Rejection Factors for a γ-Alumina Film with Preasphaltene-THF Solution (ΔP = 40 PSID), (T = 373 K).

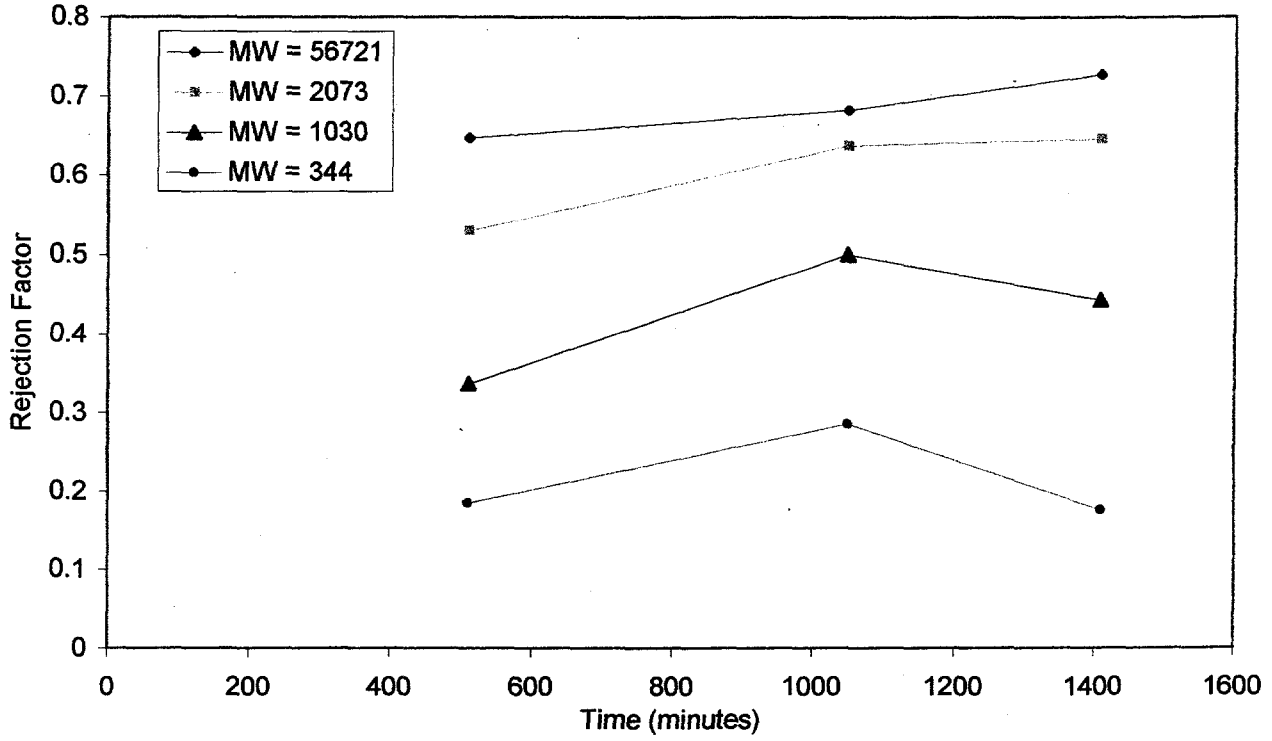

Figure 3c.3 Separation Factors for a γ-Alumina Film with Preasphaltene-THF Solution (ΔP = 40), (T = 373 K).

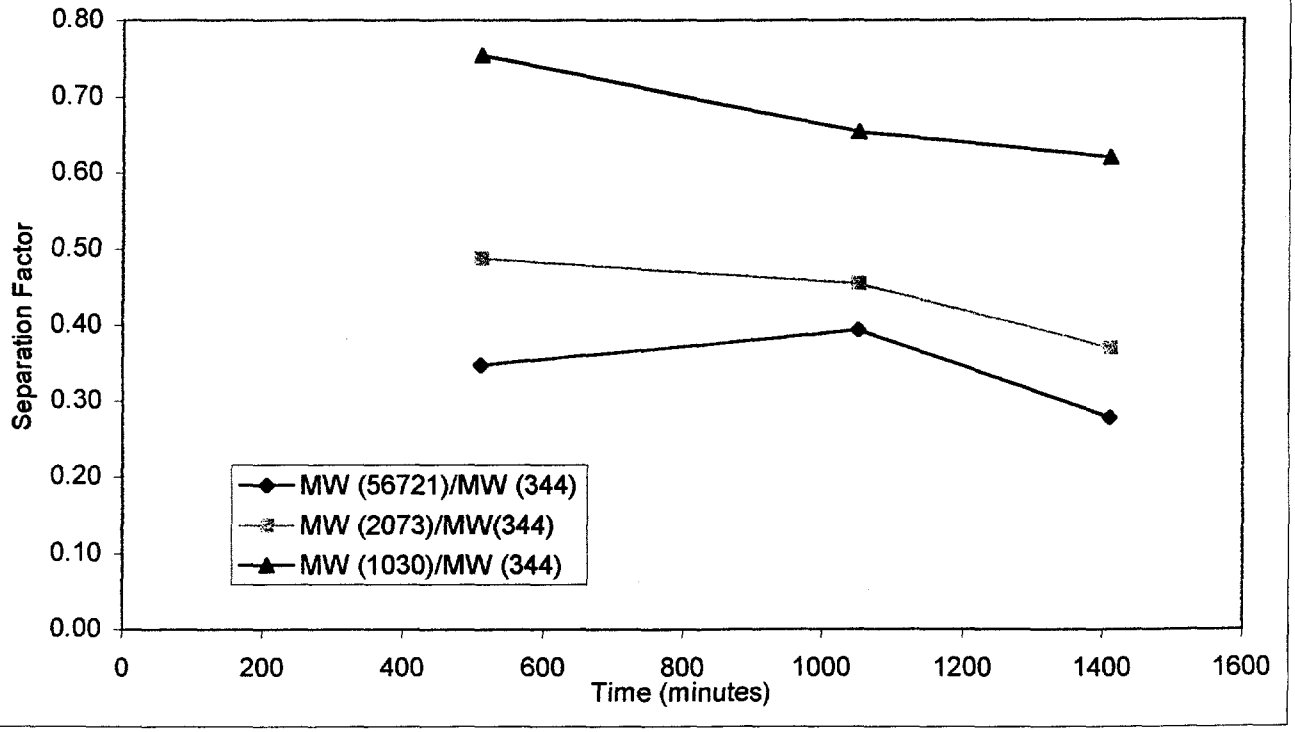

Table 3d.1 Asphaltene-THF Filtration Experiments for a γ-Alumina Film.
Nominal Shell Pressure: 0 psig Temperature: 298 K

Trial Number & Description	ΔP	Membrane Condition Time	Equil. Time	Total Area	Estimat. Conc.	Flow Rate
	(PSID)	(Min)	(Min)	(μV*Sec)	(g/L)	(ml/min)
(1.) Shell Side	61.2	300	510	38540367	0.4370	-
Tube Side		300	510	36042923	0.4050	0.0755
(2.) Shell Side	42.5	840	540	42039803	0.4818	-
Tube Side		840	540	29188773	0.3172	0.0468
(3.) Shell Side	54.9	1500	660	40376122	0.4605	-
Tube Side		1500	660	23538957	0.2449	0.0455

Table 3d.2 Rejection Factors of Asphaltenes-THF for a γ-Alumina Film.
Temperature: 298 K

	GPC Time/*Molecular Weight*				
Trial Number	6.50 ***56721***	8.50 ***2073***	9.00 ***1030***	9.80 ***344***	**Permeability (ml/min/PSID/cm^2)**
1	0.5821	0.1052	0.0523	0.0104	0.00016021
2	0.7352	0.4093	0.3288	0.1477	0.00014301
3	0.8631	0.5480	0.4438	0.1830	0.00010762

Table 3d.3 MW-MW Separation Factors of Asphaltenes-THF for a γ-Alumina Film.
Temperature: 298 K

Trial	***56721-344***	***2073-344***	***1030-344***
1	0.37	0.88	0.95
2	0.26	0.64	0.74
3	0.14	0.51	0.64

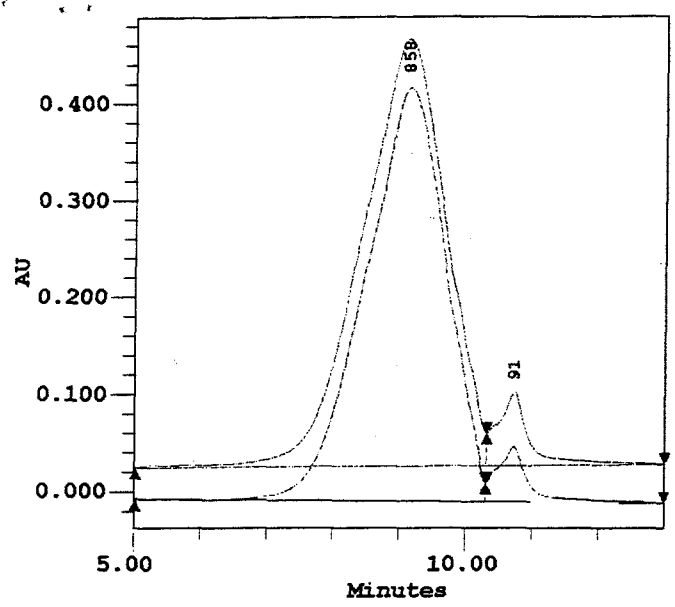

Figure 3d.1a.

GPC Analysis of Asphaltene Separation by a Gamma-Alumina Film in a THF Medium (T = 293K).
Time = 300 Minutes.
Pressure Drop: 50 PSID
1 - Downstream - Tube Side.
2 - Upstream - Shell Side.

#	Mn (Daltons)	MP (Daltons)	Mw (Daltons)
1	739	820	1568
2	759	858	2682
3		91	
4		91	

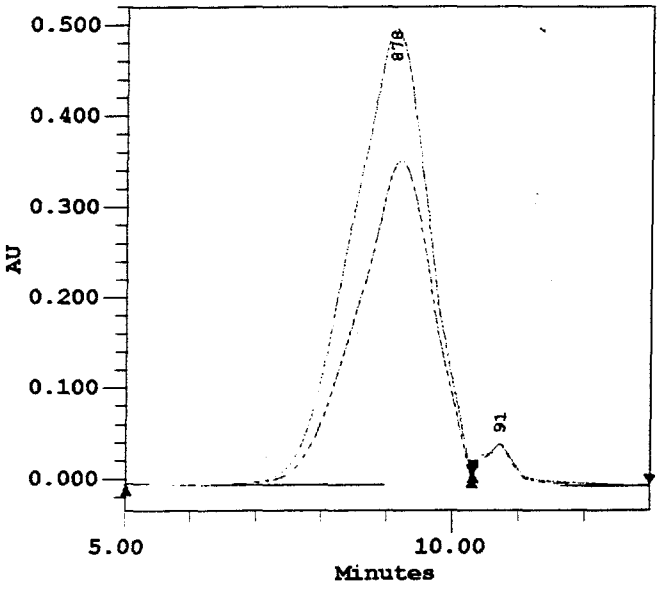

Figure 3d.1b.

GPC Analysis of Asphaltene Separation by a Gamma-Alumina Film in a THF Medium (T = 293K).
Time = 840 Minutes.
Pressure Drop: 50 PSID
1 - Downstream - Tube Side.
2 - Upstream - Shell Side.

#	Mn (Daltons)	MP (Daltons)	Mw (Daltons)
1	727	783	1570
2	794	878	1691
3		91	
4		91	

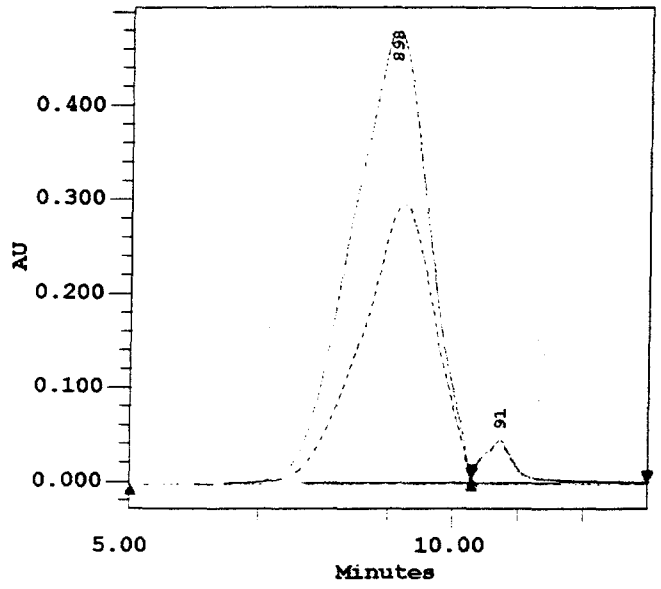

Figure 3d.1c.

GPC Analysis of Asphaltene Separation by a Gamma-Alumina Film in a THF Medium (T = 293K).
Time = 1500 Minutes.
Pressure Drop: 50 PSID
1 - Downstream - Tube Side.
2 - Upstream - Shell Side.

#	Mn (Daltons)	MP (Daltons)	Mw (Daltons)
1	709	748	1435
2	820	898	1688
3		91	
4		93	

Figure 3d.2 Rejection Factors for a γ-Alumina Film with Asphaltene-THF Solution (ΔP = 50 PSID), (T = 298 K).

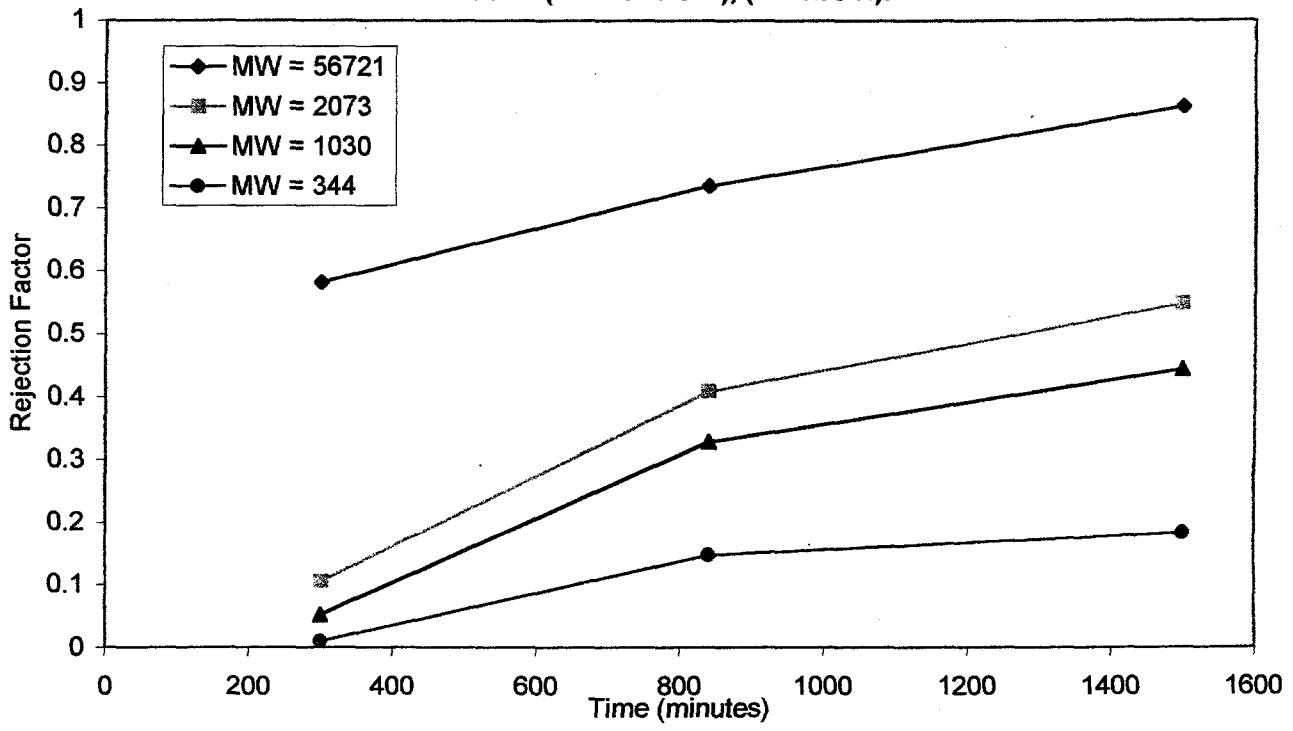

Figure 3d.3 Separation Factors for a γ-Alumina Film with Asphaltene-THF Solution (ΔP = 50), (T = 298 K).

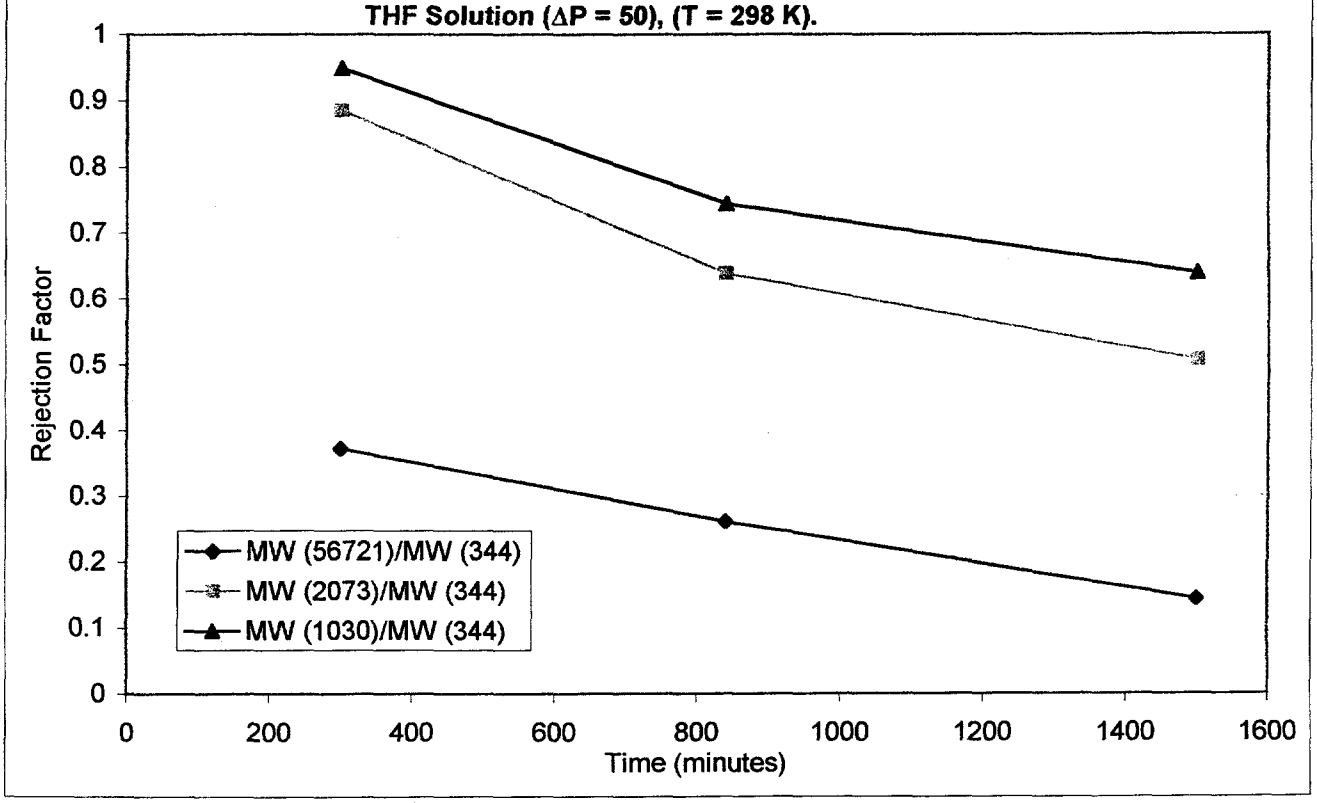

Table 3e.1 Asphaltene-THF Filtration Experiments for a γ-Alumina Film.

Nominal Shell Pressure: 400 psig Temperature: 323 K

Trial Number & Description	ΔP	Membrane Condition Time	Equil. Time	Total Area	Estimat. Conc.	Flow Rate
	(PSID)	(Min)	(Min)	(μV*Sec)	(g/L)	(ml/min)
(1.) Shell Side	42.4	630	630	38540367	0.4370	-
Tube Side		630	630	36042923	0.4050	0.0480
(2.) Shell Side	49.3	1350	720	42039803	0.4818	-
Tube Side		1350	720	29188773	0.3172	0.0463
(3.) Shell Side	54.7	1650	300	40376122	0.4605	-
Tube Side		1650	300	23538957	0.2449	0.0468

Table 3e.2 Rejection Factors of Asphaltenes-THF for a γ-Alumina Film.

Temperature: 323 K

	GPC Time/*Molecular Weight*				
Trial Number	6.50 ***56721***	8.50 ***2073***	9.00 ***1030***	9.80 ***344***	**Permeability (ml/min/PSID/cm^2)**
1	0.6091	0.5991	0.4649	0.2243	0.00014724
2	0.7416	0.7139	0.4985	0.2229	0.00012198
3	0.7821	0.7232	0.5279	0.1772	0.00011111

Table 3e.3 MW-MW Separation Factors of Asphaltenes-THF for a γ-Alumina Film.

Temperature: 323 K

Trial	***56721-344***	***2073-344***	***1030-344***
1	0.45	0.46	0.64
2	0.29	0.32	0.60
3	0.23	0.30	0.53

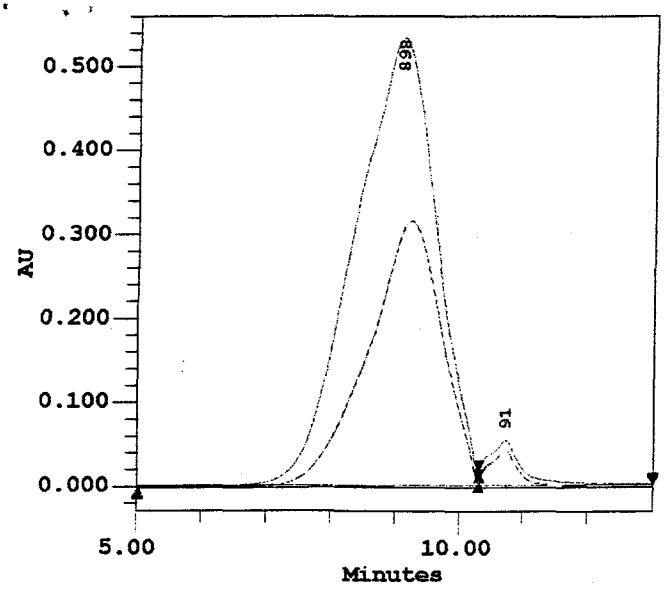

Figure 3e.1a

GPC Analysis of Asphaltene Separation by a Gamma-Alumina Film in a THF Medium (T = 323K).
Time = 630 Minutes.
Pressure Drop: 45 PSID
1 - Downstream - Tube Side.
2 - Upstream - Shell Side.

#	Mn (Daltons)	MP (Daltons)	Mw (Daltons)
1	704	748	1378
2	837	898	1691
3		91	
4		91	

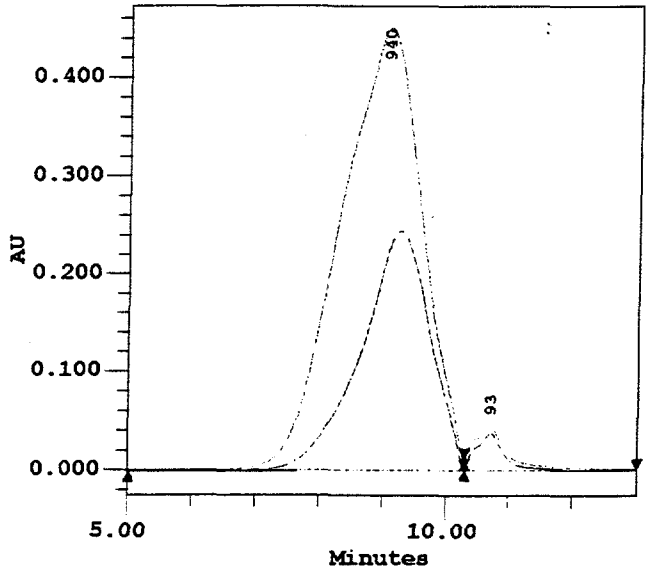

Figure 3e.1b

GPC Analysis of Asphaltene Separation by a Gamma-Alumina Film in a THF Medium (T = 323K).
Time = 1350 Minutes.
Pressure Drop: 45 PSID
1 - Downstream - Tube Side.
2 - Upstream - Shell Side.

#	Mn (Daltons)	MP (Daltons)	Mw (Daltons)
1	674	715	1314
2	866	940	1779
3		91	
4		93	

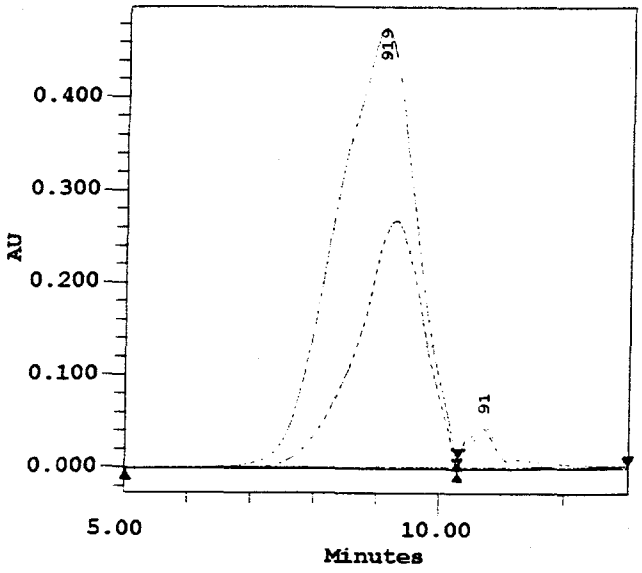

Figure 3e.1c

GPC Analysis of Asphaltene Separation by a Gamma-Alumina Film in a THF Medium (T = 323K).
Time = 1650 Minutes.
Pressure Drop: 45 PSID
1 - Downstream - Tube Side.
2 - Upstream - Shell Side.

#	Mn (Daltons)	MP (Daltons)	Mw (Daltons)
1	672	715	1324
2	869	919	1820
3		91	
4		91	

Figure 3e.2 Rejection Factors for a γ-Alumina Film with Asphaltene-THF Solution (ΔP = 45 PSID), (T = 323 K).

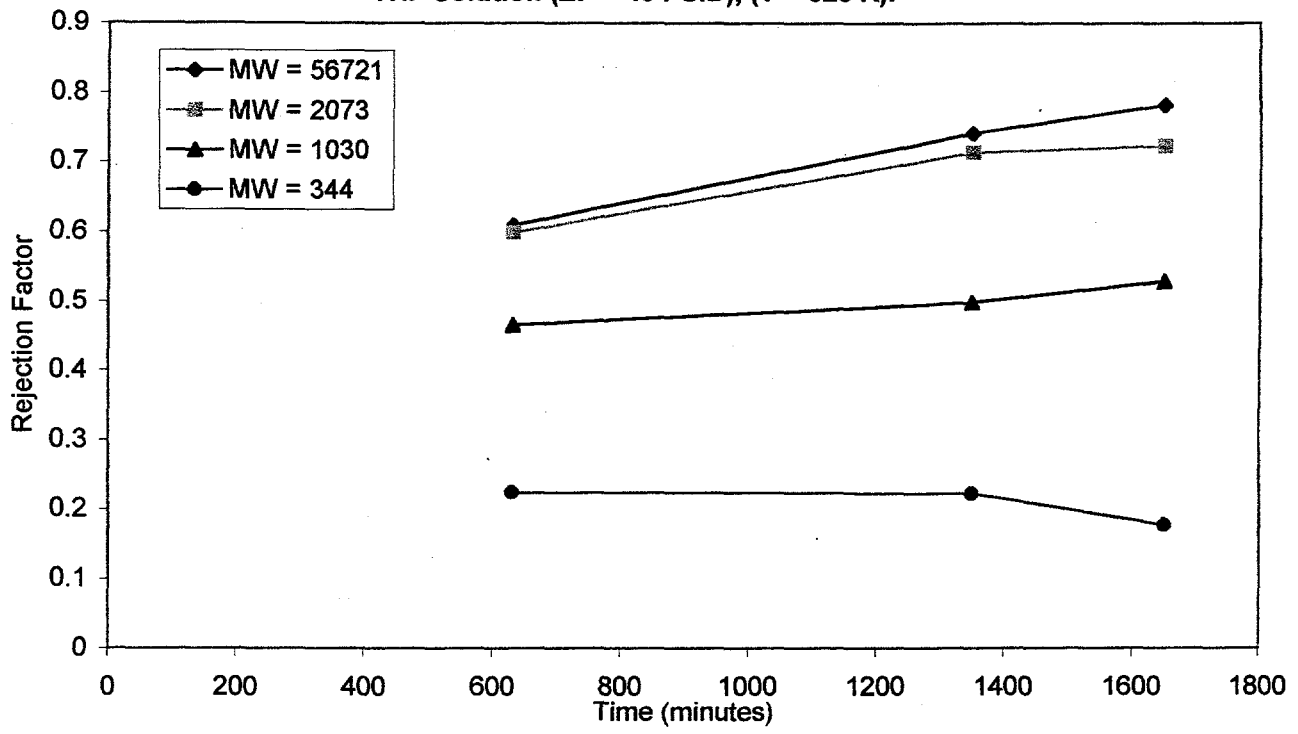

Figure 3e.3 Separation Factors for a γ-Alumina Film with Asphaltene-THF Solution (ΔP = 45), (T = 323 K).

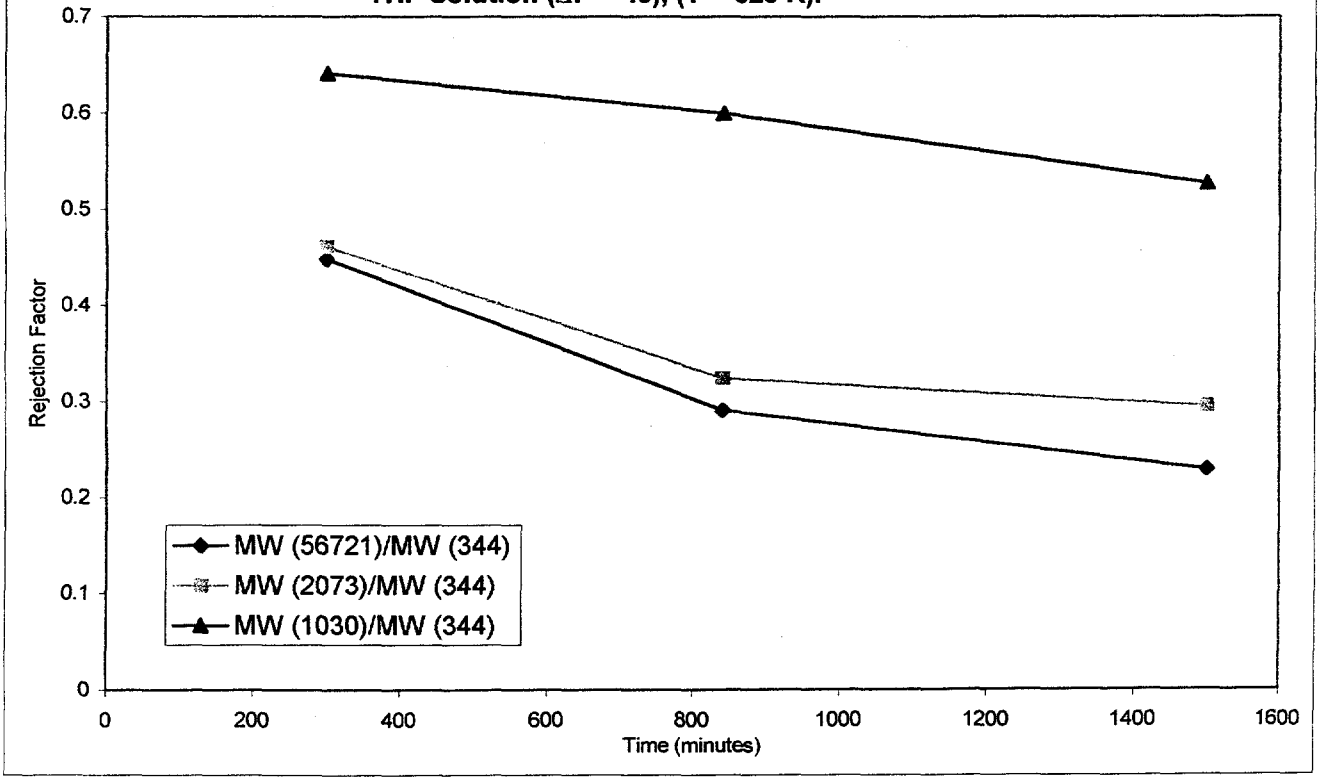

Table 3f.1 Asphaltene-THF Filtration Experiments for a γ-Alumina Film.

Nominal Shell Pressure: 600 psig Temperature: 373 K

Trial Number & Description	ΔP	Membrane Condition Time	Equil. Time	Total Area	Estimat. Conc.	Flow Rate
	(PSID)	(Min)	(Min)	(μV*Sec)	(g/L)	(ml/min)
(1.) Shell Side	36.1	360	360	60529111	0.7185	-
Tube Side		360	360	38640780	0.4383	0.0508
(2.) Shell Side	37.1	960	600	60529136	0.7185	-
Tube Side		960	600	29695241	0.3237	0.0438
(3.) Shell Side	46.1	1680	720	54772392	0.6448	-
Tube Side		1680	720	26955257	0.2886	0.0429

Table 3f.2 Rejection Factors of Asphaltenes-THF for a γ-Alumina Film.

Temperature: 373 K

	GPC Time/*Molecular Weight*				
Trial Number	6.50 *56721*	8.50 *2073*	9.00 *1030*	9.80 *344*	Permeability (ml/min/PSID/cm^2)
1	0.6284	0.5933	0.3581	0.0005	0.00018292
2	0.8685	0.7741	0.4837	0.0669	0.00015340
3	0.8962	0.7788	0.4955	0.0214	0.00012079

Table 3f.3 MW-MW Separation Factors of Asphaltenes-THF for a γ-Alumina Film.

Temperature: 373 K

Trial	*56721-344*	*2073-344*	*1030-344*
1	0.30	0.33	0.56
2	0.11	0.19	0.48
3	0.08	0.18	0.45

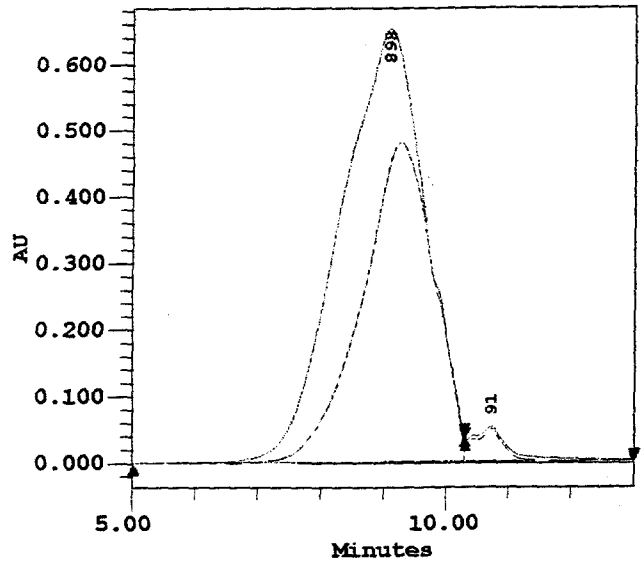

Figure 3f.1a.

GPC Analysis of Asphaltene Separation by a Gamma-Alumina Film in a THF Medium (T = 373K).
Time = 360 Minutes.
Pressure Drop: 40 PSID
1 - Downstream - Tube Side.
2 - Upstream - Shell Side.

#	Mn (Daltons)	MP (Daltons)	Mw (Daltons)
1	628	715	1243
2	821	898	1824
3		88	
4		91	

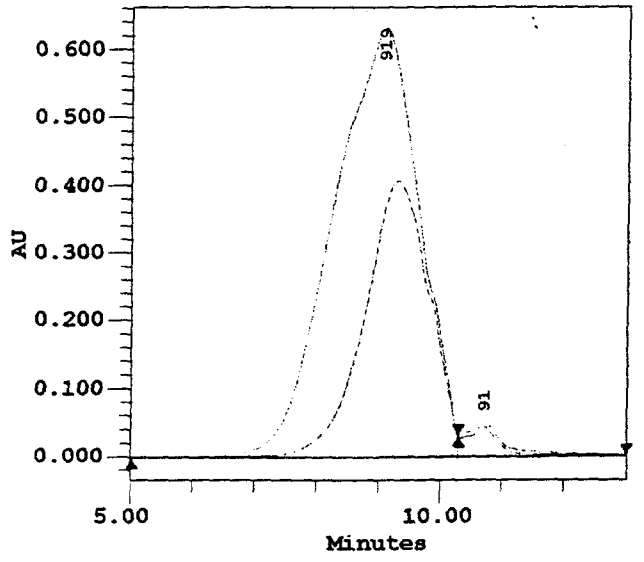

Figure 3f.1b.

GPC Analysis of Asphaltene Separation by a Gamma-Alumina Film in a THF Medium (T = 373K).
Time = 960 Minutes.
Pressure Drop: 40 PSID
1 - Downstream - Tube Side.
2 - Upstream - Shell Side.

#	Mn (Daltons)	MP (Daltons)	Mw (Daltons)
1	581	683	1031
2	840	919	1907
3		91	
4		91	

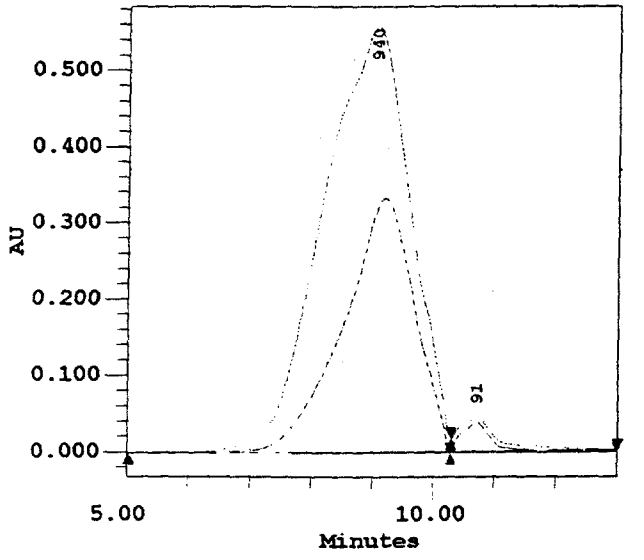

Figure 3f.1c.

GPC Analysis of Asphaltene Separation by a Gamma-Alumina Film in a THF Medium (T = 373K).
Time = 1680 Minutes.
Pressure Drop: 40 PSID
1 - Downstream - Tube Side.
2 - Upstream - Shell Side.

#	Mn (Daltons)	MP (Daltons)	Mw (Daltons)
1	741	783	1628
2	892	940	2128
3		91	
4		91	

Figure 3f.2 Rejection Factors for a γ-Alumina Film with Asphaltene-THF Solution (ΔP = 40 PSID), (T = 373 K).

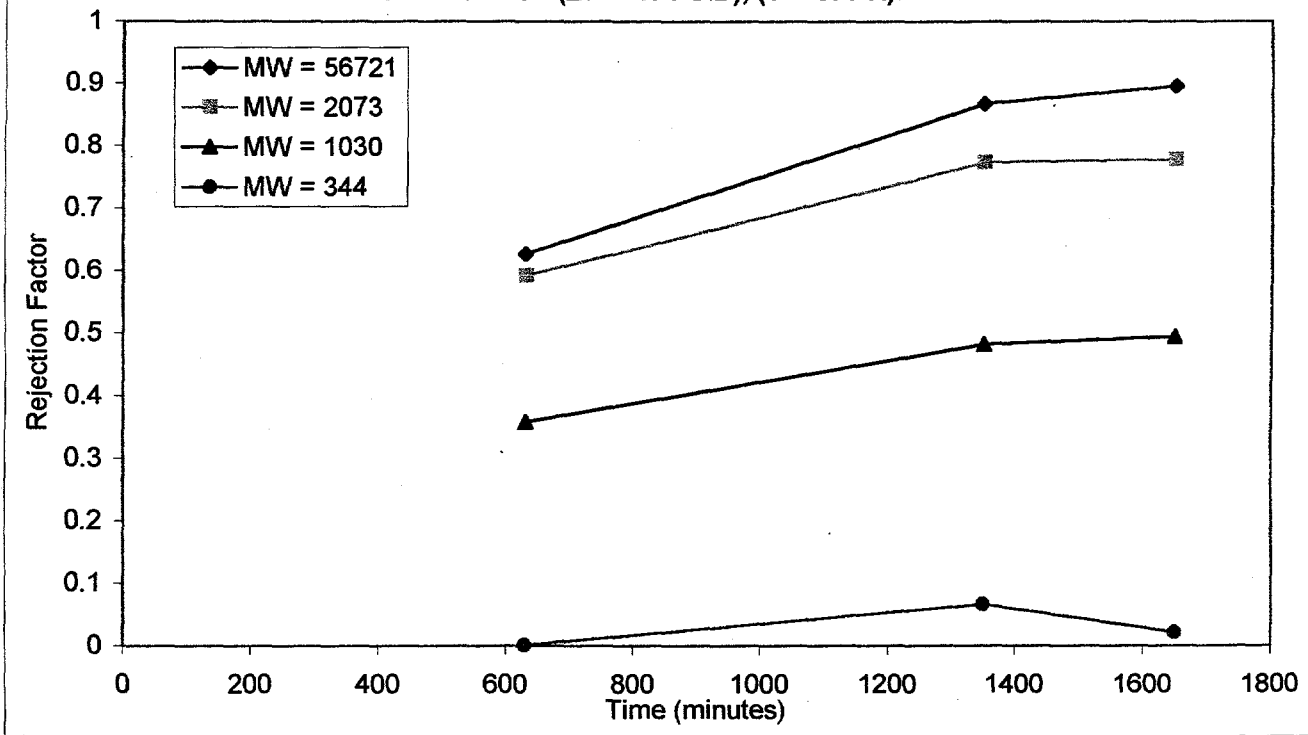

Figure 3f.3 Separation Factors for a γ-Alumina Film with Asphaltene-THF Solution (ΔP = 40), (T = 373 K).

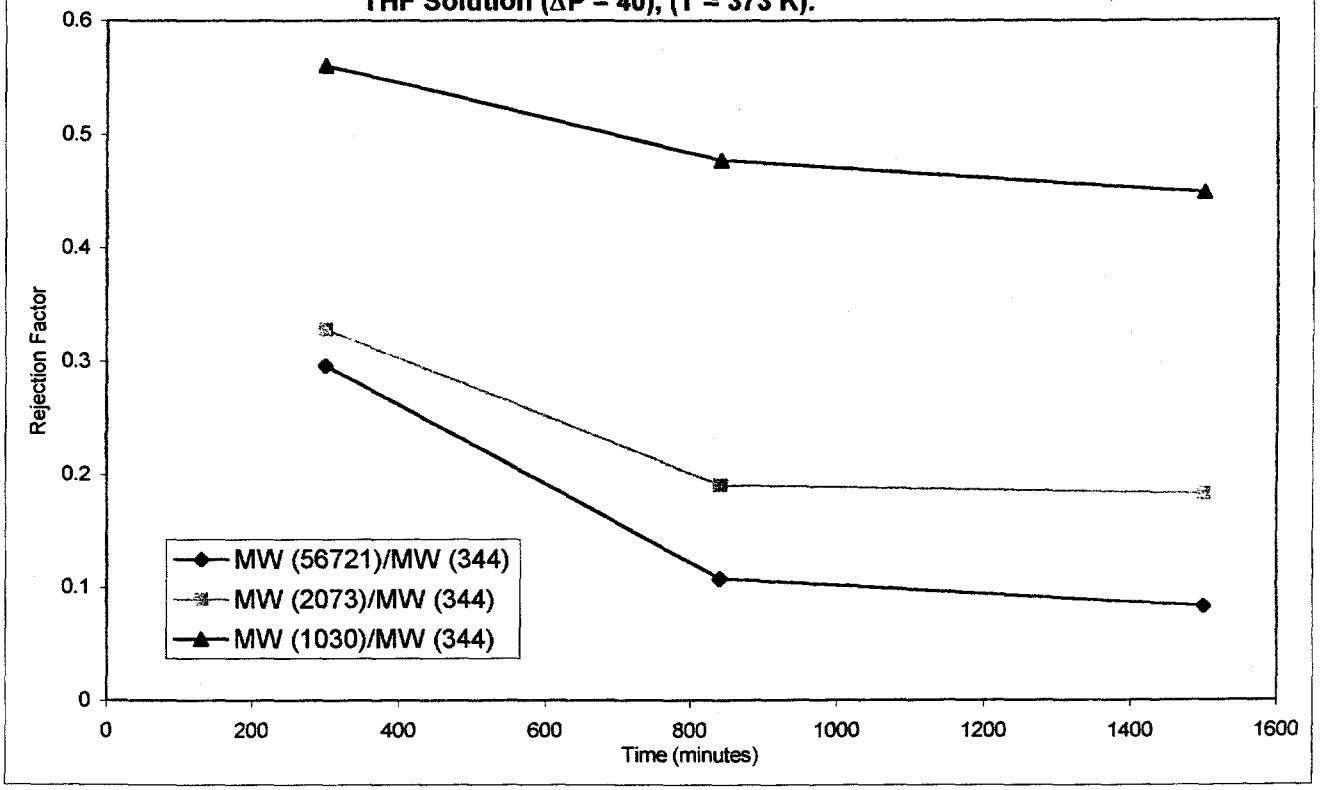

4. THE TRANSPORT OF COAL PREASPHALTENES THROUGH SIO_2 SOL GEL TYPE MEMBRANES

Silica membranes were prepared by dip-coating alumina substrates utilizing silica solutions. These are prepared by diluting 27.5 ml of tetraethylorthosilicate (TEOS, from Aldrich) with 25 ml EtOH. Under vigorous stirring, 14.2 ml of distilled water is added drop-wise to the solution. The sol is then peptized with 5.2 ml of 2 N HCl and continuously stirred for 3 hr. The membranes were dip-coated for 2 min, drawn from the solution at a rate of 2 cm/min, and allowed to dry for 48 hr. The calcination process occurs at 500 °C with the same temperature profile heating rate and hold times as described for the alumina film procedure.

The silica membranes were utilized to carry-out transport investigations of solutions of preasphaltenes in THF. As with the γ-Al_2O_3 membranes the silica membranes proved very resistant to reactive solvents like THF. The experimental results are described in Tables 4.1-4.3 and in Figures 4.1-4.5. Figures 4.1-4.3 contain the raw GPC data of the samples in the tube side and the shell side of the transport apparatus. As with the alumina experiments the membrane upon exposure requires a period of conditioning. Over the same period over which the rejection coefficients reach an asymptotic value in the alumina membrane experiments the rejection coefficients for the silica membrane was still found to be increasing. Interestingly enough, however, over the same period of time the separation factor between the different molecular weights appear to be leveling off.

Silica membrane have a significantly lower permeance than the corresponding alumina membranes, which explains some of the inaccuracies observed in the experiments with the largest molecular weights (MW 50000+) in the Figures due to the very low concentrations of these higher molecular weight species (the GPC system has trouble

dealing with such low concentration changes as previously discussed). In addition we have observed that upon conditioning of the membrane some of the gains in rejection coefficients are irreversible. These findings are most likely indicative of the fact that for the silica membranes a thin film is forming on the surface of the pore during conditioning. By comparing the SiO2 data with the data previously generated with the alumina membranes one observes that upon conditioning the attained rejection coefficients are not significantly bettter with the silica membrane than they are with alumina membranes.

Table 4.1. Preasphaltene-THF Filtration Experiments for a Silica Film.
Nominal Shell Pressure: 0 psig Temperature: 298 K

Trial Number & Description	ΔP	Membrane Condition Time	Equil. Time	Total Area	Estimat. Conc.	Flow Rate
	(PSID)	(Min)	(Min)	(μV*Sec)	(g/L)	(ml/min)
(0.) Start Sample	-	-	-	49020994	0.5712	-
(1.) Shell Side	51.2	80	80	40521020	0.4623	-
Tube Side		80	80	27382112	0.2941	0.5485
(2.) Shell Side	51.2	575	215	48172309	0.5603	-
Tube Side		575	215	25767965	0.2734	0.2565
(3.) Shell Side	54.0	1295	720	49337072	0.5752	-
Tube Side		1295	720	21192603	0.2148	0.1214
(4.) Shell Side	33.2	160	80	46561975	0.5397	-
Tube Side		160	80	42338834	0.4856	0.2127
(5.) Shell Side	33.0	375	215	43546364	0.5011	-
Tube Side		375	215	37446816	0.4230	0.1899
(6.) Shell Side	35.0	1415	120	46445337	0.5382	-
Tube Side		1415	120	19990954	0.1995	0.0707
(7.) Shell Side	60.0	4320	2880	49790487	0.5810	-
Tube Side		4320	2880	16131649	0.1500	0.0045

Table 4.2. Rejection Factors of Preasphaltenes-THF for a Silica Film .
Temperature: 298 K

	GPC Time/*Molecular Weight*					
Trial Number	6.00	7.00	8.38	9.00	9.20	**Permeability**
	167556	***27847***	***2747***	***1053***	***783***	**(ml/min/PSID/cm^2)**
1	0.2596	0.3539	0.1998	0.1313	0.1205	0.00139194
2	0.2677	0.5209	0.5023	0.4135	0.3887	0.00065084
3	0.4424	0.7268	0.6801	0.4610	0.3847	0.00029212
4	0.2144	0.2424	0.1025	0.0016	-0.0181	0.00083246
5	0.2776	0.3968	0.1652	0.0049	-0.0061	0.00074781
6	0.6552	0.7937	0.6709	0.4210	0.3312	0.00026252
7	0.7618	0.8921	0.7887	0.5495	0.4615	0.00000985

Table 4.3. MW-MW Separation Factors of Preasphaltenes-THF for a Silica Film.
Temperature: 298 K

Trial	***167556-783***	***27847-783***	***2747-783***	***1053-783***
1	0.81	0.69	0.89	0.98
2	1.24	0.76	0.79	0.95
3	0.89	0.41	0.48	0.86
4	0.70	0.67	0.84	0.97
5	0.64	0.51	0.77	0.98
6	0.46	0.26	0.44	0.84
7	0.41	0.18	0.37	0.82

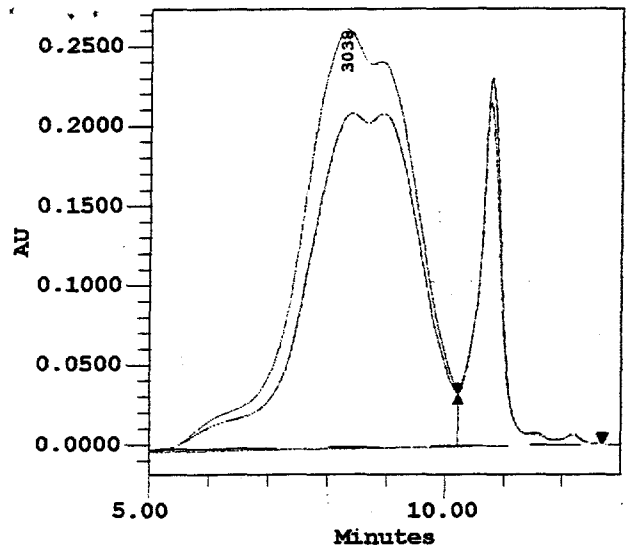

Figure 4.1a.

GPC Analysis of Preasphaltene Separation by a Silica Film in a THF Medium (T = 293K).
Time = 80 Minutes.
Pressure Drop: 50 PSID
1 - Downstream - Tube Side.
2 - Upstream - Shell Side.

#	Mn (Daltons)	MP (Daltons)	Mw (Daltons)
1	580	3038	8446
2	1162	2660	8570
3		95	

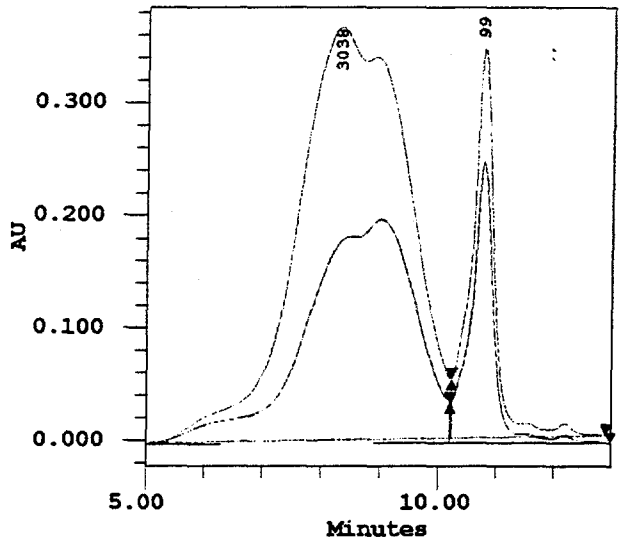

Figure 4.1b.

GPC Analysis of Preasphaltene Separation by a Silica Film in a THF Medium (T = 293K).
Time = 575 Minutes.
Pressure Drop: 50 PSID
1 - Downstream - Tube Side.
2 - Upstream - Shell Side.

#	Mn (Daltons)	MP (Daltons)	Mw (Daltons)
1	1088	1053	10357
2	1219	3038	8807
3		97	
4		99	

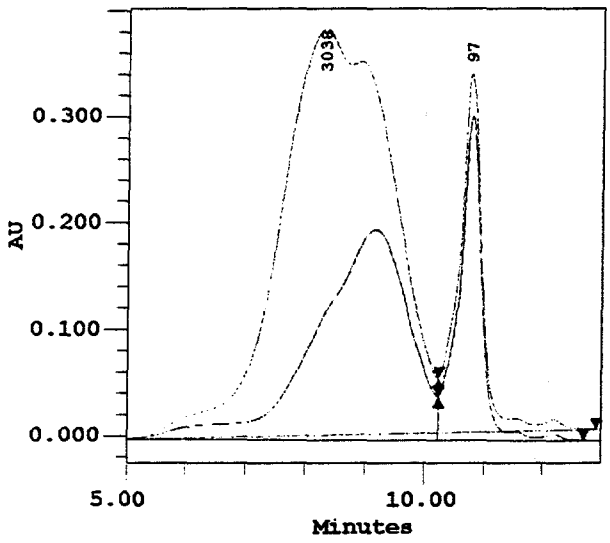

Figure 4.1c.

GPC Analysis of Preasphaltene Separation by a Silica Film in a THF Medium (T = 293K).
Time = 1295 Minutes.
Pressure Drop: 50 PSID
1 - Downstream - Tube Side.
2 - Upstream - Shell Side.

#	Mn (Daltons)	MP (Daltons)	Mw (Daltons)
1	844	822	8578
2	1225	3038	8169
3		95	
4		97	

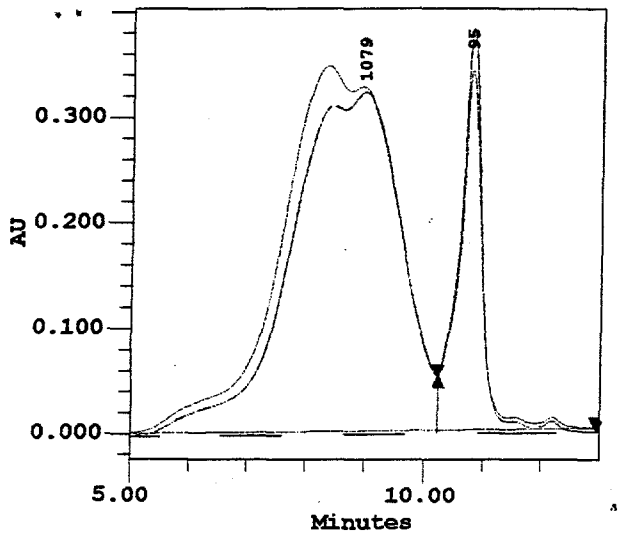

Figure 4.2a.

GPC Analysis of Preasphaltene Separation by a Silica Film in a THF Medium (T = 293K).
Time = 160 Minutes.
Pressure Drop: 30 PSID
1 - Downstream - Tube Side.
2 - Upstream - Shell Side.

#	Mn (Daltons)	MP (Daltons)	Mw (Daltons)
1	1102	1079	8879
2	1212	2958	10240
3		95	
4		97	

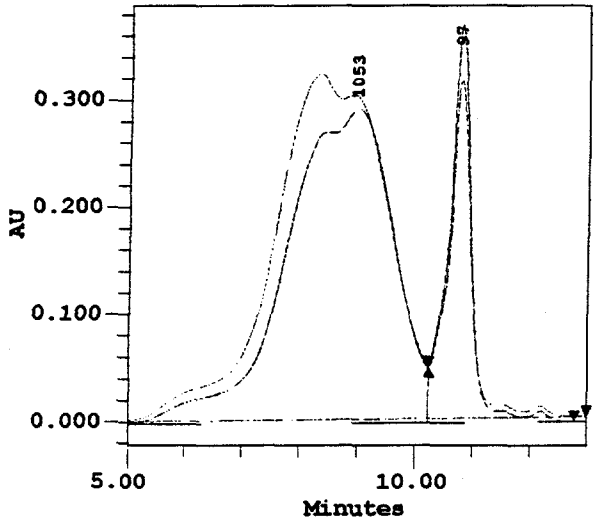

Figure 4.2b.

GPC Analysis of Preasphaltene Separation by a Silica Film in a THF Medium (T = 293K).
Time = 375 Minutes.
Pressure Drop: 30 PSID
1 - Downstream - Tube Side.
2 - Upstream - Shell Side.

#	Mn (Daltons)	MP (Daltons)	Mw (Daltons)
1	1070	1053	9121
2	1227	2958	10974
3		97	
4		99	

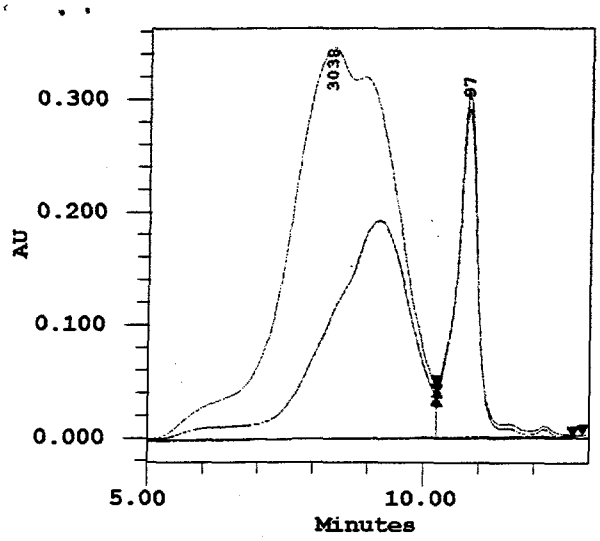

Figure 4.2c.
GPC Analysis of Preasphaltene Separation by a Silica Film in a THF Medium (T = 293K).
Time = 1295 Minutes.
Pressure Drop: 30 PSID
1 - Downstream - Tube Side.
2 - Upstream - Shell Side.

#	Mn (Daltons)	MP (Daltons)	Mw (Daltons)
1	818	802	7925
2	1262	3038	11483
3		95	
4		97	

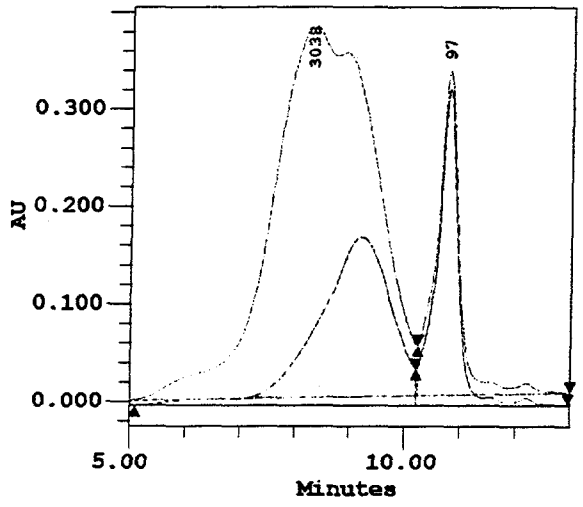

Figure 4.3.
GPC Analysis of Preasphaltene Separation by a Silica Film in a THF Medium (T = 293K).
Time = 4320 Minutes.
Pressure Drop: 60 PSID
1 - Downstream - Tube Side.
2 - Upstream - Shell Side.

#	Mn (Daltons)	MP (Daltons)	Mw (Daltons)
1	748	764	5747
2	1233	3038	9260
3		97	
4		97	

Figure 4.4a. Rejection Factors for a Silica Film with Preasphaltene-THF Solution

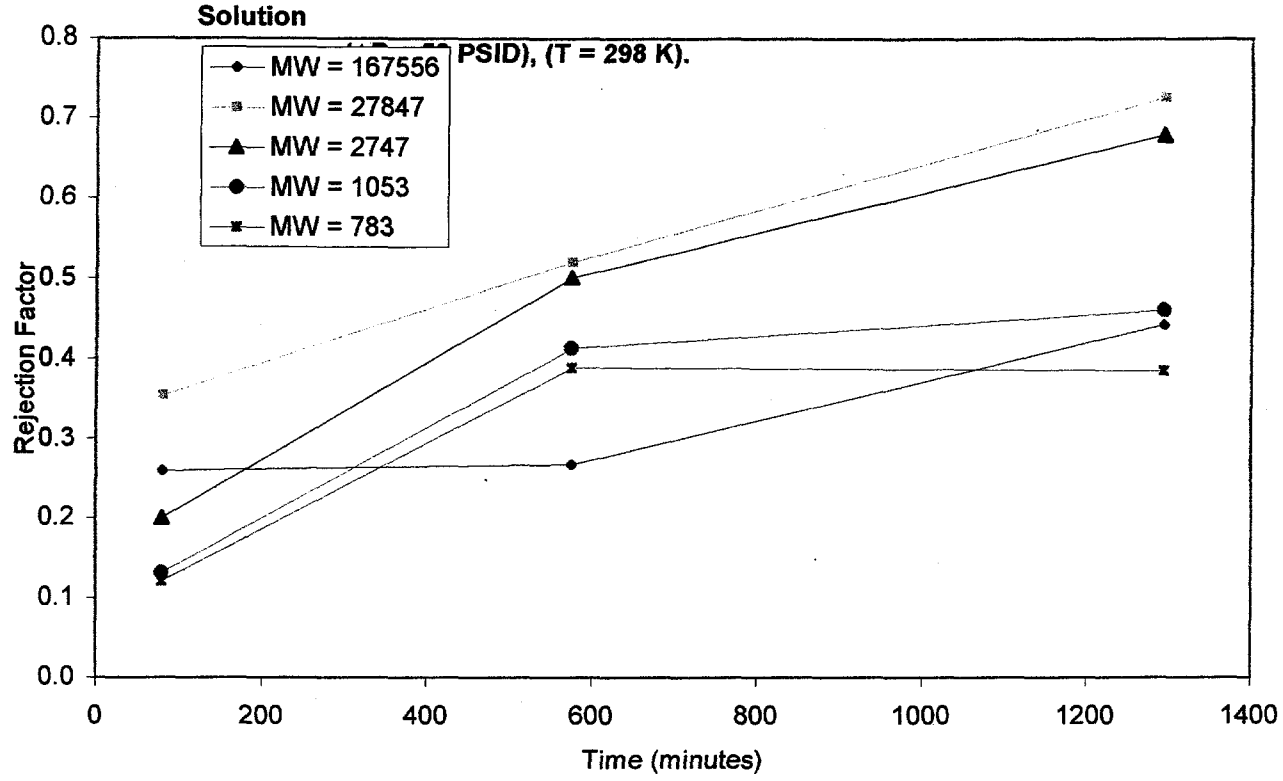

Figure 4.4b. Rejection Factors for a Silica Film with Preasphaltene-THF Solution

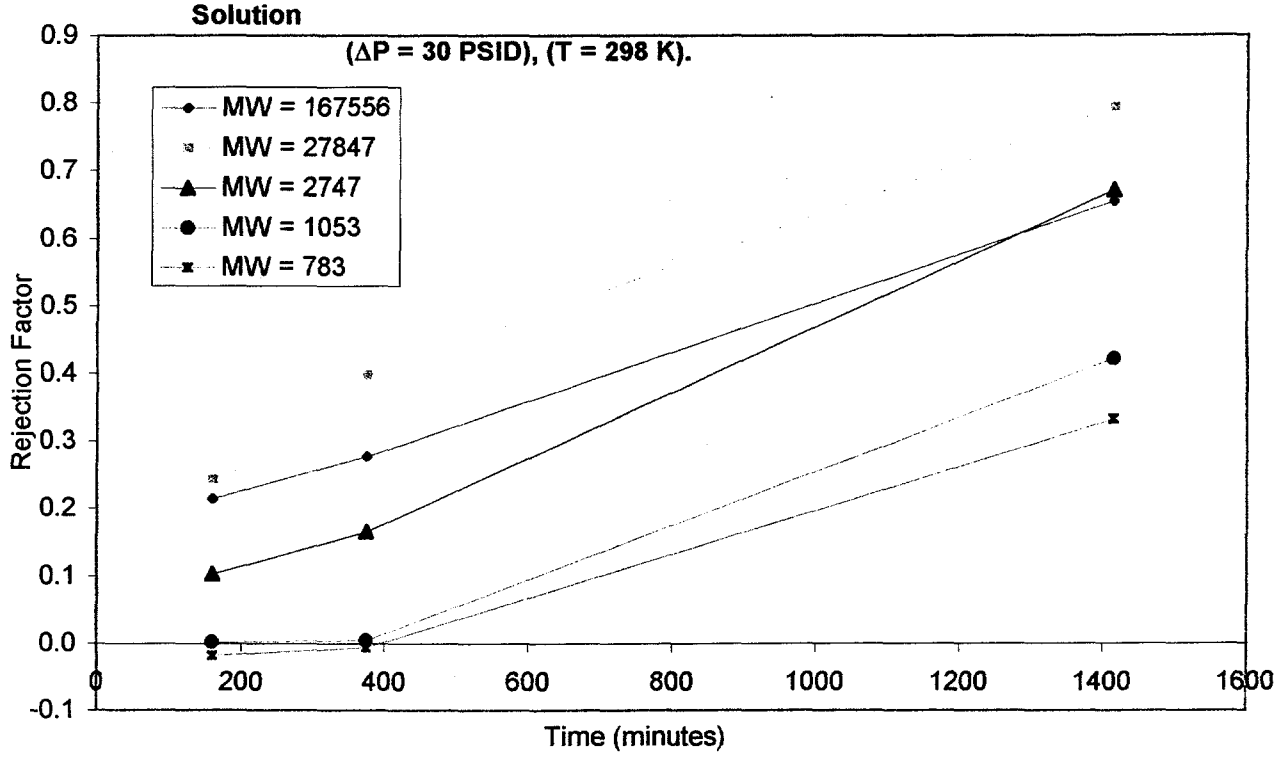

Figure 4.5a. Separation Factors for a Silica Film with Preasphaltene-THF Solution (ΔP = 50), (T = 298 K).

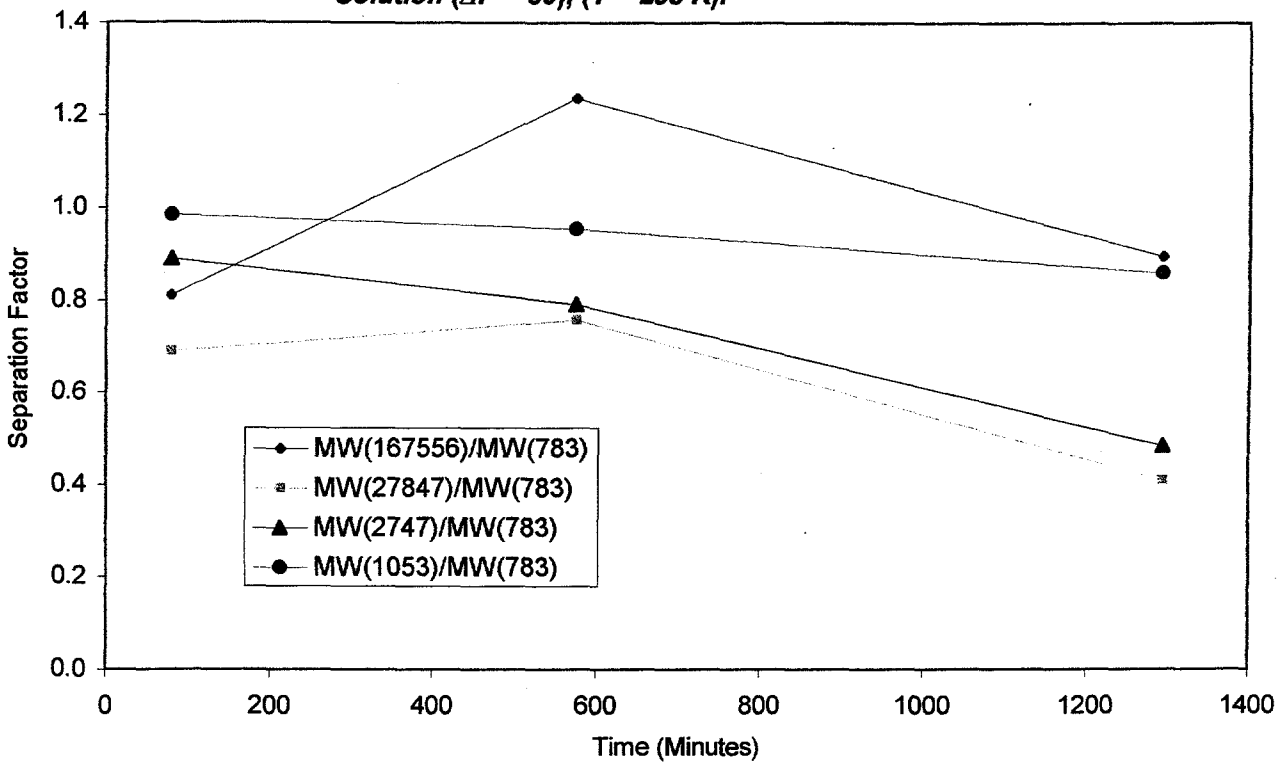

Figure 4.5b. Separation Factors for a Silica Film with Preasphaltene-THF Solution (ΔP = 30), (T = 298 K).

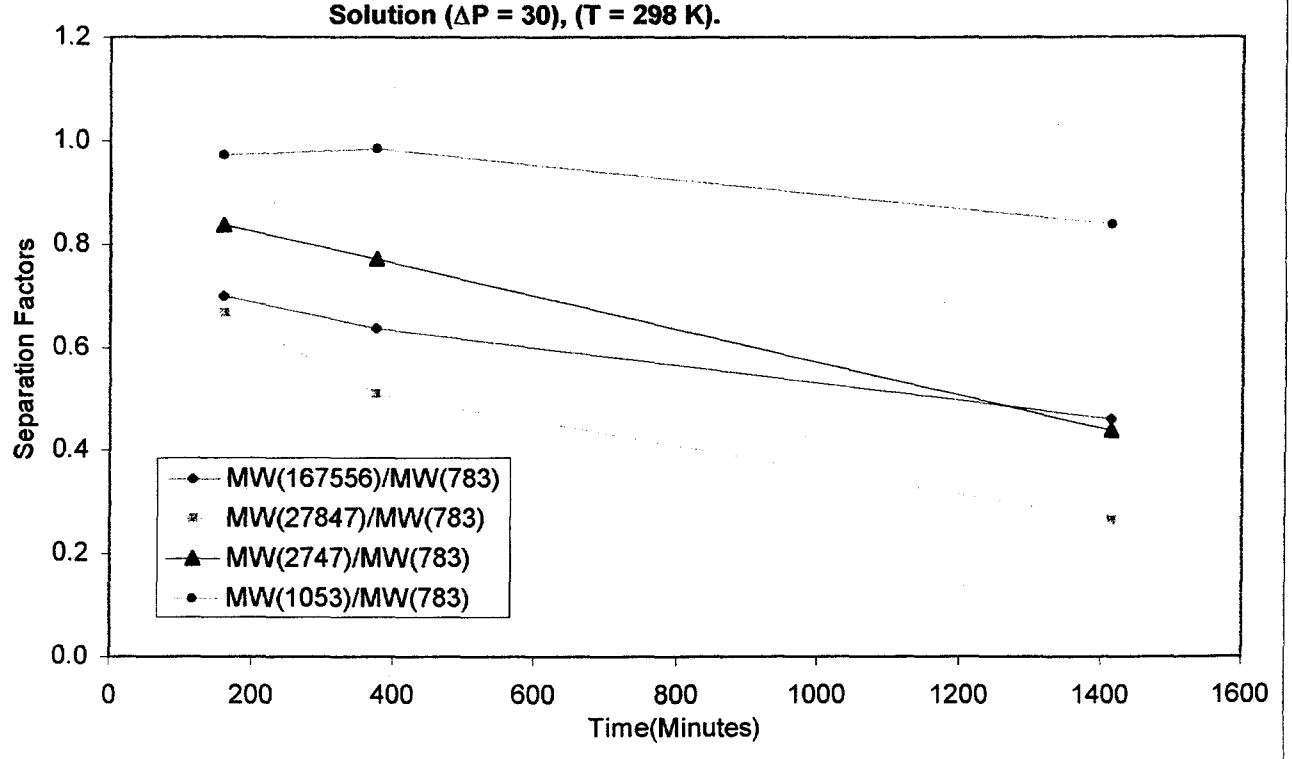

5. THE TRANSPORT OF COAL ASPHALTENES THROUGH CARBON MEMBRANES

The carbon membranes were prepared by the dip-coating and subsequent carbonization of polyfurfuryl Alcohol (PFFA) films on alumina substrates. The PFFA resin was obtained through Monomer-Polymer and Dajac Laboratories, Inc. A rough 1:1 weight ratio of PFFA resin to toluene was typically prepared by weighing out 25 g of resin and 25 g of toluene. The solution was heated to 65 °C with a moderate stirring rate for 24 hr. Afterwards, the solution was allowed to cool for 24 hr and then decanted. The remaining solution was then reheated to 40 °C for 4 hr. The resulting liquid was filtered through 0.2 μm syringe filters. The outer surface of the membrane was teflon taped and dipcoated in the solution for 3 min. The membranes were then drawn from the solution at a rate of 2 cm/min. After sufficient time, the membrane is removed and allowed to dry for at least 24 hr. The membranes are then carbonized under argon. The temperature profile chosen involves increasing the temperature at a rate of 1 °C/min to 100 °C, 200 °C, 350 °C, and 450 °C respectively. Each temperature is held there for 1 hr. The final step of the temperature profile involves holding the temperature constant at 600 °C for 4 hr.

The PFFA utilized for the deposition of these films had a nominal average molecular weight value M_n value of 1200 and a M_p value near 1600. Generally speaking, much higher molecular weights are more desirable in terms of forming smooth, durable films. Small molecular weights typically cause pore blockage and do little in the way of pore narrowing. The heating technique for polymer solution preparation described in the procedure described above serves to enhance the solubility of PFFA in toluene. However, during this heating procedure the polymer is polymerized further but also degraded to smaller molecular weight species. The lower molecular weights typically precipitate out of the toluene solvent and leave behind a slightly higher molecular weight average within the solution. This process should help in coating the substrates providing a suitable γ-alumina

film is present. Sample GPC results of the polymeric solutions utilized in the preparation of films are given in Figure 5.1.

Carbon membranes prepared as discussed from the deposition and carbonization of PFFA films have proven to be resistant to heat, but prone to degradation by THF and other reactive liquids. In testing with gases PFFA-based carbon films have shown high affinity to polar gases, like carbon dioxide, and little affinity, if any, to gases like methane. This may also explain the similar effects with polar liquids, like THF. Dip-coating of the substrates seems to work very inconsistently for these polymeric films since the process leaves much to chance due to the presence of rather small molecular weights and the rather large pore sizes of the substrates. Besides dip-coating another technique for preparing carbon membranes involves shearing and pressurizing a flow of polymeric solution through the membrane in the hope of applying an inherently smoother carbon film. Studies with such membranes are currently in progress.

We have concluded that THF cannot be used in transport studies of coal liquids with carbon membranes. The solvent is believed to break down the structure of the membrane as evidenced by the presence of small particles at the bottom of the autoclave upon conclusion of the transport experiments. We do not believe that THF, at least for the experiments taking place at lower temperatures, is hydrogenating the membrane carbon structure since no discoloration of the solvent is observed. The physical characteristics of the carbon layer superficially remain unchanged and the film still appears to be smooth and intact. On the other hand transport investigations with standard gases indicate a complete destruction of the pore structure. Obviously the THF must be attacking particular points on the surface of the film, such as pinholes, that are vulnerable to solvent attack. On the other hand our studies have shown that carbon membranes are quite stable to other aromatic solvents like xylenes. Transport of asphaltene solutions in xylene have, therefore, been investigated utilizing these membranes. The results of these studies rae shown in Tables 5.1-5.3 and in Figures 5.2-5.3. Raw GPC data of the transport experiments are shown in Figures 5a-5b.

At low transmembrane pressure drops, as shown in Figures 5.2a and 5.3a, the PFFA carbon membrane exhibits the typical behavior expected with a molecular sieve membrane. During the experiment rejection factors slowly increase with time and separation factors also improve. However, the rejection factors were observed to change upon shutting down and restarting the experiment. This indicates that the conditioning process is reversible probably being the outcome of the formation of thin film weakly held to the membrane and easily removable from the surface.

We are not exactly sure of how to explain the behavior at the higher transmembrane pressure drops, Figures 5.2b and 5.3b. The rejection factors that are initially high decrease significantly as a function of time. The separation factors on the other hand seem to be changing little as a function of experimental time. The results in these Figures have followed the experiments of Figures 5.2a and 5.3a and the initial decline in the rejection coefficients might be a manifestation of the reversibilty in the conditioning state of the membrane. It may be argued that at these relatively high transmembrane pressures, the high shear rates across the pores, results in the removal of any surface films formed during the conditioning of the surface during the lower transmembrane pressure drop experiments.

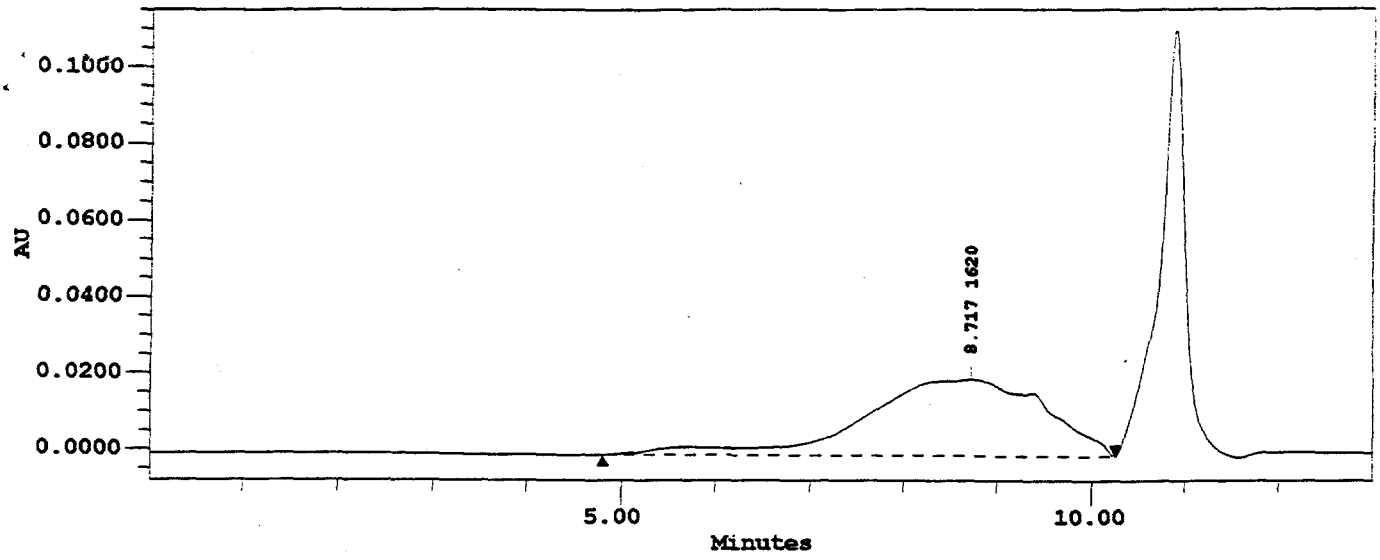

Figure 5.1 (above) Sample GPC analysis of Polyfurfuryl alcohol (PFFA) resin. M_n=1234; M_w=14739; M_p=1620.
(below) Sample GPC analysis of PFFA solution. M_n=1395; M_w=4103; M_p=1395.
(bottom) Sample GPC analysis of residual PFFA solution. M_n=994; M_w=23986; M_p=629.

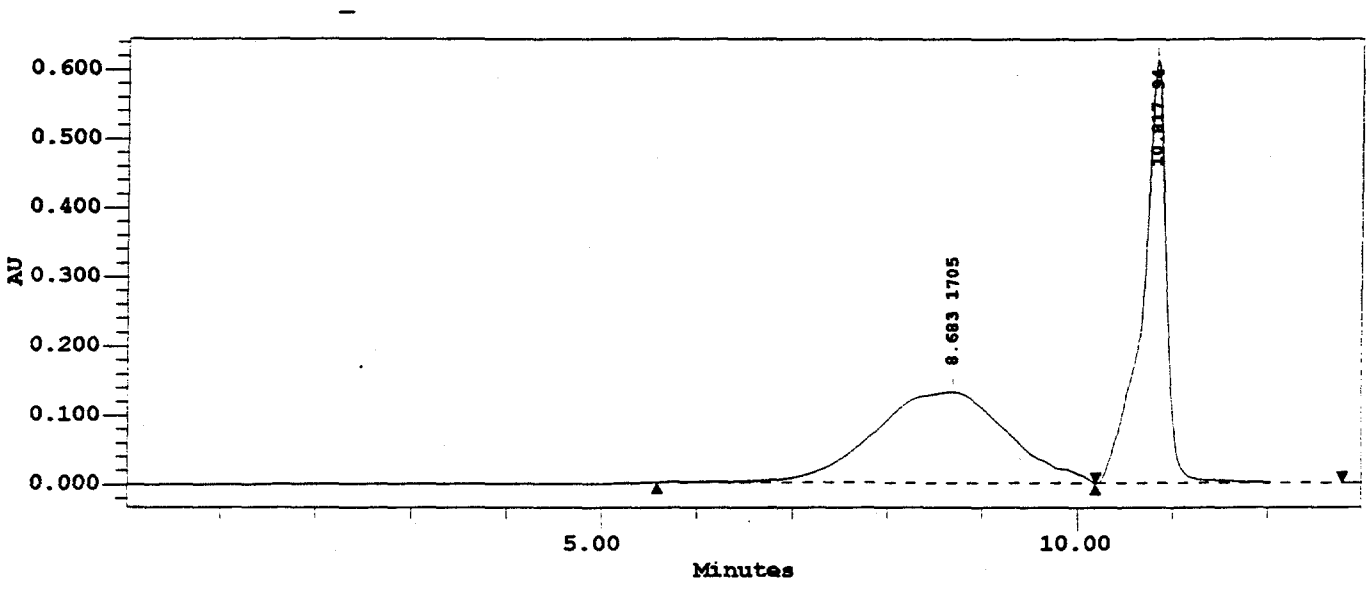

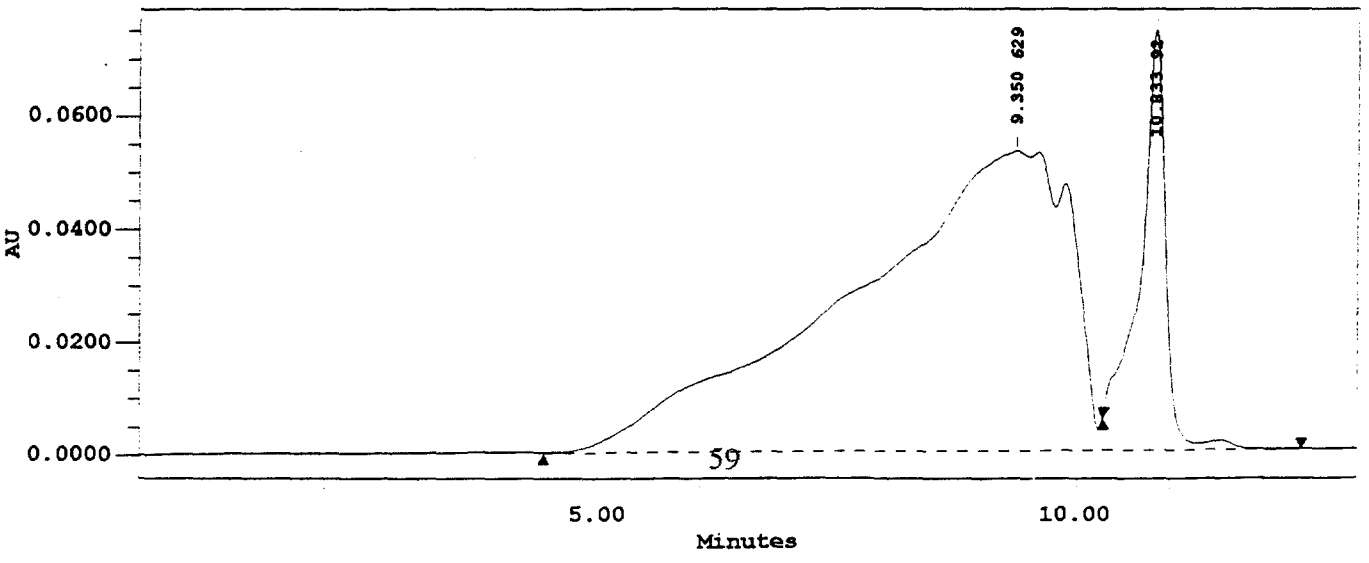

Table 5.1. Asphaltene-Xylene Filtration Experiments for a Carbon Film.
Nominal Shell Pressure: 0 psig Temperature: 298 K

Trial Number & Description	ΔP	Membrane Condition Time	Equil. Time	Total Area	Estimat. Conc.	Flow Rate
	(PSID)	(Min)	(Min)	(μV*Sec)	(g/L)	(ml/min)
(1.) Shell Side	35.1	60	60	5334707	0.4534	-
Tube Side		60	60	5089252	0.4305	0.7653
(2.) Shell Side	29.6	1410	150	6385218	0.5517	-
Tube Side		1410	150	4398265	0.3659	0.5246
(3.) Shell Side	29.8	3700	1290	5830386	0.4998	-
Tube Side		3700	1290	5717237	0.4892	0.5319
(4.) Shell Side	51.9	90	30	5005489	0.4226	-
Tube Side		90	30	4669668	0.3912	0.9899
(5.) Shell Side	49.3	1260	1170	9934978	0.4418	-
Tube Side		1260	1170	5220174	0.2214	0.8660
(6.) Shell Side	56.4	3835	135	5010170	0.4231	-
Tube Side		3835	135	4745145	0.3983	0.9363
(7.) Shell Side	53.7	4035	1200	4573743	0.3823	-
Tube Side		4035	1200	5152429	0.4364	0.9019

Table 5.2. Rejection Factors of Asphaltenes-Xylenes for a Carbon Film.
Temperature: 298 K

	GPC Time/*Molecular Weight*			
Trial Number	8.00	9.15	9.70	**Permeability**
	4311	***838***	***395***	**(ml/min/PSID/cm^2)**
1	0.0150	0.0861	0.0779	0.00283293
2	0.2805	0.0468	0.0244	0.00230274
3	0.7324	0.4042	0.4408	0.00231927
4	0.4818	0.2972	0.3312	0.00247828
5	0.2360	-0.0220	-0.0302	0.00228253
6	0.1349	0.0382	0.0292	0.00215713
7	0.0332	0.1218	0.1695	0.00218236

Table 5.3. MW-MW Separation Factors of Asphaltenes-Xylenes for a Carbon Film.
Temperature: 298 K

Trial	*4311-395*	*838-395*	*4311-838*
1	1.10	0.99	1.11
2	0.66	0.97	0.68
3	0.43	1.08	0.40
4	0.75	1.06	0.70
5	0.69	0.99	0.69
6	0.87	0.99	0.88
7	1.21	1.07	1.13

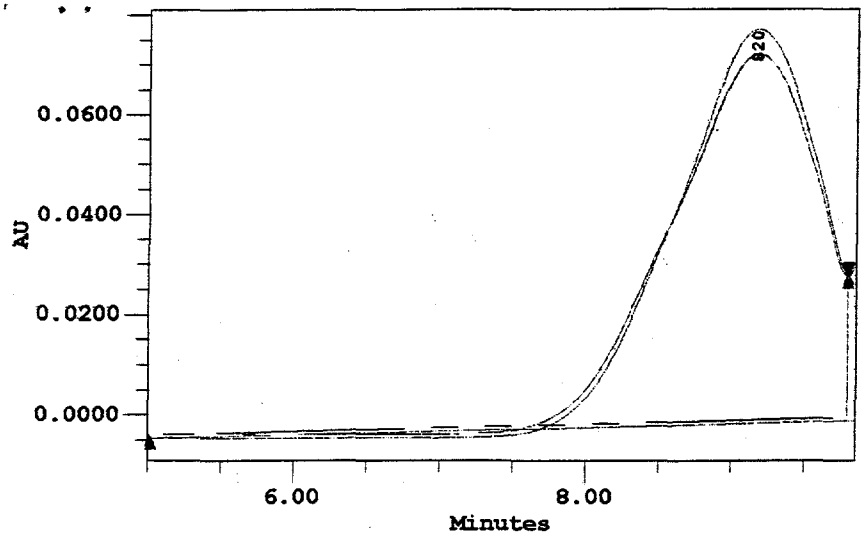

Figure 5a.1a.
GPC Analysis of Asphaltene Separation by a Carbon Film in a Xylene Medium (T = 293K).
Time = 60 Minutes.
Pressure Drop: 30 PSID
1 - Downstream - Tube Side.
2 - Upstream - Shell Side.

#	Mn (Daltons)	MP (Daltons)	Mw (Daltons)
1	842	820	3545
2	851	801	3472
3		197	
4		197	

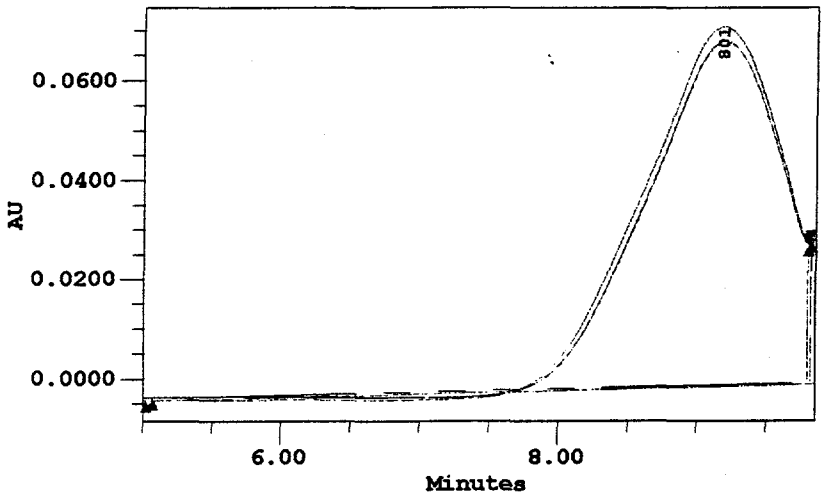

Figure 5a.1b.
GPC Analysis of Asphaltene Separation by a Carbon Film in a Xylene Medium (T = 293K).
Time = 1410 Minutes.
Pressure Drop: 30 PSID
1 - Downstream - Tube Side.
2 - Upstream - Shell Side.

#	Mn (Daltons)	MP (Daltons)	Mw (Daltons)
1	826	801	3494
2	839	801	3317
3		192	
4		192	

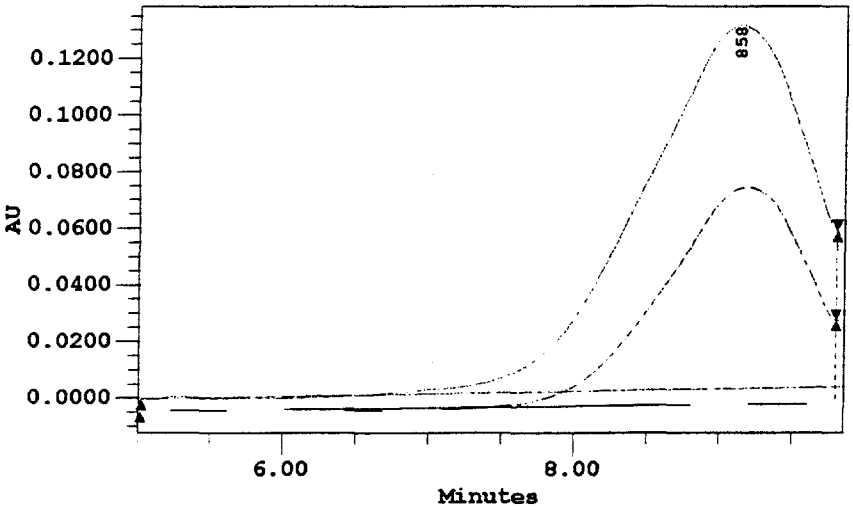

Figure 5a.1c.
GPC Analysis of Asphaltene Separation by a Carbon Film in a Xylene Medium (T = 293K).
Time = 3700 Minutes.
Pressure Drop: 30 PSID
1 - Downstream - Tube Side.
2 - Upstream - Shell Side.

#	Mn (Daltons)	MP (Daltons)	Mw (Daltons)
1	835	801	2945
2	900	858	2615
3		192	
4		197	

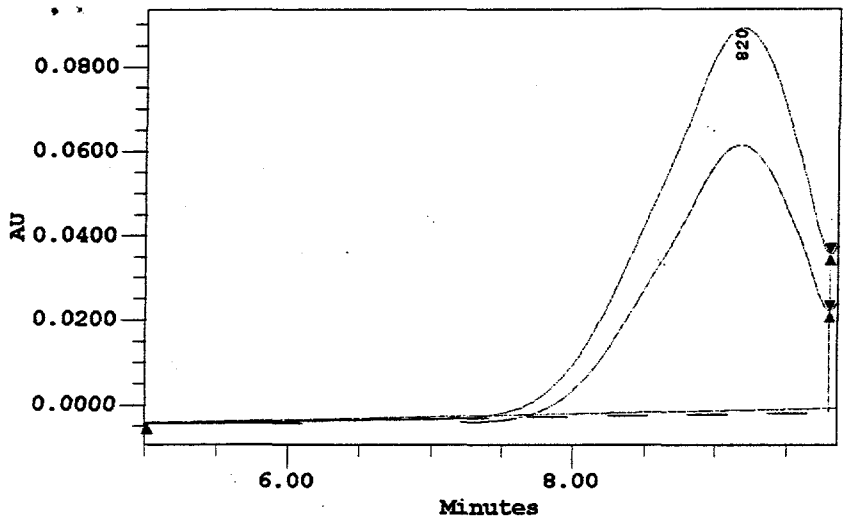

Figure 5b.1a.
GPC Analysis of Asphaltene Separation by a Carbon Film in a Xylene Medium (T = 293K).
Time = 90 Minutes.
Pressure Drop: 50 PSID
1 - Downstream - Tube Side.
2 - Upstream - Shell Side.

#	Mn (Daltons)	MP (Daltons)	Mw (Daltons)
1	851	820	3533
2	853	820	2783
3		192	
4		197	

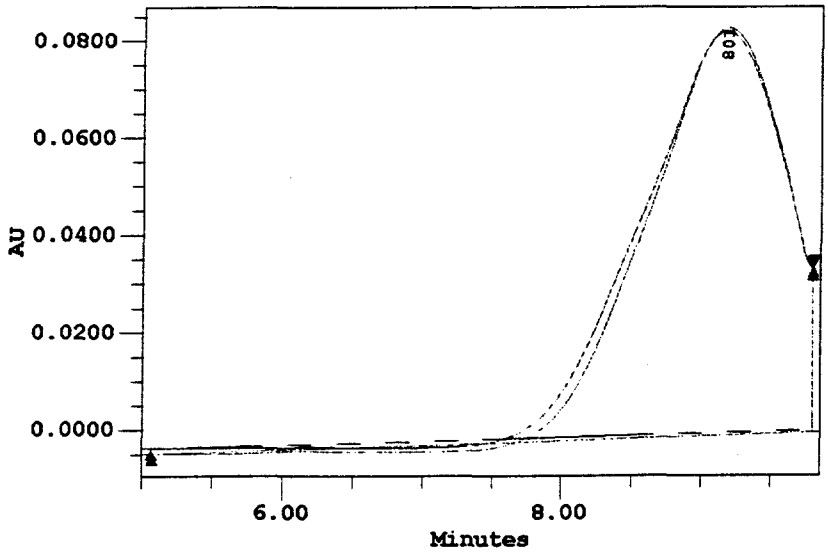

Figure 5b.1b.
GPC Analysis of Asphaltene Separation by a Carbon Film in a Xylene Medium (T = 293K).
Time = 1260 Minutes.
Pressure Drop: 50 PSID
1 - Downstream - Tube Side.
2 - Upstream - Shell Side.

#	Mn (Daltons)	MP (Daltons)	Mw (Daltons)
1	831	801	3227
2	851	801	3208
3		197	
4		197	

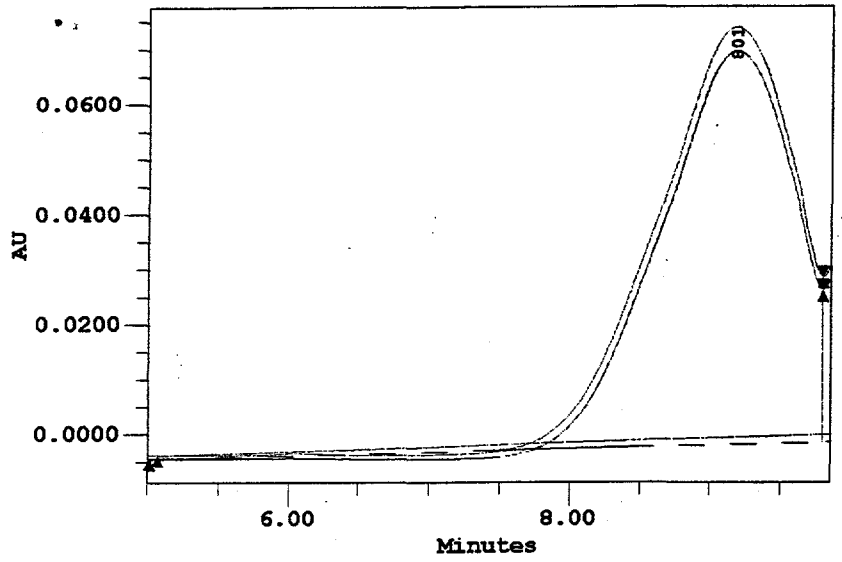

Figure 5b.1c.
GPC Analysis of Asphaltene Separation by a Carbon Film in a Xylene Medium (T = 293K).
Time = 3835 Minutes.
Pressure Drop: 50 PSID
1 - Downstream - Tube Side.
2 - Upstream - Shell Side.

#	Mn (Daltons)	MP (Daltons)	Mw (Daltons)
1	826	801	3664
2	833	801	3488
3		192	
4		197	

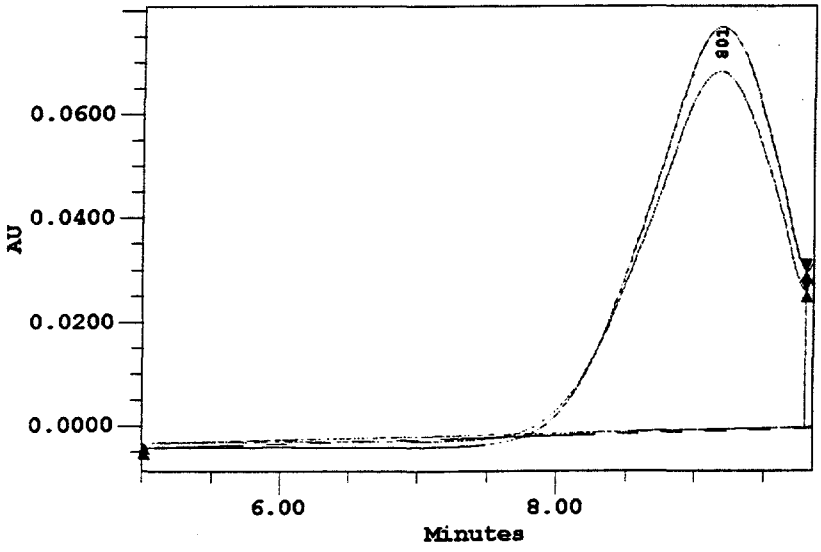

Figure 5b.1d.
GPC Analysis of Asphaltene Separation by a Carbon Film in a Xylene Medium (T = 293K).
Time = 4035 Minutes.
Pressure Drop: 50 PSID
1 - Downstream - Tube Side.
2 - Upstream - Shell Side.

#	Mn (Daltons)	MP (Daltons)	Mw (Daltons)
1	821	801	3804
2	828	820	3005
3		192	
4		197	

Figure 5.2a. Rejection Factors for a Carbon Film with Asphaltene-Xylene Solution (ΔP = 30 psid), (T = 298 K).

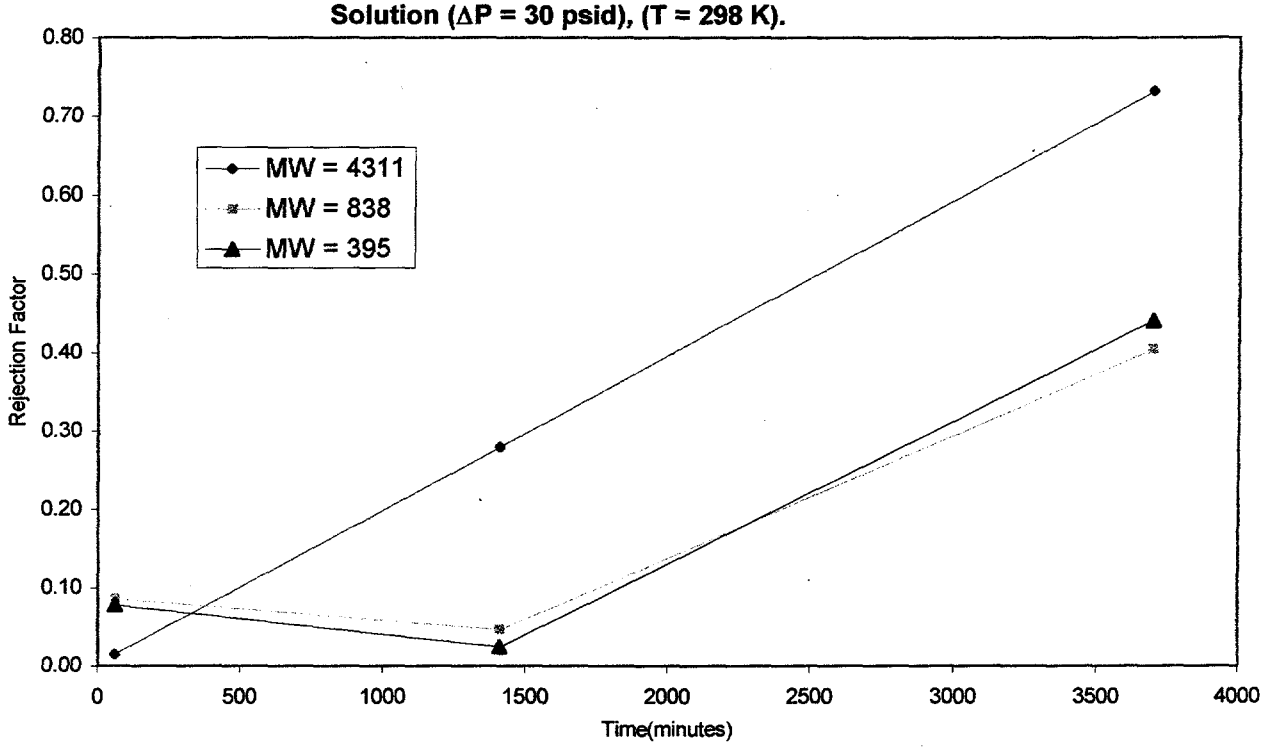

Figure 5.3a. Separation Factors for a Carbon Film with Asphaltene-Xylene Solution (ΔP = 30 psid), (T =298 K).

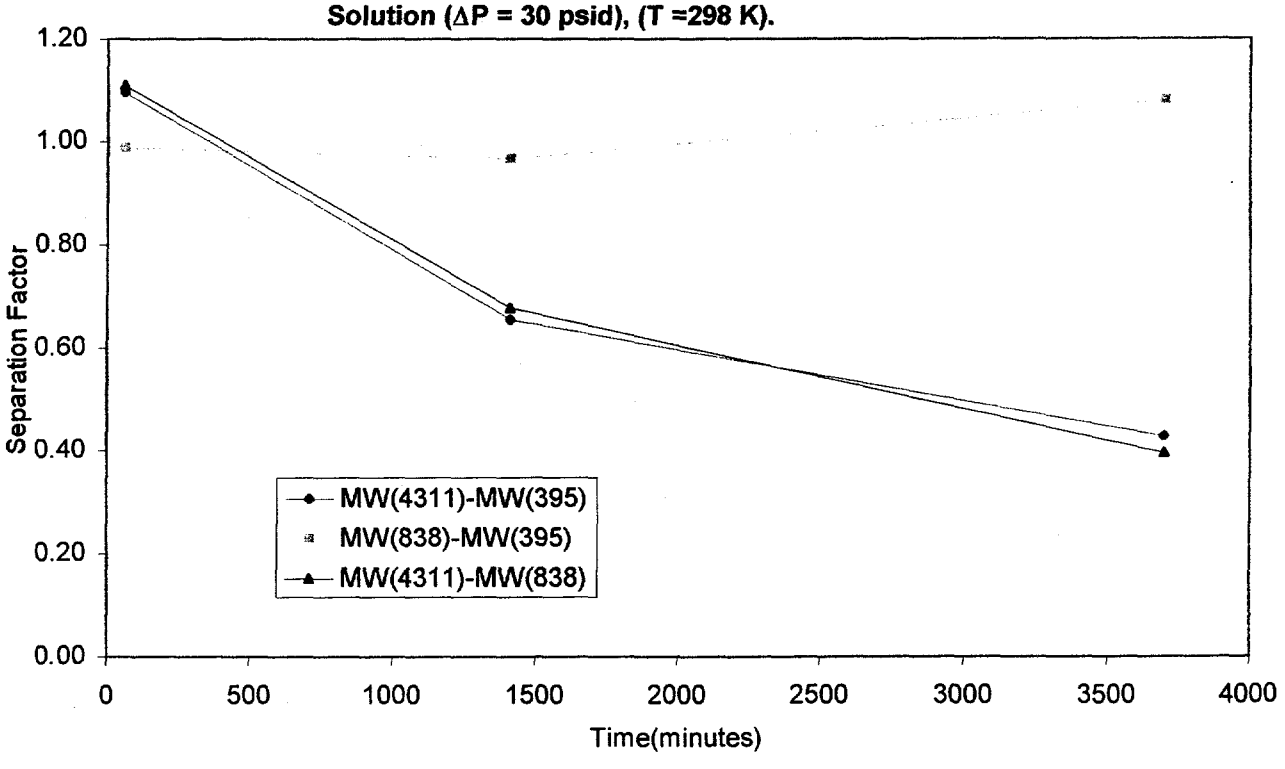

Figure 5.2b. Rejection Factors for a Carbon Film with Asphaltene-Xylene Solution (ΔP = 50 psid), (T = 298 K).

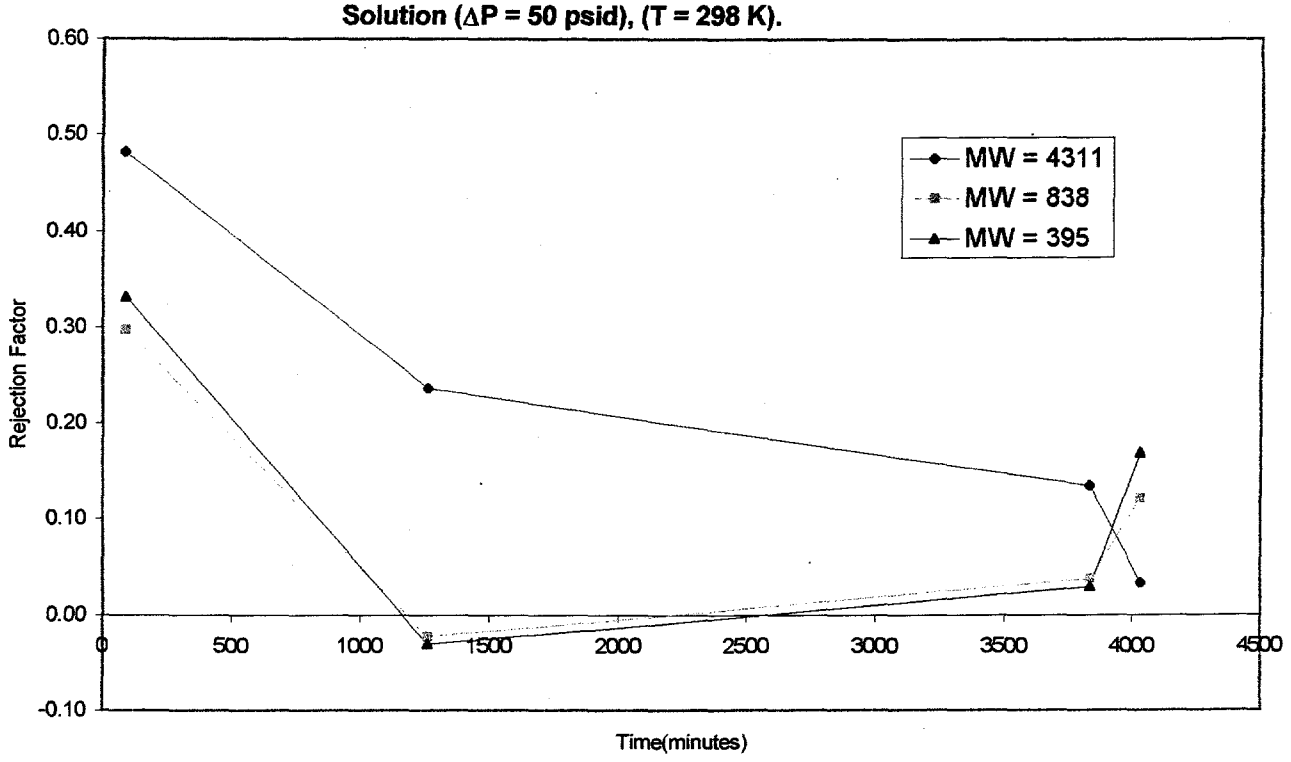

Figure 5.3b. Separation Factors for a Carbon Film with Asphaltene-Xylene Solution (ΔP = 50 psid), (T = 298 K).

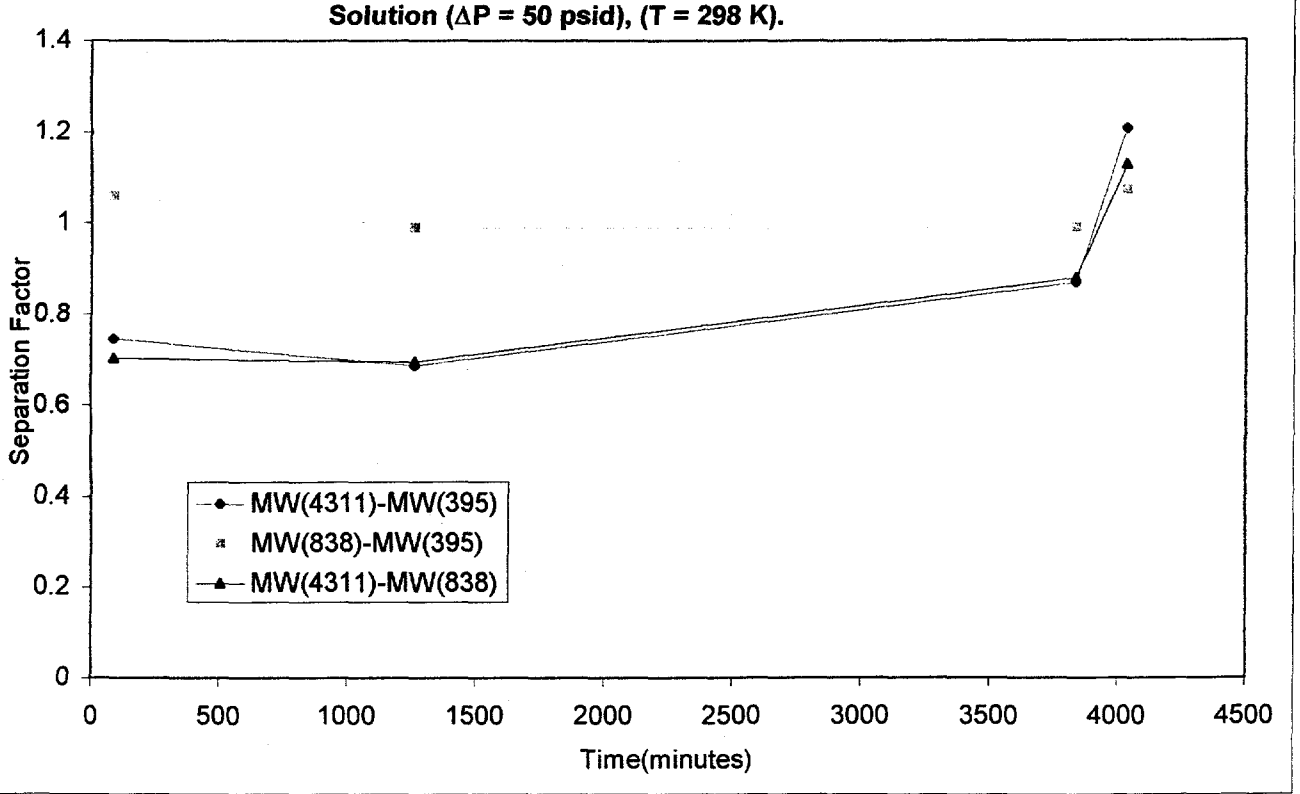

6. TRANSPORT INVESTIGATIONS OF A MODEL COAL OIL COMPOUND

As a model coal liquid molecule in this investigation we utilized 4-OH-diphenylmethane. Transport investigations with this model compound were conducted using a γ-Al_2O_3 coated US Filter membrane and a CVD SiO_2 coated US Filter membrane. The preparation of the γ-Al_2O_3 coated US Filter membrane has been previously discussed. The CVD Silica coated US Filter membrane was prepared by a chemical vapor deposition technique. Tetraethyl orthosilicate (TEOS) was used as the source of silica. A mixture of O_2 gas in He was used as the carrier gas for the TEOS to the CVD reactor where the US Filter porous alumina substrate was placed. It is important to control the concentration of O_2 in order to control the oxidation rate and prevent any damage to the substrate and excessive decomposition. The carrier gas mixture is saturated with TEOS by passing through a vaporizer that operates at different temperatures. Silica content, thickness of deposited layer and mean pore size of the composite membrane are controlled through varying the vaporizer temperature, carrier gas flow rate and composition, duration of deposition and temperature and pressure of the CVD reactor. While the exact mechanism of silica deposition is very complex and not very clear, the suggested reaction for silica deposition from TEOS is:

$$Si(OC_2H_5)_4+O_2 \rightarrow SiO_2+xC_2H_5OH+yC_2H_4+zCO_2+nH_2O$$

Ethanol can be further decomposed to H_2O and CO_2 if the concentration of oxygen in carrier gas is relatively high.

$$C_2H_5OH + O_2 \rightarrow 2CO_2 + 3H_2O$$

The final gaseous products and their component distribution basically depend on decomposition temperature and the ratio of oxygen to the other components.

The separation experiments were conducted following the following procedure: The membrane was baked in the oven at 300 °C for 24 hr to remove any surface deposits. Upon removing it from the oven the membrane was placed in a descicator to allow it to cool down to room temperature. It was immediately then installed in the experimental system described above which was subsequently heated to 200 °C for 1 hr to remove any moisture that might have been picked-up by the membrane during its transfer. All system ports were then closed and the system was pressurized with argon (during the experiment the exterior to the membrane volume was constantly purged with argon to eliminate any moisture for contaminating the system). 200 ml of model compound/xylenes solution (0.6 g/L) was pumped into the system, the permeate side valve of the membrane was opened and the autoclave pressure and temperature were increased to the desired point. Upon stabilization of the system's pressure samples were taken from both the autoclave and stirred beakers at every 5 min interval. The flow rate of solution coming out of the permeate side valve was constantly measured. The concentrations of samples from both side of the membrane (C_{high}, C_{low}) were analyzed by GC. The data are shown for three different values of transmembrane pressure in Figure 6.1. As one would have expected the γ-Al_2O_3 membrane shows little separation ability for the model compound. The CVD SiO_2 coated γ-Al_2O_3 membranes, however, exhibits a 30% rejection efficiency indicative of its much narrower pore size.

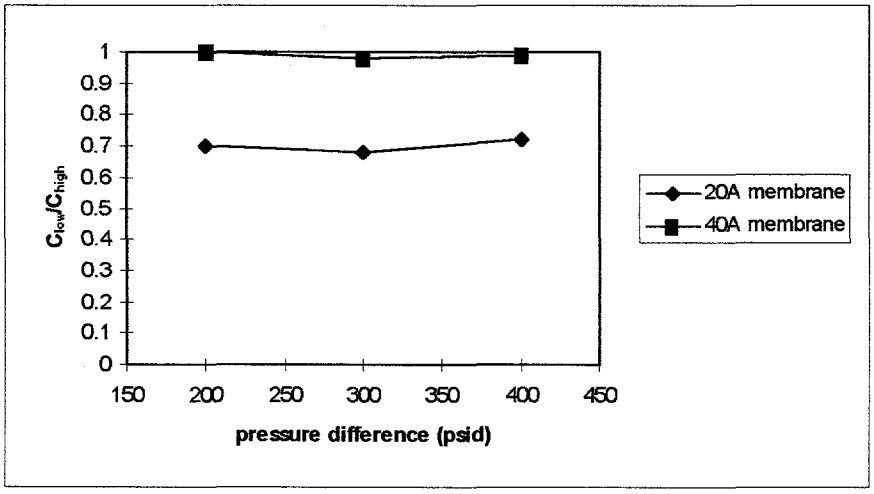

Figure 6.1. Membrane Separation of the Model Compound/Xylene Mixture at 200 °C.

7. THE TRANSPORT CHARACTERISTICS OF THE SOLVENT

In addition with the experiments with coal liquid solutions the transport characteristics of the solvents themselves through the membranes were also measured. The various solvents, whose transport characteristics were measured include tetralin, xylenes, THF and water. The measurement of the solvent's transport characteristics through each membrane was undertaken after the membrane had been wetted very well. Permeate flow rates are typically determined by weighing the amount of permeate that is collected over a predetermined period of time (e.g. 5 min). In the case of very low flows, a small, graduated capillary was attached to the permeate line, and the flow was measured by timing the rise of solvent between two points on the capillary. The goal of these experiments was first to calculate the permeance of the membranes themselves and second to investigate the effect of the solvent itself on the membrane structure. Figure shows the permeance of tetralin and xylenes through the γ-Al_2O_3 membrane and the CVD SiO_2 membranes.

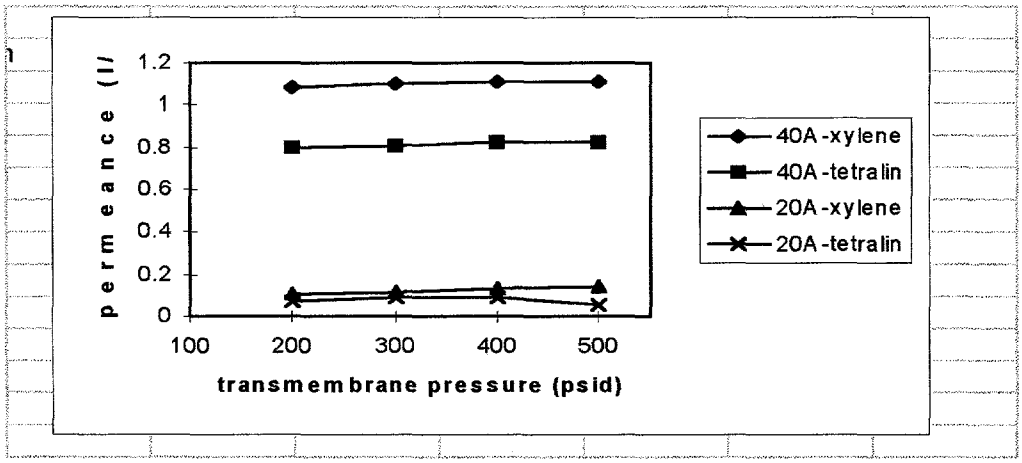

Figure 7.1. Permeances vs. Transmembrane Pressure at 80 °C

In the measurements taken to evaluate membrane stability the permeance at a

predetermined pressure gradient is studied as a function of time. The point at t=0 is taken as the intrinsic permeance (however, it should be noted there was a short time delay due to dead volume, ~20 cc, in the tube side of the system). The water, xylenes and THF permeance dropped from their initial value approximately 10%. These results indicate these two membranes have sufficient chemical stability towards these solvents.

A single γ-Al_2O_3 membrane was tested with THF for 1 year, over which time the permeance dropped only 20% (the reduction in permeability was most likely due to adsorption of trace contaminants either on the membrane surface or in the pores). The same is not true with the carbon coated microporous membranes which as previously discussed proved quite vulnerable to attack by THF. All membranes tested proved very resistant to compaction by pressure up to a transmembrane pressure gradient of 50 atm..and so did the polymeric seals and O-rings. The measured permeances for water, xylenes and THF are consistent with the leterature results of Clark et al. within the degree of scatter in the data measured for the thickness of the permselective layer between various membrane samples. In a study to specifically investigate this scatter in data three membranes were selected at random and their thickness was determined by viewing their cross-section using SEM. The thickness was measured at four different places on the photomirograph and then the four values were averaged. The thickness was fairly uniform for each sample. For the three membranes tested, the average top-layer thickness for each membrane was 3.50, 2.96 and 2.79 μm, respectively. This gave an overall average thickness of 3.1 μm and a data spread of 13% close to the error range between the values of permeances measured by us and those reported in the literature. Comparing the differences in the permeances of the various solvents measured with the same membranes we have concluded that there is an adsorbed layer of solvent molecules on the wall (no-slip condition), effectively reducing the cross-sectional area available for flow. The layer thickness however is a complicated function of parameters such as solvent size and the magnitude of long-range interactions (dispersion forces) between the solvent and pore wall.

8. CONCLUDING REMARKS

This document is an addendum to the Final Report document for DOE contract DE-FG22-92PC92527 prepared in response to the request by the DOE program manager Mr. Robert Warzinski. It contains unpublished experimental "raw" data on the transport/separation of coal liquids through membranes not included in the original report. The original goal of our University Coal Research program project was to further the fundamental understanding of the transport/separation of oil macromolecules through porous systems. Most of our experiments were carried out utilizing a variety of inorganic membranes. Additional information can be found in the original Final Report and in over 10 papers that have been published in archival journals which also describe an extensive program of research focusing on the agglomeration/delamination behavior of such systems.

9. LITERATURE CITATIONS

i. R. B. Bird, W. E. Steward, E. Lightfoot, *Transport Phenomena*, John Wiley & Sons, pp. 46, 1960.

ii. W. M. Deen, "Hindered Transport of Large Molecules in Liquid-Filled Pores", *AIChE Journal*, Vol. 33(9), pp. 1409,1987.

iii. P. M.Bungay and H. Brenner, "The Motion of a Closely Fitting Sphere in a Fluid-Filled Tube", *Int. J. Multiph. Flow*, vol. 1, pp. 25, 1973.

iv. A. M. Brites and M. N. de Pinho, "Mass Transfer in Ultrafiltration", *J. Membrane Sci.* Vol. 61, pp. 49, 1991.

v. J. Charpin, P. Bergez, F. Valin, H. Barnier, A. Maurel and J. M. Martinet, "Inorganic Membranes: Preparation, Characterization and Specific Applications," *High Tech Ceramics*, Material Sience Monographs, Vol. 38 (c), pp. 2211-2235, 1984.

vi. C. Vetier, M. Bennasar and B. Tarodo de la Feunte, "Study of the Fouling of a Mineral Microfiltration Membrane Using Scanning Electron Microscopy and Physiochemical Analyses in the Processing of Milk," *J. Dairy Research*, Vol. 55, pp. 381-400, 1988.